MICROFLUIDIC PROCESSES FOR SYNTHESIS OF PLASMONIC NANOMATERIALS

Suhanya DURAISWAMY

NATIONAL UNIVERSITY OF SINGAPORE

2011

MICROFLUIDIC PROCESSES FOR SYNTHESIS OF PLASMONIC NANOMATERIALS

Suhanya DURAISWAMY

(M.Sc. (Hons.) Physics, B.E. (Hons.) Chemical Engineering,
Birla Institute of Technology & Science, Pilani, India)

A THESIS SUBMITTED

FOR THE DEGREE OF DOCTOR OF PHILOSOPHY

DEPARTMENT OF CHEMICAL AND BIOMOLECULAR ENGINEERING

NATIONAL UNIVERSITY OF SINGAPORE

2011

To My Parents

With Love

Acknowledgements

I thank my supervisor Dr Saif A. Khan for giving me this opportunity to work in his research group. He is a wonderful guide and has always been motivating and positive in his approach giving me enough freedom to pursue my work. Thank you Dr Khan for all the valuable advice, thought provoking discussions and for encouraging me to think laterally; you helped me develop an inquisitive mind and also instilled in me the desire to learn from everything; I am proud of being your first student. Special thanks for the support and encouragement during the last year of my graduate life.

I appreciate Dr Ramam and all at IMRE for providing me access to use the clean room facilities. I acknowledge and recognize that, this research would not have been possible without the financial assistance from MOE as well as support from the Chemical and Biomolecular Engineering Department, NUS.

Life in Singapore would not have been the same without my friends and family. I thank my labmates Pravien, Sophia, Zahra, Abhinav and Dr Rahman. Special thanks to Pravien for being there always, be it discussions and help with experiments or support and encouragement during the wee hours of the night when nothing seemed to go right. Thanks Pravien, for the support throughout these years, especially for helping me with all my experiments during the last year. Many thanks to Balaji, Sounderya, Shankari, Ravi and Anjaiah for their support during the first year and for educating me about Singapura. Thanks to Randy and Jasmine, my undergrad FYP mentees for their experimental support. Thanks to all my other labmates Reno, Arpi, Carl, Dominic, Josu, Prasanna, the two Anna's and Daniel for making the lab a fun place to be in.

My eternal gratitude goes to my parents and to my sister. I thank my husband Indirakumar for his unrelenting support throughout these five years, be it sitting next to me in the lab during my late night experiments or listening to my ramblings about research progress or reading

through my drafts. Thank you Ikay for everything; I am here because of you. Finally, thanks to Kimaya, my 8 month old. You have added meaning to our lives. Thank you for bearing with me during all my experimental fiascos in lab those 10 months, especially with CO and also for adjusting with my research career without a complaint.

Contents

List of Figures

List of Publications

PATENT

1. Duraiswamy, S & Khan, S.A. 'Scalable Continuous Sub-Micron Size Material Synthesis in Multi-Phase Micro Flow System', US Provisional Application No.: 61/310,394 (2010).

PUBLICATIONS

1. Duraiswamy, S.; Khan, S. A., Plasmonic Nanoshell Synthesis in Microfluidic Composite Foams. *Nano Letters* **2010,** *10*, 3757–3763.
2. Duraiswamy, S.; Khan, S. A., Droplet-Based Microfluidic Synthesis of Anisotropic Metal Nanocrystals. *Small* **2009,** *5* (24), 2828–2834.
3. Khan, S. A.; Duraiswamy, S., Microfluidic emulsions with dynamic compound drops. Lab on a Chip 2009, 9, 1840–1842.
4. Khan, S. A.; Duraiswamy, S.,Controlling bubbles using bubbles – Microfluidic synthesis of ultra-small gold nanocrystals with gas-evolving reducing agents. (2012, on web; **DOI:** 10.1039/C2LC21198J)

PUBLICATIONS IN PROGRESS

1. Duraiswamy, S.; Rahman, M.T.; Khan, S. A., Microfluidic Compound Drops with Reactive Gas for Synthesis of Gold Nanoshells
2. Duraiswamy, S.; Khan, S. A., Integrated Microfluidic Synthesis of Anisotropic Gold Nanocrystals

CONFERENCE PUBLICATIONS

1. Plasmonic Nanoshell Synthesis in Microfluidic Composite Foams With Reactive Gases, Md. Taifur Rahman , Suhanya Duraiswamy and Saif A.Khan, *International Conferences on Materials for Advanced Technologies* ***(ICMAT),*** **August 2011**.
2. Microfluidic Compound Drops with Reactive Gases for Synthesis of Gold Nanoshells, Suhanya Duraiswamy, Md. Taifur Rahman and Saif A.Khan, *Advances in Microfluidics and Nanofluidics and Asian-Pacific International Symposium on Lab On Chip* ***(AMN-APLOC),*** **January 2011**.
3. **Continuous Colloidal Synthesis of Plasmonic Nanostructures in Flowing Microscale Foams,** Saif A. Khan and Suhanya Duraiswamy, *Materials Research Society* ***(MRS),*** **November, 2010**
4. Nanoparticle Factories in Flowing Foams, Suhanya Duraiswamy and Saif A. Khan, *International Conference on Miniaturized Systems for Chemistry and Life Sciences* ***(μTAS),*** **October 2010**.
5. Droplet-based Microfluidic Synthesis of gold nanorods and nanospheres, Suhanya Duraiswamy and Saif A. Khan, *International Conference on Biotechnology and Nanotechnology* ***(ICBN),*** **July 2010**

6. Continuous-flow digital gold nanoshell synthesis in ordered microfluidic composite foams, Suhanya Duraiswamy and Saif A. Khan, *International Conference on Biotechnology and Nanotechnology* ***(ICBN),*** **July 2010**.
7. A Novel Multiphase Microfluidic Method for Synthesis of Metallodielectric Core-Shell Nanostructures, S. Duraiswamy and S. A. Khan, *International Conferences on Microreaction Technology* ***(IMRET),*** **March 2010**.
8. Microfluidic Emulsions with Dynamic Compound Drops, S. Duraiswamy and S. A. Khan, *International Conferences on Microreaction Technology* ***(IMRET),*** **March 2010**.
9. Droplet-based Microfluidic Synthesis of Anisotropic Metal Nanocrystals, S. Duraiswamy and S. A. Khan, International Conferences on Microreaction Technology ***(IMRET),*** **March 2010.**
10. Droplet-based Microfluidic Synthesis of Anisotropic Gold Nanocrystals, S. Duraiswamy and S. A. Khan, (**ChBE-GSA), January 2010.**
11. Microfluidics with compound 'bubble-drops', Saif A. Khan and Suhanya Duraiswamy,AIChE - APS, **November 2008.**

List of Symbols

E	-	Electric field ($V.m^{-1}$)
B	-	Magnetic induction (tesla)
D	-	Electric displacement ($C.m^{-2}$)
H	-	Magnetic field ($A.m^{-1}$)
ρ_F	-	Free charge density ($C.m^{--3}$)
$\boldsymbol{J}_F$	-	Free current density ($A.m^{-2}$)
P	-	Electric polarization ($C.m^{-2}$)
M	-	Magnetization ($A.m^{-1}$)
ϵ_0	-	Permittivity of free space ($F.m^{-1}$)
μ_0	-	Permeability of free space ($H.m^{-1}$)
ϵ	-	Extinction coefficient ($m^2.mol^{-1}$)
C	-	Concentration ($mol.m^{-3}$)
A'	-	Absorbance (no unit)
λ_{max}	-	Peak wavelength (nm)
A_0	-	Frequency factor (s^{-1})
R	-	Gas constant ($J.K^{-1}.mol^{-1}$)
T	-	Absolute temperature (K)
K_e	-	Equilibrium constant $(mol.L^{-1})^n$ where n = (total number of products) – (total number of reactants)
k	-	Rate constant ($mol^{1-n}.L^{n-1}.s^{-1}$)
V_{atm}	-	Atomic volume ($m^3.kmol^{-1}$)
V_m	-	Molar volume ($m^3.mol^{-1}$)
k_B	-	Boltzmann constant ($J.K^{-1}$)
J	-	Flux of diffusing species ($Kgsolute.m^{-2}.s^{-1}$)
D	-	Diffusion coefficient ($m^2.s^{-1}$)
Q	-	Volumetric flow rate ($m^3.s^{-1}$)
p	-	Partial pressure (Pa)
ΔP	-	Pressure difference (Pa)
r	-	Radius (m)
l	-	Length (m)
d	-	Depth (m)
w	-	Width (m)
h	-	Height (m)
τ	-	Time (s)
μ	-	Viscosity ($N.s.m^{-2}$)
γ	-	Surface tension ($N.m^{-1}$)
ρ	-	Density ($Kg.m^{-3}$)
v	-	Velocity ($m.s^{-1}$)
Re	-	Reynolds number (dimensionless)
Pe	-	Peclet number (dimensionless)

List of Abbreviations

i.d.	- Inner/Internal diameter
o.d.	- Outer diameter
AA	- Ascorbic Acid
AR	- Aspect Ratio
CTAB	- Hexadecyltrimethylammonium bromide
DI	- Deionized water
DDA	- Discrete Dipole Approximation
EGFR	- Epidermal Growth Factor Receptor
EPR	- Enhanced Permeability and Retention
FCC	- Face Centered Cubic lattice
FESEM	- Field Emission Scanning Electron Microscopy
FWHM	- Full Width at Half Maximum
GNR	- Gold NanoRods
LSP	- Localized Surface Plasmons
LPR	- Longitudinal Plasmon Resonance
PC	- Poly carbonate
PDMS	- Poly (dimethylsiloxane)
PEEK	- Poly (etheretherketone)
PTFE	- Poly (tetrafluoroethylene)
PVC	- Poly (vinyl chloride)
RTD	- Residence Time Distributions
SEM	- Scanning Electron Microscopy
SERS	- Surface Enhanced Raman Spectroscopy
SPR	- Surface Plasmon Resonances
TEM	- Transmission Electron Microscopy
THPC	- Tetrakis(hydroxymethyl)phosphonium chloride
TPR	- Transverse Plasmon Resonance
UPD	- Under Potential Deposition
UV-vis	- Ultraviolet-visible

Summary

Plasmonic nanomaterials are at the forefront of current research due to their fascinating optical properties. These properties are extremely sensitive to particle morphology, composition as well as the physical structure of the nanoparticles. Nanomaterials for applications such as biomedical imaging and therapy require precisely controlled particle size distributions for reliable diagnosis and effective treatment. Conventional methods for the synthesis of such nanomaterials rely on wet chemical synthesis in small batches, and suffer from several drawbacks resulting in mixed particle populations. Controlled reagent dispensing and mixing are key challenges limiting the applicability of these lab-scale synthetic chemistry techniques in large-scale production. This thesis aims to develop microfluidic processes that overcome these limitations and are capable of controllably synthesizing such nanomaterials with precisely defined properties. The work in this thesis specifically focuses on gold nanocrystals of varying shapes and sizes and metallodielectric gold nanoshells.

As a first demonstration, anisotropic gold nanocrystal dispersions were synthesized using a droplet-based microfluidic method. An analysis of the parameter space of reagent flow rates was performed to identify the operating conditions ideal for droplet breakup and formation. Synthesis experiments were then performed using a well-established seeded growth protocol to achieve the synthesis of the desired nanostructures using pre-synthesized gold nanocrystals as seeds. A crucial limitation of this method is that the nanocrystal seeds are synthesized off-chip using a batch-based protocol. Batch-to-batch variations in seed quality can introduce disparities between successive experimental runs. In order to overcome this drawback, a method for online chip-based seed synthesis was developed using sodium borohydride as the reducing agent. Segmented gas-liquid flow formed by the injection of nitrogen gas bubbles in the microchannel was employed to transport the released hydrogen from the aqueous reagent solution into the nitrogen bubbles that acted as large inert reservoirs. This technique completely prevented the uncontrolled formation of gas bubbles in the aqueous

reagents that could potentially disrupt the flow. Attempts at integrating the seed synthesis and the use of these seeds for the synthesis of nanocrystals on a single chip are underway.

Finally, an interesting class of three phase gas-liquid-liquid flows were introduced in this thesis, and used to demonstrate the synthesis of gold nanoshells on colloidal silica surfaces. Analysis of the three phase microfluidic flows was performed to identify suitable regimes of operation and to characterize the dispensing and mixing of reagents. Initial proof-of-concept experiments were performed to show the synthesis of nanoshells of varying thickness as well as ‘nano-islands’ consisting of gold islands of varying size on the silica surfaces. As a final demonstration of the utility of the three-phase flows, a reactive gas (carbon monoxide) was used instead of the inert gas in three phase flows to demonstrate the synthesis of gold nanoshells.

1. Introduction

1.1. 'Nano-World'

Richard Feynman, in his famous lecture on nanotechnology[1] said "There's plenty of room at the bottom"; the 'room at the bottom' is now expanding explosively and rapidly. Scientists all over the world are focusing their attention on nanoscale research and the impact has had an effect in all fields of science and technology including medicine, electronics, biomaterials and energy production to cite a few. Research on nanoscience has revolutionized science and has begun to impact the world economy and society.[2]

The societal impact of nanoscience is apparent from the fact that over thirty countries including US, Japan, Korea, Taiwan, Germany, and U.K., have established nanotechnology research and development programs in the recent years in acknowledgement of the immense potential nano-research can offer to science and technology. The National Nanotechnology Initiative (NNI) launched by the U.S. government specifically for nano-research and development has invested nearly 1.8 billion USD in 2011[3] while the European Research Area through FP6 (Sixth Framework Programme 2005-2010) had budgeted 1,429 million Euros for the 'nanotechnologies and nanosciences, knowledge-based multifunctional materials and new production processes and devices'.[4] On the economy side of the impact, the National Science Foundation projected that nanotechnology will be a trillion dollar industry by 2015 worldwide.[2] To support this prediction, in August 2009, the project on emerging nanotechnologies, a leading database with an on-line inventory of nanotechnology based consumer products listed about 1015 products with new ones hitting the market at a pace of 2-3 per week.[5] Most of these applications are limited to the use of "first generation" passive nanomaterials (details in Section 1.2) such as titanium dioxide (sunscreen, cosmetics and some food products), silver particles (food packaging, clothing, disinfectants), zinc oxide (in surface coatings, paints) etc.[6]

This notwithstanding, the impact from the later generations of nanotechnology is considered to lead on to a general-purpose technology affecting all industries in common, with means for new production, exponential proliferation of manufacturing systems, cheap rapid prototyping, giving rise to economic discontinuity (due to inexpensive raw materials and potentially negligible production cost), social disruption (due to portable, desktop-like factories) and global transformations.[7] Molecular manufacturing and biomimetic nanomachines are envisioned to be the outcome of this nanorevolution. This chapter details the science and technology involved in this nanorevolution and also describes nanomaterials in detail with special focus on metallic nanomaterials. The techniques involved in the synthesis of monodisperse metallic nanomaterials are discussed and the challenges faced currently by the nanomanufacturing community are highlighted.

1.2. Nanoscience and Nanotechnology

Nanoscience is the art of manipulating a few hundred to millions of atoms to make up chemical or biological structures that are 1-100 nanometers in dimension. At this scale, these structures exhibit certain unique electrical, mechanical, optical, chemical, and/or biological properties that are fundamentally different from their bulk counterparts. Nanoscience deals with the creation of new chemical or biological structures by controlling the functionality of matter and its assembly at nanometer length scales, understanding their novel properties, and learning to organize these nanostructures into larger and more complex functional units or entities. Nanoscience is inherently a fabulous adventure, where the frontiers between fundamental science and applied science becomes an area of exchange and innovation.[8] According to the nanoscience group at MIT, "the vision of nanoscience ultimately combines the science and engineering of man-made and biological entities, controlled at the nanometer scale, and assembled into complex, engineered structures that can interact with their surroundings at dimensions ranging from that of molecules to that of humans and beyond".[9]

Nanotechnology is an emerging set of tools, techniques and unique applications of nanoscience viz. nanotechnology is the engineering of functional systems at the molecular scale and is believed to be developing in four stages according to Mihail (Mike) Roco of the U.S. National Nanotechnology Initiative as shown in Figure 1.1.[7,10] "The first generation is that of passive nanostructures, materials designed to perform one task. The second phase introduces active nanostructures for multitasking; for example, actuators, drug delivery devices, and sensors. The third generation, which we are just entering, will feature nanosystems with thousands of interacting components. A few years after that, the first integrated nanosystems, functioning much like a mammalian cell with hierarchical systems within systems, are expected to be developed".[7,10] This technology is not new, but is a combination of several existing technologies, combined with the new found ability to observe and manipulate at the atomic scale using instruments such as scanning tunnelling microscopy (STM), scanning electron microscopy (SEM), transmission electron microscopy (TEM), atomic force microscopy (AFM) and the like which makes the field appealing from the business, scientific and political viewpoints.[11]

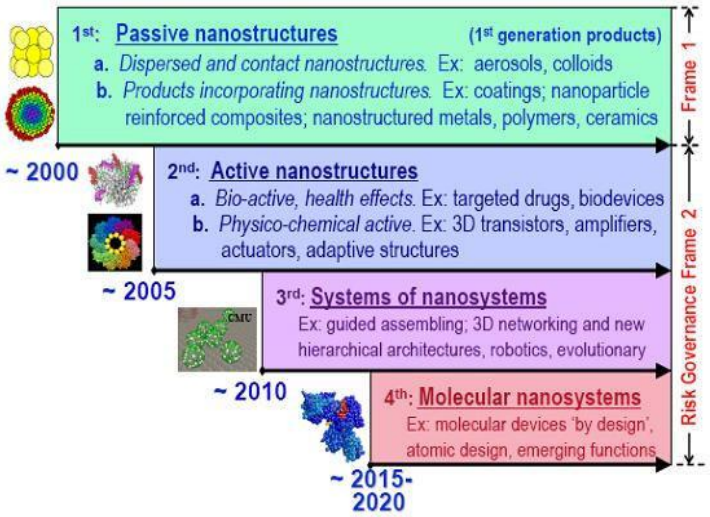

Figure 1.1. The four generations of nanotechnology[7]

The backbone of nanotechnology lies in the engineering of chemical and/or biological entities of dimensions 1-100 nm which are called nanomaterials. It is not so amazing, then, that government bodies, companies, and university researchers are joining forces or competing to synthesise, investigate, produce, and apply these amazing nanomaterials.

1.3. Nanomaterials

Nanomaterials are at the leading edge of this rapidly developing technology and they represent 31% of the total revenue in the global nanotechnology market reaching around 340 billion USD annually.[12] 'Nanomaterials' is a generic term encompassing nanoscale objects, nanoparticles, their aggregates and agglomerates among others. These materials, have attracted research attention in the 20th century for their size dependent physical and chemical properties[13] and they have entered into the commercial exploration realm in the 21st century. The scientific interest for these materials is because they are both interesting and important; interesting because working at nanoscale allows exploration of relationships between atoms, molecules and hence answering several basic questions that have plagued the research community for several centuries and important because they exhibit unique physical and chemical properties that are not exhibited by either their bulk or atomic counterparts.[14] More than thousand research articles and patents on various aspects of nanoscale chemistry have been published so far.[15,16]

Nanomaterials in general can be grouped into one of the following categories depending on the material of construction viz. carbon based nanomaterials, metals and alloys, biological nanomaterials, nano-polymers, nano-composites, nano-glasses and nanoceramics.[12] However for a chemist, colloids, micelles, polymer molecules, phase separated regions in block co-polymers, very large molecules or their aggregates, structures like bucky balls, silicon nanorods, quantum dots are nanomaterials while for physicists and electrical engineers, nanoscience is associated with quantum behaviour and the behaviour of electrons and photons.[17,18] For a biologist or a biochemist on the other hand, components of cell and other

structures from DNA to subcellular organelles are considered nanostructures.[19] Nanomaterials have thus impacted several fields of science including chemistry,[20,21] materials,[22] electronics,[23] optics,[24] bioanalysis,[25,26] medicine[19,27,28] and separation science.[29]

Nanomaterials are being investigated worldwide primarily because of the ability to engineer their characteristics, such as size, size distribution, morphology, phase and chemical composition using appropriate synthetic strategies and achieving superior control over their electrical, thermal, optical, chemical and mechanical (amongst others) properties. Each and every class of nanomaterials have their own special characteristics and applications. A detailed study of all the nanomaterials available in literature is beyond the scope of this thesis. Here, we specifically focus on metallic and metallodielectric nanomaterials and the following sections give a detailed account of these materials, highlighting some of their interesting applications, the currently established synthetic as well as manufacturing strategies and the challenges involved in engineering these nanomaterials.

1.4. Metallic Nanoparticles

Nanoparticles are a class of nanomaterials with tailored properties and metallic nanoparticles in particular are an interesting group of nanoparticles being investigated throughout the world. The nanoscale effects of metallic nanoparticles, similar to any other nanomaterial, stems from two major factors viz. increased surface to volume ratios and quantum size effects, which in turn affects the properties of these particles in isolation as well as their interaction with other particles in solution. In addition to the above mentioned nanoscale effects, metallic nanoparticles are unique due to their excellent optical properties, which has been recognized as a new branch of science called *plasmonics*. Nanoparticles of almost all metals such as Pt, Pd, Al, Ni, Pb, W, Cu, Au, Ag, and Fe have been synthesized specifically to manipulate their optical properties for use in several applications as well as in fundamental research.

Noble metallic particles, especially gold, have been of specific interest to the scientific community, dating back to the alchemists and medieval scientists to modern day researchers due to their exceptional therapeutic as well as their unique optical and electrical properties. Gold colloids or gold sol or gold nanomaterials were the first colloidal particles to be synthesized and studied from the 1800's while research on other metallic nanoparticles began in earnest during the nano-boom of the late 20th century.

1.4.1. Historical Perspective

Nanosized gold has been used in medicinal concoctions in the Arabic, Chinese and Indian cultures since the early 2500 B.C.[30] In particular, gold nanomaterials of size 55-60 nm called *swarna bhasma* (gold ash), has been used in traditional Indian Ayurvedic medicine for treating several clinical disorders including bronchial asthma, rheumatoid arthritis, diabetes mellitus, nervous disorders etc.[31] Small dispersed gold particles have also been used as colorants in ruby glasses and also to provide reddish tinge to ceramics, since the 5th century B.C., under the name 'purple of Cassius'.[32] The Lycurgus cup, dating from the 4th century A.D., made from glass that is tinted with gold is still preserved in the British Museum in London. It appears green in reflected light and red if viewed in transmitted light. The reason for yellow gold turning ruby red or purple remained a mystery to the alchemists and the ancient porcelain manufacturers and painters.

Michael Faraday was the first to recognize the fact that the ruby color of glass was due to the presence of small gold particles. He systematically synthesized gold nanoparticles using phosphorous as the reductant and analyzed their size dependent optical properties along with their coagulation behaviour which was later published in 1857.[33] The work of Faraday was followed by Zsigmondy and Svedberg who pioneered the nuclear and electrochemical methods respectively for the synthesis of colloidal ultramicroscopic gold.[34,35] Later, several key experimental and theoretical principles useful for the synthesis of gold sols and the fact that the synthetic properties of these sols depended on the pH of the solution were presented by

Ostwald.[36] Simultaneously, Mie proposed his theory for the color exhibited by spherical gold dispersions by appropriately solving Maxwell equations which was later developed by Gans for ellipsoidal particles.[37] These initial efforts later led to an explosion of research in the field of colloidal chemistry by several famous researchers like Einstein, Smoluchowski, Langevin, Perrin to name a few.

Interest in the synthesis of gold sol was revived by Turkevich et al.[38,39] when the first electron microscope was invented and particles in the micro and nanometer size ranges were visualized. Turkevich was then followed by Faulk and Taylor,[40] G. Frens[41] and Horisberger *et al.*[42] They used different salts and reducing agents to obtain varying sizes of gold sol. In recent years, the interest in gold nanoparticles has shot up owing to their increasing applications in the fields of optics, biology and catalysis, which is clearly evident from the literature survey of published articles over the past decade as shown in Figure 1.2.[43] The interest is in both fundamental as well as in the applied aspects of gold nanocrystals.

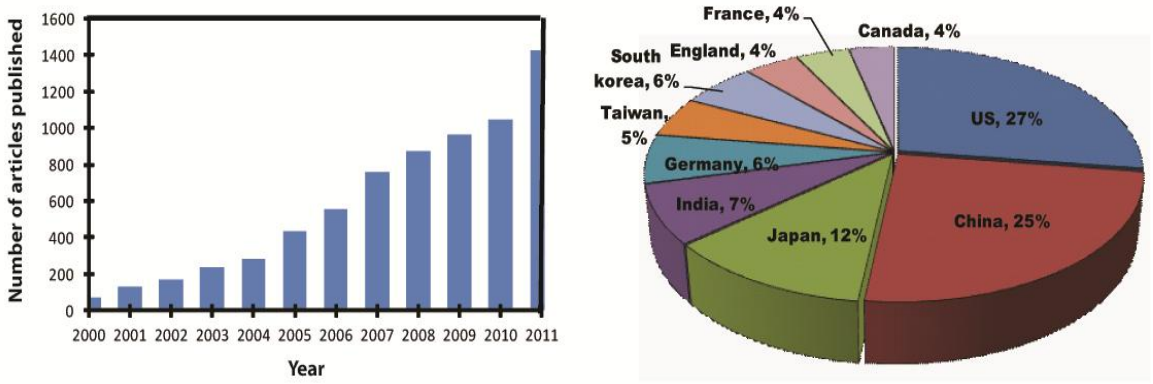

Figure 1.2. Statistical survey of articles published on gold nanoparticles over the past decade and pie chart of contributions from countries worldwide.[43]

1.4.2. Plasmonics – Nanoscale Optics

Metallic nanomaterials exhibit fascinating as well as interesting optical properties not seen in their bulk or atomic counterparts. This property is due to the high electron density of metals which leads to abundant free surface electrons at nanoscales. The interaction of surface electrons with the electromagnetic waves incident on them produces what are called plasmons.

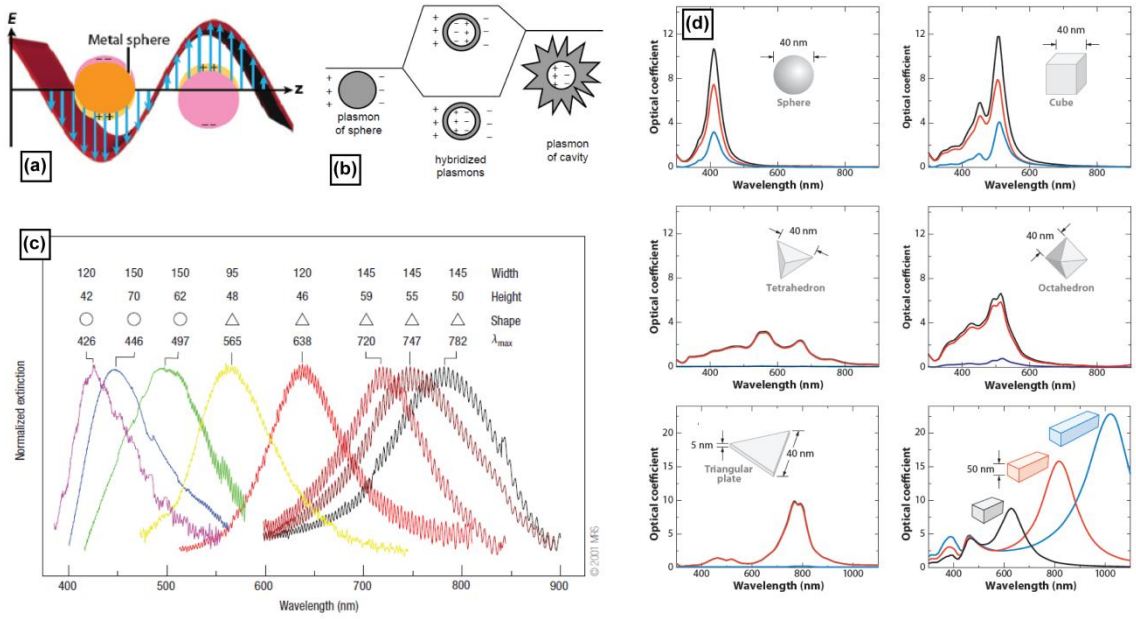

Figure 1.3. (a) Localized surface plasmons from metal nanoparticles excited by electromagnetic waves. Reproduced with permission from Reference 44. Copyright 2009, Annual Reviews Inc. **(b)** Hybridization model for the plasmon behaviour of gold nanoshells. Adapted with permission from Reference 45. Copyright 2007, American Chemical Society **(c)** Shift in the SPR extinction spectrum of silver nanodiscs and nanoprisms with change in their size. Reprinted by permission from Macmillan Publishers Ltd: Nature Materials (Reference 26), Copyright (2008) **(d)** DDA prediction of the extinction (black), absorption (red) and scattering (blue) spectrum of silver particles of varying shapes. Reproduced with permission from Reference 46. Copyright 2009, Annual Reviews Inc.

Plasmons can be described as quantized waves produced when a large number of mobile electrons are disturbed from their equilibrium position. In the case of nanocrystals whose dimensions are comparable or smaller than the wavelength of the incident electromagnetic waves, plasmons of low frequencies called localized surface plasmons (LSP) are generated.[45] As can be seen from Figure 1.3 (a)[44], these plasmons are generated due to the coherent oscillation of the free electrons in the metal at a certain resonant frequency which is

approximately the same as the frequency of the incident light. Hence the term surface plasmon resonances (SPR).[44] The electric field causes the free electrons to move away from the metal particle, producing a net negative charge in that region while the opposite side composed of cationic lattice of nuclei and localized core electrons has a net positive charge. This phenomenon thus creates a dipole plasmon resonance which can switch directions with the change in electric field. Dipole resonances are very common when light is incident on a particle less than 30 nm in size.[46] Particles of sizes greater than 30 nm usually generate quadrupole and octupole resonances. Interaction of light with particles can be predicted by solving the following Maxwell equations

$$\nabla . \mathbf{D} = \rho_F \tag{1.1a}$$

$$\nabla \times \mathbf{E} + \frac{\partial \mathbf{B}}{\partial t} = 0 \tag{1.1b}$$

$$\nabla . \mathbf{B} = 0 \tag{1.1c}$$

$$\nabla \times \boldsymbol{H} = \boldsymbol{J}_F + \frac{\partial \boldsymbol{D}}{\partial t} \tag{1.1d}$$

where **E** is the electric field, **B** is the magnetic induction, **D** is the electric displacement defined as $\epsilon_0 \boldsymbol{E} + \boldsymbol{P}$, **H** is the magnetic field defined as $\frac{\boldsymbol{B}}{\mu_0} - \boldsymbol{M}$, ρ_F is the free charge density, $\boldsymbol{J}_F$ is the free current density, **P** is the electric polarization (average electric dipole moment per unit volume), **M** is the magnetization (average magnetic dipole moment per unit volume) and ϵ_0 and μ_0 are permittivity and permeability of free space.[37] This theory also predicts the fraction of light that will be absorbed and the fraction that will be scattered by the colloidal particles, the sum of which is the extinction of light due to the particles which is what is measured by UV-vis spectrophotometer. Solution to Maxwell's equations for a particle of specific size, shape and optical properties illuminated by an arbitrarily polarized monochromatic wave predicting the electromagnetic field at all points in the particle and at all points in the homogeneous medium in which the particle is embedded in, was derived by Mie, valid specifically for spherical particles, which was later modified by Gans to include

spheroids.[37] The formulae derived by Mie can be directly used to compute the extinction spectra for spherical particles.

The resonance frequency and the intensity of the surface plasmons are dependent on three main factors: (i) pattern of surface polarization, (ii) dielectric property of the surrounding medium and (iii) the intrinsic dielectric property of the metal. Any variation in the size and shape of the particle alters the pattern of surface polarization thus changing the SPR. Generally, as the size of the spherical particles increases, the plasmon resonance frequency decreases which means the resonance frequency peak shifts to the longer wavelength region (red shift). Small particles (<20 nm) typically exhibit only absorption spectra while larger particles primarily exhibit scattering spectra. The spectral shift due to size change of spherical particles is minor compared to the spectral shift due to shape change of the particles as can be seen from Figure 1.3 (c)[26] and (d)[46]. Non-spherical particles can exhibit more than one SPR extinction frequencies; for example, gold nanorods exhibit two plasmon resonances, the longitudinal plasmon resonance which corresponds to the long axis of the rod and the transverse plasmon resonance corresponding to its short axis. In such cases, the longitudinal plasmon peak which is typically the longer wavelength peak can be red or blue shifted by just increasing or decreasing the rod length respectively while keeping the thickness constant, which keeps the transverse plasmon resonance peak (the short wavelength peak) unaltered (Figure 1.3 (d)).

Since Maxwell's equations are only known for solids, shells, spheroids and cylinders, approximations are required to solve the equations for other geometries.[47] Mie theory cannot be directly used in such cases though certain numerical methods such as Discrete Dipole Approximation (DDA), Finite Difference Time Domain (FDTD) and so on can be used for such cases. The DDA method splits the entire object into a finite array of polarisable points which can acquire dipole moments in response to the local electric field while the FDTD method is a grid based differential time domain numerical modelling method. Several

theoretical reasoning as well as models for the shape and size dependent shift of the SPR exists and one such model is the hybridization model for the shells, shown in Figure 1.3 (b).[45] In this model, the SPR of the shell is a combination of the plasmons from a solid sphere whose size is equivalent to the shell diameter and the plasmons from a spherical cavity whose size is the same as the core. These two SPRs eventually hybridize to produce both lower and higher energy plasmons which correspond to the two SPR peaks observed in the case of nanoshells. The peaks shifts to lower frequencies as the shell thickness decreases due to the stronger plasmon interactions between the plasmons from the two corresponding layers.[48]

The refractive index or the dielectric constant of the surrounding medium of the particles also affects the LSP. Typically higher the refractive index of the medium, lower is the plasmon resonance frequency.[37] Particles with sharp points or curvatures are also of interest these days due to the existence of most intense plasmon electric fields at the sharp points.[49-51]

1.4.3. Applications

The unique optical properties of the metallic nanomaterials is exploited for several different applications such as biomedical imaging, therapy, drug delivery, immunoassays, biosensors, surface-enhanced spectroscopes in addition to being used as optical waveguides, nanoscale switches, light sources, microscope and photolithographic tools. The nanosize effect of the metallic particles also finds applications in heterogeneous catalysis for organic reactions and chemical sensors. Some of the core applications are dealt with in the following sections.

1.4.3.1. Nanobiotechnology

The culmination of biotechnology and nanotechnology has led to the development of hybrid nanomaterials that incorporate the selective recognition properties of biomaterials to the existing optical properties of metallic nanoparticles. The advantages of using nanomaterials are four-fold, viz. (i) small size range (1- 20 nm) which is in the same size domain as that of the biomolecules, (ii) chemically tailorable surface and physical properties such as size, shape and

composition, (iii) target binding properties and (iv) structural robustness.[52,53] Nanoparticles are the core functional layer of these hybrid nanomaterials and the conjugation of biomolecules to the nanoparticle surface requires a biological or molecular layer or coating on the particle surface to act as the bioinorganic interface as depicted in Figure 1.4. Typically, the nanoparticle core is protected by an inert layer such as silica or organic moieties adsorbed onto the surface which also at times functions as the interface. However, in most cases, a linear linker molecule with two functional groups on either end, which can attach to the core particle as well as to the biomolecule, is used for further functionalization. This functionalization is accomplished either through electrostatic adsorption (e.g. negatively charged nanoparticle conjugates with positively charged protein), or by chemisorption or covalent binding (e.g. gold nanoparticle adsorbed or covalently bonded onto the amine or thiol groups on the protein) or by bio-affinity interactions such as antigen-antibody association or biotin-streptavidin binding. Antibodies or biopolymers like collagen can act as the intermediate layer to which enzymes, antibodies, antigens or biomolecular receptors (Figure 1.4 (a))[19] can be attached depending on the application.

Conjugation protocols exist for labelling of a broad range of biomolecules with gold particles such as protein, avidin, glucose oxidase, IgG etc. The first gold staining procedure was invented by Faulk and Taylor and the use of gold nanomaterials for diagnostics has been on the rise since then.[40] The simple application of this staining procedure is the use of nanogold as labels in light microscopy due to their high light absorbing nature.[54] Most metallic nanomaterials cannot be made to produce light unlike semiconductor nanomaterials though small nanoparticles (<5 nm) can produce photoluminescence while the larger ones can produce light through third-harmonic generation.[55,56]

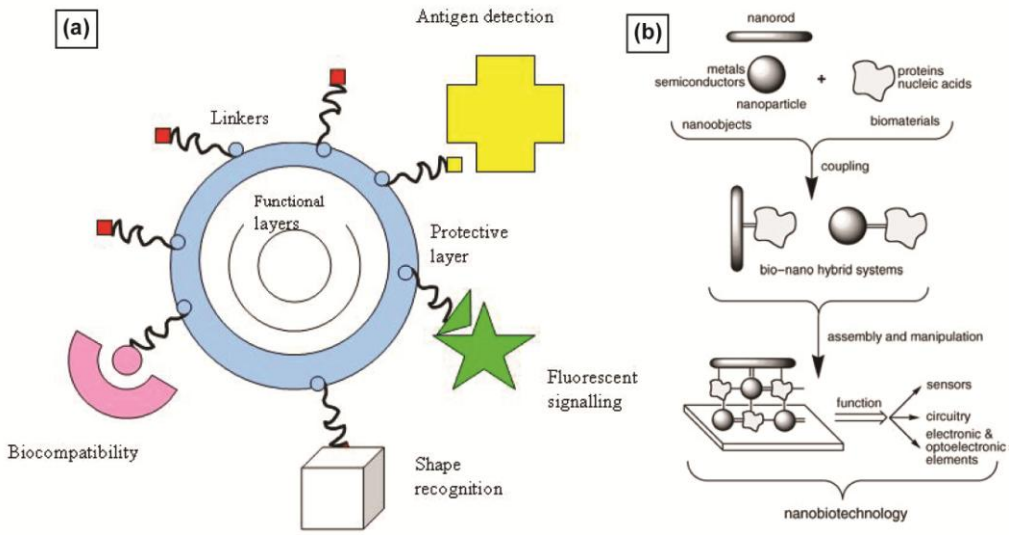

Figure 1.4. Schematic depicting the **(a)** Typical configuration of nano-bio hybrid materials used in biological applications.[19] **(b)** Concept of 2-D functional device for nanoelectronics. Reproduced with permission from Reference 53. Copyright 2004, John Wiley and Sons.

Some of the applications of these bioconjugated nanoparticles to biology or medicine that are being commercially used are fluorescent biological labels, drug and gene delivery, biodetection of pathogens, detection of proteins, probing of DNA structures, tissue engineering, tumour destruction, separation and purification of biomolecules and cells, MRI contrast enhancement and phagokinetic studies.[19] These hybrid nanomaterials can also be arrayed into 2-D and 3-D functional devices as shown in Figure 1.4 (b)[53] and can be used in nanoelectronics. The basic principle used in these applications is described in the following sections.

Diagnostics

Every living organism, virus or a pathogen, has a unique nucleic acid sequence which is being used by the medical arena to identify and combat diseases as well as to overcome or respond to bioterrorism threats. The currently established procedures to identify and recognize nucleic acid sequence are polymerase chain reaction (PCR) and molecular fluorophore

technology. However the PCR technique, a complex procedure which is highly sensitive to contaminants, is not cost effective or portable and has major multiplexing issues[57] and the molecular fluorophores susceptible to photobleaching, have a wide range of emission and absorption bands and require expensive equipments for analysis.[52]

Nano-bio hybrid nanomaterials with controllable physical and chemical properties are considered promising candidates in the biodiagnostics arena and the medical community have begun to commercialize some of the already evaluated assays.[52] Advancements in nanotechnology with the ability to tailor-make particles of definite size, shape and composition which allows specific emissive and absorptive properties make these materials ideal for multiplexed operations,[25,58] while also allowing for the measurement of properties in the presence of analytes. The general working principle of a detection system is accomplished by coupling the signal from a ligand-receptor binding reaction to a signal transducer. The signal from the reaction can be transferred to the transducer through optical[25,26], magnetic[59], electrical[60], electrochemical[61], radioactive, micromechanical and/or mass spectrometric means.[62]

Optical detection techniques are the most commonly studied detection modes of biomolecular events.[25,52] The wavelength selective SPR extinction bands in metallic nanoparticles have extremely large molar extinction coefficients (ϵ) of the order of ~3×10^{11} $M^{-1}cm^{-1}$.[63] A measure of how strongly a chemical species absorbs light is expressed using Beer-Lambert law given as

$$\epsilon = \frac{c.l}{A'} \tag{1.2}$$

Here c is the concentration of the species, l the path-length and A' the actual absorbance. Rayleigh scattering efficiency comparable to 10^6 fluorophores[64] and highly enhanced local electromagnetic field near the particle surface are responsible for the intense signals observed. Consequently there exists four different optical sensing mechanisms based on SPR scattering

or extinction intensities or shift in the SPR peak wavelength (λ_{max}) due to (i) nanoparticles aggregation[65-67] (Figure 1.5 (a)[52]), (ii) local refractive index changes[62,68] (Figure 1.5 (b)[26,68]), (iii) charge-transfer interaction at nanoparticles surface[69,70] and (iv) nanoparticles labels analogous to fluorescent labels[71,72] (Figure 1.5 (c) [52,72]). These techniques are used in the detection of nucleic acids, proteins and biologically relevant small molecules as well as metal ions.

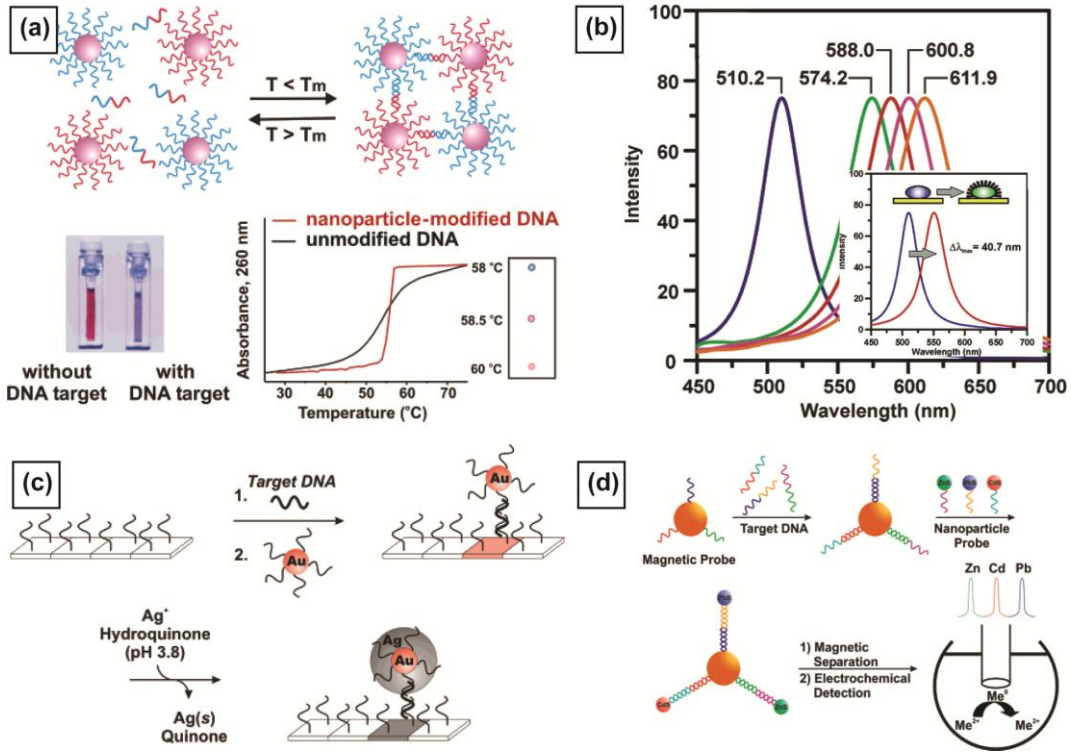

Figure 1.5. (a) Oligonucleotide-functionalized gold nanoparticles aggregate in the presence of complementary target DNA resulting in solution color change from red to blue which can be monitored by UV spectroscopy or by spotting on a silica support. **(b)** SPR spectrum of a single Ag particle in various solvent environments. SPR peaks from left to right: nitrogen, methanol, 1-propanal, chloroform and benzene; peak shift is due to the change in the refractive index of the medium. Inset shows a shift of 41 nm in the SPR peak due to the adsorption of 1-hexadecanethiol molecule on the particle surface. Reprinted by permission from Macmillan Publishers Ltd: Nature Materials (Reference 26), Copyright (2008). **(c)** A scanometric assay where the surface-bound capture oligonucleotide binds to one end of the target DNA while an oligonucleotide-functionalized gold nanoparticle probe binds to other end. Catalytic reduction of silver on the capture-target-probe results in signal that can be detected scanometrically. **(d)** Magnetic microparticles labelled with DNA capture strands can be used to code specific target DNA of interest after they bind with target DNA and oligonucleotide-functionalized nanoparticle labels with varying electrochemical signatures. Panels **(a), (c)** and **(d)** adapted with permission from Reference 52. Copyright 2005, American Chemical Society.

Several other detection and sensor techniques based on the bio-nano hybrid technology are also available such as molecular beacon technique[73,74], 'fingerprint' spectrum detection through SERS techniques[75], superconducting quantum interference device magnetometry[59], bio-bar-code based detection methods[57], magnetic relaxation techniques, quartz crystal microbalance[76] and laser diffraction techniques[77]. Several reviews on these topics are listed for further information.[52,53,78-81]

Imaging

Optical imaging techniques using organic fluorescent dyes suffer from limitations such as weak optical signals and subtle spectral differences between normal and diseased tissues though they offer high resolution and non-invasive imaging of tissues at competitive cost.[82] Cellular imaging using nanomaterials is gaining momentum, though potential toxicity and cytotoxicity are major problems (for specific particle groups) for the in vivo applications. Combining the advances in biophotonics and nanotechnology will significantly impact the detection and treatment of diseases long before pathologic changes occur at the atomic level. For example, gold nanoparticles being non-cytotoxic, with intense light scattering ability and ease of bioconjugation have proved to be excellent materials for cellular imaging through electron microscopy, confocal scanning microscopy, multiphoton plasmon resonance microscopy, optical coherence microscopy and third-harmonic microscopy.[83]

The optical properties of the gold nanoparticles provide them enhanced absorbing and scattering ability, and the morphology and size of these particles can be tuned such that their optical resonance includes 800 – 1300 nm which is considered the 'water window' of the near infrared (NIR) spectrum. This region of the spectrum is best suited for biomedical imaging and treatment because of the high physiological transmission, with a penetration depth of 10 cms depending on the type of tissue, due to low absorption and scattering from the intrinsic tissue chromophores.[84] Figure 1.6, row 1 shows light scattering images of normal and diseased cells without gold nanomaterials. The green light in this case is due to auto fluorescence and

scattered light from the cells and membranes; when these cells are incubated with gold nanospheres which strongly scatter yellow light or gold nanorods that scatter orange-red light due to their longitudinal plasmon resonance, the individual cells are easily visible.[83] This is because the nanoparticles are accumulated predominantly in the cytoplasm of the cells.

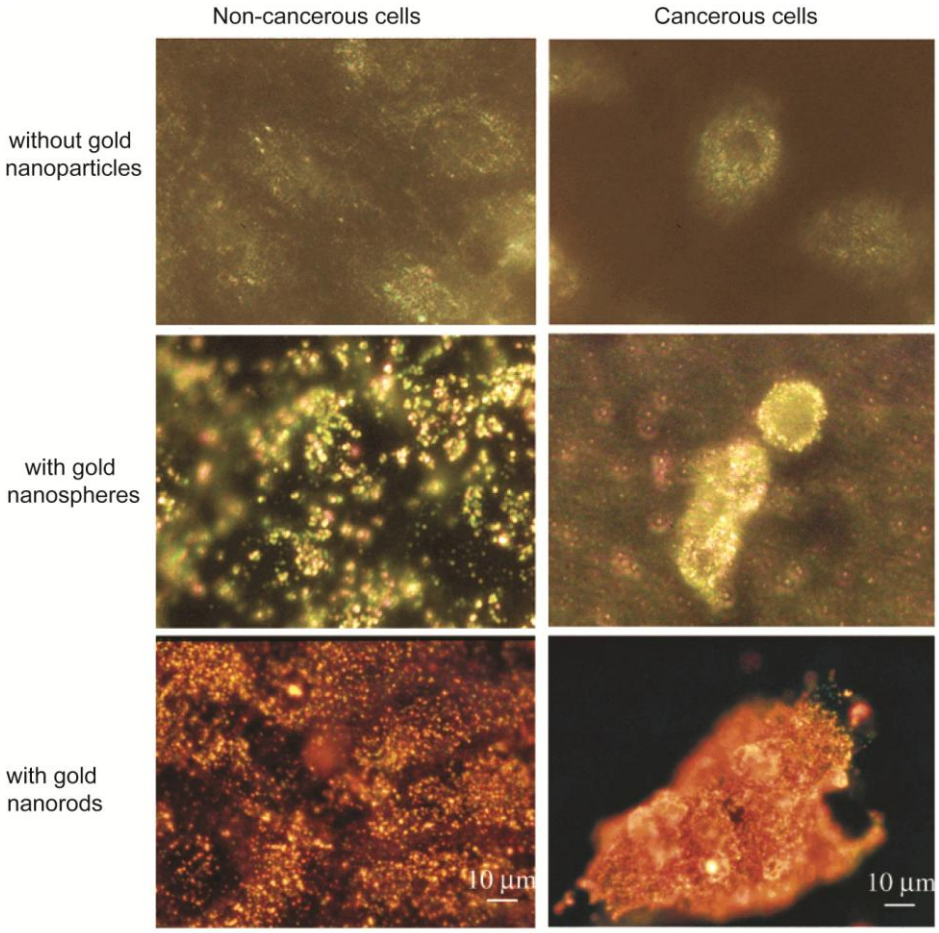

Figure 1.6. Light scattering images of HaCat non-cancerous cells (left column) and HSC cancerous cells (right column) without gold nanoparticles (row 1), with anti-EGFR conjugated gold nanospheres (row 2, reproduced with permission from Reference 83. Copyright 2005, American Chemical Society) and with anti-EGFR conjugated gold nanorods (row 3, adapted with permission from Reference 84. Copyright 2006, American Chemical Society).

On the other hand, since cancerous cells are known to overexpress epidermal growth factor receptor (EGFR) on their cell cytoplasm membrane to different degrees, conjugation of anti-EGFR antibodies with the gold nanoparticles (gold nanospheres and gold nanorods) before incubation led to a greater contrast difference between the cancerous and non-cancerous

cells (Figure 1.6, rows 2 and 3).[84] The difference in the distribution of the particles within the cell reflects the difference in the cell differentiation and proliferation process between the cancerous and non-cancerous cells. The same principle is also used in other imaging techniques such as optical contrast tomography using gold nanomaterials of different shapes and sizes.[82,85]

Therapy

The use of gold nanomaterials for photothermal therapy is another important application of bionanotechnology. Several different heat sources such microwave, ultrasound and laser light have been used as minimally invasive techniques causing necrosis of the cells through lysis and rupture of the membrane thus destroying the cells. However all these techniques are not very specific and lead to the death of normal cells as well.[86,87] The absorption capability of the gold nanomaterials is six orders of magnitude higher than the conventional indocyanine green dye used for the photothermal therapy techniques. In addition, the gold nanomaterials are less susceptible to photobleaching and are biocompatible which makes them ideal photothermal coupling agents.[88]

Nanophotothermolysis with pulsed laser and absorbing nanoparticles have proved effective for the destruction of bacteria, virus, cancer cells and DNA.[89] As soon as the nanoparticles are exposed to short laser pulses, the local temperature rise leads to non-linear effects such as microbubble formation due to the explosive vaporization of the thin layer of liquid in contact with the particle. The microbubble expands and immediately collapses to generate acoustic shock waves that travel outward interacting with and rupturing the cell and membranes. This leads to irreparable damage to the tissue surrounding the particles, as shown in Figure 1.7 (a).[90] Leaky nature of the cancer cells leads to 'enhanced permeability and retention' (EPR) effect which helps in the accumulation of nanomaterials of sizes between 60-400 nm in these cells rather than in the benign cells.[87] Due to this EPR effect, more severe damage to the cancer cells occurs at relatively low laser fluencies, as can be seen from Figures

1.7 (b) and (c). The cancerous cells (Figure 1.7 (b))[86] turn blue indicating cell death at 19 W.cm^{-2} while the normal cells show low cell death even at 51 W.cm^{-2} indicating the accumulation of anti-EGFR conjugated gold nanorods in the cancer cells than in the benign cells. Similarly, HER-2 (molecular marker for breast cancer) labelled gold nanoshell cells (Figure 1.7 (c)) are specifically killed as depicted by the green fluorescence test.[82]

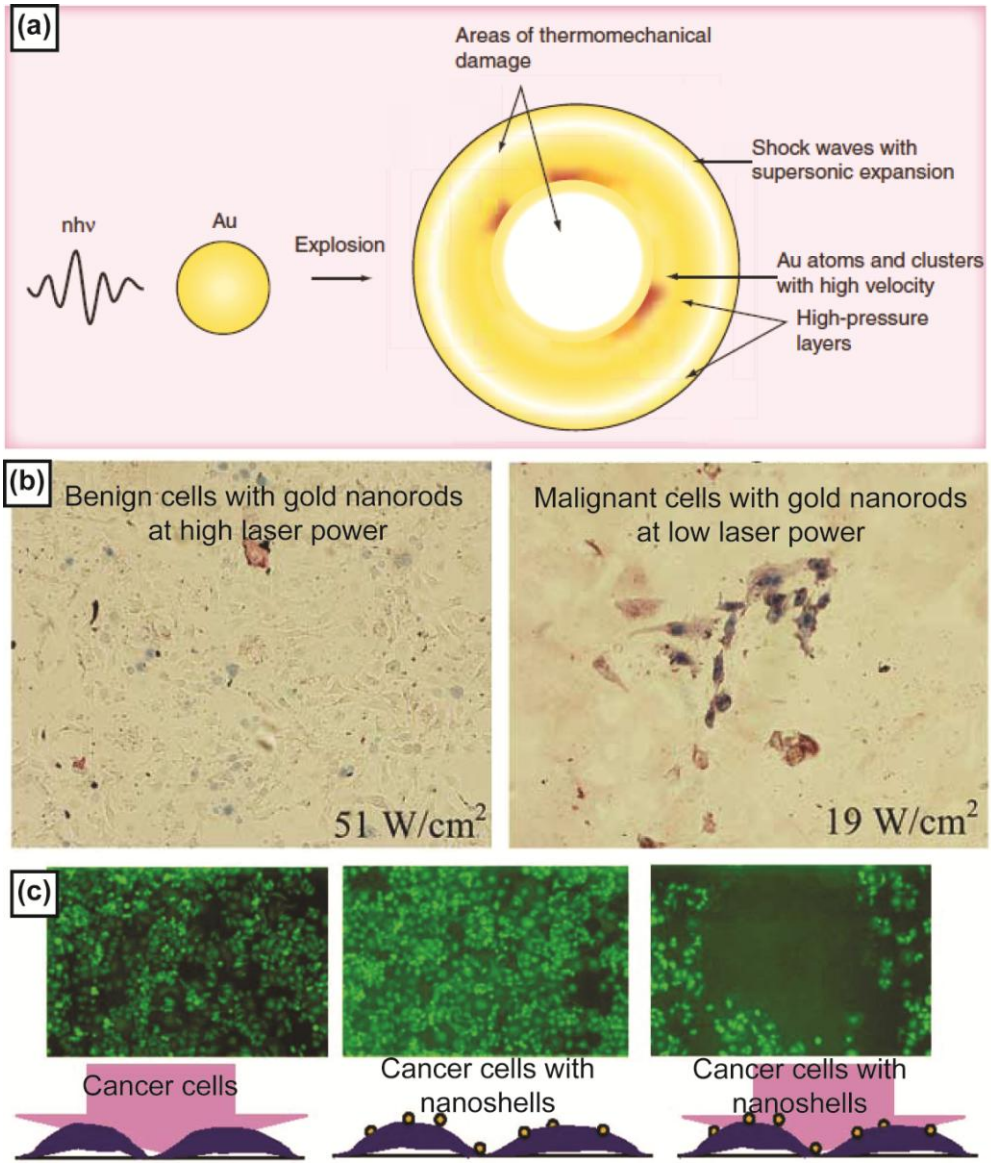

Figure 1.7. **(a)** Schematic depicting the phenomenological effect of nanophotothermolysis.[90] **(b)** Cell death caused by different laser powers in benign and cancerous cells incubated with anti-EGFR conjugated gold nanorods which are stained with trypan blue to indicate dead cells.[86] **(c)** Cancerous cells exposed to laser (left), cells tagged with HER2 conjugated gold nanoshells (middle) and cells tagged to HER2 conjugated gold nanoshells after exposure to laser (right). Green fluorescence depicts cellular viability.[82]

The same principle has also been used for photothermal drug delivery, where the nanomaterials are either embedded on the surface of a thermally reversible hydrogel containing the drug, or the drug molecules are directly conjugated to the nanomaterials, which are released due to their structural modifications at high temperatures.[91,92] This essentially enables targeted drug delivery as well as combination therapies which involves timely release of each drug for drug efficacy and treatment.[27]

1.4.3.2. Nanoelectronics

Functionalized nanomaterials as well as nanomaterial arrays on surfaces are extensively used in the construction of functional electrodes for electronic components, fuel cells, in bioelectroanalytical chemistry, bioelectronics and biosensing.[53] The conductive properties of the metals have been exploited in the fabrication of wires or electrode, conductivity circuitry or an array of electrodes for microelectronic devices.[93,94] Electronic properties of gold nanomaterials have also been used in the construction of electrical components such as 'metal-insulator-nanoparticle-insulator-metal' (MINIM) composites while single-electron transistors have been constructed with source, drain and gate electrodes.[95] Further research on the concept of single-electron tunnelling effects and coulomb staircase are in progress for the construction of solid-state devices using functionalized nanomaterials.[96-98]

1.4.4. Particle Synthesis

The unique properties and innumerable applications of nanoparticles are dependent on the size, shape, morphology and uniformity of the synthesized nanoparticles. These in turn depend on the synthetic strategy adopted. In order to explore the novel physical properties and realize potential applications of nanoparticles, the ability to controllably synthesise and process them becomes the first corner stone of the technology. Several chemists have worked in this field and have come up with numerous protocols for the synthesis of different nanoparticle types, sizes and shapes. Nevertheless there is no one mechanism that can be proclaimed efficient, effective and reproducible. Selection of a synthesis method, experimental technique

to be used and the choice of material for the synthesis are the first set of decisions to be made while synthesizing nanoparticles. The main challenge is relating the final product properties and production rates to the material properties of the precursor and the process condition. The product maybe homogeneous or composite, in dispersion, or on surfaces or in a matrix, generated using physical, chemical or biological techniques using gaseous, liquid or solid precursors.[99]

Synthetic strategies can be classified in several different ways depending on one or more of the above mentioned criteria. For example, synthesis methods can be classified into five groups depending on the medium from which the product is generated such as (a) liquid-phase methods including bulk precipitation in solutions, sol-gel processing, inverse micelle, spray conversion and various aqueous or non-aqueous chemical routes, (b) gas-phase methods such as gas evaporation, condensation and deposition, laser vaporization and pyrolysis, combustion, chemical routes in aerosol reactors etc., (c) vacuum synthesis techniques - sputtering, laser ablation, exploding wires, ionized-beam deposition, (d) from bulk solids by size reduction (mechanical attrition, alloying, spark erosion, plastic deformation) and (e) from molecules by self-assembly.[99]

In general, there are two approaches to the synthesis of nanoparticles: the 'top-down' and the 'bottom-up' approach. The 'top-down' approach is to start with bulk materials and chisel down to the nano level by a suitable technique like lithography, micromachining and etching.[100] The 'bottom-up' approach as the name indicates is to start from individual molecules and build up to the nano level. The top-down approach introduces major surface structure imperfections and crystallographic damages, leading to significant impact on the physical as well as surface properties of nanomaterials.[101] On the other hand, since the driving force in bottom-up approach is the reduction in Gibb's free energy, homogeneous nanostructures with less or no defects are observed.[99] However different synthesis and processing approaches in the bottom-up method often results in appreciable differences in

crystallinity, chemical composition and microstructure of material due to kinetic reasons leading to varying physical properties of the material.

In almost all cases of nanoparticles synthesis, the application dictates the nature of the product which in turn determines the synthetic protocol to be adopted. In this thesis, we focus on the synthesis of metallic nanoparticles of varying shapes, sizes and morphology for specialty applications such as biomedical imaging, therapy, biosensors, catalysis, opto-electronics and photovoltaics. These applications require monodisperse, homogeneous particles of controlled size, shape and morphology, which can only be achieved using bottom-up strategies. Wet chemical synthesis is one of the most common bottom-up strategies.

1.4.5. Liquid-phase Synthesis

Wet chemical synthesis or liquid-phase synthesis method is usually the preferred route for nanoparticles synthesis because it is versatile, simple and the materials needed are inexpensive. Manipulation of matter at the molecular level like molecular mixing is possible in this technique which helps in achieving chemical homogeneity. An understanding of the interaction of matter at the molecular or atomistic scale will enable tailoring of synthesis thus achieving better control of the size, shape and size distribution.[102]

1.4.5.1. Mechanism – Classical Approach

The general mechanism of particle formation usually follows the nucleation and growth model proposed by LaMer and Dinegar[103] as shown in Figure 1.8.[104] The reaction is in an aqueous or non-aqueous solution containing soluble or suspended salts. As soon as the solution is supersaturated with the solute, heterogeneous or homogeneous nucleation occurs, which is the formation of stable nuclei with or without an external species. The next step is the growth phase, when the nuclei begin to grow in size and this phase is diffusion controlled. The chemistry of the nucleation and growth process can be explained as follows:[105,106] The formation of metallic particles is due to the redox reaction between an oxidised metallic

species and an appropriate reducing agent where the electrons from the reducing agent are transferred to the metals, forming metal atoms according to the following chemical equation.

$$a\ Metal^{\,b} + b\ Redu \rightarrow a\ Metal^{\,0} + b\ Ox \tag{1.3}$$

The magnitude of the driving force for this equation, which is the difference in the redox potentials, ΔE, is determined from the equilibrium equation,

$$\ln K_e = A_0 \left({}^{\Delta E}/_{RT}\right) \tag{1.4}$$

Where K_e, A_0, R and T are equilibrium constant, frequency factor, gas constant and temperature respectively.

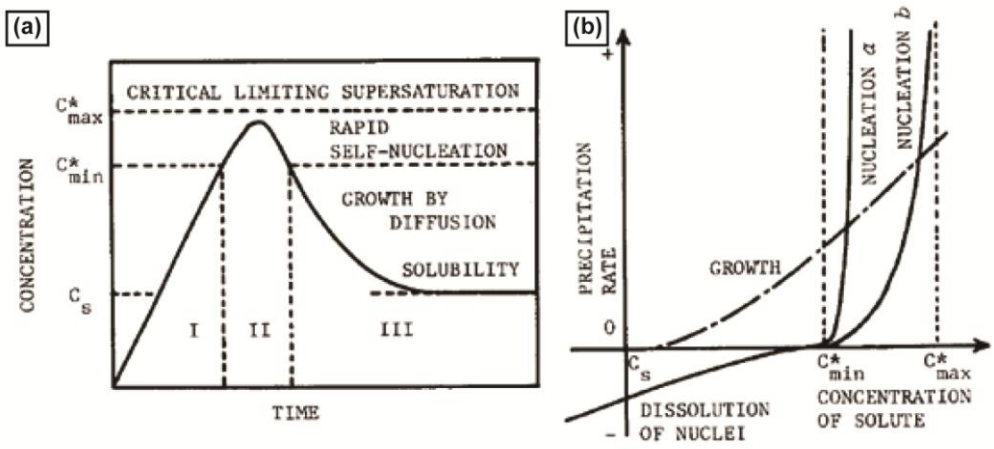

Figure 1.8. (a) LaMer model of nucleation and growth of monodisperse colloids in solution **(b)** A plot of the precipitation rate for nucleation and growth vs. the concentration of solute. Panels **(a)** and **(b)** reprinted from Reference 107, Copyright 1987 with permission from Elsevier.

The redox reaction is thermodynamically possible only if ΔE is positive i.e. the redox potential (E_0) of the metallic species is atleast 0.3 V – 0.4 V higher than that of the reducing agent. Hence strong electropositive metals such as Au, Ag, Pt, Pd and Rh with $E_0 > 0.7$ V can react with any reducing agent under ordinary conditions while more electronegative metals ($E_0 < -0.2$ V) need a very strong reducing agent and harsh conditions of temperature and pressure to react and form metal atoms. The redox potentials of the solute as well as the

reducing agent are also affected by the pH of the solution as predicted by the Nernst equation. In addition, ΔE of the reaction can also be varied by skilfully manipulating conditions such as temperature of the reaction mixture, metal-complexation chemistry or pH of the reaction medium.

The metal atoms formed are generally insoluble in the solution and begin to aggregate into dynamic entities called embryos (Eq. 1.5) which continuously dissociate or condense to reach a favoured state. These favoured states are more stable cluster of metal atoms containing what are called the 'magic number' of atoms. Once the embryos reach a critical size, they separate out from the liquid solution as solid particles called nuclei (Eq. 1.6). A number of parameters such as solute concentration, temperature, redox potential of the reactants, presence of surfactant, their concentration, viscosity and the surface tension of the solution determine the number and the size of nuclei formed.

$$n\ Metal^{\,0} \leftrightarrow (Metal_n^0)_{embryo} \tag{1.5}$$

$$(Metal_n^0)_{embryo} + p\ Metal^{\,0} \rightarrow\ (Metal_{n+p}^0)_{nuclei} \tag{1.6}$$

$$(Metal_n^0)_{nuclei} +\ \ p\ Metal^{\,0} \rightarrow \left(Metal_{n+p}^0\right)_{part} \tag{1.7}$$

$$x\ (Metal^0)_{part} + y\ Metal^{\,0} \rightarrow\ Metal_{np}^0 \tag{1.8}$$

According to the Lamer model, monodisperse particles are formed if the nucleation process happens within a short burst when the solute concentration crosses the nucleation threshold for a short period of time (stage II in Figure 1.8 (a)), with subsequent growth of these nuclei (stage III in Figure 1.8 (a)) without further nucleation. The concentration of the solute should be increased such that supersaturation is reached instantaneously leading to nucleation. The decrease in concentration due to the nucleation burst is such that the solute concentration remains below the nucleation threshold as shown in Figure 1.8. Hence isolating the nucleation

phase from the growth phase should lead to monodisperse particle population (more details in Section 1.4.5.3).[104]

1.4.5.2. Mechanism – Contemporary Approach

Recently, researchers have shown that the growth of primary particles into nanometre sized particles not only follows the diffusion mechanism but also follows the aggregation route where the primary particles themselves aggregate to form the desired size metallic particle as given by Eq. 1.9. In this case, the Lamer model for nucleation and growth is as shown in Figure 1.9.[13] However, the growth of these particles in this mechanism is very rapid leading to formation of micrometre sized particles depending on the number of particles (x) involved in aggregation.[105]

$$x\ (Metal^0)_{part} \rightarrow Metal^0_{np} \tag{1.9}$$

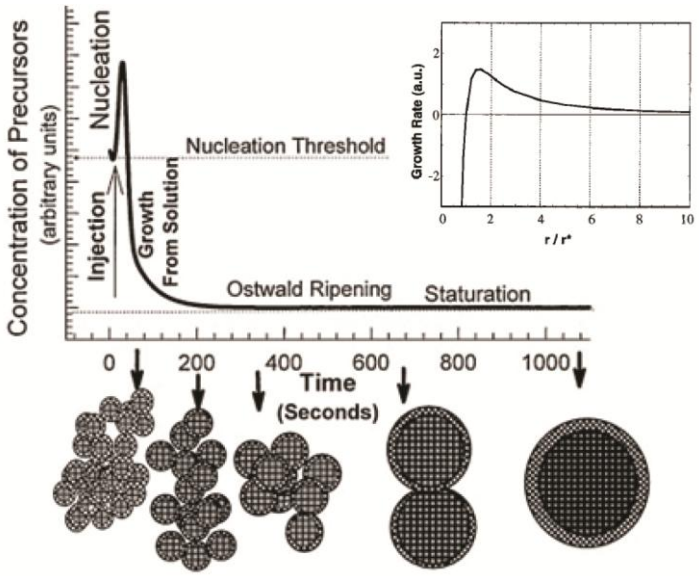

Figure 1.9. LaMer model of nucleation and growth of monodisperse colloids in solution. Inset : Growth rate variation with particle size - Sugimoto's model. Reproduced with permission from Reference 13. Copyright 2000, Annual Reviews Inc.

In order to prevent aggregation of primary particles into microparticles, the aggregation process has to be arrested by one of the following mechanisms:

1. Electrostatic mechanism deals with the balancing of attractive and repulsive forces by manipulating the double layer around the particles and is effective only in dilute systems.
2. Steric and electrosteric mechanisms deal with the adsorption of polymers or surfactants or polyelectrolyte molecules onto the surface of the metal thus shielding each other from the attractive van der Waals forces.
3. Hydration stabilization is a very potent tool that is applicable only for nanosized, hydrophilic solids. Both steric repulsion and hydration stabilization can be used for dilute as well as concentrated solutions.[108] The effectiveness of stabilizers is system specific and the choice is with the chemist.

Recent researches have shown that the Lamer model is not always true and is applicable only in limited situations.[109,110] There are chemistries (formation of spherical hematite α-Fe_2O_3 particles) in which short nucleation bursts occur throughout the growth phase and the final particle size is still uniform. This is due to the self-sharpening growth process of the particles where smaller ones grow more rapidly than the larger ones.[111] There are also reports of other cases where directional or non-directional aggregation leads to the formation of monodisperse nanometre sized particles due to desorption and ripening or internal cementing respectively.[112]

Models for growth by size focusing and Ostwald ripening (or size defocusing) have also been presented in the recent past for the formation of monodisperse particles.[107] In these models, the final size of the particles is determined by the Gibbs-Thomson effect, given by the equations

$$\frac{p}{p_{eq}} = exp\left(\frac{r_{crit}}{r}\right) \tag{1.10}$$

$$r_{crit} = \frac{2.\gamma.V_{atm}}{k_B.T} \tag{1.11}$$

where γ is the surface tension, V_{atm} is the atomic volume, k_B is the Boltzmann constant, T is the absolute temperature, p_{eq} and p are the equilibrium and normal partial pressures or chemical potentials or concentrations respectively and r is the radius of the particle. According to the Gibbs-Thomson equation, particles smaller than the critical nucleation radius (r_{crit}) dissolve and disappear while the others grow at rates which depend strongly on their sizes as shown in the inset in Figure 1.9. This phenomenon is called defocusing or Ostwald ripening.[107] When the sizes of all the particles in the solution are above r_{crit}, the smaller particles grow faster than the larger ones due to the difference in their surface energies leading to what is called size focusing. In effect, the depletion of monomer concentration causes the defocusing of particle population leading to broader particle size distribution in the solution and tge injection of reactants at this stage leads to focused growth of particles. Hence by injecting reactants periodically into the solution such that the concentration is just below the critical supersaturation or the nucleation threshold, focusing and defocusing growth lead to final monodisperse particle population.[13,113]

Both the diffusion mechanism and aggregation mechanism of particle growth described above have advantages as well as disadvantages and the choice of the mechanism to be adopted depends on the final product quality required. Addition of metal atoms on the surface of nuclei as in the diffusion-growth mechanism usually leads to the formation of regularly shaped crystals with facets and edges, and very few irregularities in the crystal lattice and internal grain boundaries. Aggregation of particles on the other hand leads to polycrystalline particles with very low density and large internal grain boundaries. In general, diffusion controlled growth can be used to get both nano and micro sized particles. For example, high supersaturation of the metal atoms will generate large number of nuclei, exhausting most of the metal atoms in the process and if aggregation is appropriately prevented, further growth occurs only till the metal species in the solution is depleted which leads to nanosized monodisperse particle population. However, lesser the number of nuclei generated, lesser is the depletion of metallic species in the nucleation process which leads to

growth at the expense of the available metal species in the solution. This is possible by slow reducing agent, hence slow reaction or by the periodic addition of metallic species into the solution or by seeding i.e. addition of already formed nuclei into the system as seeds which initiate growth without nucleation.[105]

1.4.5.3. Monodisperse Particles

Several different factors affect the monodispersity of a particle population and most of these factors are system specific and have to be determined by thorough analysis of the individual system on hand. However, there are some general requirements for the preparation of monodisperse particles and some of these are presented here.[107,114]

Isolation of nucleation and growth stages

According to the Lamer model, isolating the growth stage from the nucleation stage is a sufficient condition for monodispersity. However it has been proven since that the separation of the two stages is a necessary but not sufficient condition. A more detailed analysis of the Figure 1.8 will help understand the reasons for the necessity of the condition. There is no nucleation in stage I when the solute concentration $C < C^*_{min}$, C^*_{min} being the minimum concentration for nucleation. As soon as $C = C^*_{min}$ stage II, the nucleation stage sets in, when C climbs for a while and begins to drop as the solute is consumed due to nucleation. As the solute concentration drops, the growth stage, stage III begins (as soon as $C = C^*_{min}$) and goes on until $C = C_S$, the solubility concentration of the solute.[103] The ideal condition for monodispersity will be the nucleation curve 'a' in Figure 1.8 (b)[107] where nucleation rate strongly depends on the supersaturation (as the nucleation rate shoots up as soon as $C = C^*_{min}$) and the growth rate is rather low. If the nucleation rate is not high enough or is not highly dependent on supersaturation, and follows the nucleation curve 'b', then the solute concentration will remain between C^*_{min} and C^*_{max} (maximum concentration for nucleation), leading to simultaneous particle growth which is undesirable. In such cases, if C is only

slightly above C^*_{min} a short period of nucleation will cause C to fall lower than C^*_{min} hence avoiding the long stay in stage II.[107]

The isolation of nucleation and growth stages is hence a prime requirement for monodispersity. This can be achieved by lowering the pH or by increasing the solvent concentration and diluting the solution or by sudden change in temperature as soon as nucleation begins or by adding chelating agents which will quench the nucleation process. Seeding process or nuclear growth method can also help in isolating the two stages. Seeded growth involves the addition of preformed small particles or nuclei into a monomer solution at concentrations less than C^*_{min}, when there is no nucleation but only growth in the presence of the introduced nuclei.[107]

Growth models

Assuming that the nucleation and growth stages are successfully isolated, the possibility of getting monodisperse particles is still low if growth starts with polydisperse nuclei i.e. the nuclei could have grown at different rates even within the short nucleation burst. An analysis of the growth phase is necessary in this case to understand the limitations and the possibilities for monodispersity.[107,114] The rate limiting steps in the growth of a particle are

(i) The diffusion of metal atoms or monomer towards the particle

(ii) Surface reaction between the particle and the diffused monomer/metal atom.

This is depicted in Figure 1.10[107] where C_e, C_i and C_b correspond to the concentrations of monomer, that would be in equilibrium with the particle (this is a function of the size of the particle), at the surface of the particle and in the bulk solution respectively and δ the thickness of the diffusion layer around a particle of radius r.

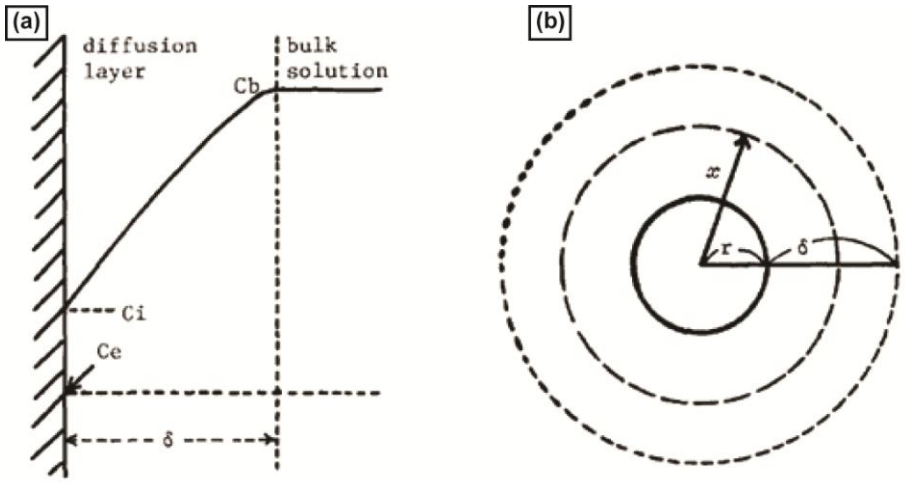

Figure 1.10. (a) Concentration of the solute in the diffusion layer **(b)** A schematic showing the diffusion layer around a spherical particle. Reprinted from Reference 107, Copyright 1987 with permission from Elsevier.

The total flux (J) of the monomer/metal atom diffusing through a spherical surface of radius x is given by Fick's law as

$$J = 4\pi x^2 D \frac{dC}{dx} \tag{1.12}$$

Here D is the diffusion coefficient and C is the concentration of monomer at radius x. Assuming that the diffusion is at steady state, only C varies linearly in the diffusion layer and the flux can be written as

$$J = 4\pi r D \frac{r + \delta}{\delta} (C_b - C_i) \tag{1.13}$$

The flux due to first order surface reaction with rate constant k is given as

$$J = 4\pi r^2 k (C_i - C_e) \tag{1.14}$$

At steady state, the two fluxes due to diffusion and surface reaction are the same. If the growth of the particle is **diffusion-controlled**, then $D \ll k$ and $C_i = C_e$, since the particle surface is in local equilibrium with the solution concentration, and Eq. 1.12 becomes

$$J = 4\pi r D \frac{r+\delta}{\delta} (C_b - C_e) \tag{1.15}$$

This flux is equal to the growth rate of the particle which is given by the increase in the number of atoms in the particle (crystal lattice) with time and can be written in terms of the molar volume, V_m of the solid as

$$J = \frac{4\pi r^2}{V_m} \frac{dr}{dt} \tag{1.16}$$

Substituting Eq. (1.15) into the growth rate equation (Eq. (1.16)) leads to

$$\frac{dr}{dt} = V_m D (C_b - C_e) \left(\frac{1}{r} + \frac{1}{\delta}\right) \tag{1.17}$$

$$\Delta r \approx constant \left(1 + \frac{\delta}{r_{avg}}\right) \tag{1.18}$$

The $C_b - C_e$ in Eq. 1.17 is supersaturation condition, which is smaller for small particles compared to larger particles (small particles have higher C_e than large particles due to their higher vapour pressure). This tends to make the large particles grow faster than small particles. However at high supersaturations, $C_b - C_e$ is large and can be treated as a constant which is used to derive the standard deviation of the size distribution (Δr) in terms of the mean particle radius r_{avg} Eq. 1.18. In this case Eq. 1.17 implies that dr/dt is lowered with an increase in r i.e. size distribution of the particles becomes narrower as the particle size increases. This model implies that the size distribution of the particles can be focused.

On the other hand, if the growth of the particle is **reaction-controlled**, then $D \gg k$ and $C_i \cong C_b$, since the growth rate is limited by the surface reaction, the bulk concentration will be equivalent to the surface concentration, and Eq. 1.14 becomes

$$J = 4\pi r^2 k (C_b - C_e) \tag{1.19}$$

Once again the flux due to surface reaction produces a change in the radius of the particle as given by Eq. 1.16. Combining Eq. 1.19 and Eq. 1.16 gives

$$\frac{dr}{dt} = V_m k(C_b - C_e) \tag{1.20}$$

This implies that the growth rate is independent of particle size and Δr remains constant throughout the growth stage.

The above mentioned is the simplest growth model in which the same concentration of monomer is in equilibrium with particles of all sizes (C_e is independent of r). Growth of particles can be focused using the diffusion-controlled growth mechanism while all the particles grow relatively at the same rate in the kinetic controlled growth mechanism. However the effect of surface energies, given by the Gibbs-Thomson effect is not considered in these cases.[107,114]

There are several factors that have to be considered to obtain monodisperse particles as described in this section. Control of one factor does not necessarily mean other factors will not contribute to polydispersity in the particle population. Hence every system and its chemistry need to be treated individually and all the factors have to be taken into consideration while synthesizing particles of definite shape, size, composition and morphology for a particular application.

1.4.6. Current Trends in Particle Synthesis

The commercialization of nanotechnology has led to the need for large-scale manufacturing of nanomaterials of desired size, shape and morphology.[15] Some of the key challenges faced by the nanomanufacturing community are the requirements to manufacture monodisperse particles of desired size, morphology, composition and crystallinity at a large scale and the necessity to control the potential interactions of the particles with stabilizing ligands to enhance their surface properties (for applications as well as for further aggregation

steps). Improvements and better methods are continually being reported in the synthesis of nanomaterials using a variety of reagents, strategies, and a wide spectrum of reaction conditions, by researchers throughout the world. However the scalability of many of these synthetic protocols is still an unresolved issue and one such example, the case of gold nanorods, is provided in Chapter 2. The scalability issue is due to the direct dependence of the product quality on the reaction conditions. Large-scale synthesis of metallic nanomaterials is also performed in small scale batches which in essence suffers from batch-to-batch variations.[115] Several research groups as well as commercial organizations are working to better these techniques for commercial production of these particles. Some of the synthetic protocols for the synthesis of metal nanoparticles, specifically gold and silver are listed in the following sections.

1.4.6.1. Gold Nanoparticles

Gold nanomaterials are usually synthesized by the reduction of a metal salt, usually a halide ($HAuCl_4$), in the presence of a stabilizer in solution. The first such method was reported by Faraday using phosphorous as the reducing agent.[33] Several other reducing agents and stabilizers have been discovered since then which has made possible the reproducible and large scale syntheses of spherical gold nanomaterials under mild conditions. Size and morphology of gold nanoparticles can be tuned by varying the concentration ratio of the capping agent to metal salts and by choosing a suitable reducing agent.[116,117] Weak reducing agents such as citrate usually yield faceted and smaller particles due to slow reaction and longer growth times, while fast reducing agents yield bigger and spherical particles.[118] The best known methods among these are the citrate method established by Turkevich[38] and later modified by Frens[41], and the Brust protocol[38,41,119]. Citrate method involves the addition of sodium citrate to a boiling solution of chloroauric acid ($AuCl_4^-$); varying reagent concentrations lead to particles of sizes 10's to 100's of nanometres.[41] The Brust method on the other hand involves the reduction of chloroauric acid by strong reducing agent, sodium borohydride in the presence of

an alkanethiol. The reduction is performed after $AuCl_4^-$ is completely transferred from its original aqueous phase to organic phase using a phase transfer reagent. Particles synthesized by this method are 1-3 nm in size and they can be isolated and preserved in solid state after solvent evaporation. The preserved solid particles can also be redissolved in nonpolar solvents and are considered to be extremely stable due to the excellent stabilizing nature of thiols owing to the strong Au-S bond.[120]

The other method of obtaining Au nanocrystals of diameters 1-2 nm is using tetrakis(hydroxymethyl)phosphonium chloride (THPC) as the reducing agent (and the capping agent) of $HAuCl_4$.[121] Amines,[122,123] carboxylates,[124] polymers[125] and phosphines[126] are also used as other good protective agents to synthesise gold nanomaterials. There has also been a report on the large scale synthesis of gold nanoplates[127] though the synthesis of other shapes has not been accomplished on large scale yet.

1.4.6.2. Silver Nanoparticles

Silver nanomaterials, similar to gold are obtained by the reduction of a suitable salt (usually silver nitrate or silver acetate) in the presence of stabilizers in solution.[128] Many reducing agents such as sodium borohydride,[129] ascorbic acid,[130] dimethyl formamide,[131] sodium citrate[132] and alcohols[133] have been successfully used for the synthesis of nearly monodisperse particle population. Long chain n-alkanethiols are most commonly used capping agent while aromatic anilines, carboxylic acids and polymers are also being employed as capping agents.[128,132,133] Sun and Xia reported the synthesis of monodisperse, large scale synthesis of 100 nm silver nanocubes using silver nitrate, ethylene glycol (reductant) and poly (vinylpyrrolidone) as the capping agent. Experimental conditions such as temperature, metal salt concentration, growth time, metal/stabilizer ratios act as parameters to obtain nanocubes of varying dimensions (50 – 100 nm).[58] Continuous synthesis of silver nanomaterials using a spin disk reactor has also been achieved recently giving rise to the possibility for commercialization.[134]

A list of reviews on the topic is provided for interested readers.[79,117,120,128,135-138] These reviews provide detailed discussions of the various strategies available till date for small scale as well as large scale synthesis of metallic nanomaterials including Pt, Pd, Cu, Ni, Fe and Co.

1.4.6.3. Challenges

As already pointed out in the preceding sections, controlled synthesis of monodisperse nanomaterials of definite size, shape, composition and morphology is a challenge faced by the nanotechnology community at the moment since the chemistry of the reaction is dependent on the physical parameters under which the reaction is performed. The order and mode of reagent's addition, temperature distribution, concentration of reactants, pH, presence or absence of surfactants, chelating agents and their concentrations, viscosity and the surface tension of the solution are some of the factors that determine the nature of the final particles. Control of nucleation and growth is possible only when there is spatial and temporal homogeneity of the parameters mentioned above. Concentration gradient in the solution usually leads to secondary and tertiary nucleation resulting in polydisperse particle population requiring further purification and size classification steps. These challenges essentially affect the commercial viability of these processes thus creating the need for innovatively engineered processes for particle synthesis. Traditional synthesis usually involves bench-scale stirred batch reactors where the spatial and temporal control of reagent concentrations, temperature distribution and other physical parameters such as pH is limited or ineffective leading to concurrent nucleation and growth phases and hence polydisperse particles.[139] These macro-scale reactors also depend on turbulence or agitation for mixing which in turn introduces high shear rates, often leading to irreversible colloidal aggregation.[140] In addition, batch-to-batch variation in the sample is another major drawback of these stirred batch reactors. These issues can be overcome using plug flow reactors; however micromixing is still an issue in these plug flow reactors.[141,142]

Microfluidics is one of the options for the controlled and continuous synthesis of nanomaterials. Microfluidics[143] and microreactors[144,145] overcome the disadvantages posed by bench-scale systems as well as traditional chemical reactors for particle synthesis. The essential features of microreactors viz. small channel dimensions (typically 10 - 300μm)[146] and high surface to volume ratios, offers advantages such as rapid heating or cooling of reagent mixtures[147] and efficient mixing[148] (due to increased driving force for heat and mass transfer[149]) leading to temperature control along the flow profile and homogeneous reaction environment. Microfluidics also enables continuous synthesis with the ability for reagent addition downstream,[150] variation of reagents concentration by varying the rate of reagent injection,[151] and the use of minimal amount of reagents under precisely controlled conditions of temperature, concentrations, density or pressure.[152] Scale-up to commercial volumes is possible in-principle by increasing the number of individual reactors with the same design, performing the same reaction thus increasing the yield per time known as scaling-out.[153] The advantages offered by microfluidics and microreactors have been successfully used by several research groups for the synthesis of nanomaterials which will be dealt with in detail in Chapter 2.

1.5. Thesis Objectives and Layout

In this thesis, we leverage the advantages of microfluidics to controllably synthesise metallic nanoparticles for specialty applications such as biomedical imaging, therapy, biosensors, catalysis and optoelectronics. We focus on the synthesis of metallic nanocrystals (specifically gold) of varying size, shape and morphology and synthesis of plasmonic "nanoshells" of varying thickness (metallodielectric core-shell particles). The main disadvantages of the currently established synthetic and manufacturing strategies have been highlighted with gold nanorods as the model system and the need for better techniques for nanomaterial synthesis are further detailed in Chapter 2. The reasons for pursuing microfluidic methods for particle synthesis and a literature survey of the state of the art developments in the

field are also done in Chapter 2. The general design guidelines for designing a microreactor and the basic fabrication techniques are also explained here. Droplet microfluidic method is used for the synthesis of gold nanomaterials and the intricacies involved in the experimental techniques, analysis of flow profile and the strategies for synthesis of gold nanocrystals of different shapes, sizes and morphology are presented in Chapter 3. Synthesis of small gold nanoparticles usually requires the use of fast reducing agents such as sodium borohydride which in turn introduces a further level of complexity in the microfluidic method which is dealt with in Chapter 4. Chapter 5 deals with the synthesis of metallodielectric core-shell particles of varying thickness using the conventional flask based methods, the disadvantages of using droplet microfluidic method for such synthesis and an introduction of three phase segmented microfluidic method. A detailed analysis of the parameter space of liquid flow rates is then performed to identify the regimes for the synthesis of gold nanoshells using the gas-liquid-liquid method. Foams, a subset of the three phase segmented microfluidic method, are then used for the synthesis of gold nanoshells of varying thickness while compound-drops another class of the three phase method is used for the same synthesis using reactive gas, carbon monoxide, as the reducing agent. Design strategies involved in integrating the growth of small gold nanocrystals and subsequently using them as seeds for further growth into particles of different shapes like nanorods and nanospheres on the same microchip are presented in Chapter 6. Chapter 7 is the general discussion of the thesis with future scope and outlook as well as a discussion of scale-out and the possibilities for commercialization.

1.6. References

1 Feynman, R. P. There's Plenty of Room at the Bottom. *Journal of Microelectromechanical Systems* **1**, 60 - 66 (1992).

2 Roco, M. C. & Bainbridge., W. S. *Societal Implications of Nanoscience and Nanotechnology* (Kluwer Academic Publishers, 2001).

3 *http://www.nano.gov/*.

4 *http://cordis.europa.eu/*.

5 *http://www.nanotechproject.org*.

6 *http://www.americanelements.com/nanotech.htm*.

7 *http://www.crnano.org/*.

8 Nouailhat, A. *An Introduction to Nanoscience and Nanotechnology*. (John Wiley & Sons, Inc., 2008).

9 *http://web.mit.edu/chemistry/www/faculty/nanoscience.html*.

10 Roco, M. C. & Subcommittee, N. Nanoscale Science and Engineering: Unifying and Transforming Tools. *AIChE Journal* **50**, 890-897 (2004).

11 Cao, G. *Nanostructures & Nanomaterials: Synthesis, Properties & Applications* (Imperial College Press, 2004).

12 *http://www.nanoroad.net*.

13 Murray, C. B., Kagan, C. R. & Bawendi, M. G. Synthesis and Characterization of Monodisperse Nanocrystals and Close-packed Nanocrystal Assemblies. *Annual Review of Materials Science* **30**, 545-610 (2000).

14 Herron, N. & Thorn, D. L. Nanoparticles: Uses and Relationships to Molecular Cluster Compounds. *Advanced Materials* **10**, 1173-1184 (1998).

15 Mazzola, L. Commercializing Nanotechnology. *Nature Biotechnology* **21**, 1137-1143 (2003).

16 Paull, R., Wolfe, J., Hebert, P. & Sinkula, M. Investing in Nanotechnology. *Nature Biotechnology* **21**, 1144-1147 (2003).

17 Whitesides, G. M. Nanoscience, Nanotechnology, and Chemistry. *Small* **1**, 172-179 (2005).

18 Alivisatos, A. P. Nanocrystals: Building Blocks for Modern Materials Design. *Endeavour* **21**, 56-60 (1997).

19 Salata, O. V. Applications of Nanoparticles in Biology and Medicine. *Journal of Nanobiotechnology* **2** (2004).

20 Sergeev, G. B. *Nanochemistry* (Elsevier B.V., 2006).

21 Ozin, G. A., Arsenault, A. C. & Cademartiri, L. *Nanochemistry : A Chemical Approach to Nanomaterials*. 2nd edn, (Royal Society of Chemistry, 2009).

22 Liz-Marz´an, L. M. & Kamat, P. V. *Nanoscale Materials*. (Kluwer Academic Publishers, 2003).

23 Wolf, E. L. *Quantum Nanoelectronics : An Introduction to Electronic Nanotechnology and Quantum Computing* (Wiley-VCH 2009).

24 Novotny, L. & Hecht, B. *Principles of Nano-Optics* (Cambridge University Press, 2006).

25 Alivisatos, P. The Use of Nanocrystals in Biological Detection. *Nature Biotechnology* **22**, 47-52 (2004).

26 Anker, J. N. *et al.* Biosensing with Plasmonic Nanosensors. *Nature Materials* **7**, 442-453 (2008).

27 Brigger, I., Dubernet, C. & Couvreur, P. Nanoparticles in Cancer Therapy and Diagnosis. *Advanced Drug Delivery Reviews* **54**, 631-651 (2002).

28 Yavuz, M. S. *et al.* Gold Nanocages Covered by Smart Polymers for Controlled Release with Near-infrared Light. *Nature Materials* **8**, 935-939 (2009).

29 Guihen, E. & Glennon, J. D. Nanoparticles in Separation Science—Recent Developments. *Analytical Letters* **36**, 3309 - 3336 (2003).

30 Huaizhi, Z. & Yuantao, N. China's Ancient Gold Drugs. *Gold Bulletin* **34**, 24-29 (2001).

31 Brown, C. L. *et al.* Nanogoldpharmaceutics. *Gold Bulletin* **40**, 245-250 (2007).

32 Hunt, L. The True Story of Purple of Cassius. *Gold Bulletin* **9**, 134-139 (1976).

33 Faraday, M. The Bakerian Lecture: Experimental Relations of Gold (and Other Metals) to Light. *Philosophical Transactions of the Royal Society of London* **147**, 145-181 (1857).

34 Zsigmondy, R. *The Chemistry of Colloids*. (John Wiley & Sons, Inc., 1917).

35 Svedberg, T. *The Formation of Colloids*. (D. Van Nostrand Company,Inc., 1921).

36 Ostwald, W. *An Introduction to Theoretical and Applied Colloid Chemistry*. (John Wiley & Sons, Inc., 1917).

37 Bohren, C. F. & Huffman, D. R. *Absorption and Scattering of Light by Small Particles*. (Wiley, 1983).

38 Turkevich, J. & Hillier, J. Electron Microscopy of Colloidal Systems. *Analytical Chemistry* **21**, 475-485 (1949).

39 Turkevich, J., Stevenson, P. C. & Hillier, J. A Study of The Nucleation and Growth Processes in The Synthesis of Colloidal Gold. *Discussions of the Faraday Society* **11**, 55-75 (1951).

40 Faulk, W. P. & Taylor, G. M. An Immunocolloid Method for the Electron Microscope. *Immunochemistry* **8**, 1081-1083 (1971).

41 Frens, G. Controlled Nucleation for the Regulation of the Particle Size in Monodisperse Gold Solutions. *Nature Physical Science* **241**, 20-22 (1973).

42 Horisberger, M. & Rossett, J. Colloidal Gold, a Useful Marker for Transmission and Scanning Electron Microscopy. *Journal of Histochemistry and Cytochemistry* **25**, 295–305 (1977).

43 http://*apps.isi**knowledge**.com/*

44 Henzie, J., Lee, J., Lee, M. H., Hasan, W. & Odom, T. W. Nanofabrication of Plasmonic Structures. *Annual Review of Physical Chemistry* **60**, 147-165, (2009).

45 Campbell, D. J. & Xia, Y. Plasmons: Why Should We Care? *Journal of Chemical Education* **84**, 91-96 (2007).

46 Lu, X., Rycenga, M., Skrabalak, S. E., Wiley, B. & Xia, Y. Chemical Synthesis of Novel Plasmonic Nanoparticles. *Annual Review of Physical Chemistry* **60**, 167-192 (2009).

47 Hu, M. *et al.* Gold Nanostructures: Engineering Their Plasmonic Properties for Biomedical Applications. *Chemical Society Reviews* **35**, 1084–1094 (2006).

48 Prodan, E., Radloff, C., Halas, N. J. & Nordlander, P. A Hybridization Model for the Plasmon Response of Complex Nanostructures. *Science* **302**, 419-422 (2003).

49 Yuan, H. *et al.* Shape and SPR Evolution of Thorny Gold Nanoparticles Promoted by Silver Ions. *Chemistry of Materials* **19**, 1592-1600 (2007).

50 Bakr, O. M., Wunsch, B. H. & Stellacci, F. High-Yield Synthesis of Multi-Branched Urchin-Like Gold Nanoparticles. *Chemistry of Materials* **18**, 3297-3301 (2006).

51 Jena, B. K. & Raj, C. R. Seedless, Surfactantless Room Temperature Synthesis of Single Crystalline Fluorescent Gold Nanoflowers with Pronounced SERS and Electrocatalytic Activity. *Chemistry of Materials* **20**, 3546–3548 (2008).

52 Rosi, N. L. & Mirkin, C. A. Nanostructures in Biodiagnostics. *Chemical Reviews* **105**, 1547-1562 (2005).

53 Katz, E. & Willner, I. Integrated Nanoparticle–Biomolecule Hybrid Systems: Synthesis, Properties, and Applications. *Angewandte Chemie - International Edition* **43**, 6042 – 6108 (2004).

54 L.West, J. & Halas, N. J. Engineered Nanomaterials for Biophotonics Applications: Improving Sensing, Imaging, and Therapeutics. *Annual Review of Biomedical Engineering* **5**, 285–292 (2003).

55 Lippitz, M., Dijk, M. A. v. & Orrit, M. Third-Harmonic Generation from Single Gold Nanoparticles. *Nano Letters* **5**, 799-802 (2005).

56 Wilcoxon, J. P., Martin, J. E., Parsapour, F., Wiedenman, B. & Kelley, D. F. Photoluminescence from Nanosize Gold Clusters. *The Journal of Chemical Physics* **108**, 9137-9143 (1998).

57 Nam, J.-M., Thaxton, C. S. & Mirkin, C. A. Nanoparticle-Based Bio–Bar Codes for the Ultrasensitive Detection of Proteins. *Science* **301**, 1884-1886 (2003).

58 Sun, Y. & Xia, Y. Shape-Controlled Synthesis of Gold and Silver Nanoparticles. *Science* **298**, 2176-2179 (2002).

59 Chemla, Y. R. *et al.* Ultrasensitive Magnetic Biosensor for Homogeneous Immunoassay. *Proceedings of the National Academy of Sciences of the United States of America* **97**, 14268–14272 (2000).

60 Velev, O. D. & Kaler, E. W. In Situ Assembly of Colloidal Particles into Miniaturized Biosensors. *Langmuir* **15**, 3693-3698 (1999).

61 Wang, J., Liu, G. & Merkocüi, A. Electrochemical Coding Technology for Simultaneous Detection of Multiple DNA Targets. *Journal of the American Chemical Society* **125**, 3214-3215 (2003).

62 Haes, A. J. & Duyne, R. P. V. A Nanoscale Optical Biosensor: Sensitivity and Selectivity of an Approach Based on the Localized Surface Plasmon Resonance Spectroscopy of Triangular Silver Nanoparticles. *Journal of the American Chemical Society* **124**, 10596-10604 (2002).

63 Jensen, T. R., Malinsky, M. D., Haynes, C. L. & Duyne, R. P. V. Nanosphere Lithography: Tunable Localized Surface Plasmon Resonance Spectra of Silver Nanoparticles *Journal of Physical Chemistry B* **104**, 10549-10556 (2000).

64 Michaels, A. M., Nirmal, M. & Brus, L. E. Surface Enhanced Raman Spectroscopy of Individual Rhodamine 6G Molecules on Large Ag Nanocrystals. *Journal of the American Chemical Society* **121**, 9932-9939 (1999).

65 Storhoff, J. J. *et al.* What Controls the Optical Properties of DNA-Linked Gold Nanoparticle Assemblies? *Journal of the American Chemical Society* **122**, 4640-4650 (2000).

66 Connolly, S., Cobbe, S. & Fitzmaurice, D. Effects of Ligand-Receptor Geometry and Stoichiometry on Protein-Induced Aggregation of Biotin-Modified Colloidal Gold. *Journal of Physical Chemistry B* **105**, 2222-2226 (2001).

67 Elghanian, R., Storhoff, J. J., Mucic, R. C., Letsinger, R. L. & Mirkin, C. A. Selective Colorimetric Detection of Polynucleotides Based on the Distance-Dependent Optical Properties of Gold Nanoparticles. *Science* **277**, 1078-1080 (1997).

68 McFarland, A. D. & Duyne, R. P. V. Single Silver Nanoparticles as Real-Time Optical Sensors with Zeptomole Sensitivity. *Nano Letters* **3**, 1057-1062 (2003).

69 Henglein, A. & Meisel, D. Spectrophotometric Observations of the Adsorption of Organosulfur Compounds on Colloidal Silver Nanoparticles. *Journal of Physical Chemistry B* **102**, 8364-8366 (1998).

70 Llnaert, T., Mulvaney, P. & Henglein, A. Surface Chemistry of Colloidal Silver: Surface Plasmon Damping by Chemisorbed I^-, SH^-, and $C_6H_5S^-$. *Journal of Physical Chemistry* **97**, 679-682 (1993).

71 Bao, P. *et al.* High-Sensitivity Detection of DNA Hybridization on Microarrays Using Resonance Light Scattering. *Analytical Chemistry* **74**, 1792-1797 (2002).

72 Taton, T. A., Mirkin, C. A. & Letsinger, R. L. Scanometric DNA Array Detection with Nanoparticle Probes. *Science* **289**, 1757-1760 (2000).

73 Maxwell, D. J., Taylor, J. R. & Nie, S. Self-Assembled Nanoparticle Probes for Recognition and Detection of Biomolecules. *Journal of the American Chemical Society* **124**, 9606-9612 (2002).

74 Dubertret, B., Calame, M. & Libchaber, A. J. Single-Mismatch Detection Using Gold-Quenched Fluorescent Oligonucleotides. *Nature Biotechnology* **19**, 365-370 (2001).

75 Tian, Z.-Q., Ren, B. & Wu, D.-Y. Surface-Enhanced Raman Scattering: From Noble to Transition Metals and from Rough Surfaces to Ordered Nanostructures. *Journal of Physical Chemistry B* **106**, 9463-9468 (2002).

76 Weizmann, Y., Patolsky, F. & Willner, I. Amplified Detection of DNA and Analysis of Single-base Mismatches by the Catalyzed Deposition of Gold on Au-nanoparticles. *Analyst* **126**, 1502–1504 (2001).

77 Bailey, R. C., Nam, J.-M., Mirkin, C. A. & Hupp, J. T. Real-Time Multicolor DNA Detection with Chemoresponsive Diffraction Gratings and Nanoparticle Probes. *Journal of the American Chemical Society* **125**, 13541-13547 (2003).

78 Liu, J. & Lu, Y. Colorimetric Biosensors Based on DNAzyme-Assembled Gold Nanoparticles. *Journal of Fluorescence* **14**, 343-354 (2004).

79 Sardar, R., Funston, A. M., Mulvaney, P. & Murray, R. W. Gold Nanoparticles: Past, Present, and Future. *Langmuir* **25**, 13840-13851 (2009).

80 Agasti, S. S. *et al.* Nanoparticles for Detection and Diagnosis. *Advanced Drug Delivery Reviews* **62**, 316–328 (2010).

81 Wittenberg, N. J. & Haynes, C. L. Using Nanoparticles to Push the Limits of Detection. *Nanomedicine and Nanobiotechnology* **1**, 237–254 (2009).

82 Loo, C. *et al.* Nanoshell-Enabled Photonics-Based Imaging and Therapy of Cancer. *Technology in Cancer Research & Treatment* **3**, 33-40 (2004).

83 El-Sayed, I. H., Huang, X. & El-Sayed, M. A. Surface Plasmon Resonance Scattering and Absorption of anti-EGFR Antibody Conjugated Gold Nanoparticles in Cancer Diagnostics: Applications in Oral Cancer. *Nano Letters* **5**, 829-834 (2005).

84 Huang, X., El-Sayed, I. H., Qian, W. & El-Sayed, M. A. Cancer Cell Imaging and Photothermal Therapy in the Near-Infrared Region by Using Gold Nanorods *Journal of the American Chemical Society* **128**, 2115-2120 (2006).

85 Cang, H. *et al.* Gold Nanocages as Contrast Agents for Spectroscopic Optical Coherence Tomography. *Optics Letters* **30**, 3048-3050 (2005).

86 El-Sayed, I. H., Huang, X. & El-Sayed, M. A. Selective Laser Photo-Thermal Therapy of Epithelial Carcinoma using Anti-EGFR Antibody Conjugated Gold Nanoparticles. *Cancer Letters* **239**, 129–135 (2006).

87 O'Neal, D. P., Hirsch, L. R., Halas, N. J., Payne, J. D. & West, J. L. Photo-Thermal Tumor Ablation in Mice using Near Infrared-Absorbing Nanoparticles. *Cancer Letters* **209**, 171–176 (2004).

88 Hirsch, L. R. *et al.* Nanoshell-Mediated Near-Infrared Thermal Therapy of Tumors under Magnetic Resonance Guidance. *Proceedings of the National Academy of Sciences of the United States of America* **100**, 13549–13554 (2003).

89 Gu, F. X. *et al.* Targeted Nanoparticles for Cancer Therapy. *Nano Today* **2**, 14-21 (2007).

90 Letfullin, R. R., Joenathan, C., George, T. F. & Zharov, V. P. Laser-Induced Explosion of Gold Nanoparticles: Potential Role for Nanophotothermolysis of Cancer. *Nanomedicine* **1**, 473-480 (2006).

91 Sershen, S. R., Westcott, S. L., Halas, N. J. & West, J. L. Temperature-Sensitive Polymer–Nanoshell Composites for Photothermally Modulated Drug Delivery. *Journal of Biomedical Materials Research* **51**, 293–298 (2000).

92 Wijaya, A., Schaffer, S. B., Pallares, I. G. & Hamad-Schifferli, K. Selective Release of Multiple DNA Oligonucleotides from Gold Nanorods. *ACS Nano* **3**, 80-86 (2009).

93 Shipway, A. N., Lahav, M. & Willner, I. Nanostructured Gold Colloid Electrodes. *Advanced Materials* **12**, 993-998 (2000).

94 Chen, S. *et al.* Gold Nanoelectrodes of Varied Size: Transition to Molecule-Like Charging. *Science* **280**, 2098-2101 (1998).

95 Homberger, M. & Simon, U. On The Application Potential of Gold Nanoparticles in Nanoelectronics and Biomedicine. *Philosophical Transactions of the Royal Society A* **368**, 1405-1453 (2010).

96 Moth-Poulsen, K. & Bjørnholm, T. Molecular Electronics with Single Molecules in Solid-State Devices. *Nature Nanotechnology* **4**, 551-556 (2009).

97 Schull, G., Frederiksen, T., Arnau, A. s., Sánchez-Portal, D. & Berndt, R. Atomic-Scale Engineering of Electrodes for Single-Molecule Contacts. *Nature Nanotechnology* (2010).

98 Quek, S. Y. *et al.* Mechanically Controlled Binary Conductance Switching of a Single-Molecule Junction. *Nature Nanotechnology* **4**, 230-234 (2009).

99 Chow, G.-M. & Noskova, N. I. *Nanostructured Materials Science & Technology (NATO Science Partnership Sub-Series: 3:)* Vol. 50 (Kluwer Academic Publishers, 1998).

100 Whitesides, G. M. & Love, J. C. The Art of Building Small. *Scientific American* **285**, 39-47 (2001).

101 Das, B., Subramaniam, S. & Melloch, M. R. Effects of Electron-Beam-Induced Damage on Leakage Currents in Back-Gated GaAs/AlGaAs Devices. *Semiconductor Science and Technology* **8**, 1347-1351 (1993).

102 Edelstein, A. S. & Cammarata, R. C. *Nanomaterials : Synthesis, Properties, and Applications* (Institute of Physics Pub., 1996).

103 LaMer, V. K. & Dinegar, R. H. Theory, Production and Mechanism of Formation of Monodispersed Hydrosols. *Journal of the American Chemical Society* **72**, 4847-4854 (1950).

104 LaMer, V. K. Nucleation in Phase Transitions. *Industrial and Engineering Chemistry* **44**, 1270-1277 (1952).

105 Goia, D. V. & Matijevic, E. Preparation of Monodispersed Metal Particles. *New Journal of Chemistry* **22**, 1203 - 1215 (1998).

106 Matijevic, E. Production of Monodisperse Colloidal Particles. *Annual Review of Material Science* **15**, 483-516 (1985).

107 Sugimoto, T. Preparation of Monodispersed Colloidal Particles. *Advances in Colloid and Interface Science* **28**, 65-108 (1987).

108 Goia, D. V. & Matijevic, E. Tailoring the Particle Size of Monodispersed Colloidal Gold. *Colloids and Surfaces A: Physicochemical and Engineering Aspects* **146**, 139–152 (1999).

109 Calvert, P. And They All Look Just the Same. *Nature* **367**, 119-120 (1994).

110 Ouden, C. J. J. D. & Thompson, R. W. Analysis of the Formation of Monodisperse Populations by Homogeneous Nucleation. *Journal of Colloid and Interface Science* **143**, 77-84 (1991).

111 Morales, M. P., Gonzalez-Carreno, T. & Serna, C. J. The Formation of a-Fe2O3 Monodispersed Particles in Solution. *Journal of Materials Research* **7**, 2538-2545 (1992).

112 Ocana, M., Rodriguez-Clemente, R. & Serna, C. J. Uniform Colloidal Particles in Solution : Formation Mechanisms. *Advanced Materials* **7**, 212-216 (1995).

113 Peng, X., Wickham, J. & Alivisatos, A. P. Kinetics of II-VI and III-V Colloidal Semiconductor Nanocrystal Growth: "Focusing" of Size Distributions. *Journal of the American Chemical Society* **120**, 5343-5344 (1998).

114 Overbeek, J. T. G. Monodisperse Colloidal Systems, Fascinating and Useful. *Advances in Colloid and Interface Science* **15**, 251-277 (1982).

115 Hiramatsu, H. & Osterloh, F. E. A Simple Large-Scale Synthesis of Nearly Monodisperse Gold and Silver Nanoparticles with Adjustable Sizes and with Exchangeable Surfactants. *Chemistry of Materials* **16**, 2509-2511 (2004).

116 Leff, D. V., Ohara, P. C., Heath, J. R. & Gelbart, W. M. Thermodynamic Control of Gold Nanocrystal Size: Experiment and Theory. *Journal of Physical Chemistry* **99**, 7036-7041 (1995).

117 Rao, C. N. R., Vivekchand, S. R. C., Biswas, K. & Govindaraj, A. Synthesis of Inorganic Nanomaterials. *Dalton Transactions*, 3728-3749 (2007).

118 Matijevic, E. Preparation and Properties of Uniform Size Colloids. *Chemistry of Materials* **5**, 412-426 (1993).

119 Brust, M., Walker, M., Bethell, D., Schiffrin, D. J. & Whyman, R. Synthesis of Thiol-derivatised Gold Nanoparticles in a Two-phase Liquid-Liquid System. *Chemical Communications* **7**, 801-802 (1994).

120 Daniel, M.-C. & Astruc, D. Gold Nanoparticles: Assembly, Supramolecular Chemistry, Quantum-Size-Related Properties, and Applications toward Biology, Catalysis, and Nanotechnology. *Chemical Reviews* **104**, 293-346 (2004).

121 Duff, D. G., Baiker, A. & Edwards, P. P. A New Hydrosol of Gold Clusters. 1. Formation and Particle Size Variation. *Langmuir* **9**, 2301-2309 (1993).

122 Aslam, M., Fu, L., Su, M., Vijayamohanan, K. & Dravid, V. P. Novel One-Step Synthesis of Amine-Stabilized Aqueous Colloidal Gold Nanoparticles. *Journal of Materials Chemistry* **14**, 1795 – 1797 (2004).

123 Leff, D. V., Brandt, L. & Heath, J. R. Synthesis and Characterization of Hydrophobic, Organically-Soluble Gold Nanocrystals Functionalized with Primary Amines. *Langmuir* **12**, 4723-4730 (1996).

124 Yao, H., Momozawa, O., Hamatani, T. & Kimura, K. Stepwise Size-Selective Extraction of Carboxylate-Modified Gold Nanoparticles from an Aqueous Suspension into Toluene with Tetraoctylammonium Cations. *Chemistry of Materials* **13**, 4692-4697 (2001).

125 Corbierre, M. K. *et al.* Polymer-Stabilized Gold Nanoparticles and Their Incorporation into Polymer Matrices. *Journal of the American Chemical Society* **123**, 10411-10412 (2001).

126 Weare, W. W., Reed, S. M., Warner, M. G. & Hutchison, J. E. Improved Synthesis of Small (d_{CORE}=1.5 nm) Phosphine-Stabilized Gold Nanoparticles. *Journal of the American Chemical Society* **122**, 12890-12891 (2000).

127 Sun, X., Dong, S. & Wang, E. Large-Scale Synthesis of Micrometer-Scale Single-Crystalline Au Plates of Nanometer Thickness by a Wet-Chemical Route. *Angewandte Chemie - International Edition* **43**, 6360-6363 (2004).

128 Brust, M. & Kiely, C. J. Some Recent Advances in Nanostructure Preparation from Gold and Silver Particles: A Short Topical Review. *Colloids and Surfaces A: Physicochemical and Engineering Aspects* **202** 175–186 (2002).

129 He, S. *et al.* Formation of Silver Nanoparticles and Self-Assembled Two-Dimensional Ordered Superlattice. *Langmuir* **17**, 1571-1575 (2001).

130 Sondi, I., Goia, D. V. & Matijevic, E. Preparation of Highly Concentrated Stable Dispersions of Uniform Silver Nanoparticles. *Journal of Colloid and Interface Science* **260**, 75–81 (2003).

131 Pastoriza-Santos, I. & Liz-Marzan, L. M. Formation and Stabilization of Silver Nanoparticles through Reduction by N,N-Dimethylformamide. *Langmuir* **15**, 948-951 (1999).

132 Tan, Y., Li, Y. & Zhu, D. Preparation of Silver Nanocrystals in the Presence of Aniline. *Journal of Colloid and Interface Science* **258**, 244-251 (2003).

133 Ayyappan, S., Gopalan, R. S., Subbanna, G. N. & Rao, C. N. R. Nanoparticles of Ag, Au, Pd, and Cu Produced by Alcohol Reduction of the Salts. *Journal of Materials Research* **12**, 398-401 (1997).

134 Tai, C. Y., Wang, Y.-H., Tai, C.-T. & Liu, H.-S. Preparation of Silver Nanoparticles Using a Spinning Disk Reactor in a Continuous Mode. *Industrial and Engineering Chemistry* **48**, 10104–10109 (2009).

135 Cozzoli, P. D., Pellegrino, T. & Manna, L. Synthesis, Properties and Perspectives of Hybrid Nanocrystal Structures. *Chemical Society Reviews* **35**, 1195-1208 (2006).

136 Grzelczak, M., Perez-Juste, J., Mulvaney, P. & Liz-Marzan, L. M. Shape Control in Gold Nanoparticle Synthesis. *Chemical Society Reviews* **37**, 1783–1791 (2008).

137 Ṕerez-Juste, J., Pastoriza-Santos, I., Liz-Marzan, L. M. & Mulvaney, P. Gold Nanorods: Synthesis, Characterization and Applications. *Coordination Chemistry Reviews* **249**, 1870–1901 (2005).

138 Toma, H. E., Zamarion, V. M., Toma, S. H. & Araki, K. The Coordination Chemistry at Gold Nanoparticles. *Journal of Brazilian Chemical Society* **21**, 1158-1176 (2010).

139 DeMello, J. & DeMello, A. Microscale Reactors: Nanoscale Products. *Lab on a Chip* **4**, 11N-15N (2004).

140 Torres, F. E., Russel, W. B. & Schowalter, W. R. Floc Structure and Growth Kinetics for Rapid Shear Coagulation of Polystyrene Colloids. *Journal of Colloid and Interface Science* **142**, 554-574 (1991).

141 Levenspiel, O. *Chemical Reaction Engineering*. (Wiley, 1962).

142 Fogler, S. *Elements of Chemical Reaction Engineering*. (Prentice-Hall, Inc. , 1992).

143 Whitesides, G. M. The Origins and the Future of Microfluidics. *Nature* **442**, 368-373 (2006).

144 Jensen, K. F. Microreaction Engineering - Is Small Better? *Chemical Engineering Science* **56**, 293-303 (2001).

145 Worz, O., Jackel, K. P., Richter, T. & Wolf, A. Microreactors - A New Efficient Tool for Reactor Development. *Chemical Engineering and Technology* **24**, 138-142 (2001).

146 Ehrfeld, W., Hessel, V. & Löwe., H. *Microreactors : New Technology for Modern Chemistry*. (Wiley-VCH, 2000).

147 Hardt, S., Ehrfeld, W., Hessel, V. & Vanden Bussche, K. M. Strategies for Size Reduction of Microreactors by Heat Transfer Enhancement Effects. *Chemical Engineering Communications* **190**, 540-559 (2003).

148 Nam-Trung, N. & Zhigang, W. Micromixers-A Review. *Journal of Micromechanics and Microengineering* **15**, 1-16 (2005).

149 DeMello, A. J. Control and Detection of Chemical Reactions in Microfluidic Systems. *Nature* **442**, 394-402 (2006).

150 Haswell, S. J. & Watts, P. Green Chemistry: Synthesis in Micro Reactors. *Green Chemistry* **5**, 240-249 (2003).

151 Haswell, S. J. *et al.* The Application of Micro Reactors to Synthetic Chemistry. *Chemical Communications* **7**, 391-398 (2001).

152 Geyer, K., Codee, J. D. C. & Seeberger, P. H. Microreactors As Tools for Synthetic Chemists - the Chemists' Round-Bottomed Flask of the 21st Century? *Chemistry - A European Journal* **12**, 8434-8442 (2006).

153 Gunther, A. & Jensen, K. F. Multiphase Microfluidics: From Flow Characteristics to Chemical and Materials Synthesis. *Lab on a Chip* **6**, 1487-1503 (2006).

2. Microreactors for Particle Synthesis

This chapter describes in detail the limitations of the currently established nanomanufacturing techniques using the synthesis of anisotropic gold nanoparticles as the model system. The basic drawbacks of batch manufacturing techniques and the advantages of microfluidic methods in overcoming these disadvantages are outlined, thus further emphasizing the thesis objectives. A literature survey of the state of the art developments in microfluidic methods as well as the general guidelines for designing a microreactor and the typical fabrication techniques are also explained here.

A detailed analysis of the factors to be controlled to obtain monodisperse particles was done in Chapter 1 along with a discussion of the current trends in the manufacturing of metallic nanomaterials, specifically gold and silver. Most of these techniques however are for spherical particles of varying sizes. Recently, synthesis and manipulation of the properties of anisotropic shapes of these nanomaterials such as nanorods, disks, triangular prisms, multipods, cubes, nanoshells etc., have become important for many fundamental reasons as well as technological applications. These particles, as pointed out earlier (Chapter 1) have superior optical properties than the spherical particles and the control of their size and shape is far more complicated. There is no one single method for the controlled synthesis of these particles and their continuous synthesis for commercial applications has not been reported so far. A brief discussion of anisotropic metallic nanomaterials follows.

2.1. Anisotropic Nanomaterials

Several different techniques for the synthesis of noble metallic nanomaterials or nanocrystals of varying shapes and sizes have been put forward in the past few decades. Understanding the mechanism of crystallization, formation of different crystal shapes, orientation and structure after homogeneous or heterogeneous nucleation and growth in the

reaction solution are currently the most researched area of material science.[1] Noble metals typically crystallize in face centered cubic lattice (FCC†) and tend to grow into twinned‡ or multiply twinned‡ particles with their surface bound by the lowest-energy facet. Thus in the solution phase synthesis of noble metallic nanoparticles, formation of isotropic shapes such as spheres (case of gold) is energetically favorable. Hence, most synthetic protocols in the early half of the century dealt with the synthesis and characterization of these isotropic structures. Once the protocol for size and monodispersity of the particles has been reasonably established, shape control or synthesis of anisotropic particles (non-spherical) can be looked at as the next level of sophistication. Control over the size as well as other topological aspects of a particle population in solution phase synthesis is possible by judiciously choosing the experimental conditions and additives. Additives such as surfactants, ligands, chelating agents, polymers, adsorbates or passivants are used for shape control to bind onto the surface of nanoparticles.[2]

Some of the key parameters to be considered for shape selective solution phase synthesis of nanomaterials are (1) Control of the nucleation and growth phases, (2) Availability of high monomer concentration for better stability of anisotropic nanoparticle embryos[3] and (3) Suitable use of surfactants. The control of these parameters leads to the formation of anisotropic particles for anisotropic nanomaterials.[4] However, control of these parameters alone is not very successful for the shape control of highly symmetric cubic systems such as gold, silver etc.[4] In most cases, the specific mechanism and growth kinetics of the different shapes of particles are not well defined and most of the proposed mechanisms are still under discussion. In accordance to almost all of these proposed mechanisms, seeded growth leads to anisotropic shapes and the shape of the final particle is primarily determined by the twin defects in the initial seed.

---

†Face centered cubic lattice (FCC) is a type of arrangement of atoms within a crystal.

‡Two separate crystals sharing some of the crystal lattice points in a symmetrical manner lead to crystal twinning which can take several different configurations.

Different structures of seeds hence can grow into different particle shapes depending on the other key synthetic conditions.[5] Examples of such directional growth are shown in Figure 2.1 where a single crystal seed can be made to grow into either a cube or a cubeoctahedron or octahedron, using appropriate capping agents. These can be further grown into octagonal nanorods or nanobars by activating or deactivating the corresponding facets. Similarly, nanobeams from right bipyramids and rods from decahedron and icosahedron are in turn obtained from singly and multiply twinned seeds respectively.[6,7]

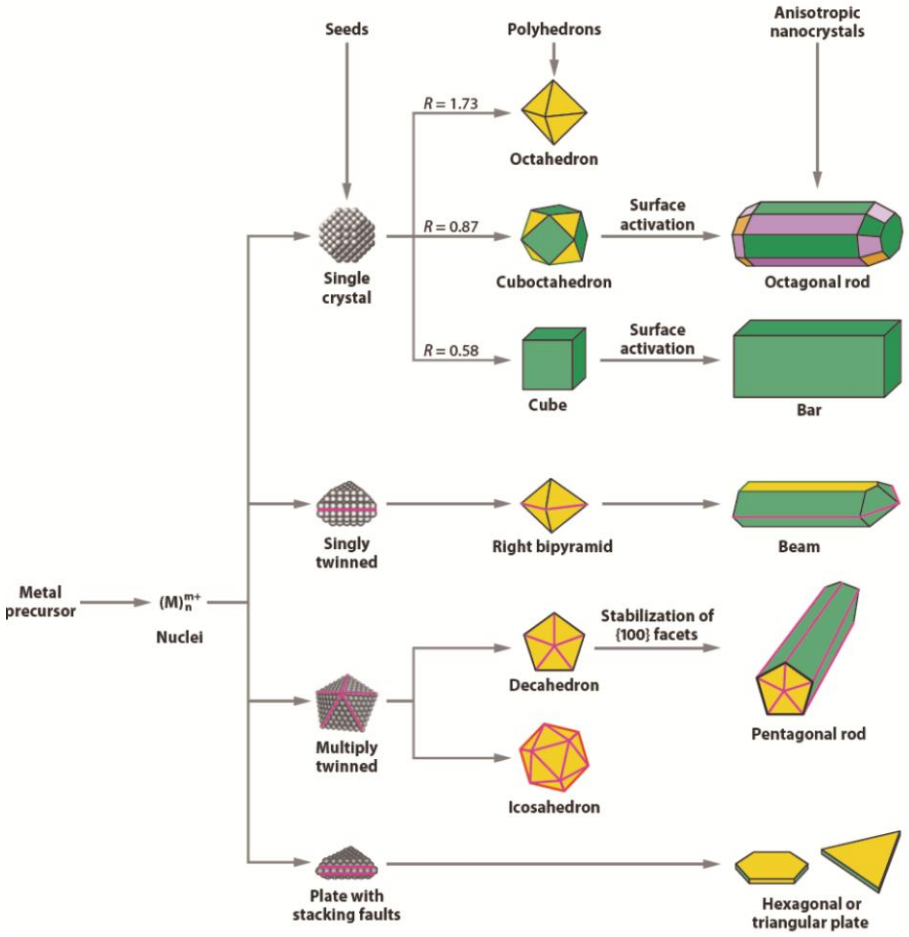

Figure 2.1. Schematic showing the mechanism of formation of different nanoparticle shapes in noble metals, from seeds that are single-crystal, singly-twinned, multiply-twinned and plate with stacking defect. The {100}, {111} and {110} facets are represented by green, orange and purple colors respectively. Parameter *R* represents the ratio between the growth rates along the <100> and <111> directions. Stacking faults lead to plate like seeds and hence plate shaped particle shapes. Reproduced with permission from Reference 5. Copyright 2009, Annual Reviews Inc.

Hence, the two main factors that control the formation of anisotropic nanocrystals are internal seed structure and growth conditions for the transformation of the twinned structure on the seeds to the desired shape.[4,5] Control of these parameters in solution-phase synthesis is essential and slight fluctuations in growth conditions will lead to variations in the expected particle morphologies.

2.2. Anisotropic Gold Nanomaterials

Gold nanomaterials have been synthesized since the early 2500 B.C. as was discussed in Chapter 1 and several researchers have perfected the art of synthesizing spherical gold nanoparticles of varying sizes from 3 nm to a few hundred nm. Since the optical properties of anisotropic gold nanomaterials were identified, interest in the synthesis of anisotropic gold is at the forte of current research. In particular, interest in synthesizing particles with their optical spectra covering the entire visible and infrared range (400 nm to 1100 nm) such as prisms, shells, cubes, rods and wires is high.

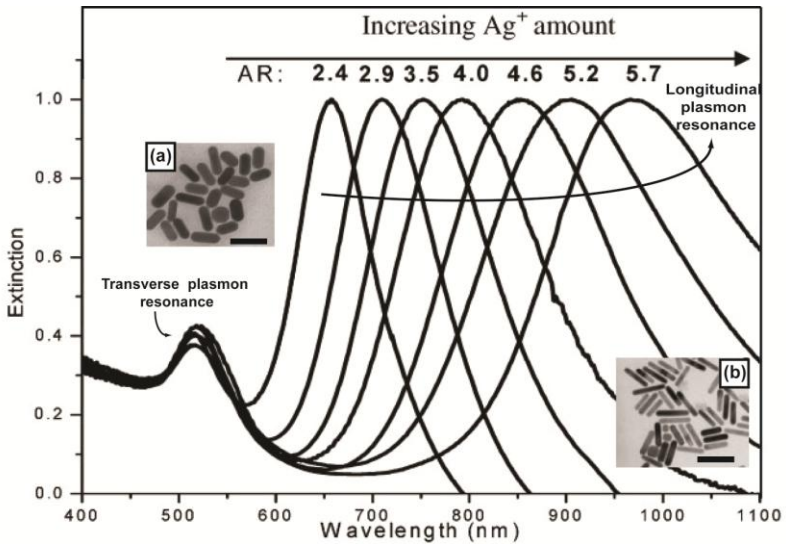

Figure 2.2. UV-visible-IR extinction spectra of gold nanorods of increasing aspect ratios (AR): The extinction maxima due to the short axis of the rods, transverse plasmon resonance, is at 520 nm while that due to the long axis of the rods, the longitudinal plasmon resonance ranges from 600 nm to 1000 nm depending on the particle AR. **(a)** and **(b)** SEM images of a population of rods of AR **(a)** 2.4 and **(b)** 5.2. Scale bars represent 100 nm. Adapted with permission from Reference 8. Copyright 2009, John Wiley and Sons.

Rod like structures are promising candidates for such studies since their optical properties can be easily tuned from 650 nm to 1000 nm by varying their aspect ratio (referred to as AR hereafter) which is the ratio of length to width of a particle, from 13 to 1 respectively.[9] Nanorods exhibit two kinds of plasmon resonance (a brief mention was made in Section 1.4.2) viz., the longitudinal plasmon resonance (LPR) which is due to the extinction of the incident light along the long axis of the rods and the transverse plasmon resonance (TPR) due to the extinction along the short axis of the rods, as can be seen in Figure 2.2.[8,10] The extinction maxima for the LPR is at longer wavelengths compared to the TPR and can be tuned by varying the length of the nanorods. This tunability of the extinction spectra has been used successfully in several different applications as pointed out in Chapter 1. However, the synthesis of these particles in large scale still remains a challenge to both the research and manufacturing community. The synthesis of other shapes of particles such as prisms, stars etc., will be possible by modifying the protocol for rods synthesis appropriately. Several methods for the synthesis of gold nanorods (specified as GNR hereafter) have been developed during the past decade such as the hard template method,[11,12] electrochemical method[13] and seeded growth method[14,15]. A brief description of these methods is provided in the following sections.

2.2.1. Template Method

Martin and co-workers first introduced the template method wherein gold is deposited onto a nanoporous polycarbonate or alumina template membrane by electrochemical deposition.[16,17] The size of the rods depends on the size of the pores on the membrane and the AR of the rods is varied by changing the membrane used as template. SEM images of a 12 nm porous alumina membrane is shown in Figures 2.3 (a) and (b) while the schematic for the growth of GNR by this method is shown in Figure 2.3 (c).[12] A conducting silver film is initially sputtered onto the surface of the porous alumina (Al_2O_3) membrane (stage I in Figure 2.3 (c)), which is used as a foundation for electrodeposition of gold (stage II). In subsequent stages the silver film and the porous membrane are dissolved, in the presence of polymeric

stabilizer such as poly (vinylpyrrolidone) and the GNR are dispersed in the required medium. TEM images of the so formed rods of varying AR are shown in Figure 2.3 (e).[11,12] The main disadvantage of the GNR synthesis through this method is the yield.[2]

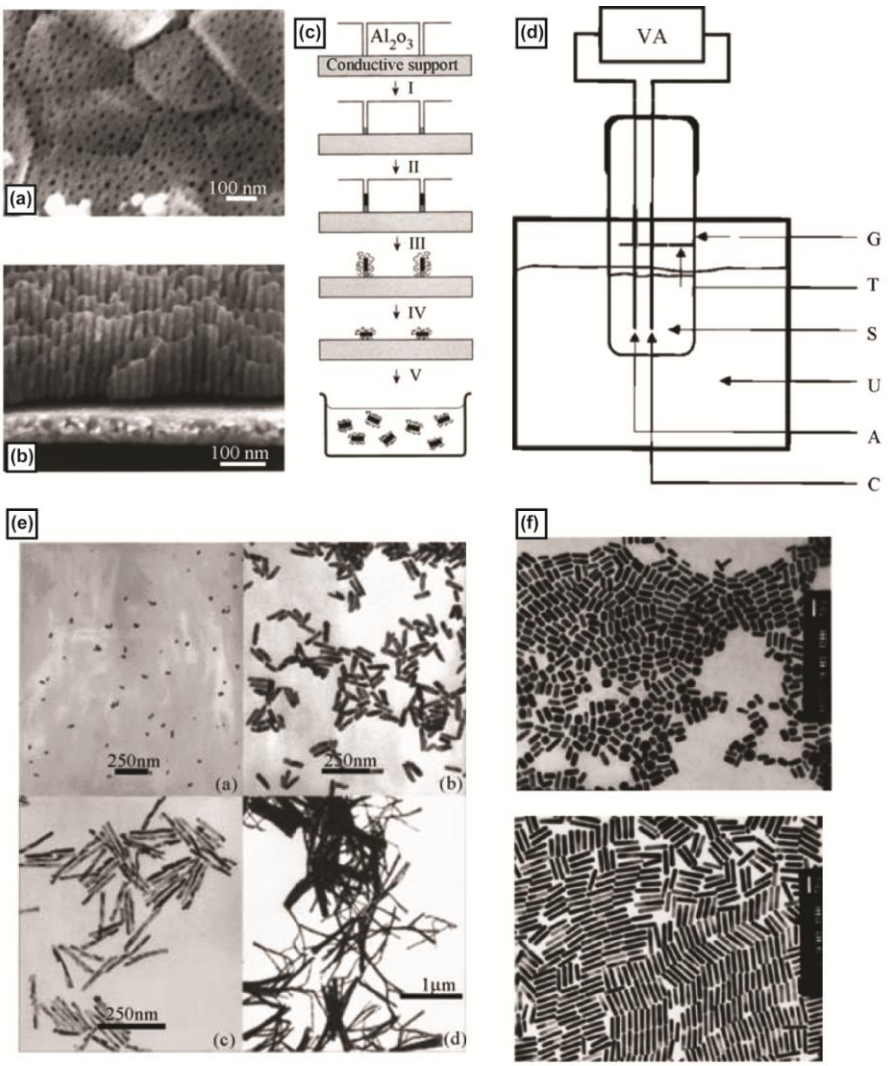

Figure 2.3. (a) and **(b)** SEM images of a porous alumina membrane. **(c)** Schematic showing the successive steps involved in the template mediated synthesis of gold nanorods. **(d)** Schematic showing the electrochemical method for the synthesis of gold nanorods; VA - power supply, G - glassware electro chemical cell, T - teflon spacer, S - electrode holder, U - ultrasonic cleaner, A – anode, C - cathode. **(e)** TEM images of GNR obtained from the template method. **(f)** TEM images of GNR with different aspect ratios 2.7 (top) and 6.1 (bottom). Scale bars represent 50 nm. Panels **(a)**, **(b), (c)** and **(e)** are adapted with permission from Reference 12. Copyright (2000), American Chemical Society. Panels **(d)** and **(f)** are adapted with permission from Reference 18. Copyright (1999), American Chemical Society.

2.2.2. Electrochemical Method

The method was pioneered by Wang and co-workers and the method consists of electrochemically reducing gold metal, used as the sacrificial anode, in the presence of a cationic surfactant, hexadecyltrimethylammonium bromide (CTAB). CTAB acts as a stabilizer preventing aggregation of the formed particles while the cosurfactant tetradodecyl ammonium bromide, acts as the rod-inducing agent (schematic in Figure 2.3 (d)).[18] A silver plate immersed behind the platinum cathode determines the AR of the rods formed. Rods of AR 2 - 7 are obtained from this method depending on the rate and time of release of silver ions. The controlled current electrolysis is carried out for 30 mins with 3 mA current.[13,18] Rods formed from this method (TEM images shown in Figure 2.3 (f))[18] are single crystalline particles and the selectivity is good; however the growth mechanism and the facet stabilization for growth into rods, remains unclear.[9,19]

2.2.3. Seeded Growth Method

This method for the growth of GNR was pioneered by Jana *et al.*[20] though the synthesis of anisotropic gold nanomaterial through seeded growth method was first reported by Wiesner and Wokaun.[21] They synthesized the nuclei or seeds by reducing hydrogen tetrachloroaurate ($HAuCl_4$, gold salt) with phosphorous which were then added to the $HAuCl_4$ growth solution and were reduced using hydrogen peroxide (H_2O_2) to form anisotropic crystals. The currently established protocol proposed by Jana *et al.* was inspired by the idea of CTAB acting as soft template in the electrochemical GNR growth method. This process is as shown in Figure 2.4 (a)[22] in which citrate capped small gold nanospheres act as seeds or nuclei for the formation of rods. The seeds are added to the growth solution containing excess CTAB and $HAuCl_4$. GNR are formed by the reduction of $HAuCl_4$ in the growth solution by ascorbic acid in the presence of seeds which act as the nucleating centers. The protocol has further been improved over a period of few years for the synthesis of long and short GNR of varying ARs by the same group (Murphy *et al.*).[4,15,22-27]

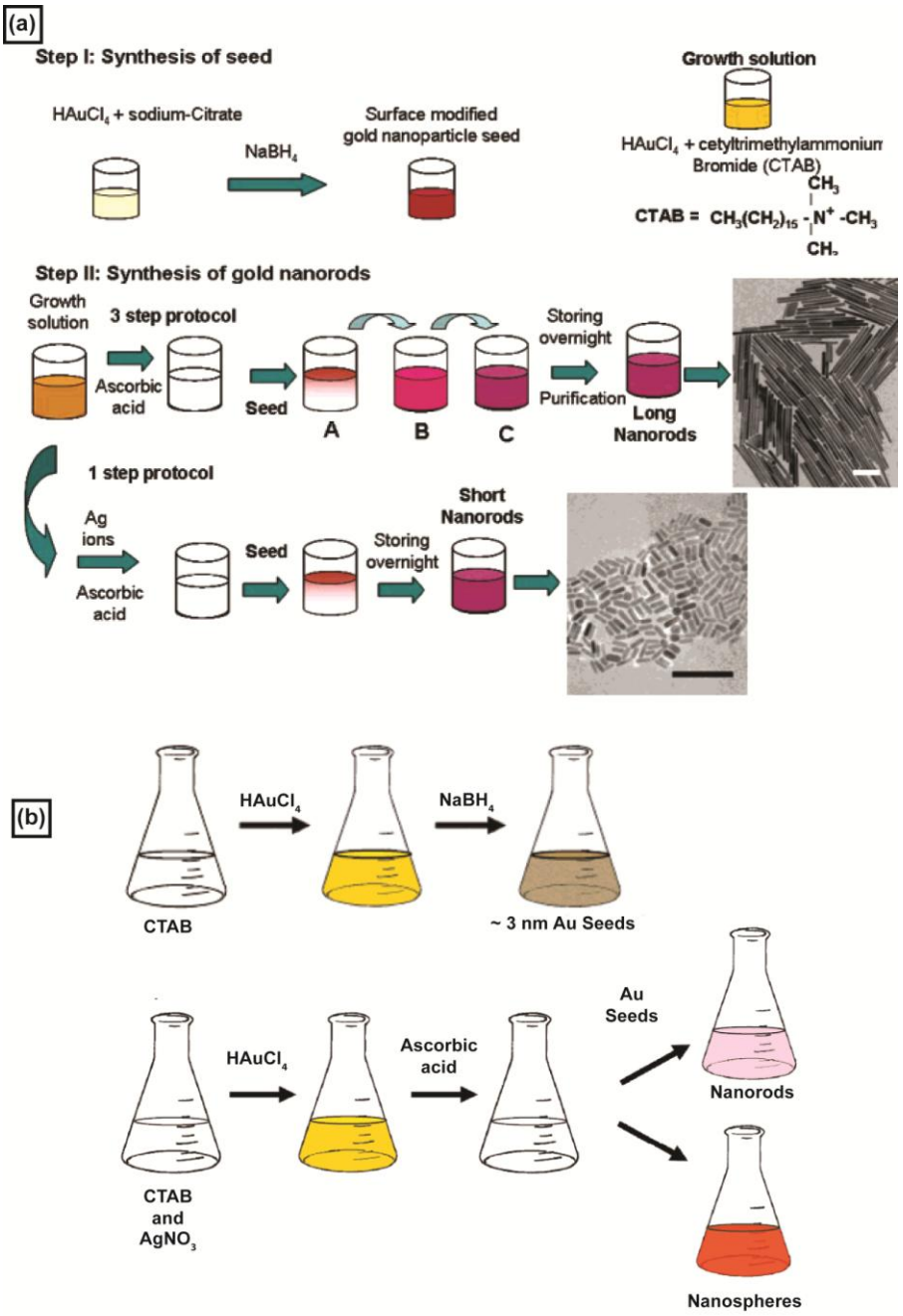

Figure 2.4. Schematic of the seeded growth method proposed by **(a)** Jana *et al.* where the seeds are prepared by the reduction of $HAuCl_4$ by sodium borohydride ($NaBH_4$) in the presence of trisodium citrate. Subsequently ascorbic acid is added to the growth solution containing CTAB and $HAuCl_4$ followed by the seed (one step protocol). Short GNR are obtained in the presence of silver nitrate ($AgNO_3$) using the one step protocol while long GNR are produced by the three step growth protocol. The three step growth protocol involves synthesis of GNR in stages where the GNR from the first stage is used as seeds in the second stage and so on sequentially. TEM images of the so formed rods are shown on the right. Scale bar represent 200 nm. Adapted with permission from Reference 22. Copyright (2006), American Chemical Society. **(b)** Nikoobakht and El-Sayed following a two-step seeded-growth method. Seeds are synthesized in step 1 with CTAB as stabilizers and step 2 involves synthesizing rods and spheres using the as-prepared seeds added to an aqueous mixture of CTAB, $HAuCl_4$ and $AgNO_3$ as the shape directing agent.

The protocol has also been extended to other shapes of gold colloids such as dog-bones, stars, multipods etc.[26,28] The main disadvantage of this protocol is the large fraction of gold nanospheres produced requiring time-consuming separation steps.[8] Simultaneously, Nikoobakht and El-Sayed modified the seeded growth protocol proposed by Jana *et al.* to produce high yield gold nanorods (99%) of ARs 1.5 to 4.5.[14] Their method did not require repetitive centrifugation steps to separate the rods from spheres due to the drastic reduction in the spheres synthesized. The modification introduced to the protocol includes using CTAB as the stabilizer for seeds instead of sodium citrate and using silver ions to achieve control over the AR of the rods as shown in Figure 2.4 (b). They were also able to obtain higher AR rods (upto 10) using a co-surfactant, benzyl dimethylhexadecylammonium chloride along with CTAB in the original growth solution.[14]

Some of the typical mechanisms put forth for the synthesis of GNR are the surfactant preferential binding mediated method, electric field mediated method, under potential deposition and a combination of these methods. A brief description of these methods follows.

2.2.4. Surfactant Preferential Binding Mediated

This mechanism was put forth by Murphy and co-workers[26] for rods synthesized using citrate capped seeds, based on an analysis of the structure of rods during their growth and formation in high resolution TEM. According to the mechanism, the anisotropic growth in metals is due to symmetry breaking in FCC metals which in turn is due to their intrinsic structural twinning as shown in Figure 2.5 (a). The rods obtained from citrate capped seeds are pentatetradedral twinned and the authors postulate that this is due to the preferential binding of CTAB. The head group of the surfactant CTAB in the solution preferentially binds to the {100} facet of the seeds and forms a bilayer of CTAB along the facet in a "Zipper" fashion. This bilayer thus stabilizes the {100} facet leading to growth along the {111} facet.[26,29] (The facets on a multiply twinned as well as on a single crystalline gold nanorod are shown in Appendix A.)

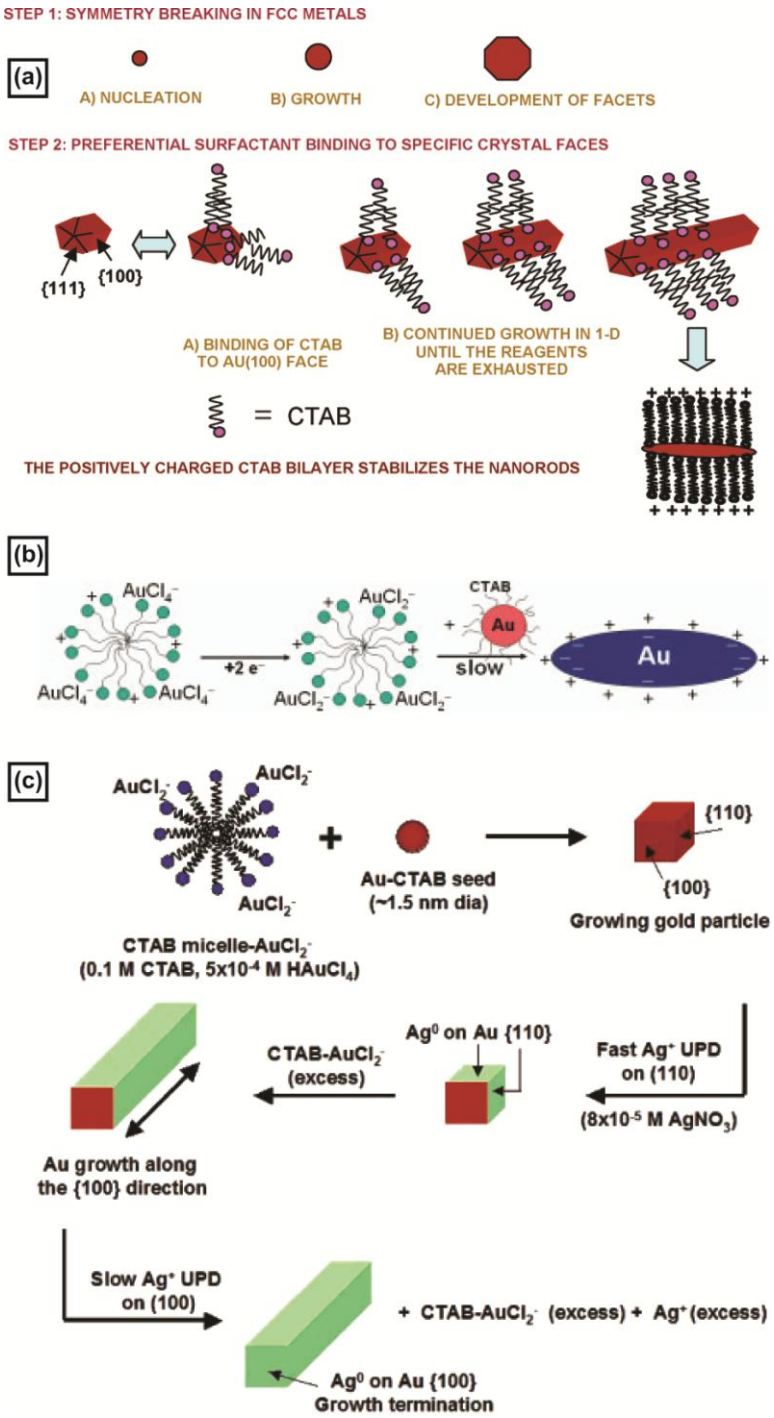

Figure 2.5. Mechanisms of seeded growth **(a)** Surfactant mediated mechanism proposed by Murphy *et al.* in the absence of $AgNO_3$ due to preferential attachment of CTAB bilayer along one facet which allows the other facet to grow. Adapted with permission from Reference 26. Copyright (2005), American Chemical Society. **(b)** The electric field mediated mechanism proposed by Perez-Juste *et al.* The electrostatic interaction between the positively charged seeds and negatively charged $AuCl_2^-$ - CTAB complex determines the growth of GNR. Reproduced with permission from Reference 1. Copyright 2004, John Wiley and Sons. **(c)** GNR growth mechanism in the presence of silver ions, proposed by Orendorff and Murphy, combining the surfactant mediated, electric field mediated and the under-potential deposition mechanisms. (Details in text) Adapted with permission from Reference 32. Copyright (2006), American Chemical Society.

This mechanism of growth has also been supported by Gai and Harmer.[30] According to them, the twin defect structure along the {110} facet has high surface energy, thus allowing the CTAB bilayer to stabilize this face. This mechanism however fails to explain the formation of rods in the case of CTAB capped seeds which are single crystalline.

2.2.5. Electric Field Mediated

According to this mechanism proposed by Perez-Juste *et al.*,[1] the $AuCl_4^-$ ions bind to CTAB micelles to form $AuCl_2^-$- CTAB complex, after being reduced to $AuCl_2^-$ as shown in Figure 2.5 (b).[1] The growth of GNR depends on the electrostatic interaction between the positively charged CTAB protected seeds and the negatively charged $AuCl_2^-$- CTAB complex which is controlled by their electrical double layer. These interactions are believed to be faster at the tips leading to its growth and hence the formation of GNR. However the mechanism fails to explain the formation of tips on the seeds in the first place.

2.2.6. Under Potential Deposition

The effect of $AgNO_3$ on the growth of GNR was first studied by Nikoobakht and El-Sayed[14] and was later analyzed by Liu and Guyot-Sionnest.[9] They make two main claims in their work which relate to the mechanism of rods formation viz. (1) Rods grown from single-crystalline CTAB protected seeds are single-crystalline with {110} facet on the sides and {100} on the end. The citrate protected seeds which are multiply twinned on the other hand lead to pentatwinned bypyramidal nanorods. Hence they conclude that the gold atoms deposited onto the seeds during the growth of the nanorods preserve the seed structure and do not create any stacking defaults. (2) The reducing agent, ascorbic acid cannot reduce $Ag^{[+]}$ ions to $Ag^{[0]}$ in the surfactant solution due to the acidic pH.[32] However, in the presence of a metal substrate, the $Ag^{[+]}$ ions can be reduced to $Ag^{[0]}$ in the form of a metal monolayer at a potential much less than that required for bulk reduction, known as 'under potential deposition' (UPD).[33] Also the reduction potential for silver deposition on {100} or {111} facet is higher

than other facets which leads to slower silver deposition on these facets. Hence the growth is along this facet rather than the {110} facet leading to formation of GNR.[9,20]

2.2.7. Combined Growth Method

Orendorff and Murphy combine the three mechanisms above and arrive at the silver UPD mechanism as shown in Fig 2.5 (c).[32] According to this mechanism, the $AuCl_2^-$ - CTAB complex, (formed according to the electric field mediated method), diffuses to the positively charged seeds causing symmetry breaking of the sphere into different facets. The CTAB bilayer is formed onto the {110} facet due to their preferential binding to this facet (preferential binding of surfactant mediated method). In addition, the deposition of silver ions on this facet is faster than that on the {100} facet leading to particle growth along the [110] direction (UPD of silver method). Once the silver ions are fully deposited onto the {100} facet, growth completely stops due to the blocking of the end facet of the GNR.[14] This mechanism is an all-inclusive mechanism for formation of GNR and is most widely accepted as the possible mechanism.

The seeded growth method is useful and is the most widely used method for the synthesis of GNR because the procedure is simple, yielding relatively high quality GNR. GNR growth eexperiments using the seeded growth method were performed to check the reproducibility and the scalability of the synthesis protocol and the method proposed by Nikoobakht and El-Sayed was adopted for this purpose.[14] The following section describes the experimental techniques and the results obtained.

2.2.8. Seeded Growth of GNR

2.2.8.1. Experimental

Materials

Sodium borohydride (98%), hydrogen tetrachloroaurate(III) trihydrate ($HAuCl_4$, 99.99%), hexadecyltrimethyl ammonium bromide (CTAB, 99%), all from Sigma-Aldrich Co. Ltd., Singapore, silver nitrate (99.9% of Ag) from Strem Chemicals, Singapore, L-(+) ascorbic acid (99%) from Alfa Aesar Co. Inc., Singapore and deionised water (18MΩ). All glassware used were new while the stirrer bars used were washed with aqua regia, rinsed thoroughly with water and dried prior to use.

Seed synthesis

Nearly spherical gold nanoparticle seeds (<4 nm in size) were synthesized by adding freshly prepared, ice cold sodium borohydride solution (0.6 mL of 0.01 M) to a mixture of aqueous $HAuCl_4.3H_2O$ (0.25 mL of 10 mM) and CTAB (7.5 mL of 100 mM) solution, while stirring vigorously (700 rpm, Heidolph) using a magnetic stirrer (teflon, 2 mm) in a borosilicate vial (20mL, scintillation, Kimble glass Inc., Singapore). The solution was brownish yellow and was maintained at 35°C to prevent CTAB from crystallizing.

Nanorods synthesis

Four different sizes (AR) of GNR were synthesized using the proposed protocol, which was achieved by varying the volume of $AgNO_3$ added to the growth solution. CTAB (5 mL, 200 mM) was added to 0.05, 0.15, 0.2 and 0.25 mL of 4 mM $AgNO_3$ in four different borosilicate vials (20 mL, scintillation, Kimble glass Inc., Singapore) and maintained at 35ºC. 5 mL of $HAuCl_4$ (1 mM) was added to this solution and was mixed gently. 70 µL of ascorbic acid (78.8 mM) solution was added to this dark yellow colored solution and mixed by slow inversion (4-5 times) until the solution turned colorless. To this colorless solution 12 µL of the prepared seed solution was added gently and the solution was left undisturbed for 30 mins.

Scale-up to 15 mL

CTAB (7.5 mL, 200 mM) was added to 0.3 mL of 4 mM $AgNO_3$ in a borosilicate vial (20 mL) and maintained at 35ºC. 7.5 mL of $HAuCl_4$ (1 mM) was added to this solution and was mixed gently. 105 µL of ascorbic acid (78.8 mM) solution was added to this dark yellow colored solution and mixed by slow inversion (4-5 times) until the solution turned colorless. To this colorless solution 18 µL of the prepared seed solution was added gently and the solution was left undisturbed for 30 mins.

Scale-up to 100 mL

CTAB (50 mL, 200 mM) was added to 2 mL of 4 mM $AgNO_3$ in a borosilicate vial (20 mL) and maintained at 35ºC. 50 mL of $HAuCl_4$ (1 mM) was added to this solution and was mixed gently. 700 µL of ascorbic acid (78.8 mM) solution was added to this dark yellow colored solution and mixed by slow inversion (4-5 times) until the solution turned colorless. To this colorless solution 120 µL of the prepared seed solution was added gently and the solution was left undisturbed for 30 mins.

2.2.8.2. Analysis

The samples were first analyzed using UV-vis spectrometer (Shimadzu UV-2450). They were then analyzed using either TEM (JEOL 2010, accelerating voltage 200 kV) or FESEM (JEOL JSM-6700f, accelerating voltage 25 kV). 2 mL of the nanoparticle suspension was centrifuged (7000 rpm, 8 mins) to remove excess CTAB and re-dispersed in DI water. The centrifugation and re-dispersion in DI water was repeated thrice to concentrate the sample as well as to remove the excess CTAB. 10 µL of this concentrated solution was then gently placed onto a 200 mesh formvar protected copper grid and was allowed to dry overnight before being analyzed.

2.2.8.3. Results

The color of the solutions varied from violet to reddish brown, depending on the silver ion content in them.

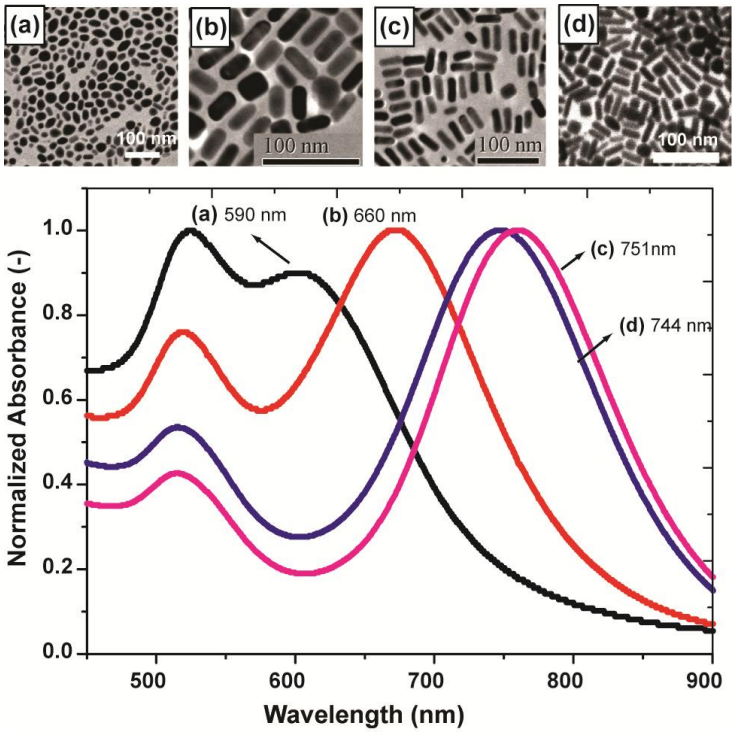

Figure 2.6. TEM images and UV-vis absorbance spectra of the GNRs synthesized using the Nikoobakht and El-sayed protocol. The AR and the corresponding volumes of $AgNO_3$ in the sample soluiton are **(a)** 1.5±1, 0.05 mL **(b)** 2.8±1, 0.15 mL **(c)** 4.5±2.5, 0.2 mL and **(d)** 3.5 ±0.5, 0.25 mL.

The absorbance spectra of these particles along with their TEM images are shown in Figure 2.6. The volume of $AgNO_3$ and the silver ion content in the samples in Figures 2.6 (a), (b), (c) and (d) are 0.05 mL and 0.02 mM, 1.5 mL and 0.06 mM, 2 mL and 0.08 mM and 2.5 mL and 0.1 mM respectively. As proposed by the authors in their work,[14] the AR of these particles vary from 1.5±1 (Figure 2.6 (a)) to 4.5±2.5 (Figure 2.6 (c)). The UV-vis absorbance spectra of these particles exhibit two resonance peaks, one in the lower wavelength region, ~ 520 nm (TPR) and the other peak at higher wavelength region between ~550 nm to ~ 900 nm (LPR) and the corresponding values are shown in the Figure 2.6.

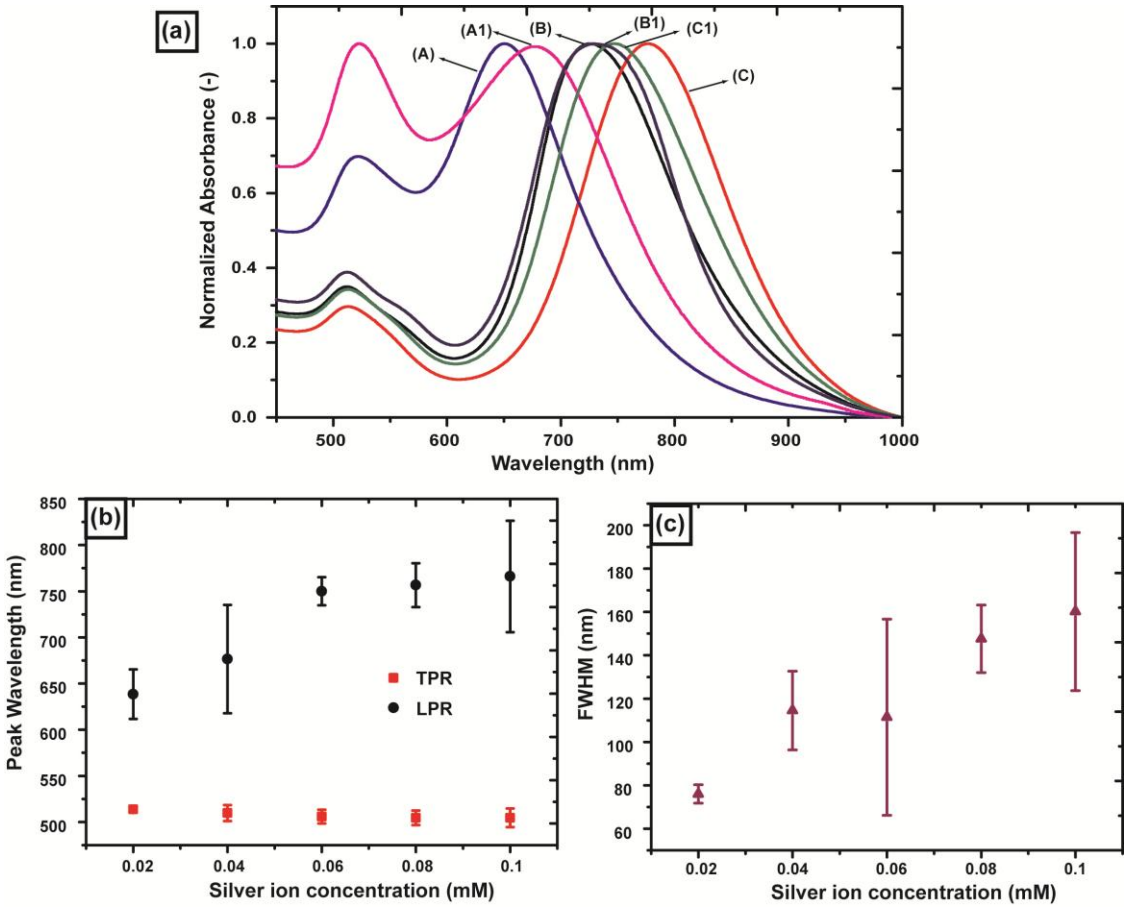

Figure 2.7. (a) UV-visible absorbance spectra of the gold nanorods synthesized using the same stock solutions and seed solution; Variations in **(b)** The LPR and TPR peak wavelengths and **(c)** Full width at half maximum of five different GNR samples synthesized using individual sets of stock solutions and seed solutions.

Experiments were performed to check the reproducibility of the protocol. The UV-vis absorbance spectra of GNR samples obtained using the same stock solutions as well as the same seed solution are presented in Figure 2.7 (a). The silver ion content in the three sets of GNR samples synthesized are, in A and A1: 0.02 mM, in B and B1: 0.04 mM and in C and C1: 0.08 mM. Similar analysis of the spectra of seven sets of five different GNR samples (of varying silver ion content) obtained using individual sets of stock solutions and seed solutions were performed. The variations in the LPR as well as the TPR peak wavelengths are shown in Figure 2.7 (b) whereas the variations in the full width at half maximum (FWHM) of the LPR peaks of the five GNR samples are shown in Figure 2.7 (c). Since the only difference between

the five different GNR samples synthesized is the silver ion content, the GNR samples in Figures 2.7 (b) and (c) are plotted against the silver ion concentrations.

The wavelength of the LPR peak signifies the rod length and is expected to shift to higher wavelengths (red shift) with increase in the length of the rods in the sample while the TPR peak is due to the breadth of the rods. An increase in the absolute absorbance of the spectra is due to an increase in the concentration of the rods in the sample and an increase in the width of the peaks indicates the presence of polydisperse particles in the sample.[34] The spectra of GNR samples typically exhibit higher or equal TPR peak absorbance than that of LPR peak absorbance. The spectra of samples obtained using the same stock solutions and seed solution should in essence overlap, since the only difference between the two sets is the glassware used. However, the spectra of the three sets of samples (Figure 2.7 (a)) show variation in their LPR peak wavelengths (of upto ~ 20 nm between samples A and A1 and C and C1) as well as in the width of the peaks (of B and B1). The LPR peak shifts shown in Figure 2.7 (b) as well as the variations in the width of the peaks plotted in terms of FWHM in Figure 2.7 (c) are significant in case of samples obtained from different sets of stock solutions and seeds. 100 nm shift in the peak wavelength signifies considerable change in length of the rods in the sample; while a shift of ~ 10 nm in the peak wavelength is considered within limits for end user applications, a 100 nm shift is substantial and renders the synthesized particles unusable for end user applications.

In another set of experiments, the direct scalability of the protocol was tested by increasing the volume of the solutions added proportionately. The spectra of the best samples from several different trials are shown in Figure 2.8. The wavelengths of the LPR peaks of these samples vary considerably from ~730 nm to ~820 nm. In addition, there is an increase in the absolute absorbance (from ~0.4 a.u. to ~1.5 a.u) when the usual 10 mL sample is scaled-up to 15 mL. However, the absorbance falls to ~0.9 a.u. on scaling-up to 100 mL. Overlapping spectral signatures are expected since the process of direct scale-up merely involves an

increase in the volume of the solutions added. However the variations listed above suggests a significant increase in the yield of the GNR synthesized.

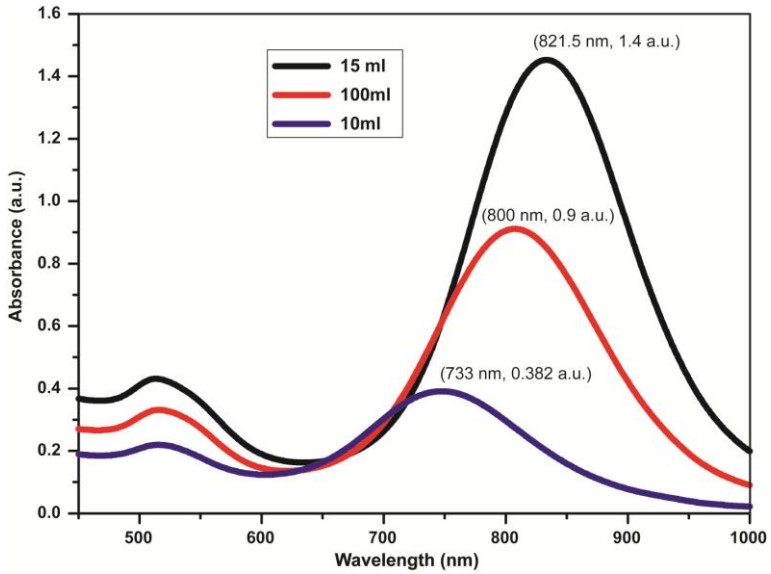

Figure 2.8. UV-visible absorbance spectra of the gold nanorods synthesized to check the scalability of the protocol using the same stock solution, same batch of seeds and the same silver ion content.

These variations in the synthesized particles are surprising considering the fact that the synthesis protocol adopted and the experimental conditions were exactly the same. Several authors report that the yield, size, shape and monodispersity of GNR produced by the seeded growth method are affected by many parameters, such as pH, temperature of the reactant solution, concentration, size and structure of the seed, concentration of the reducing agent (ascorbic acid), gold precursor concentration, surfactant concentration, the use of other surfactants, additives, solvents and nanorods ageing time.[26,27,35-40] The impurity in the surfactant, CTAB is also found to have an effect on the GNR growth and AR as shown by Smith and Korgel.[40] Synthetic skills and recipes have improved over the years though the presence of other shapes and sizes of particles in the final product solution persists and several procedures to purify and isolate the desired particle population are still being investigated.[41] Most of these parameters and effects depend on the dispensing strategy adopted by the chemist and the time taken for homogeneous mixing of the reagents in the solution. The dispensing of

reagents is practically an art and depends on the skills of the chemist while mixing, however fast, is not instantaneous. Instantaneous homogeneity will not be possible in spite of using the most efficient mixers (which might also lead to shear induced aggregation of the particles [42,43]) giving rise to spatial inhomogeneity in reagent concentration which leads to variations in the growth rate of the seeds and hence polydisperse particles as well as variations between individual batches thus affecting the reproducibility of such processes. Hence the need for an alternative approach is imperative for the advantages of nanotechnology to be realized commercially.

2.3. Microfluidics

Microfluidics refers to devices and methods for manipulating minute amounts (from 10^{-9} L to 10^{-18} L) of fluids in channels of dimensions tens to hundreds of micrometers enabled using a microfluidic reactor.[44] Microreactors were first developed in the early 1990s; however the utilization of these reactors in pharmaceutical, biological and chemical research for applications such as synthesis, diagnosis, analysis, screening etc. have developed in the recent years due to the improvement of machining techniques enabling rapid and cheap fabrication of these reactors.[44-46] A brief mention of the salient features of these reactors was made in Chapter 1. The following sections contain a detailed description of microreactors and their use in particle synthesis.

2.3.1. Microreactors

The small dimensions of microreactors offer several advantages in chemical processing due to the easy control over process parameters such as temperature, pressure, flow rates, residence times and mixing of reagents.[47] The following are some of these advantages[48]:

1. Hydrodynamic flow in microreactors with channel dimensions ranging from a few micrometer upto hundreds of micrometers is essentially laminar compared to the turbulent flow prominent in macroscale systems.

2. The time taken for homogenization of reagents across the microchannels are small, of the order of few milliseconds given by

$$\tau = \frac{l^2}{D} \tag{2.1}$$

where l is the channel dimension and D is the diffusion coefficient. Hence the mixing times in these reactors can be tailored from a few milliseconds to hours.

3. Reagent consumption in these reactors at any point in time is minimal, of the order of few nL, thus overcoming safety concerns in transportation, storage, leakage of toxic and flammable solvents.[49] Minimal reagent consumption also enables easy and systematic process optimization and high-throughput screening.

The high surface-to-volume ratios in these reactors on the other hand allows for rapid heat transfer thus heating and cooling reagents rapidly as well as maintaining isothermal conditions when needed.[47,50]

Hence the small reaction volumes combined with the high heat and mass transfer rates in microreactors provide a controlled environment to carry out both simple/placid as well as aggressive reactions that require high temperatures and pressures and also to confine potentially toxic and highly reactive starting materials.[51] Integrating chemical detection systems to the reactor enables online sample analysis along with the ability to control parameters such as reagent concentration, temperature and pressure online.[52] The possibility of performing reactions continuously as well as the ability to add reagents downstream and quench or cease reactions as soon as the product is formed is another advantage of using microreactors for better product control.[53] In addition, the possibility of performing multiple processing steps in a single reactor and the ability to perform parallel operations makes them far more superior to conventional reactors.[54]

Fluid flows in channels of small dimensions can be manipulated by external or internal forces such as pressure, electric, magnetic or capillary effects as well as other forces such as

acoustics and rotational forces. Pressure driven flows are of primary interest in this thesis and further discussions will pertain to these flows. Details of flows due to other forces can be found in Stone *et al.* and references thereof.[55] The driving force for fluid flow can also be influenced by manipulating the surface properties of the channel such as geometrical, chemical and mechanical features, in addition to modifying the fluid rheology. Volumetric flow rate, Q, in pressure driven flows for cylindrical channels of radius r and length L is given by the Hagen-Poiseuille equation,

$$Q = \frac{\Delta P \pi r^4}{8\mu L} \tag{2.2}$$

For a rectangular channel, the equation is written as

$$Q = \frac{wh^3 \Delta P}{12\,\mu L}\left[1 - 0.63\frac{h}{w}\right] \tag{2.3}$$

where ΔP is the pressure drop across the channel of width w and height h and μ is the viscosity of the fluid in the channel.[55]

Reduced channel dimensions essentially lead to increased importance of diffusion, surface tension, and viscosity. Fluid flows in these channels are typically laminar due to the very low Reynolds numbers given by the expression

$$Re = \frac{\rho d v}{\mu} \tag{2.4}$$

ρ and μ being the density and viscosity of the fluid flowing through channels of depth d at velocity v. Re in these channels is usually of the order of unity or lower or such that the convective forces are negligible. For example, Re in channels of depth 100 μm in which water (ρ and μ, 1000 Kg.m^{-3} and 0.001 Kg.m^{-1}.s^{-1} respectively) is flowing through with a velocity of 0.01 m.s^{-1} is 1. Consequently diffusion is the main phenomenon for mixing fluids in these

channels which exhibit parabolic velocity profiles. On the other hand, the Peclet number (Pe), which is the ratio of convective to diffusive transport given by

$$Pe = {}^{vh}/_{D} \tag{2.5}$$

where v is the axial velocity, h the channel cross-section and D the molecular diffusion, is usually large in these channels. Typical values of Pe correspond to $10 < Pe < 10^5$ where v ranges from 0.1 - 1 $cm.s^{-1}$, h being 10 – 100 µm and D being 10^{-11} – 10^{-9} $m^2.s^{-1}$. This suggests that in most cases convective transport in these channels is faster than diffusive transport.[55,56] The very low values of Re and very high Pe values in microchannels hence enable spatial and temporal control over the transport of chemical substances in the microreactor.[56]

2.3.2. Single Phase and Multi Phase Microfluidics

Chemistries in microreactors essentially involve controlled meeting, mixing and reaction of fluids and collection of products along the channel length. The meeting of fluids is usually made possible by infusing them through inlet channels in a particular order at appropriate positions/lengths along the channel using cross flow or coflow geometries. Once the fluids meet, they interact by diffusion across the fluidic interface, which enables mixing of miscible fluids as shown in Figure 2.9 (a), in single-phase microfluidic systems.[46] The absence of turbulence in these channels has a direct consequence on the mixing of reagents. As stated in Section 2.3.1, the mixing timescales due to diffusion in a microchannel is very small. However in the case of fast reactions where the rate of reaction is limited by the diffusion rates rather than reaction kinetics, the possibility of formation of secondary products along with the required product is high. In such cases, the yield of the primary product is solely dependent on the mixing rate of the individual reagent streams. Diffusive mixing of reagent streams in such cases is disadvantageous and might lead to poor yield, low product quality and also to clogging of the reactor.[51]

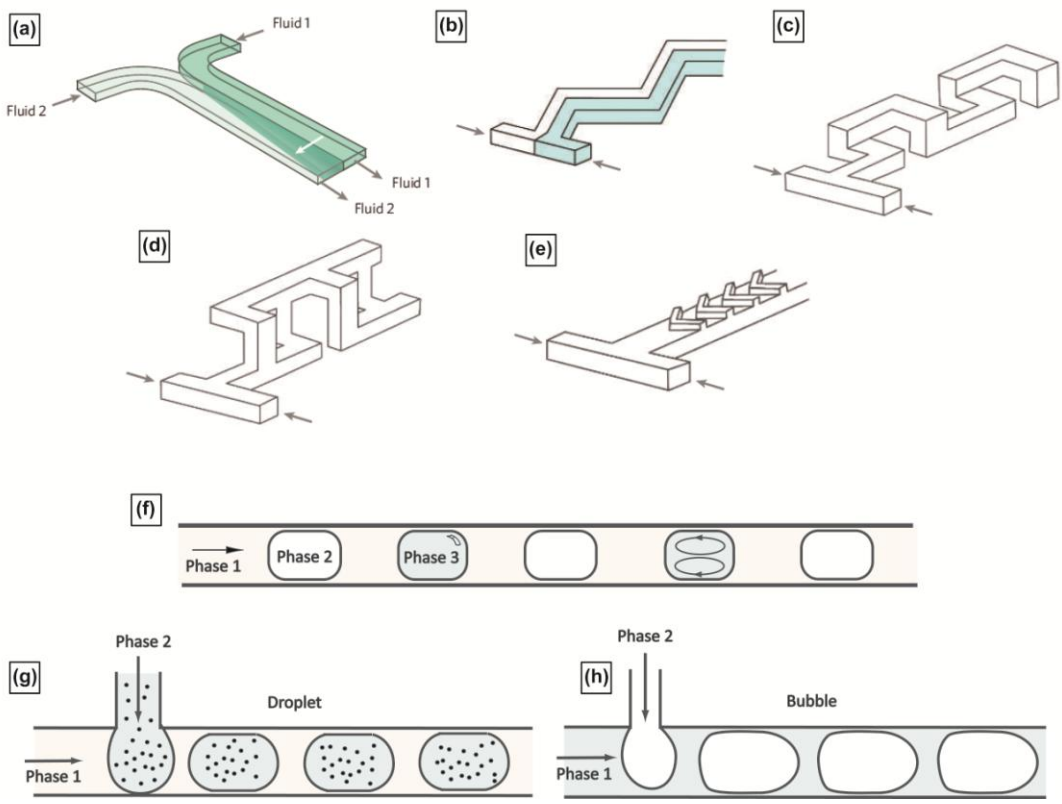

Figure 2.9. (a) Diffusive mixing across fluidic interface between Fluid 1 and Fluid 2.[46] Chaotic advection achieved[46] in **(b)** Zigzag-shaped channel[57] **(c)** Three dimensional L-shaped channels[58] **(d)** Three dimensional, connected out-of-plane serpentine channels[46] **(e)** Channels with staggered-herringbone grooves[59]. Schematic of **(f)** Concept of multiphase microfluidics **(g)** Multiphase microfluidic system where both the phases are liquids called droplet microfluidics **(h)** Multiphase microfluidic system where gas is dispersed in continuous liquid phase often called segmented microflows. Panels **(a)**, **(b)**, **(c)**, **(d)** and **(e)** reprinted by permission from Macmillan Publishers Ltd: Nature (Reference 46), Copyright (2006).

In addition, a significant problem in these single-phase microfluidic systems is dispersion. In most cases, as mentioned already, parabolic velocity profile is established over the fluid cross-section with zero fluid velocity near the walls of the channel and maximum at the center. The main impact of axial dispersion is residence time variation between the fluids near the channel walls and the channel center, which has an effect on the product yield, quality and efficiency.[46,60] A range of microfluidic mixing systems have been designed over a period of time to cater to such reactions and they fall into two main categories viz. active and passive mixers.[46] Active mixers directly control the flow field through moving parts or through varying pressure gradients.[61] Though the mixing efficiency of these mixers is quiet high, they are

usually difficult to fabricate and integrate with the microfluidic device and also pose problems with operation and cleaning.[46] Passive mixers on the other hand enhance mixing by increasing the active area for diffusion either by manipulation of channel geometry or by modifying the properties of the fluid and they are of interest to us since they are relatively simple to implement.[62] One method to passively mix fluids in the microchannels is through "chaotic advection" which is to continuously stretch and refold concentrated fluids to decrease the striation thickness exponentially.[63,64] This is achieved by either introducing obstacles in the fluid path or by modifying the channel geometry. Examples of such modifications are provided in Figure 2.9 where zigzag-shaped channels (Figure 2.9 (b)),[57] serpentine three dimensional channels (Figure 2.9 (c)[58] and (d)[46]) and herringbone grooves on channels (Figure 2.9 (e))[59] are used to mix miscible fluids at high, low to intermediate and 1 to 100 Reynolds numbers respectively.[46]

Although these alternative mixing strategies overcome the mixing and dispersion problems of single-phase microfluidic systems, the main drawback of these flows is that the reagents are in contact with the channel walls. In case of fast reactions between the two fluids leading to nanoparticles or solid products, the products formed will adhere to the walls of the reactor due to physical effects and will lead to heterogeneous reaction with the channel walls. This gives rise to deposition on the walls of the reactor which leads to fouling or clogging of reactors as well as deterioration of product quality and yield.[46,60,65,66]

Multiphase microfluidics containing two or more immiscible fluids in which one of the phases is dispersed in the other phase (Figure 2.9 (f)) is another alternative to single-phase microfluidic systems. The reactive fluid in this case can either be continuous or dispersed or both. Examples of liquid dispersed in another liquid such as oil-water system where water forms discrete drops in a continuous phase of oil and gas dispersed in a liquid are shown in Figure 2.9 (g) and (h) respectively. The dispersed phase either forms discrete drops or films wetting the channel walls, or slugs of varying lengths, depending on the interfacial, viscous,

inertial forces and their interactions, as well as on the channel geometry.[67-70] The mechanism of breakup and formation of the discrete drops/films/slugs (referred to as fluid segments hereafter) in the continuous fluid and the flow dynamics is beyond the scope of this thesis. References are suggested for interested readers.[56,71-75]

Long diffusion times and dispersion limitations of single phase flows are overcome in multiphase flows with narrow residence time distribution.[60,76] The recirculating motion induced in the moving fluid segments flowing in an immiscible continuous fluid enhances mixing and transverse channel transport.[76,77] Mixing of reagents in multiphase microchannels is accomplished in few seconds due to the recirculatory motion within the fluid segments and can be decreased to few milliseconds by reducing the microchannel width and increasing the velocity of the dispersed phase.[78] In addition, liquid-liquid multiphase microfluidics, referred to as droplet microfluidics, helps in preventing direct contact of the liquid forming the droplets, which typically contains the reagents, and the channel walls. This essentially isolates the reagents and the products from the channel walls and prevents deposition on the channel walls thereby reducing or eliminating fouling and clogging of the channels.[77,79]

The large interfacial areas, fast mixing and mass transfer are some of the criteria that make multiphase microfluidics superior to conventional as well as single-phase microfluidic reactors. Some examples are provided in Section 2.4. Further analysis of multiphase microfluidics and the advantages of droplet microfluidics are provided in Chapter 3. Multiphase microfluidics is used in this thesis to overcome limitations posed by the traditional batch systems as well as single-phase microflows for particle synthesis.

2.3.3. Microreactor Design and Fabrication

Microreactors have progressed from simple tubings to complicated devices integrated with control systems for optimization of parameters and *in situ* characterization. Simple experiments with well-known hydrodynamics, requiring easy manipulation of operating

parameters such as residence times can be performed either in silica or stainless steel or polymer capillary tubings.[80,81] With the developments in lithography and other fabrication techniques, use of silicon, pyrex, glass, stainless steel, ceramic and various types of polymer reactors are on the rise. Each of these materials has its own advantages as well as disadvantages and the use of a particular material as reactor depends on the final application of the reactor.

Glass/glass (glass bonded to another glass) based reactors are preferred for reactions that require high pressures though they cannot be used for reactions requiring heat transfer due to their low thermal conductivity.[82] Silicon/Pyrex reactors are best suited for high pressures, temperatures and have good chemical stability as well. They also have optical access through the pyrex side. However the fabrication of these reactors is time consuming and require expensive machinery for silicon etching and anodic bonding with pyrex.[51] Poly (dimethylsiloxane) (PDMS), a soft silicone elastomer bonded to glass or to PDMS coated glass slide, is often used for the fabrication of microfluidic reactors. Some of the attractive physical and chemical properties of PDMS are optical transparency, elasticity, non-toxic nature, ability to cure at low temperatures, controllable surface chemistry, less permeability to water, low electrical conductivity and rapid prototyping capabilities among other features. Interfacing devices made of PDMS with external devices and users is convenient and simple compared to devices made of other hard materials. Though these devices are easy and cheap to fabricate, the operating range of pressures and temperatures in these devices are low and are not compatible with most organic solvents (PDMS swells in organic solvents).[83-86] Fluoropolymers, SU-8, poly (etheretherketone) (PEEK), poly (vinyl chloride) (PVC), poly carbonate (PC) are some other polymers used as microreactor materials though bonding techniques for them are yet to be well established.[87,88] Metal based microreactors are chemically compatible and thermally resistant except for strong acids while ceramic reactors can stand temperatures of 800º C.[51]

Once the reactors are fabricated, they are connected to the external macroscopic components such as syringe pumps, pressure regulators and the like using connectors and tubings. They can either be permanent connections such as epoxy gluing[89], metal soldering[90], glass brazing[91] or non-permanent connections such as nanoport fittings and compression sealing with rubber O-rings[92,93]. The pressure requirements and the ease of fabrication dictate the preferred technique.[51] PDMS is used for the current work for fabrication of microreactors. Step by step protocol of photolithography, soft lithography for rapid prototyping, bonding and packaging are provided in Appendix B.

Thus the possibility of designing reactors according to the reaction requirement and the ability to flexibly control the reaction kinetics, by changing the flow rates (which essentially changes the concentration of reagents), mode and sequence of reagent addition, temperature and pressure variations as and when required and quenching reaction when required are some of the features of microfluidics which can be used advantageously for nanomaterial synthesis. The challenge is to ingeniously use the advantages of microfluidics to tailor-make nanomaterials in large quantities. Several research groups are working with microfluidic synthesis of nanomaterials and the following section summarises some of the current research in this area.

2.4. Microreactors for Particle Synthesis

Several research groups are working in the field of microfluidics and microreactors for nanoparticle synthesis throughout the world. The choice of the reactor material, microfluidic technique adopted (single phase laminar flow methods or multiphase methods) and the reactor design are some of the parameters that determine mixing, dispersion, separation of nucleation and growth phases and control of reaction kinetics during particle synthesis. The synthesis protocol determines the number of reactants, mode of addition of these reactants along the reactor as well as the residence time for complete reaction. These parameters are used as variables for reactor design while the microfluidic technique adopted along with the product

type and synthesis protocol play vital roles in the selection of reactor material. Several reviews and edited books have been published in recent years emphasizing the opportunity provided by microfluidic methods to controllably synthesise polymeric as well as inorganic nanomaterials on small scale as well as commercial scales.[45,51,94-101] Preliminary lab-scale experiments with a variety of microreactors have shown that the control of size and morphology of nanomaterials such as quantum dots, nanoparticles, nanocomposites and nanorods is possible by direct manipulation of some of the critical parameters that govern the nucleation and growth process.[102-106] Some examples of such microfluidic synthesis are presented in the following sections. Though the reactors are used for synthesis of nano as well as micro particles, we restrict the discussion to nanoparticles. The reviews pointed out earlier and the references therein can be consulted for polymer microparticles, microgels as well as mesoporous silica microparticles.

2.4.1. Synthesis of Semiconductor Nanocrystals

Quantum dots, especially cadmium selenide (CdSe) are the most studied nanoparticles among the microfluidic community. Synthesis of these particles requires high reaction temperatures of ~ 200 - 350°C. Initially, single-phase flows in silica capillaries were used for this synthesis and the growth kinetics were analyzed offline.[46,81,107-109] The silica capillaries were then replaced with glass-glass microchips for design flexibility and for online detection of reaction kinetics (using fluorescence detectors).[110] The main drawback of this method was long mixing times and axial dispersion within the capillaries leading to broad particle sizes.[108] Further modifications to achieve short mixing times were introduced by convective advection[111] or hydrodynamic focusing.[112] As an improvement multiphase microfluidics, both gas-liquid (silicon-pyrex rector, Figure 2.10 (a))[70,91] and liquid-liquid (glass-glass reactors, Figure 2.10 (b))[102] methods were used for the particle synthesis which essentially narrowed the residence time distribution in the reactor.[70,91]

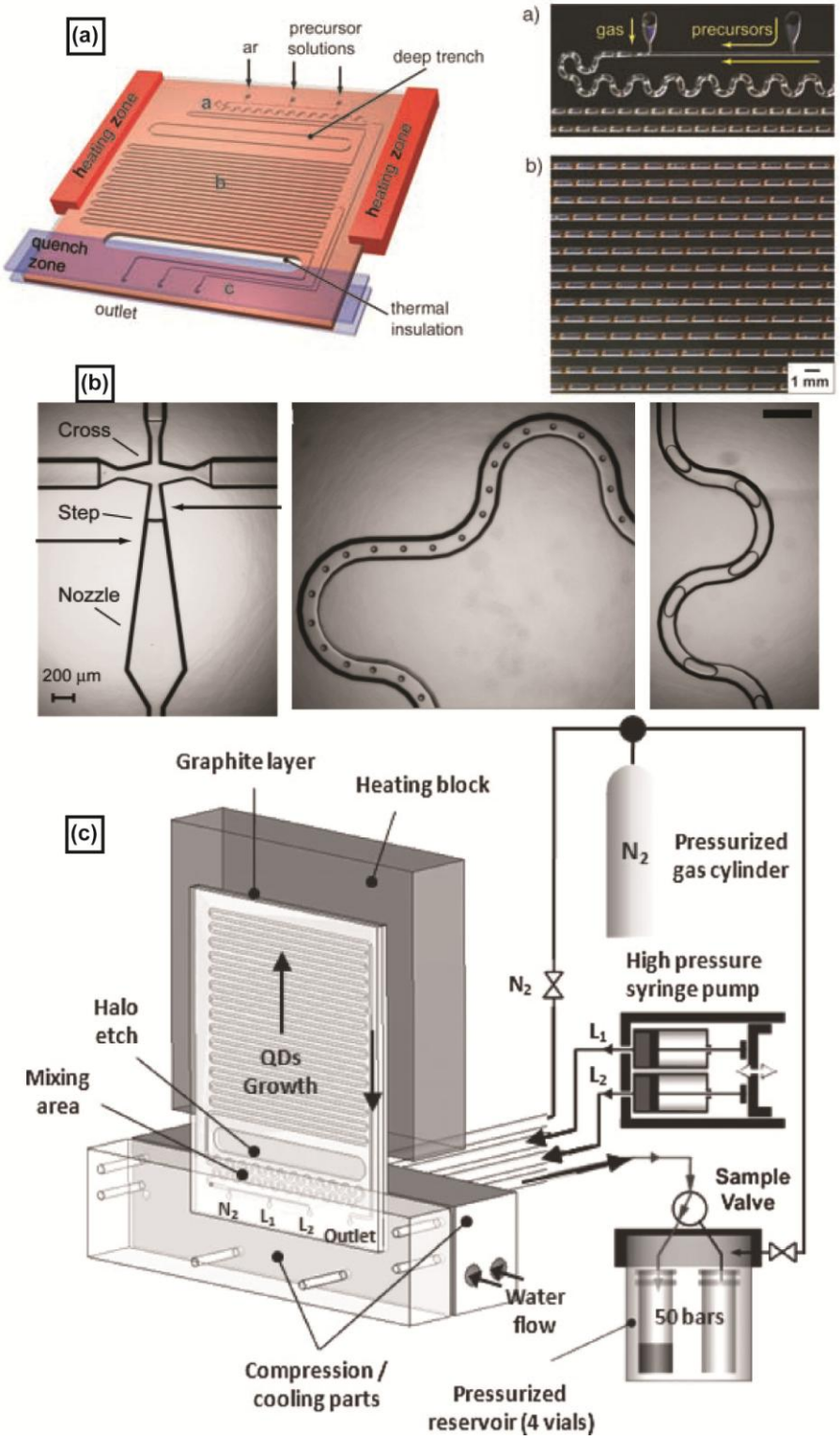

Figure 2.10. Microfluidic processes for the synthesis of CdSe nanoparticles **(a)** Gas liquid multiphase flows in a silicon-pyrex microreactor. Reproduced with permission from Reference 91. Copyright 2005, John Wiley and Sons. **(b)** Liquid-liquid microfluidic method in a glass-glass reactor. Adapted with permission from Reference 102. Copyright 2005, American Chemical Society. **(c)** Silicon based single phase microfluidic reactor using supercritical fluid. Reproduced with permission from Reference 93. Copyright 2008, John Wiley and Sons.

Recently, Marre *et al.* used supercritical fluid, hexane as the solvent in a silicon-based microreactor to overcome the disadvantages posed by single phase microfluidic methods and produced excellent-quality CdSe particles (Figure 2.10 (c)).[93] Similarly, room-temperature synthesis of CdS nanoparticles has been achieved using single phase as well as multiphase microfluidics.[104,113,114] Indium Phosphide is yet another type of semiconductor nanomaterial synthesized using ceramic microreactors due to the very high temperature requirements of about 1300 to 1400ºC

2.4.2. Synthesis of Oxide Nanocrystals

Microfluidic methods have been used for the synthesis of iron oxide[115-117] and silica nanoparticles as well as microparticles.[60,118,119] Multiphase gas-liquid flows in PDMS reactors are used for the synthesis of silica particles which prevents axial dispersion and also achieves sharp particle size distribution as shown in Figure 2.11 (a).[60] Multiphase flows[115] and 3D injection[116,117] have been effectively used for the synthesis of iron oxide particles which prevents deposition on the channel walls as well as achieves narrower residence time distribution and hence better particle dispersity. In one of the methods, the precursor salt is introduced coaxially through silica capillary tubing into a 3D millifluidic channel containing the strong base. This method achieves precise positioning of the precursor flow in the center of the channel thus preventing the adsorption of particles onto the walls of the capillary. The gradual change in pH from the center to the periphery of the channel enables the co-precipitation reaction to occur at the neutral interface, away from the channel wall.[116,117] A variation of the synthesis was performed using droplet coalescence as shown in Figure 2.11 (b) where the precursor salt and base form droplets separately by hydrodynamic coupling of two spatially separated nozzles and are brought in contact by electrocoalescence in a PDMS reactor. This approach produces fast mixing of reagents as compared to the coaxial approach and the droplets prevent contact of reagents from the channel walls.[115] Synthesis of titania

nanorods has also been achieved using multiphase gas-liquid flows where the reaction happens at the interface between the two liquids.[120]

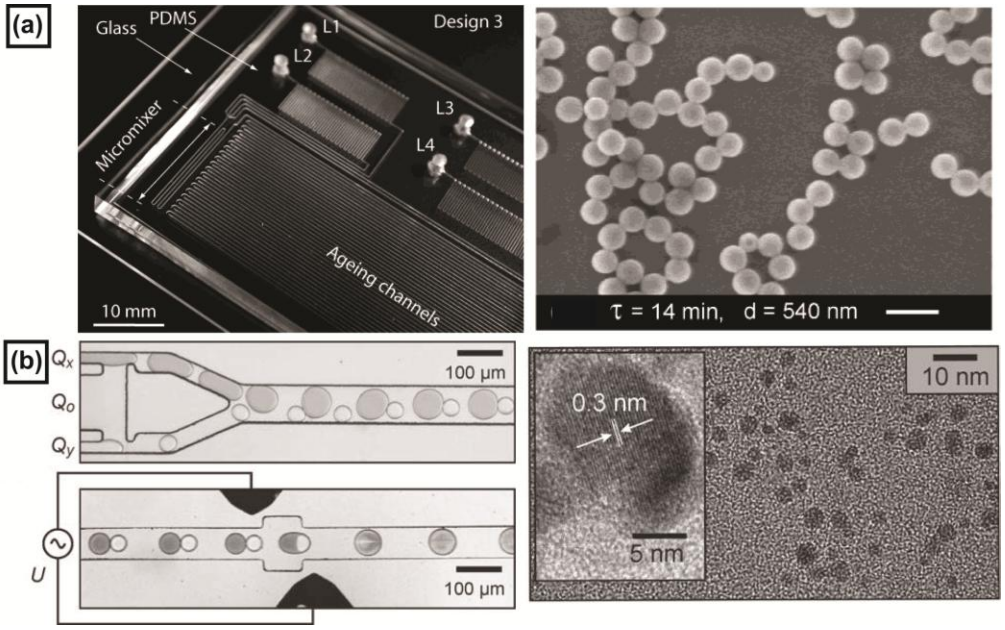

Figure 2.11. Examples of microfluidic processes for the synthesis of oxide nanoparticles **(a)** Photograph of PDMS microreactor used for multiphase gas-liquid flows and a SEM of the silica particles synthesized from the reactor. Adapted with permission from Reference 60. Copyright 2004, American Chemical Society. **(b)** Schematic showing the hydrodynamic coupling of spatially separated nozzles generating individual droplets and the fusion zone attached with electrodes enabling the electrocoalescence of the droplets. The TEM shows the synthesized particles with the inset showing crystal lattice on these particles. Reproduced with permission from Reference 115. Copyright 2008, John Wiley and Sons.

2.4.3. Synthesis of Core Shell Nanostructures

The advantages of connecting microreactors in series and the ability to add reagents downstream are made use of for the synthesis of heterogeneous core-shell nanostructures. A first example of such synthesis was performed by Wang *et al.*, in which they overcoat CdSe particles with ZnS in a silicon-pyrex microreactor that can handle two separate temperature zones.[121]

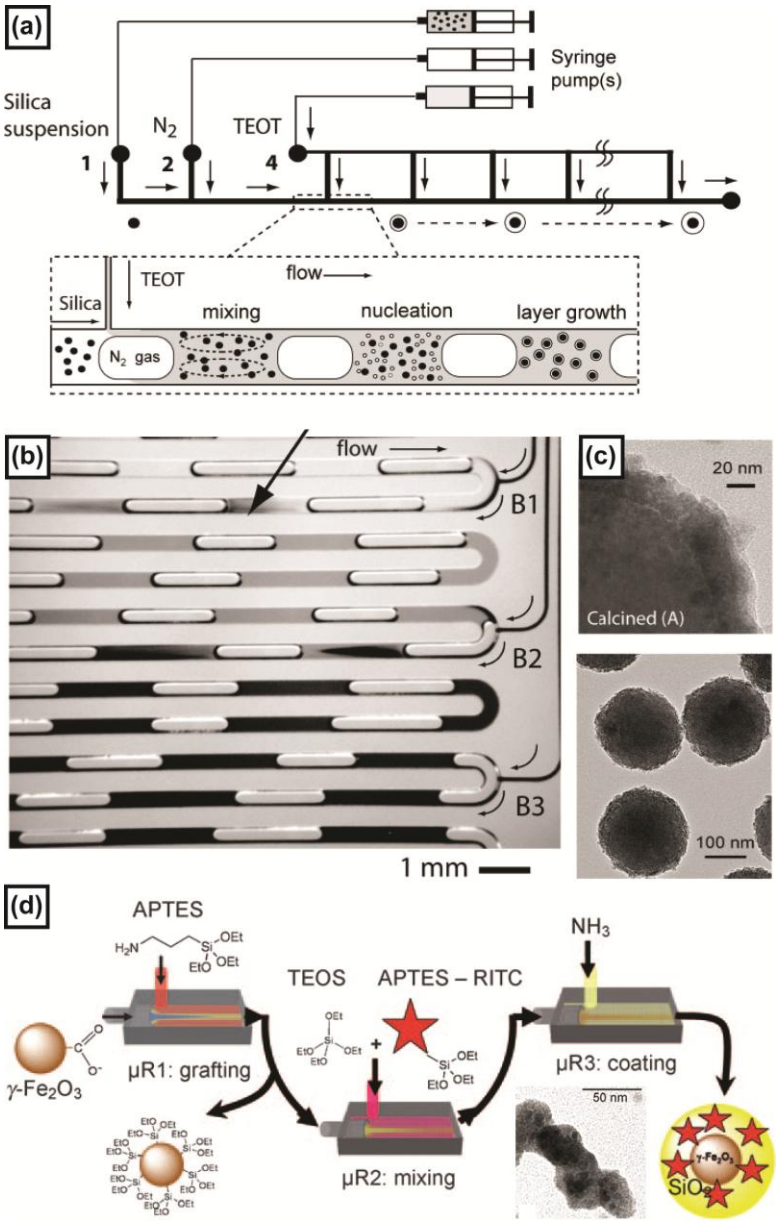

Figure 2.12. Examples of microfluidic processes for the synthesis of core-shell nanostructures **(a)** Schematic of the concept of synthesis of silica-titania core-shell structures. **(b)** Stereomicroscopic image of the flow visualization experiment. **(c)** TEM images of the core-shell structures after calcination. **(d)** Schematic of the synthesis of γ-Fe_2O_3@SiO_2 nanoparticles in a coaxial silica-capillary-in-PDMS–Glass microreactors; inset shows the TEM of the synthesized particles. Panels **(a)**, **(b)** and **(c)** Reproduced with permission from Reference 122. Copyright 2007, John Wiley and Sons. Panel **(d)** Reproduced with permission from Reference 88. Copyright 2009, John Wiley and Sons.

Synthesis of hybrid core shell, titania coating over colloidal silica, nanoparticles using a multiphase gas-liquid flow device made of PDMS has been demonstrated by Khan and Jensen. The reactor is designed to incrementally deliver the same amount of overcoating reactant at several locations along the entire reactor using a manifold arrangement as shown in

Figure 2.12 (a) which is similar to dropwise addition of a reactant in a stirred flask equivalent. This process allows the concentration of one of the reagent to build up slowly along the reactor length, thus preventing uncontrolled precipitation and agglomeration of titania particles. In addition, it also prevents the formation of polydisperse mixture of coated silica particles, secondary titania particles and large, irregularly shaped agglomerates which form when the same total amount of reactant was introduced through a single inlet.[122] The image of flow visualization experiment showing the incremental addition of reagents is shown in Figure 2.12 (b) while the TEM images of the particles after calcination is shown in Figure 2.12 (c). Another example recently reported for the synthesis of γ-Fe_2O_3@SiO_2 nanoparticles in a coaxial silica-capillary-in-PDMS–Glass microreactors is shown in Figure 2.12 (d) with the inset showing the particles.[88]

2.4.4. Synthesis of Metallic Nanocrystals

Synthesis of metallic nanomaterials such as Au, Ag, Cu, Co and Pd has been achieved using microfluidic reactors. The main purpose of the microfluidic synthesis of these particles is to overcome the disadvantages posed by synthesis in conventional batches (described in Chapter 1 and in the previous sections). The most studied system is gold with the aqueous chemistry usually involving reduction of metal salt with strong or mild reducing agents such as sodium borohydride or ascorbic acid respectively, along with stabilizing agents such as surfactants or polymers. Wagner, Kohler and co-workers,[66,123-126] Boleininger *et al.*,[65] Shalom *et al.*[127] and Lee *et al.*[128] performed single phase flow studies for the synthesis of gold nanoparticles of varying shapes and sizes.

Wagner, Kohler and co-workers use a silica-glass interdiffusion microreactor to synthesize 15 to 24 nm particles using ascorbic acid as the reducing agent and poly (vinyl pyrrolidone) as the stabilizer. To achieve this they first synthesize 12 nm particles with sodium citrate as the reducing agent and use these particles as seeds in the next step to grow them into

bigger particles. They used a range of reactant flow rates, gold-to-reducing agent concentration ratios and also varied the order of reagent addition to obtain particles of varying sizes.[66] They further developed this method for the synthesis of other shapes and sizes of nanomaterial with a new reactor (mixer) make and design which is used in all their further work. The mixer is a chip-shaped two or three-layered assembly of wet etched pyrex glass and silicon, anodically bonded to each other (Figure 2.13 (a)). They use a three layer assembly initially to directly mix reducing agent (ascorbic acid) with the gold salt and get 5 nm to 50 nm particles. They were able to obtain an average two times narrower particle size distribution than the conventional batch procedures. They also note that hydrophobic channels and elevated pH of the reagents during reaction reduce fouling of channel walls.[126] In their later work, they use the same kind of micromixer but use a combination of ascorbic acid and Fe(II) as the reducing agent and citric acid, sodium metasilicate, $AgNO_3$ and poly (vinyl alcohol) as stabilizers. Changing the reaction condition led to the formation of single particles of different sizes, simple particle aggregates, core–shell particles as well as complex aggregates and hexagonal nanocrystallites along with isolated and clustered nanoparticles as shown in Figure 2.13 (b) and (c).[123-125] Reactors with channels wet etched on pyrex glass, covered with a layer of silicon and bonded to glass were used and they found that silanization of the inner microchannel surface and increased pH values helped suppress fouling in the microreactor.[124-126] Though they tried a combination of reagents and stabilizers, varied the reaction conditions such as pH, temperature, channel wall coating material, they were not able to prevent fouling of their reactors.

Boleininger *et al.* synthesized gold and silver nanorods using a tubular reactor maintained at 30°C in a hot water bath using the seeded growth strategy. Presynthesized seeds and growth solution consisting of CTAB, $HAuCl_4$ or $AgNO_3$ and ascorbic acid were introduced through the two inlets to form gold or silver nanorods respectively while NaOH was introduced for synthesis of silver particles. Several different tubing material such as PVC, PEEK, PTFE (teflon) and silicone, as well as variations in flow rate, syringe type and material,

reaction temperature and reagent concentration ratios were tested to check for aggregation and deposition on the channel walls.[65]

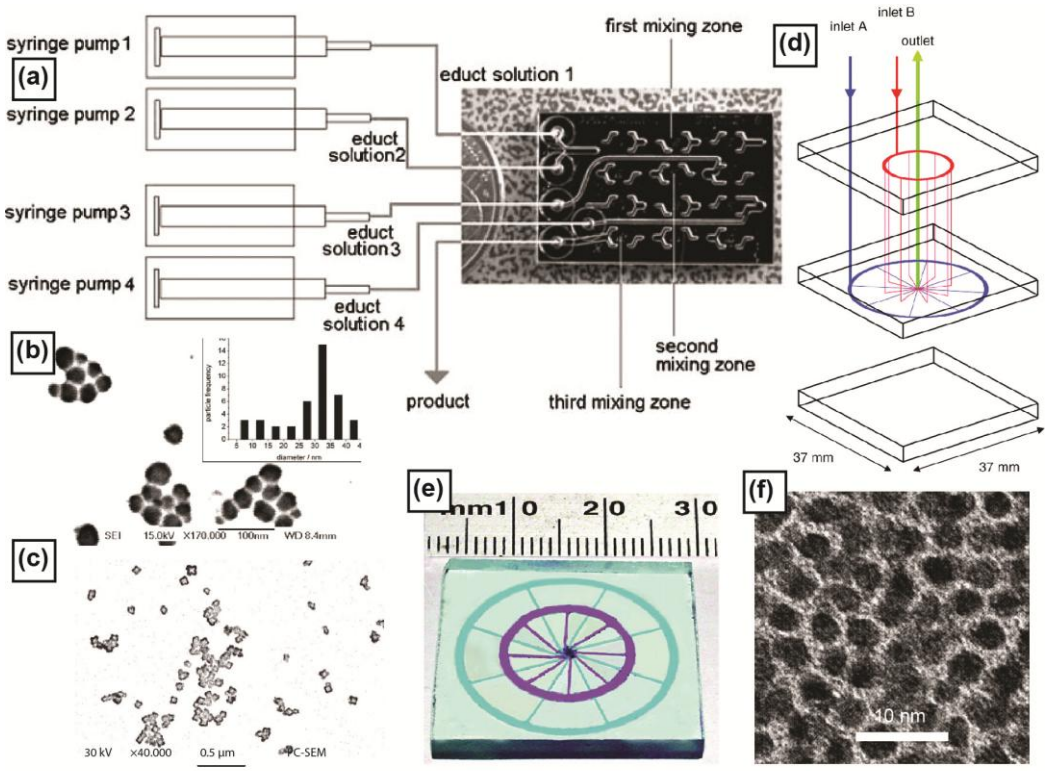

Figure 2.13. Examples of microfluidic metal nanoparticle synthesis **(a)** Experimental setup of three step micromixer reactor;[123] SEM image of **(b)** Hexagonal nanocrystallites (adapted with permission from Reference 126. Copyright 2005, American Chemical Society) and **(c)** Au/Ag nanoparticles[123] **(d)** Schematic of the interdigitated mixer setup. **(e)** Photograph of the mixer filled with dye. **(f)** TEM image of the synthesized particles. Panels **(d), (e)** and **(f)** Reprinted from Reference 127, Copyright 2007 with permission from Elsevier.

Shalom *et al.* synthesized thiol stabilized gold nanoparticles using a multilayer microreactor in which a stream of precursor liquid was split into eight identical laminar streams. Streams of aqueous gold solution and the reducing agent were delivered into a mixing chamber through radially coherent channels. Diffusion-controlled mixing was achieved as radial precursor streams were brought together in the center of the chamber.[127] A schematic of the reactor used for the purpose along with a photograph of the mixer filled with dye is shown in the Figure 2.13 (d) and (e) respectively. They were able to synthesise gold nanoparticles

stabilized by a monolayer of thiol with improved monodispersity as can be seen from the TEM image in Figure 2.13 (f).

Lee and co-workers on the other hand use a microreactor integrated with a micromixer, micropumps, a microvalve, microheaters and a microtemperature sensor on a single chip for the synthesis of hexagonal gold nanoparticles. They report that precise control of the mixing and heating times are essential for the synthesis and show how their reactor is capable of achieving this control.[128] In their later work, they use a microfluidic chip capable of mixing, transporting and controlling reactions for the synthesis of gold nanoparticles of tunable sizes. The micromixer generates vortex type flow fields which achieves 95% mixing in 1 s. The volume of reagents used were changed to vary the size of the gold nanoparticles synthesized.[129] In all these cases, the disadvantages of the single-phase method, fouling and blockage of channels and subsequent inhomogeneity in the particle size resulted due to dispersion and broad residence-time distribution and contact of reagents with the channel walls.

Copper and cobalt nanoparticles were synthesized by Song *et al*. using SU-8 based microfluidic reactor sealed to PEEK substrate.[87,130] Sulfobetaine-stabilized Cu nanoparticles were synthesized and they found that the stability of the intermediate (Cu(I) complex) depended on the sulfobetaine concentration and the rate of addition of the reducing agent. They also report that the Cu nanoparticles of smaller size and narrower size distribution can be synthesized through this technique. They also succeeded in synthesizing Co nanoparticles of three different crystal structures by varying the reaction times, flow rates and the quenching procedure in a similar kind of polymer reactor.

The above discussion of microreactors for the synthesis of metallic nanomaterials describes the prior work in the field and provides the relevant background for this thesis. According to the literature cited, multiphase microfluidics has not been used for the synthesis of metallic nanomaterials so far. This is because of the chemistries involved i.e. most synthesis

protocols are aqueous based and performing *multiphase* experiments with aqueous solutions is complicated. In addition, synthesis of metallic nanomaterials without the need for 'coating of channel walls' or 'changing the actual chemistry' (either by adding a surfactant or polymer) to prevent fouling and clogging of channel walls has also not been accomplished. In addition, the methods described cannot be used commercially for the high yield synthesis of required nanomaterials due to issue such as reactor fouling and low yield. We have leveraged our knowledge of chemical engineering, microfluidics, fluid mechanics and reaction engineering to come up with strategies that make this synthesis in multiphase microfluidics possible. This is essentially the scope of this thesis.

2.5. Summary

The disadvantages of the currently established synthetic strategies for the synthesis of metallic nanomaterials were outlined in this chapter. Gold nanorods were used as the model system for this purpose and a mention of the synthesis protocols available, the mechanisms proposed for synthesis were made in order to better understand the drawbacks that prevent the commercial viability of these methods of synthesis. An introduction to microfluidics and microreactors and state of the art developments in the technology along with the different microfluidic methods available for chemical processing were discussed. A literature survey of the currently available microfluidic methods for particle synthesis was done pointing out the advantages and disadvantages of using these for particle synthesis thus laying out the scope of this thesis.

2.6. References

1 P´erez-Juste, J., Liz-Marz´an, L. M., Carnie, s., Chan, D. Y. C. & Mulvaney, P. Electric-Field-Directed Growth of Gold Nanorods in Aqueous Surfactant Solitions. *Advanced Functional Materials* **14**, 571-579 (2004).

2 P´erez-Juste, J., Pastoriza-Santos, I., Liz-Marz´an, L. M. & Mulvaney, P. Gold Nanorods: Synthesis, Characterization and Applications. *Coordination Chemistry Reviews* **249**, 1870–1901 (2005).

3 Peng, X. Mechanisms for The Shape-Control and Shape-Evolution of Colloidal Semiconductor Nanocrystals. *Advanced Materials* **15**, 459-463 (2003).

4 Jana, N. R. Gram-Scale Synthesis of Soluble, Near-Monodisperse Gold Nanorods and Other Anisotropic Nanoparticles. *Small* **1**, 875-882 (2005).

5 Lu, X., Rycenga, M., Skrabalak, S. E., Wiley, B. & Xia, Y. Chemical Synthesis of Novel Plasmonic Nanoparticles. *Annual Review of Physical Chemistry* **60**, 167-192 (2009).

6 Xiong, Y. & Xia, Y. Shape-Controlled Synthesis of Metal Nanostructures: The Case of Palladium. *Advanced Materials* **19**, 3385–3391 (2007).

7 Wang, Z. L. Transmission Electron Microscopy of Shape-Controlled Nanocrystals and Their Assemblies. *Journal of Physical Chemistry B* **104**, 1153-1175 (2000).

8 Huang, X., Neretina, S. & El-Sayed, M. A. Gold Nanorods: From Synthesis and Properties to Biological and Biomedical Applications. *Advanced Materials* **21**, 4880–4910 (2009).

9 Liu, M. & Guyot-Sionnest, P. Mechanism of Silver(I)-Assisted Growth of Gold Nanorods and Bipyramids. *Journal of Physical Chemistry B* **109**, 22192-22200 (2005).

10 El-Sayed, M. A. Some Interesting Properties of Metals Confined in Time and Nanometer Space of Different Shapes. *Accounts of Chemical Research* **34**, 257-264 (2001).

11 Zande, B. M. I. v. d., Bohmer, M. R., Fokkink, L. G. J. & Schonenberger, C. Aqueous Gold Sols of Rod-Shaped Particles. *Journal of Chemical Physics B* **101**, 852-854 (1997).

12 Zande, B. M. I. v. d., Bohmer, M. R., Fokkink, L. G. J. & Schonenberger, C. Colloidal Dispersions of Gold Rods: Synthesis and Optical Properties. *Langmuir* **16**, 451-458 (2000).

13 Yu, Y.-Y., Chang, S.-S., Lee, C.-L. & Wang, C. R. C. Gold Nanorods: Electrochemical Synthesis and Optical Properties. *Journal of Physical Chemistry B* **101**, 6661-6664 (1997).

14 Nikoobakht, B. & El-Sayed, M. A. Preparation and Growth Mechanism of Gold Nanorods (NRs) Using Seed-Mediated Growth Method. *Chemistry of Materials* **15**, 1957-1962 (2003).

15 Jana, N. R., Gearheart, L. & Murphy Catherine, J. Wet Chemical Synthesis of High Aspect Ratio Cylindrical Gold Nanorods. *Journal of Physical Chemistry B* **105**, 4065-4067 (2001).

16 Foss, C. A., Hornyak, C. L., Stocked, J. A. & Martin, C. R. Optical Properties of Composite Membranes Containing Arrays of Nanoscopic Gold Cylinders. *Journal of Physical Chemistry* **96**, 7497-7499 (1992).

17 Martin, C. R. Nanomaterials: A Membrane-Based Synthetic Approach. *Science* **266**, 1961-1966 (1994).

18 Chang, S.-S., Shih, C.-W., Chen, C.-D., Lai, W.-C. & Wang, C. R. C. The Shape Transition of Gold Nanorods. *Langmuir* **15**, 701-709 (1999).

19 Wang, Z. L., Gao, R. P., Nikoobakht, B. & El-Sayed, M. A. Surface Reconstruction of the Unstable {110} Surface in Gold Nanorods. *Journal of Physical Chemistry B* **104**, 5417-5420 (2000).

20 Jana, N. R., Gearheart, L. & Murphy, C. J. Seed-Mediated Growth Approach for Shape-Controlled Synthesis of Spheroidal and Rod-Like Gold Nanoparticles using a Surfactant Template. *Advanced Materials* **13**, 1389-1393 (2001).

21 Wiesner, J. & Wokaun, A. Anisometric Gold Colloids. Preparation, Characterization, and Optical Properties. *Chemical Physics Letters* **157**, 569-575 (1989).

22 Murphy, C. J., Gole, A. M., Hunyadi, S. E. & Orendorff, C. J. One-Dimensional Colloidal Gold and Silver Nanostructures. *Inorganic Chemistry* **45**, 7544-7554 (2006).

23 Jana, N. R., Gearheart, L. & Murphy, C. J. Evidence for Seed-Mediated Nucleation in the Chemical Reduction of Gold Salts to Gold Nanoparticles. *Chemistry of Materials* **13**, 2313-2322 (2001).

24 Jana, N. R., Gearheart, L. & Murphy, C. J. Wet Chemical Synthesis of Silver Nanorods and Nanowires of Controllable Aspect Ratio. *Chemical Communications* **7**, 617-618 (2001).

25 Murphy, C. J. & Jana, N. R. Controlling the Aspect Ratio of Inorganic Nanorods and Nanowires. *Advanced Materials* **14**, 80-82 (2002).

26 Murphy, C. J. *et al.* Anisotropic Metal Nanoparticles: Synthesis, Assembly, and Optical Applications. *Journal of Physical Chemistry B* **109**, 13857-13870 (2005).

27 Sau, T. K. & Murphy, C. J. Seeded High Yield Synthesis of Short Au Nanorods in Aqueous Solution. *Langmuir* **20**, 6414-6420 (2004).

28 Sau, T. K. & Murphy, C. J. Room Temperature, High-Yield Synthesis of Multiple Shapes of Gold Nanoparticles in Aqueous Solution. *Journal of the American Chemical Society* **126**, 8648-8649 (2004).

29 Gao, J., Bender, C. M. & Murphy, C. J. Dependence of the Gold Nanorod Aspect Ratio on the Nature of the Directing Surfactant in Aqueous Solution. *Langmuir* **19**, 9065-9070 (2003).

30 Gai, P. L. & Harmer, M. A. Surface Atomic Defect Structures and Growth of Gold Nanorods. *Nano Letters* **2**, 771-774 (2002).

31 Orendorff, C. J., Gearheart, L., Jana, N. R. & Murphy, C. J. Aspect Ratio Dependence on Surface Enhanced Raman Scattering Using Silver and Gold Nanorod Substrates. *Physical Chemistry Chemical Physics* **8**, 165–170 (2006).

32 Orendorff, C. J. & Murphy, C. J. Quantitation of Metal Content in the Silver-Assisted Growth of Gold Nanorods. *Journal of Physical Chemistry B* **110**, 3990-3994 (2006).

33 Herrero, E., Buller, L. J. & Abrun˜a, H. c. D. Underpotential Deposition at Single Crystal Surfaces of Au, Pt, Ag and Other Materials. *Chemical Reviews* **101**, 1897-1930 (2001).

34 Zhu, J. *et al.* Shape Dependent Resonance Light Scattering Properties of Gold Nanorods. *Materials Science and Engineering B* **121**, 199–203 (2005).

35 Wang, C., Wang, T., Ma, Z. & Su, Z. pH-Tuned Synthesis of Gold Nanostructures from Gold Nanorods with Different Aspect Ratios. *Nanotechnology* **16**, 2555–2560 (2005).

36 Park, H. J. *et al.* Temperature-Induced Control of Aspect Ratio of Gold Nanorods. *Journal of Vacuum Science & Technology A.* **24** (2006).

37 Gou, L. & Murphy, C. J. Fine-Tuning the Shape of Gold Nanorods. *Chemistry of Materials* **17**, 3668-3672 (2005).

38 Jiang, X. C., Brioude, A. & Pileni, M. P. Gold Nanorods: Limitations on Their Synthesis and Optical Properties. *Colloids and Surfaces A: Physicochemical and Engineering Aspects* **277** 201–206 (2006).

39 Gulati, A., Liao, H. & Hafner, J. H. Monitoring Gold Nanorod Synthesis by Localized Surface Plasmon Resonance. *Journal of Physical Chemistry B* **110**, 22323-22327 (2006).

40 Smith, D. K. & Korgel, B. A. The Importance of the CTAB Surfactant on the Colloidal Seed-Mediated Synthesis of Gold Nanorods. *Langmuir* **24**, 644-649 (2008).

41 Khanal, B. P. & Zubarev, E. R. Purification of High Aspect Ratio Gold Nanorods: Complete Removal of Platelets. *Journal of the American Chemical Society* **130**, 12634–12635 (2008).

42 Torres, F. E., Russel, W. B. & Schowalter, W. R. Simulations of Coagulation in Viscous Flows. *Journal of Colloid and Interface Science* **145**, 51-73 (1991).

43 Torres, F. E., Russel, W. B. & Schowalter, W. R. Floc Structure and Growth Kinetics for Rapid Shear Coagulation of Polystyrene Colloids. *Journal of Colloid and Interface Science* **142**, 554-574 (1991).

44 Whitesides, G. M. The Origins and the Future of Microfluidics. *Nature* **442**, 368-373 (2006).

45 Song, Y., Hormes, J. & Kumar, C. S. S. R. Microfluidic Synthesis of Nanomaterials. *Small* **4**, 698–711 (2008).

46 DeMello, A. J. Control and Detection of Chemical Reactions in Microfluidic Systems. *Nature* **442**, 394-402 (2006).

47 Ehrfeld, W., Hessel, V. & Löwe, H. *Microreactors: New Technology for Modern Chemistry*. (Wiley-VCH, 2000).

48 Abou-Hassan, A., Sandre, O. & Cabuil, V. Microfluidics in Inorganic Chemistry. *Angewandte Chemie - International Edition* **49**, 6268 – 6286 (2010).

49 Pennemann, H., Hessel, V. & Löwe, H. Chemical Microprocess Technology—from Laboratory-Scale to Production. *Chemical Engineering Science* **59**, 4789 – 4794 (2004).

50 Hessel, V., Hardt, S. & Löwe, H. *Chemical Micro Process Engineering : Fundamentals, Modelling and Reactions*. (Wiley-VCH, 2006).

51 Marre, S. & Jensen, K. F. Synthesis of Micro and Nanostructures in Microfluidic Systems. *Chemical Society Reviews* **39**, 1183–1202 (2010).

52 Jensen, K. F. Microreaction Engineering - Is Small Better? *Chemical Engineering Science* **56**, 293-303 (2001).

53 Song, Y., Kumar, C. S. S. R. & Hormes, J. Synthesis of Palladium Nanoparticles Using a Continuous Flow Polymeric Micro Reactor *Journal of Nanoscience and Nanotechnology* **4**, 788-793 (2004).

54 Sahoo, H. R., Kralj, J. G. & Jensen, K. F. Multistep Continuous-Flow Microchemical Synthesis Involving Multiple Reactions and Separations. *Angewandte Chemie - International Edition* **46**, 5704 –5708 (2007).

55 Stone, H. A., Stroock, A. D. & Ajdari, A. Engineering Flows in Small Devices: Microfluidics Toward a Lab-on-a-Chip. *Annual Review of Fluid Mechanics* **36**, 381-411 (2004).

56 deMenech, M., Garstecki, P., Jousse, F. & Stone, H. A. Transition From Squeezing to Dripping in a Microfluidic T-Shaped Junction. *Journal of Fluid Mechanics* **595**, 141-161 (2008).

57 Mengeaud, V., Josserand, J. & Girault, H. H. Mixing Processes in a Zigzag Microchannel: Finite Element Simulations and Optical Study. *Analytical Chemistry* **74**, 4279-4286 (2002).

58 Chen, H. & Meiners, J.-C. Topologic Mixing on a Microfluidic Chip. *Applied Physics Letters* **84**, 2193-2195 (2004).

59 Stroock, A. D. *et al.* Chaotic Mixer for Microchannels. *Science* **295**, 647-651 (2002).

60 Khan, S. A., Gunther, A., Schmidt Martin, A. & Jensen Klavs, F. Microfluidic Synthesis of Colloidal Silica. *Langmuir* **20**, 8604-8611 (2004).

61 Evensen, H. T., Meldrum, D. R. & Cunninghama, D. L. Automated Fluid Mixing in Glass Capillaries. *Review of Scientific Instruments* **69**, 519-526 (1998).

62 Liu, R. H. *et al.* Passive Mixing in a Three-Dimensional Serpentine Microchannel. *Journal of Microelectromechanical Systems* **9**, 190-197 (2000).

63 Ottino, J. M. The mixing of fluids. *Scientific American* **260**, 40-49 (1989).

64 Ottino, J. M. Mixing, Chaotic Advection, and Turbulence. *Annual Review of Fluid Mechanics* **22**, 207-253 (1990).

65 Boleininger, J., Kurz, A., Reuss, V. & Sonnichsen, C. Microfluidic Continuous Flow Synthesis of Rod-Shaped Gold and Silver Nanocrystals. *Physical Chemistry Chemical Physics* **8**, 3824-3827 (2006).

66 Wagner, J., Kirner, T., Mayer, G., Albert, J. & Kohler, J. M. Generation of Metal Nanoparticles in a Microchannel Reactor. *Chemical Engineering Journal* **101**, 251-260 (2004).

67 Garstecki, P. *et al.* Formation of Monodisperse Bubbles in a Microfluidic Flow-Focusing Device. *Applied Physics Letters* **85**, 2649-2651 (2004).

68 Link, D. R., Anna, S. L., Weitz, D. A. & Stone, H. A. Geometrically Mediated Breakup of Drops in Microfluidic Devices. *Physical Review Letters* **92** (2004).

69 Anna, S. L., Bontoux, N. & Stone, H. A. Formation of Dispersions Using "Flow Focusing" in Microchannels. *Applied Physics Letters* **82**, 364-366 (2003).

70 Günther, A., Khan, S. A., Thalmann, M., Trachsel, F. & Jensen, K. F. Transport and Reaction in Microscale Segmented Gas–Liquid Flow. *Lab on a Chip* **4**, 278-286 (2004).

71 Ajaev, V. S. & Homsy, G. M. Modeling Shapes and Dynamics of Confined Bubbles. *The Annual Review of Fluid Mechanics* **38**, 277-307 (2006).

72 Anna, S. L. & Mayer, H. C. Microscale Tipstreaming in a Microfluidic Flow Focusing Device. *Physics of Fluids* **18**, 121512 (2006).

73 Baroud, C. N. & Willaime, H. Multiphase Flows in Microfluidics. *C. R. Physique* **5**, 547–555 (2004).

74 Garstecki, P., Fuerstman, M. J., Stone, H. A. & Whitesides, G. M. Formation of Droplets and Bubbles in a Microfluidic T-Junction - Scaling and Mechanism of Break-up. *Lab on a Chip* **6**, 437-446 (2006).

75 Guillot, P., Ajdari, A., Goyon, J., Joanicot, M. & Colin, A. Droplets and Jets in Microfluidic Devices. *Comptes Rendus Chimie* **12**, 247-257 (2009).

76 Song, H., Tice, J. D. & Ismagilov, R. F. A Microfluidic System for Controlling Reaction Networks in Time. *Angewandte Chemie - International Edition* **42**, 768-772 (2003).

77 Günther, A. & Jensen, K. F. Multiphase Microfluidics: from Flow Characteristics to Chemical and Materials Synthesis. *Lab on a Chip* **6**, 1487-1503 (2006).

78 Günther, A., Jhunjhunwala, M., Thalmann, M., Schmidt, M. A. & Jensen, K. F. Micromixing of Miscible Liquids in Segmented Gas-Liquid Flow. *Langmuir* **21**, 1547-1555 (2005).

79 Song, H., Chen, D. L. & Ismagilov, R. F. Reactions in Droplets in Microflulidic Channels. *Angewandte Chemie-International Edition* **45**, 7336-7356 (2006).

80 Wang, H., Li, X., Nakamura, H., Miyazaki, M. & Maeda, H. Continuous Particle Self-Arrangement in a Long Microcapillary. *Advanced Materials* **14**, 1662-1666 (2002).

81 Wang, H. *et al.* Synthesis of CdSe Magic-Sized Nanocluster and its Effect on Nanocrystal Preparation in a Microfluidic Reactor. *MRS Bulletin* **19**, 3157-3161 (2004).

82 Weng, C.-H., Huang, C.-C., Yeh, C.-S., Lei, H.-Y. & Lee, G.-B. Synthesis of Hexagonal Gold Nanoparticles Using a Microfluidic Reaction System. *Journal of Micromechanics and Microengineering* **18**, 035019 (2008).

83 Ng, J. M. K., Gitlin, I., Stroock, A. D. & Whitesides, G. M. Components for Integrated Poly(dimethylsiloxane) Microfluidic Systems. *Electrophoresis* **23**, 3461–3473 (2002).

84 Love, J. C., Anderson, J. R. & Whitesides, G. M. Fabrication of Three-Dimensional Microfluidic Systems by Soft Lithography. *MRS Bulletin* **26**, 523-528 (2001).

85 Duffy, D. C., McDonald, J. C., Schueller, O. J. A. & Whitesides, G. M. Rapid Prototyping of Microfluidic Systems in Poly(dimethylsiloxane). *Analytical Chemistry* **70**, 4974-4984 (1998).

86 Deng, T., Wu, H., Brittain, S. T. & Whitesides, G. M. Prototyping of Masks, Masters, and Stamps/Molds for Soft Lithography Using an Office Printer and Photographic Reduction. *Analytical Chemistry* **72**, 3176-3180 (2000).

87 Song, Y. et al. Investigations into Sulfobetaine-Stabilized Cu Nanoparticle Formation: Toward Development of a Microfluidic Synthesis. *Journal of Physical Chemistry B* **109**, 9330-9338 (2005).

88 Abou-Hassan, A., Bazzi, R. & Cabuil, V. Multistep Continuous-Flow Microsynthesis of Magnetic and Fluorescent γ-Fe2O3@SiO2 Core/Shell Nanoparticles. *Angewandte Chemie - International Edition* **48**, 7180 –7183 (2009).

89 Tiggelaar, R. M. *et al.* Fabrication, Mechanical Testing and Application of High-Pressure Glass Microreactor Chips. *Chemical Engineering Journal* **131**, 163–170 (2007).

90 Trachsel, F., Hutter, C. & Rohr, P. R. v. Transparent Silicon/Glass Microreactor for High-Pressure and High-Temperature Reactions. *Chemical Engineering Journal* **135**, S309-S316 (2008).

91 Yen, B. K. H., Gunther, A., Schmidt, M. A., Jensen, K. F. & Bawendi, M. G. A Microfabricated Gas-Liquid Segmented Flow Reactor for High-Temperature Synthesis: The Case of CdSe Quantum Dots. *Angewandte Chemie - International Edition* **44**, 5447-5451 (2005).

92 Nittis, V., Fortt, R., Legge, C. H. & Mello, A. J. d. A High-Pressure Interconnect for Chemical Microsystem Applications. *Lab on a Chip* **1**, 148-152 (2001).

93 Marre, S. *et al.* Supercritical Continuous-Microflow Synthesis of Narrow Size Distribution Quantum Dots. *Advanced Materials* **20**, 4830-4834 (2008).

94 Hung, L.-H. & Lee, A. P. Microfluidic Devices for the Synthesis of Nanoparticles and Biomaterials. *Journal of Medical and Biological Engineering* **27**, 1-6 (2007).

95 Jahn, A. *et al.* Preparation of Nanoparticles by Continuous-Flow Microfluidics. *Journal of Nanoparticle Research* **10**, 925–934 (2008).

96 Winterton, J. D., Myers, D. R., Lippmann, J. M., Pisano, A. P. & Doyle, F. M. A Novel Continuous Microfluidic Reactor Design for the Controlled Production of High-Quality Semiconductor Nanocrystals. *Journal of Nanoparticle Research* **10**, 893–905 (2008).

97 Dendukuri, D. & Doyle, P. S. The Synthesis and Assembly of Polymeric Microparticles Using Microfluidics. *Advanced Materials* **21**, 4071–4086 (2009).

98 Tumarkin, E. & Kumacheva, E. Microfluidic Generation of Microgels from Synthetic and Natural Polymers. *Chemical Society Reviews* **38**, 2161–2168 (2009).

99 Abou-Hassan, A., Sandre, O. & Cabuil, V. Microfluidics in Inorganic Chemistry. *Angewandte Chemie International Edition* **49**, 6268 – 6286 (2010).

100 Park, J. I., Saffari, A., Kumar, S., Gunther, A. & Kumacheva, E. Microfluidic Synthesis of Polymer and Inorganic Particulate Materials. *Annual Review of Materials Research* **40**, 415–443 (2010).

101 Kumar, C. S. S. R. *Microfluidic Devices in Nanotechnology*. (John Wiley & Sons., 2010).

102 Chan, E. M., Alivisatos, A. P. & Mathies, R. A. High-Temperature Microfluidic Synthesis of CdSe Nanocrystals in Nanoliter Droplets. *Journal of the American Chemical Society* **127**, 13854-13861 (2005).

103 Chen, D. L., Gerdts, C. J. & Ismagilov, R. F. Using Microfluidics to Observe the Effect of Mixing on Nucleation of Protein Crystals. *Journal of the American Chemical Society* **127**, 9672-9673 (2005).

104 Edel, J. B., Fortt, R., DeMello, J. C. & DeMello, A. J. Microfluidic Routes to the Controlled Production of Nanoparticles. *Chemical Communications* **8**, 1136-1137 (2002).

105 He, S., Liu, Y., Uehara, M. & Maeda, H. Continuous Micro Flow Synthesis of ZnO Nanorods with UV Emissions. *Materials Science & Engineering B (Solid-State Materials for Advanced Technology)* **137**, 295-298 (2007).

106 Nisisako, T., Torii, T. & Higuchi, T. Novel Microreactors for Functional Polymer Beads. *Chemical Engineering Journal* **101**, 23-29 (2004).

107 Nakamura, H. *et al.* Preparation of CdSe Nanocrystals in a Micro-Flow-Reactor. *Chemical Communications* **8**, 2844-2845 (2002).

108 Yen, B. K. H., Stott, N. E., Jensen, K. F. & Bawendi, M. G. A Continuous-Flow Microcapillary Reactor for the Preparation of a Size Series of CdSe Nanocrystals. *Advanced Materials* **15**, 1858-1862 (2003).

109 Nakamura, H. *et al.* Application of a Microfluidic Reaction System for CdSe Nanocrystal Preparation: Their Growth Kinetics and Photoluminescence Analysis. *Lab on a Chip* **4**, 237-240 (2004).

110 Krishnadasan, S., Tovilla, J., Vilar, R., DeMello, A. J. & DeMello, J. C. On-line Analysis of CdSe Nanoparticle Formation in a Continuous Flow Chip-Based Microreactor. *Journal of Materials Chemistry* **14**, 2655-2660 (2004).

111 Nam-Trung, N. & Zhigang, W. Micromixers-a Review. *Journal of Micromechanics and Microengineering* **15**, 1-16 (2005).

112 Knight, J. B., Vishwanath, A., Brody, J. P. & Austin, R. H. Hydrodynamic Focusing on a Silicon Chip: Mixing Nanoliters in Microseconds. *Physical Review Letters* **80**, 3863-3866 (1998).

113 Shestopalov, I., Tice, J. D. & Ismagilov, R. F. Multi-Step Synthesis of Nanoparticles Performed on Millisecond Time Scale in a Microfluidic Droplet-Based System. *Lab on a Chip* **4**, 316-321 (2004).

114 Sounart, T. L. *et al.* Spatially-Resolved Analysis of Nanoparticle Nucleation and Growth in a Microfluidic Reactor. *Lab on a Chip* **7**, 908–915 (2007).

115 Frenz, L. *et al.* Droplet-Based Microreactors for the Synthesis of Magnetic Iron Oxide Nanoparticles. *Angewandte Chemie-International Edition* **47**, 6817–6820 (2008).

116 Abou-Hassan, A., Sandre, O., Cabuila, V. & Tabeling, P. Synthesis of Iron Oxide Nanoparticles in a Microfluidic Device: Preliminary Results in a Coaxial Flow Millichannel. *Chemical Communications*, 1783–1785 (2008).

117 Abou-Hassan, A., Sandre, O., Neveu, S. & Cabuil, V. Synthesis of Goethite by Separation of the Nucleation and Growth Processes of Ferrihydrite Nanoparticles Using Microfluidics. *Angewandte Chemie - International Edition* **48**, 2342 –2345 (2009).

118 Carroll, N. J. *et al.* Droplet-Based Microfluidics for Emulsion and Solvent Evaporation Synthesis of Monodisperse Mesoporous Silica Microspheres. *Langmuir* **24**, 658-661 (2008).

119 Lee, I., Yoo, Y., Cheng, Z. & Jeong, H.-K. Generation of Monodisperse Mesoporous Silica Microspheres with Controllable Size and Surface Morphology in a Microfluidic Device. *Advanced Functional Materials* **18**, 4014–4021 (2008).

120 Cottam, B. F., Krishnadasan, S., DeMello, A. J., DeMello, J. C. & Shaffer, M. S. P. Accelerated Synthesis of Titanium Oxide Nanostructures Using Microfluidic Chips. *Lab on a Chip* **7**, 167-169 (2007).

121 Wang, H. *et al.* Continuous synthesis of CdSe-ZnS Composite Nanoparticles in a Microfluidic Reactor. *Chemical Communications* **10**, 48-49 (2004).

122 Khan, S. A. & Jensen, K. F. Microfluidic Synthesis of Titania Shells on Colloidal Silica. *Advanced Materials* **19**, 2556-2560 (2007).

123 Kohler, J. M., Romanus, H., Hubner, U. & J.Wagner. Formation of Star-Like and Core-Shell AuAg Nanoparticles during Two- and Three-Step Preparation in Batch and in Microfluidic Systems. *Journal of Nanomaterials* (2007).

124 Kohler, J. M., Held, M., Hubner, U. & Wagner, J. Formation of Au/Ag Nanoparticles in a Two Step Micro Flow-Through Process. *Chemical Engineering and Technology* **30**, 347-354 (2007).

125 Kohler, J. M., Wagner, J. & Albert, J. Formation of Isolated and Clustered Au Nanoparticles in the Presence of Polyelectrolyte Molecules using a Flow-Through Si Chip Reactor. *Journal of Materials Chemistry* **15**, 1924-1930 (2005).

126 Wagner, J. & Kohler, J. M. Continuous Synthesis of Gold Nanoparticles in a Microreactor. *Nano Letters* **5**, 685-691 (2005).

127 Shalom, D. *et al.* Synthesis of Thiol Functionalized Gold Nanoparticles using a Continuous Flow Microfluidic Reactor. *Materials Letters* **61**, 1146–1150 (2007).

128 Weng, C.-H., Huang, C.-C., Yeh, C.-S., Lei, H.-Y. & Lee, G.-B. Synthesis of Hexagonal Gold Nanoparticles using a Microfluidic Reaction System. *Journal of Micromechanics and Microengineering* **18**, 035019 (2008).

129 Yang, S.-Y., Cheng, F.-Y., Yeh, C.-S. & Lee, G.-B. Size-Controlled Synthesis of Gold Nanoparticles using a Micro-Mixing System. *Microfluidics and Nanofluidics* **8**, 303–311 (2010).

130 Song, Y. *et al.* Microfluidic Synthesis of Cobalt Nanoparticles. *Chemistry of Materials* **18**, 2817-2827 (2006).

3. Droplet-Based Microfluidic Synthesis of Anisotropic Metal Nanocrystals

A droplet-based microfluidic method for the preparation of anisotropic gold nanocrystal dispersions is presented in this chapter. Gold nanoparticle seeds and growth reagents are dispensed into monodispersed picoliter droplets within a microchannel. Confinement within small droplets prevents contact between the growing nanocrystals and the microchannel walls. Challenges posed by surfactant-rich wet chemical syntheses of gold nanocrystals during their implementation into the droplet-based microfluidic platform, which typically constitute the critical factors in translating macroscale flask-based methods to a flow-based microfluidic method, are highlighted and addressed here. Further, approaches to flexibly fine-tune nanoparticle shapes into three broad classes: spheres/spheroids, rods and extended sharp-edged structures are also demonstrated.

3.1. Detailed Background

One of the main aims of this thesis is to develop technological platforms for continuous synthesis of gold nanocrystals of varying shapes and sizes that can be directly adopted for commercial-scale production. As a first step towards this goal, synthesis of anisotropic gold nanomaterials with specific focus on the synthesis of gold nanorods (GNR) using one of the protocols described in Chapter 2 was pursued. A literature survey of the various methods used for the synthesis of nanoparticles in microreactors shows that the synthesis of nanomaterials in single phase flows requires reactors with complex channel design/geometry along with the use of polymers and additives or chemically modified channel walls to achieve fast mixing, prevent broad residence time distributions (RTD) and to prevent deposition on channel walls (2.4). In particular, isolation of growing particles from the microchannel walls is a critical requirement in the implementation of continuous flow

microfluidic methods to prepare colloidal metal dispersions. However, most of the strategies mentioned earlier were not entirely successful for the synthesis of monodisperse metallic nanomaterials (Section 2.4.4).

The alternative approach is liquid-liquid multiphase microfluidics also referred to as droplet microfluidics. This method is capable of isolating the reactants from the channel walls as well as achieves fast mixing and narrower RTD (Section 2.3.2). In this approach, aqueous reagents are injected as discrete droplets into a flowing immiscible carrier liquid that prevents contact between the reagents and the microchannel walls.[1] Droplet methods have been successfully implemented in the synthesis of monodisperse semiconductor nanocrystals (Section 2.4.1).[2] The main drawback limiting the general applicability of such methods is the sensitive dependence of flow pattern on fluid properties such as interfacial tension.[3,4] Fluid properties are usually dictated by the reagents required for synthesis, and may not be independent design variables. For example, the injection of surfactant-rich aqueous reagents into immiscible carrier fluids does not necessarily form droplets but instead may form other flow patterns such as parallel co-flow or aqueous jets.[5,6] These limitations of droplet-based microfluidic methods are particularly relevant in wet chemical syntheses of metallic dispersions that typically require high concentrations of surfactant molecules to direct shape evolution and also ensure colloidal stability. The challenges posed by surfactant-rich wet chemical nanocrystal syntheses during their implementation into a droplet-based microfluidic platform are addressed in the next section.

3.2. Method Development

Pre-synthesized gold nanoparticle seeds and growth reagents are dispensed into monodispersed picoliter droplets that are continuously generated at a microfluidic T-junction. (Pre-synthesized seeds are used in order to reduce the complexity of the method.) Droplets flow in a regular stable train within a co-flowing immiscible silicone oil in a certain range of

volumetric flow rates of aqueous and oil phases. Confinement within small droplets prevents contact between the growing nanocrystals and the microchannel walls.

3.2.1. Concept

Figure 3.1 is a schematic illustrating the method. An aqueous gold nanoparticle seed suspension (S) and aqueous reagent solutions (R1 and R2) are separately delivered into one arm of a microfluidic T-junction. Immiscible cross-flowing oil is delivered into the other arm of the T-junction. Droplets are pinched off at the T-junction and form a stable and non-coalescing train downstream. Chaotic advection within the droplets rapidly mixes nanoparticle seeds with the aqueous reagents. The oil forms a thin lubricating layer around the translating droplets, thus isolating growing particles from the microchannel walls and preventing wall deposition.[7]

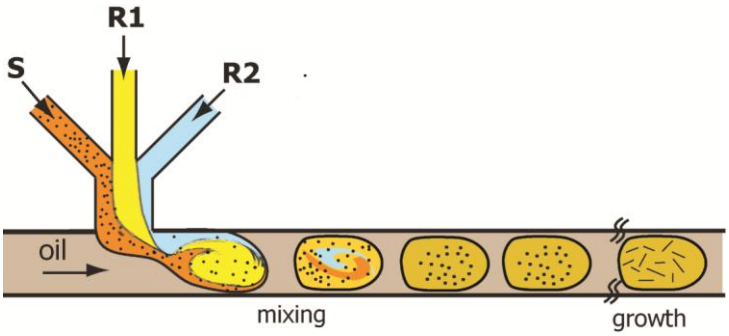

Figure 3.1. Schematic illustration of the droplet microfluidic method for particle synthesis.

3.2.2. Synthesis Protocol: Translating from Batch to Continuous-Flow

Rod-shaped gold nanocrystal dispersions were prepared using the seeded growth method originally proposed by Nikhoobakht *et al*.[8] In this method, small and nearly spherical gold nanoparticle seeds (size <2 nm) are grown into rod-shaped nanocrystals by the reduction of tri-valent gold ($Au^{[3+]}$) to zero-valent gold ($Au^{[0]}$) with ascorbic acid (AA) in the presence of cationic surfactant (CTAB) and small amounts of dissolved silver nitrate ($Ag^{[+]}$). Silver ions,

by influencing the relative growth rates of different crystal facets, induce shape anisotropy during growth (2.2.6 and 2.2.7).[9] A first attempt at implementing the continuous-flow synthesis was made using the same stock solutions, with the respective volumes mixed in the batch method translating to volumetric delivery rates of flowing reagent streams in the continuous version. The small-scale batch method proposed by Nikoobakht and El-Sayed involves addition of minute volumes of seed suspension ~10 μL to ~10 mL of a mixture of growth reagents. A flow version of this method would be difficult to implement in practice, as it would require impractically large flow ratios of incoming reagent streams (~1:1000). The original method was hence modified by diluting the seed solution, thereby requiring addition of comparable volumes (flow rates) of seed and reagent. A pre-mixed $Au^{[3+]}$, $Ag^{[+]}$ and CTAB solution (reagent solution R1), an aqueous solution of AA (reagent solution R2) and seed suspension (S) are fed separately through individual inlets into one arm of the T-junction as is depicted in Figure 3.1. Silicone oil, the continuous liquid, is fed to the perpendicular arm of the T-junction. Reagent contacting is achieved at the microfluidic T-junction, where reagents are dispensed into small picoliter droplets.

3.3. Experimental

3.3.1. Materials

Sodium borohydride (98%), hydrogen tetrachloroaurate(III) trihydrate ($HAuCl_4.3H_2O$) (99.99%) and hexadecyltrimethyl ammonium bromide (99%) (CTAB) were purchased from Sigma-Aldrich Co. Ltd., Singapore while silver nitrate (99.9% of Ag) from Strem Chemicals, Singapore and L-(+) ascorbic acid (99%) from Alfa Aesar Co. Inc., Singapore. 18MΩ-cm ultrapure deionised water was used for all experiments and all reagents were used without further purification.

3.3.2. Seed Synthesis

Nearly spherical gold nanoparticle seeds (< 4 nm in size) were synthesized by adding freshly prepared, ice cold sodium borohydride solution (0.6 mL of 0.01 M) to a mixture of aqueous $HAuCl_4.3H_2O$ (0.25 mL of 10 mM) and CTAB (7.5 mL of 100 mM) solution, while stirring vigorously (700 rpm, Heidolph) using a magnetic stirrer (teflon, 2 mm) in a borosilicate vial (20mL, scintillation, Kimble glass Inc., Singapore). The color of the solution turned brown as soon as $NaBH_4$ solution was added indicating the formation of small gold nanocrystals. The solution was maintained at 35ºC till use and was used within 5 hrs of synthesis.

3.3.3. Microfabrication

The microchannels were moulded in PDMS, from master patterns fabricated on silicon wafers by photolithography on a negative photoresist (SU-8 2050). Details of the fabrication of the master are provided in Appendix B while the actual channel design is shown in Figure 3.2. The channel has rectangular cross-section and were 300 μm wide, ~155 μm deep and 0.45 m long. Moulded channel patterns were sealed to glass slides pre-coated with a thin layer of cured PDMS after 35 s air plasma treatment (Harrick PDC 32G).

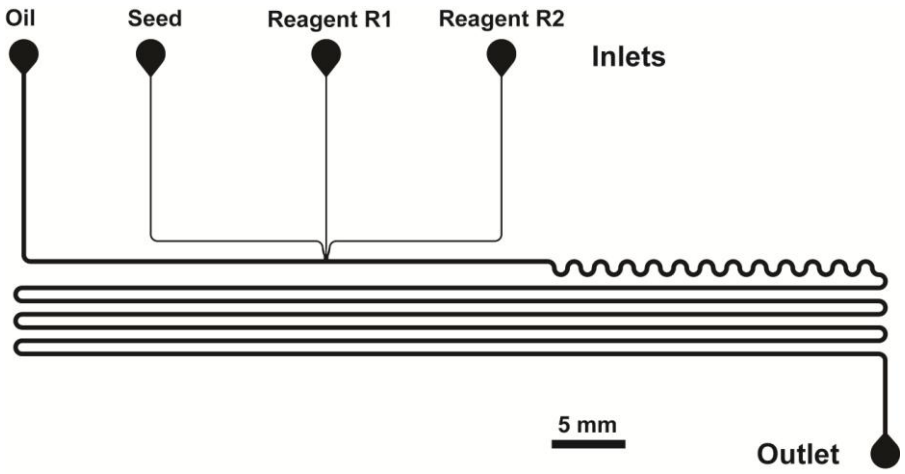

Figure 3.2. AutoCAD drawing of the microchannel.

3.3.4. Reactor Setup and Operation

Reagent R1 was a mixture of CTAB (4 mL of 250 mM), gold salt solution (4 mL of 1.25 mM) and varying volumes of silver nitrate solution (0.05 mL to 0.25 mL of 4mM). Reagent R2 was 5.16 mM of ascorbic acid. The dilute aqueous seed solution (S) was prepared by adding 0.35 mL of the original seed solution in 5 mL water. Silicone oil (Dow Corning DC50, viscosity 10 cP), gold nanoparticle seed suspension (S) and aqueous reagent solutions (R1 and R2) were delivered by separate syringe pumps (Harvard, PHD 2000) into the respective inlets. The entire setup (reactor along with the fittings and tubings) was immersed into a hot water bath maintained at 35ºC to prevent the crystallization of CTAB at temperatures < 28ºC (Figure 3.3). The premixed solution of CTAB and gold salt solution was also maintained at 35ºC using a heating coil wound around the syringe.

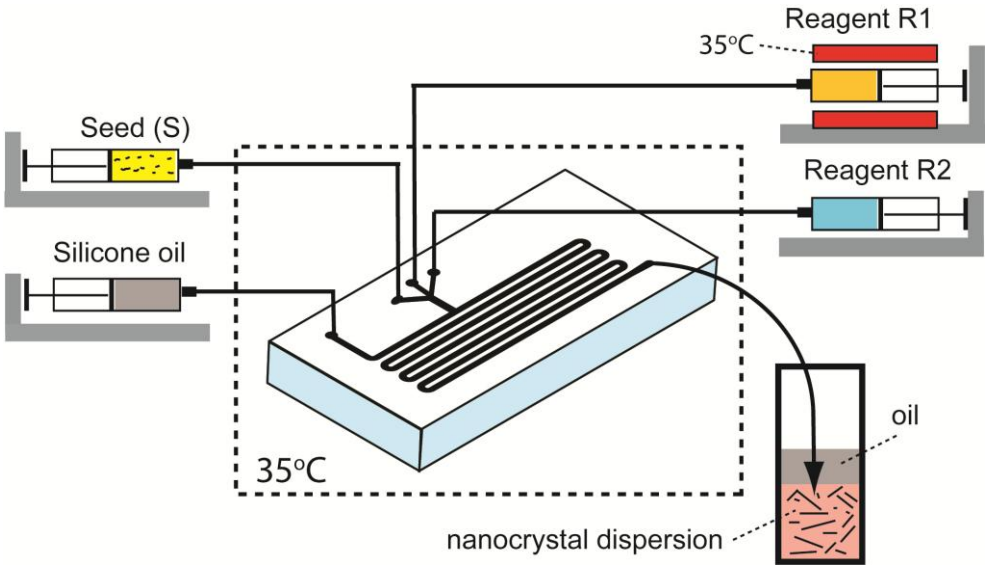

Figure 3.3. Schematic of the experimental setup (details in text).

Heating Coil: The heating coil used for the experiment was fabricated and assembled in-house using nichrome wire of length 1 m and thickness 350 μm. The wire was placed inside an insulated sleeve; when used in experiments, the wire was wound around the gas tight syringe (Hamilton) and the ends of the wire were connected to a power supply (Agilent) at constant

voltage mode. A photograph of the heating coil wound around a syringe with the ends attached to the power supply is shown in Figure 3.4.

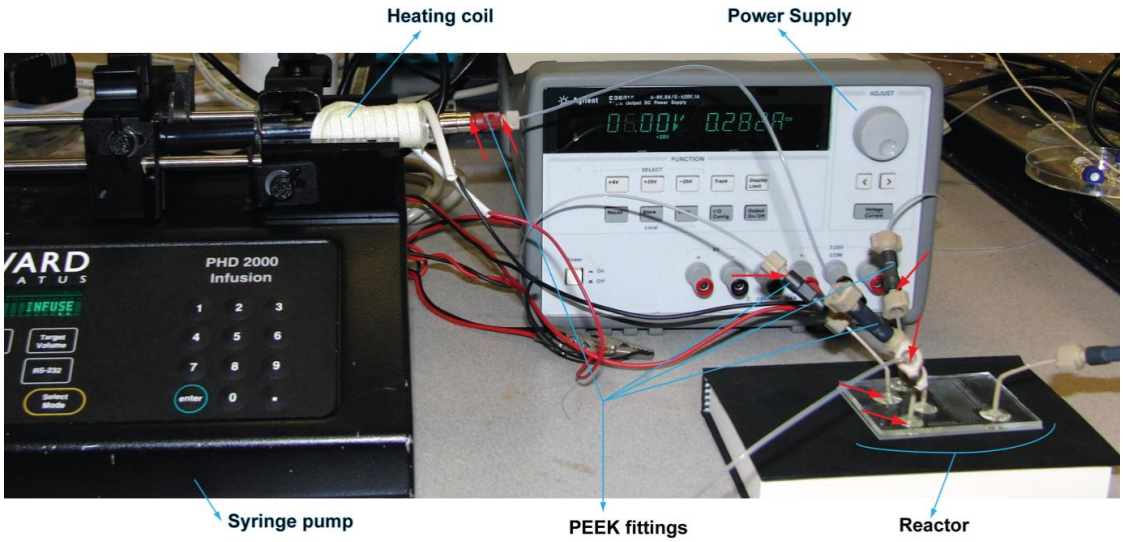

Figure 3.4. Photograph of the heating coil wound around a syringe and connected to the power supply.

The heating coil was initially calibrated to determine the voltage required to maintain the temperature of the solution inside the syringe at 35ºC. The coil was calibrated for waterflow by mounting the syringe filled with water onto a syringe pump infusing at a constant rate of 10 μL.min^{-1}. The temperature of the water from the syringe was measured and plotted against the voltage applied. Accordingly ~2.6 V was required to maintain the water temperature in the syringe at 35ºC in constant voltage mode and was used for the synthesis experiments.

Hot Water Bath: A 2 cm wide crystallization flask filled with water was used as the hot water bath into which the reactor along with the tubings and fittings were immersed. A photograph of the bath with the reactor and the tubings is provided in Figure 3.5. The bath was placed on a hot plate maintained at 40ºC. The temperature of the water bath was regularly checked to be >35ºC which allows the temperature in and of the reactor to be at 35ºC. The use of hot water bath prevents the crystallization of CTAB. Crystallization of CTAB in the channels leads to blockage of the channels and eventually to delamination of the microreactor while crystals in

the tubings lead to leaks from the fittings connecting the tubing to the syringe or to reactor as well as from the tubing glued to the reactor. Such locations prone to leaks are pointed out using red arrows in Figure 3.4.

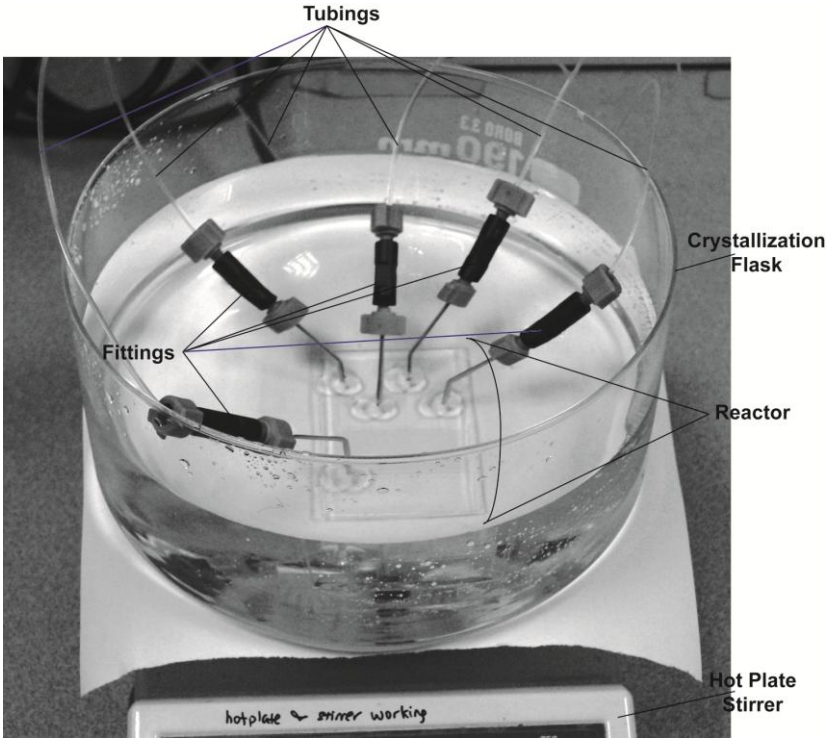

Figure 3.5. Photograph of the hot water bath with the reactor and the tubings on a hot plate.

Startup Protocol: All the syringe pumps were turned on at a flow rate of 10 μL.min^{-1}. However the flow rates of the pumps infusing aqueous reagents were reduced to 2 μL.min^{-1} as soon as the aqueous solutions begin to flow into their respective tubings while the pump infusing oil was set to the desired flow rate. The trapped gas in the tubing flowed out first before the liquid flow, hence preventing the aqueous solutions from flowing into the channels before the oil flowed in, thus coating the reactor with oil. To begin with, the trapped gas in the tubing formed segmented gas-liquid flows with the oil flowing into the channels. The pumps infusing aqueous reagents were set to the desired flow rates only after the reactor was completely wet by the oil. This step was followed to prevent the flow (back flow) of oil into the T- junction or the aqueous inlets and also to prevent the aqueous solutions from reaching

the channels before the oil. This helped in the formation of a thin oil film between the droplets and the channel walls which prevented their contact.[3] In addition, this also ensured that the oil does not wet the aqueous channel inlets. Droplet breakup at the T-junction was altered which led to erratic flow patterns if the oil reached the aqueous section of the T-junction.[3] Moreover, this also prevented the flow of individual aqueous reagents into the inlet channels meant for other aqueous reagents, for example, seeds into the inlet channel for reagent R1, which led to reaction in the inlet channel and hence to channel wall deposition and clogging of the reactor. Once the reagents flowed into the reactor and formed regular droplets, their flow rates were varied in steps of 3 $\mu L.min^{-1}$ for every five mins interval to the desired value. The flow of reagents was then allowed to stabilize for 30 mins after reaching the desired flow rates.

3.3.5. Sample Collection and Analysis

The outlet from the reactor led to a 2 mL centrifuge tube which was initially filled with 50 µL of water. Approximately 1 mL of the sample was collected for every condition and the collected samples were left undisturbed for at least 60 mins to ensure completion of nanocrystal growth. The sample preparation procedure is pictorially represented in Figure 3.6. Drops containing the particle dispersion settled to the bottom of the centrifuge tube and the aqueous phase separated from the oil as shown in Figure 3.6 (a). The oil layer was carefully decanted (Figure 3.6 (a) to (b)) and the samples were first analyzed using UV-vis spectrometer (Shimadzu UV-2450) in microcuvettes (Helma). The remnant oil in the sample tends to leave a thin oil film on the cuvette. Hence the cuvette was thoroughly washed with acetone and DI water between every sample and was finally washed with hexane to completely remove the remnant oil. Samples were then analyzed using either TEM (JEOL 2010, accelerating voltage 200 kV) or FESEM (JEOL JSM-6700f, accelerating voltage 25 kV).

TEM sample preparation is very crucial in order to obtain good quality images of samples that can be used for image analysis. The excess CTAB and the remnant oil in the sample affects the image quality by forming a thick impenetrable (to electrons) layer on the

particles (due to the crystals of CTAB) or by forming dark patches on the image that eventually engulf it (presence of very thin oil layer). Hence samples were centrifuged (7000 rpm, 8 mins) to remove excess CTAB and re-dispersed in DI water. After every centrifugation step (Figure 3.6 (c)), instead of decanting the top layer of CTAB and remnant oil (Figure 3.6 (c) to (d)), the particles at the bottom were pipetted out into a fresh centrifuge tube and dispersed in DI water (Figure 3.6 (c) to (e)) for the next centrifugation.

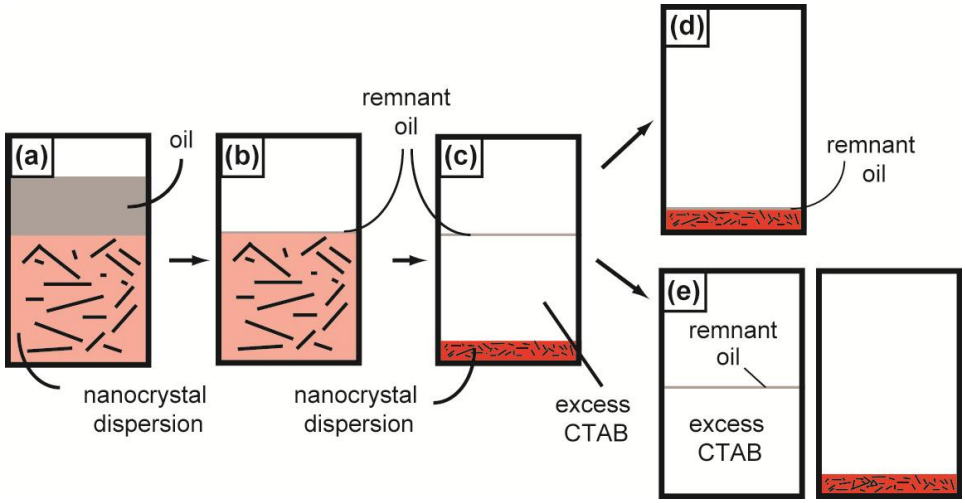

Figure 3.6. Schematic of the procedure for TEM sample preparation **(a)** Collected original sample **(b)** After the top layer of oil was decanted **(c)** After one centrifugation step **(d)** Sample if the excess CTAB was decanted **(e)** Sample if the pellet was pipetted out into a new centrifuge tube

The centrifugation and re-dispersion in DI water was repeated thrice to concentrate the sample as well as to clean the sample of the remaining oil. It was observed that decanting the top layer after centrifugation essentially led to the redeposition of the thin oil film on the pellet at the bottom as shown in Figure 3.6 (c) and (d). However, pipetting out the pellet from the bottom helped in removing the oil film completely from the pellet as shown in Figure 3.6 (c) and (e). In addition, centrifugation speed and time if increased, led to aggregation or disintegration of the GNR as has also been reported by other authors.[10] However, less centrifugation steps or low speeds were not sufficient to remove the excess CTAB from the sample which in turn crystallized. Hence the speed and time for centrifugation were followed strictly. A drop of this centrifuged sample was placed on the 200 mesh formvar protected

copper grid and allowed to dry overnight before analysis. It was observed that air drying or vacuum drying the copper grid in a clean dessicator were the best ways to dry the sample. The ARs of the particles were then calculated by measuring the length and the width of at least 300 particles at various locations across the grid.

3.4. Microfluidic Droplet Generation

Controlled synthesis without wall deposition requires the formation of isolated droplets, which break off regularly near the T-junction.[11] Microchannel inlet geometry, fluid viscosities and interfacial tension, as well as the relative flow rates of the two immiscible fluids are known to dictate the formation of droplets at the junction.[12,13] 'T-junction' as well as 'flow focusing' geometries were used for the initial prototyping experiments. These experiments indicated that the T-junction geometry was more suitable for nanocrystal synthesis, since the flow focusing geometry was prone to rapid and severe clogging at the small (<40 μm) orifices. Furthermore, 'square' T-junction geometry was chosen for further experiments, where the aqueous inlet is of the same width *w*, as the main flow channel.

Silicone oil (10 cP) was used as the continuous fluid as it wets the PDMS channel walls preferentially, and is immiscible with aqueous solutions. A dilute aqueous mixture of reagents and nanoparticle seeds formed the dispersed phase. The viscosity ratio between the continuous and dispersed phases is therefore nearly constant at ~10. The seed suspension (S) and reagent R1 contain surfactant (CTAB) above its critical micelle concentration (CMC). The presence of excess surfactant in the aqueous reagent stream rapidly reduces the interfacial tension σ, between the two immiscible fluid phases to <5 Nm^{-1}, as indicated by pendant drop tensiometry measurements.

The upper bound on total volumetric flow rate of the fluids is dictated by the pressure required to pump the silicone oil through the microchannel. Delamination and leakage of the microchannel was observed at oil flow rates, Q_O > 40 $\mu L.min^{-1}$. The maximum allowable

pressure drop is therefore estimated as ~50 kPa, by calculating the pressure drop across the device for single phase flow of oil at Q_O = 40 µL.min^{-1}, using

$$\Delta P = \frac{12\,\mu UL}{h^2\left(1 - 0.63\,{}^{h}/_{w}\right)} \tag{3.1}$$

for rectangular channels, where μ and U are viscosity and velocity of the oil, L, h and w are the channel length, height and width respectively.[14] Of course, this is only a lower bound on the two-phase pressure drop, which can be a more complicated function of droplet sizes, speeds and fluid properties. A capillary number based on the continuous phase is defined as

$$Ca = {}^{\mu_O U_O}/_{\sigma} \tag{3.2}$$

where the subscript 'O' denotes oil. The Ca in these experiments is ~0.1 and therefore both interfacial and viscous forces play a role in droplet formation at the T-junction. Interfacial tension tends to promote droplet breakup at the T-junction, whereas viscous forces exerted on the aqueous thread by the advancing oil tend to deform and stretch it downstream. When operating within the above constraints of geometry, fluids and flow rates, the flow ratio of the oil to aqueous reagent streams R = Q_O / Q_A dictates the final mode of droplet formation and its volume. (The volume of each droplet is determined by the flow ratio R and the uniformity of the drop volume is determined by the pinch-off location.)

Representative stereomicroscope images of the flow patterns obtained are shown in Figure 3.7. Droplets are formed in the *dripping* mode, where breakup of the aqueous thread occurs a small distance downstream of the T-junction, when R is below 2.5. Figure 3.7 (a) shows an example of this mode of droplet formation, with R = 1.2 (Q_O = 18 µL.min^{-1} and Q_A = 15 µL.min^{-1}). As R is reduced below 1, the breakup location starts moving further downstream of the junction. This is depicted in Figure 3.7 (b) where R = 0.88, with Q_O = 22 µL.min^{-1} and Q_A = 25 µL.min^{-1}. On the other hand, increasing R beyond 2.5 leads to a transition to the so-called *jetting* mode, where the aqueous stream begins to flow coaxially along with the oil and

the breakup event is shifted far (several thousand channel widths) downstream. This condition is shown in Figure 3.7 (c), where R = 4.16, with Q_O = 25 µL.min^{-1} and Q_A = 6 µL.min^{-1}. In the particle synthesis experiments conducted, R was maintained ~ 1. Finally, droplets flow in a stable, non-coalescing train downstream of the point of breakup, regardless of the mode of breakup, as indicated in Figure 3.7 (a), (b), and (c).

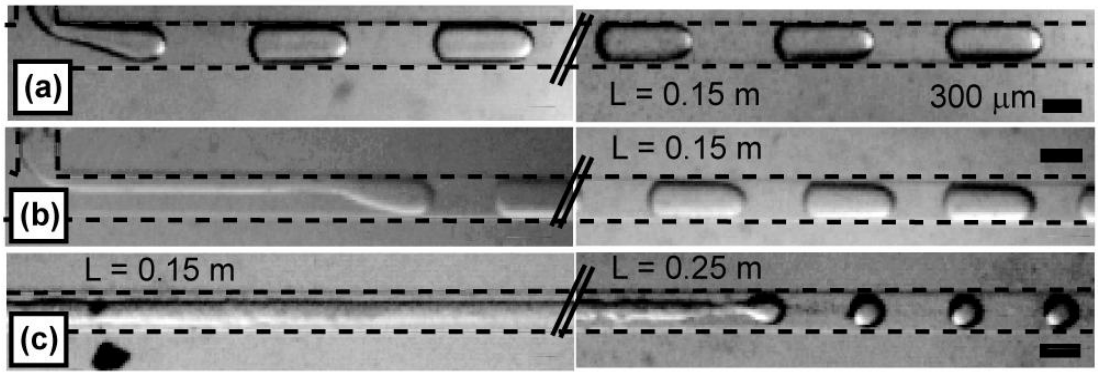

Figure 3.7. Stereomicroscope images of flow patterns observed in the microchannel under different flow conditions. **(a)** Dripping at T-junction: R = 1.2 with Q_O = 18 µL.min^{-1} and Q_A = 15 µL.min^{-1}. Breakup occurs within a downstream distance w **(b)** R = 0.88, with Q_O = 22 µL.min^{-1} and Q_A = 25 µL.min^{-1}. Breakup occurs at a downstream distance ~5w **(c)** Jetting mode of droplet formation, where a co-axial aqueous thread is formed, and breakup occurs far downstream of the T-junction. R = 4.16 with Q_O = 25 µL.min^{-1} and Q_A = 6 µL.min^{-1}. Scale bars represent w = 300 µm.

3.5. Results and Discussion

Excellent shape, size and spectral tunability were achieved by manipulating reagent concentrations in and feed rates of the individual aqueous streams entering the microfluidic device. Optical absorbance spectra and representative TEM images of nanocrystal dispersions obtained from our method are provided in Figures 3.8, 3.9 and 3.10. The obtained nanocrystal dispersions are classified into three categories, based on characteristic *shapes* of individual particles, as spherical-spheroidal (Figure 3.8), rod-shaped (Figure 3.9), and 'sharp-edged' (Figure 3.10) dispersions respectively.

Spherical gold nanoparticles exhibiting a single absorbance maximum at 520 nm, and anisotropic spheroids with an additional absorbance maximum at ~600 nm are presented in

Figure 3.8. These particles are significantly larger than the seed crystals (that are typically less than 5 nm in size), and have multiple crystalline facets. Such particles are synthesized either when there are no silver ions in reagent stream R1, or when the concentration of reducing agent (AA) in R2 is less than 1 mM or greater than 60 mM. Particle growth is prematurely terminated at low AA concentrations due to insufficient $Au^{[0]}$ supply in the droplets, while at high AA concentrations almost all the $Au^{[3+]}$ is rapidly reduced onto the nanocrystal seeds to yield nearly spherical particles.

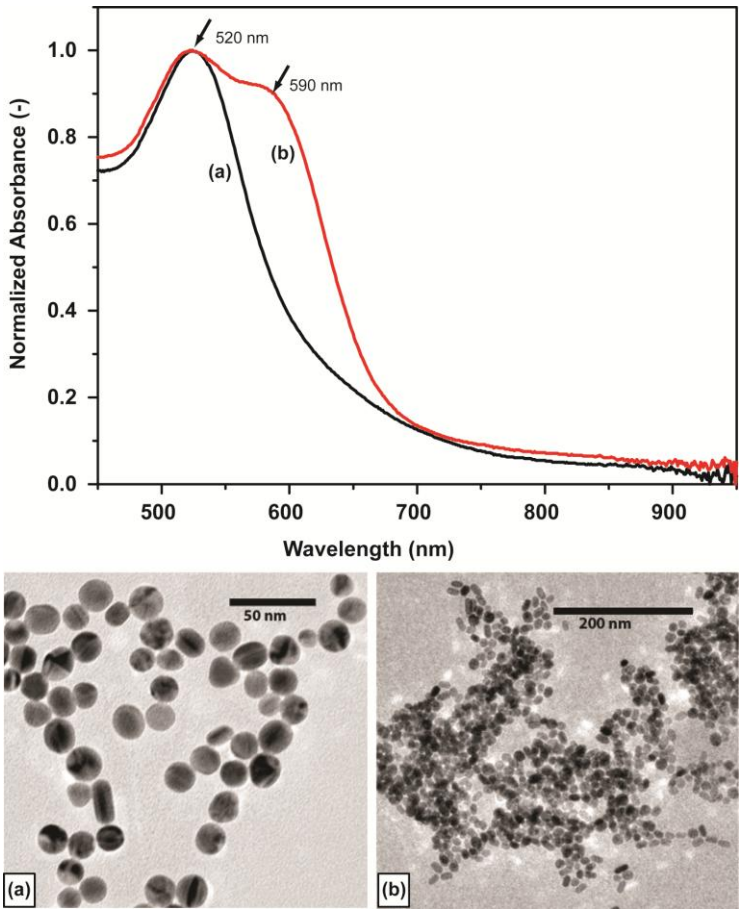

Figure 3.8. UV-vis absorbance spectra and TEM images of spherical-spheroidal particles synthesized using the droplet method. The concentrations of $Au^{[3+]}$ and CTAB in reagent R1 and ascorbic acid (AA) in reagent R2 are 0.6 mM, 126 mM and 5.2 mM respectively. The silver content in R1, and volumetric flow rates of fluid streams S, R1 and R2 are varied to yield different nanocrystal dispersions: (a) $Q_S/Q_{R1}/Q_{R2}$ = 2.5/20/2.5 μL.min^{-1}, $[Ag^{[+]}(R1)]$ = 0 mM,(b) $Q_S/Q_{R1}/Q_{R2}$ = 9/20/9 μL.min^{-1}, $[Ag^{[+]}(R1)]$ = 0.02 mM.

Rod-shaped nanocrystals with smooth rounded tips are shown in Figure 3.9, and correspond to the second broad category of particles synthesized.

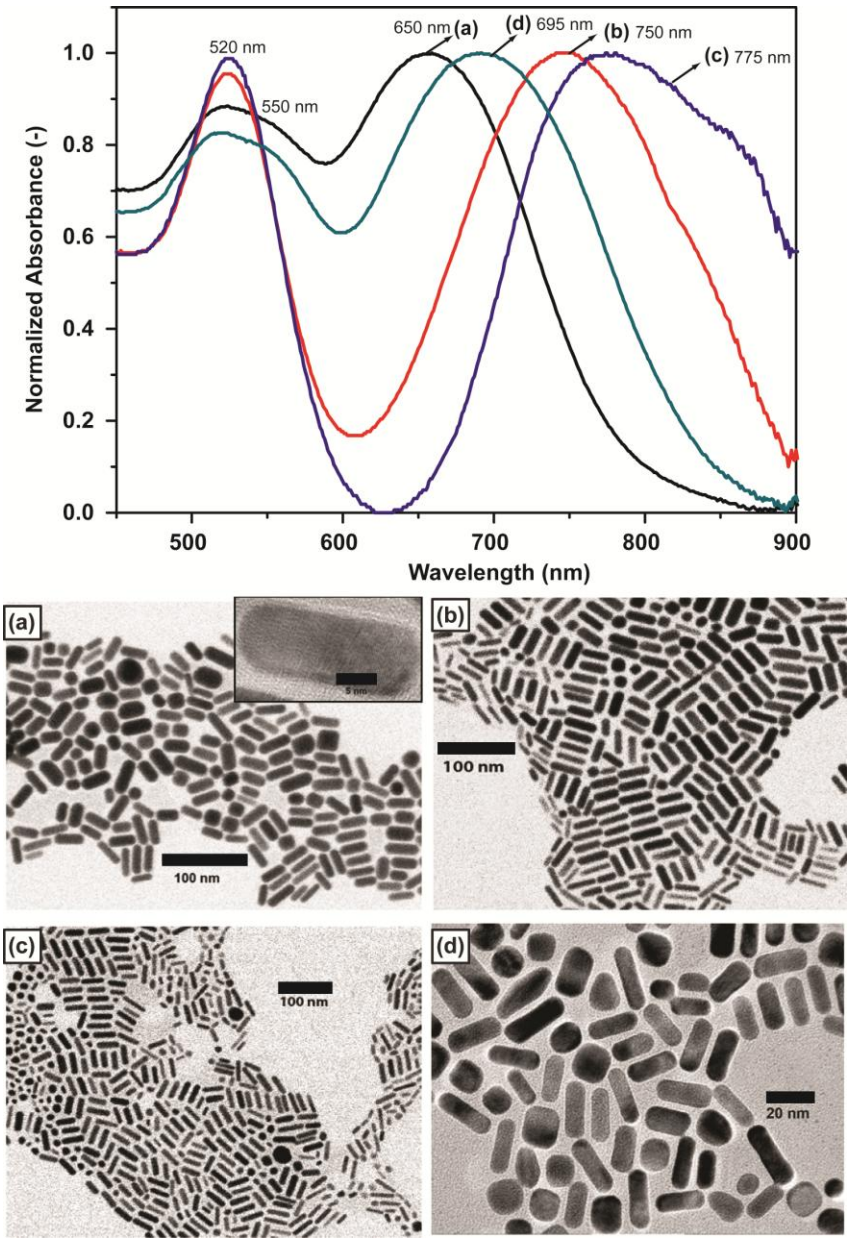

Figure 3.9. UV-vis absorbance spectra and corresponding TEM images of rod-shaped particle of varying aspect ratios: The concentrations of $Au^{[3+]}$ and CTAB in reagent R1 and ascorbic acid (AA) in reagent R2 are 0.62 mM, 123 mM and 5.2 mM respectively. The silver content in R1, and volumetric flow rates of fluid streams S, R1 and R2 are varied to yield different nanocrystal dispersions: (a) $Q_S/Q_{R1}/Q_{R2}$ = 2.6/20/2.6 µL.min^{-1}, $[Ag^{[+]}(R1))]$ = 0.05 mM, (b) $Q_S/Q_{R1}/Q_{R2}$ = 2.6/20/2.6 µL.min^{-1}, $[Ag^{[+]}(R1)]$ = 0.07 mM, (c) $Q_S/QR_1/Q_{R2}$ = 2.6/20/2.6 µL.min^{-1}, $[Ag^{[+]}(R1)]$ = 0.1 mM, (d) $Q_S/Q_{R1}/Q_{R2}$ = 9/20/9 µL.min^{-1}, $[Ag^{[+]}(R1)]$ = 0.1 mM. The corresponding aspect ratios are 2.3±0.5, 3.2±0.5, 4±0.5, 2.7±0.3 respectively.

All absorbance spectra exhibit two resonance maxima. The first of the two peaks at 520 nm corresponds to TPR of anisotropic particles and the single plasmon resonance of nearly isotropic spherical particles. The second peak, usually obtained between 550 nm to near-IR wavelengths (~1200 nm) represents the LPR of anisotropic particles. A comparison of the LPR and TPR peak intensities and wavelengths provides a qualitative idea of the particle morphology and AR, while the breadth of the peak determines polydispersity in particle population.[15] The wavelength of the LPR peak is known to red shift with an increase in the AR. The ARs of the rod-shaped nanocrystals was varied by gradual variations of $Ag^{[+]}$ concentration in R1. The LPR maxima thus obtained at different conditions range from the small shoulder exhibited at 610 nm by spheroids (Figure 3.8 (b)), to peaks at 650, 690 and 790 nm with particle ARs between ~2 and 4 (Figure 3.9 (a) – (d)). The optical resonances of the rod-shaped dispersions can therefore be tuned across a substantial wavelength range (~200 nm) with the microfluidic method.

Finally, in the third category, a miscellany of peculiarly shaped particles, all of which share the common characteristic of terminating in sharp, acute-angled edges were synthesized. The predominant particle shape in this case, obtained in high yield, were the sharp-tipped 'dog-bone' structure previously reported by Guo and Murphy.[16] Such particles are obtained when working at relatively high $Ag^{[+]}$ (>0.07 mM) and AA concentrations (>10 mM) in R1 and R2 respectively. Other shapes synthesized include cubes, tetrapods and four-edged stars, as seen in Figure 3.10. Such nanoparticle shapes have been reported in previous investigations on shape control of gold nanoparticles, although the methods used were exclusively based on small-scale batch synthesis.[16-18] The above observations highlight the crucial role played by $Ag^{[+]}$ and reducing agent concentration in the formation of anisotropic nanocrystals, and echo the results reported by several groups.[8,9,17,19] A table containing the list of operational parameters used to achieve the growth of the various sizes and shapes of the nanocrystal dispersions is provided in Appendix C.

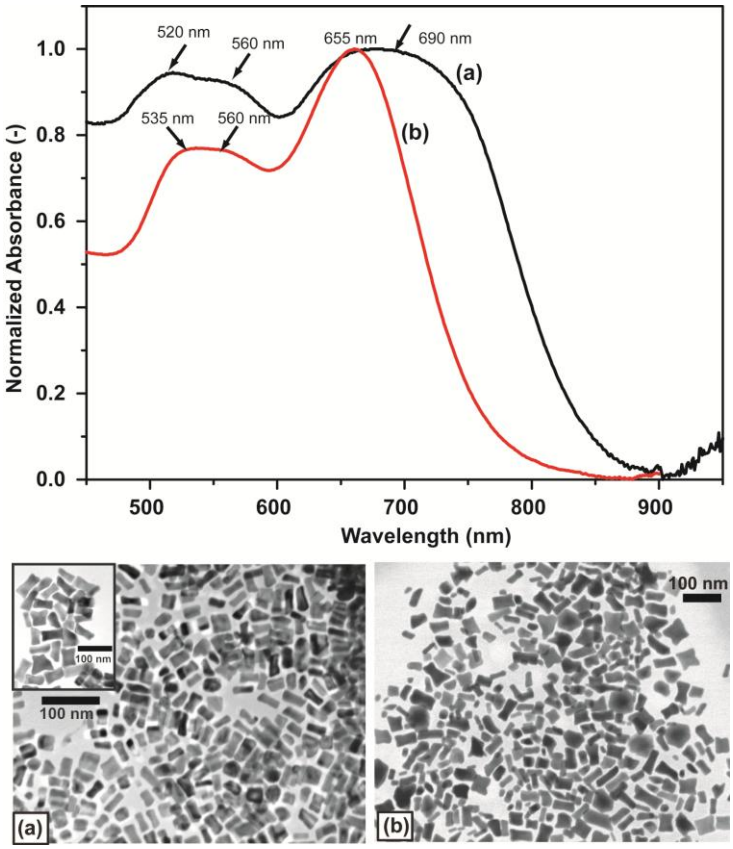

Figure 3.10. UV-vis absorbance spectra and representative TEM images of extended, sharp-edged gold nanoparticles: The concentrations of $Au^{[3+]}$ and CTAB and $Ag^{[+]}$ in reagent R1 are 0.6 mM, 123 mM and 0.08 mM respectively. The concentration of AA in reagent R2, and volumetric flow rates of fluid streams S, R1 and R2 are varied to yield different nanocrystal dispersions: (a) $Q_S/Q_{R1}/Q_{R2}$ = 10/10/10 μL.min^{-1}, [AA] = 40 mM, ~90% of the particle population consists of extended dog-bones and (b) $Q_S/Q_{R1}/Q_{R2}$ = 2.6/8/2.6 μL.min^{-1}, [AA] = 10 mM, where cubes, stars and tetrapods are also observed in addition to dog-bones.

The microfluidic device can be operated for over 12 hrs without any wall deposition or blockage of microchannel cross-section. Multiple samples collected from the device for the same synthesis conditions have nearly overlapping UV-vis spectra (Figure 3.11 (a)), thus underscoring the robustness of the method. The quality of pre-synthesized seeds is an important factor governing reproducibility between different experiments, as also asserted previously by several authors.[8,17,20-25] Hence, for example, dispersions synthesized from the *same* batch of seeds in *different* reactors at the same reagent conditions show overlapping spectra (Figure 3.11 (b)).

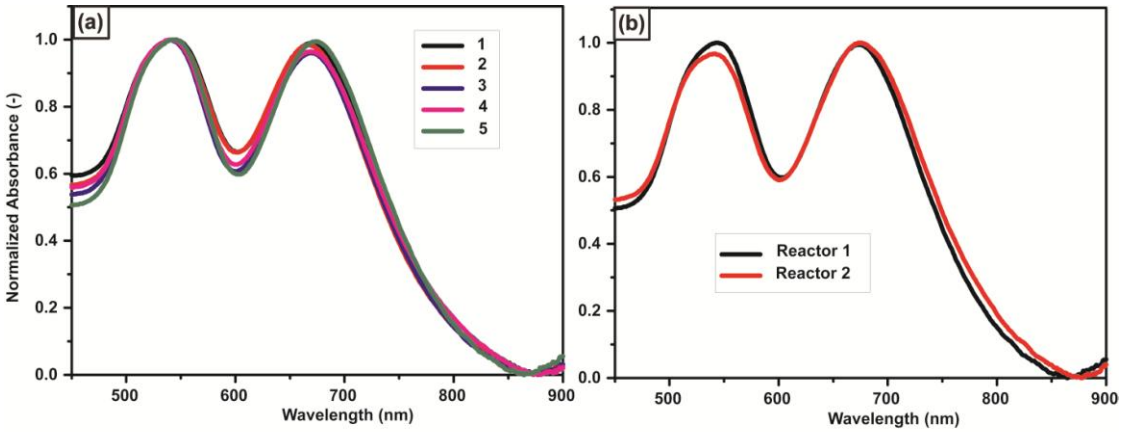

Figure 3.11. UV-visible absorbance spectra of (a) Multiple samples collected from the same device for the same synthesis conditions over a period of 6 hrs. (b) Nanocrystal dispersions synthesized from the same batch of seeds in different reactors at the same reagent conditions. (a) and (b) The concentrations of $Au^{[3+]}$, $Ag^{[+]}$ and CTAB in reagent R1 and AA in reagent R2 are 0.6 mM, 0.12 mM, 121 mM and 5.2 mM respectively. The volumetric flow rates of the fluid streams S, R1 and R2 for all samples collected is $Q_S/Q_{R1}/Q_{R2}$ = 9/20/9 µL.min^{-1}. The ratio of oil to aqueous flow rate R = Q_O/Q_A is ~1 in all cases.

Future versions of the method will incorporate online seed synthesis, to overcome seed variability issues and ensure uniform product quality. Also, strictly speaking, the current method must be classified as *semi-batch*. Control over the initial reagent contacting and mixing is achieved by forming small droplets that spend between 5-90 s in the microchannel. The droplets are subsequently collected in a sampling reservoir where the nanocrystal dispersion is aged for several hours to ensure completion of particle growth. Nevertheless, the method still enables solid control over the *initial* (early stage) reagent contacting, mixing and growth, which usually determines the quality of the final product. Contacting between reagents and particles of different ages during sample collection may also broaden the final size distribution in the present method. To overcome this limitation, devices with extended on-chip particle residence times of several minutes can be used by simply increasing the overall device length, while still operating below the threshold pressure drop for leakage.

In the microfluidic method, chemical reactions occur within drops translating through a silicone oil carrier fluid. Each drop is equivalent to an intensely stirred picoliter ‘flask’ with moving liquid (oil) walls. The high rates of shear within this confined reaction flask (>100 s^{-1}),

in conjunction with high surface-to-volume ratios, can profoundly influence particle growth and therefore yield very different results compared to macroscale batch methods.

3.6. Summary

A droplet-based microfluidic method for the preparation of anisotropic gold nanocrystal dispersions, where gold nanoparticle seeds and growth reagents are dispensed into monodispersed picoliter droplets within a microchannel is presented. Nanocrystals of various shapes are successfully prepared and the tunability of optical resonances of the synthesized dispersions is demonstrated. Moreover, wet-chemical synthesis protocols for several different metal nanocrystals contain the same basic set of ingredients, viz. metal precursor, reducing agent, surfactant, etc., and hence the method is generally applicable to a broad class of metallic nanocrystal dispersions. The method is therefore a first step towards realizing tunable and reproducible microfluidic methods for shape-tailored metallic nanocrystal synthesis.

3.7. References

1 Song, H., Tice, J. D. & Ismagilov, R. F. A Microfluidic System for Controlling Reaction Networks in Time. *Angewandte Chemie - International Edition* **42**, 768-772 (2003).

2 Shestopalov, I., Tice, J. D. & Ismagilov, R. F. Multi-Step Synthesis of Nanoparticles Performed on Millisecond Time Scale in a Microfluidic Droplet-Based System. *Lab on a Chip* **4**, 316-321 (2004).

3 Christopher, G. F. & Anna, S. L. Microfluidic Methods for Generating Continuous Droplet Streams. *Journal of Physics D : Applied Physics* **40**, R319–R336 (2007).

4 Dreyfus, R., Tabeling, P. & Willaime, H. Ordered and Disordered Patterns in Two-Phase Flows in Microchannels. *Physical Review Letters* **90**, 144505-144501- 144504 (2003).

5 Anna, S. L. & Mayer, H. C. Microscale Tipstreaming in a Microfluidic Flow Focusing Device. *Physics of Fluids* **18**, 121512 (2006).

6 Garstecki, P., Fuerstman, M. J., Stone, H. A. & Whitesides, G. M. Formation of Droplets and Bubbles in a Microfluidic T-Junction—Scaling and Mechanism of Break-Up. *Lab on a Chip* **6**, 437–446 (2006).

7 Bringer, M. R., Gerdts, C. J., Song, H., Tice, J. D. & Ismagilov, R. F. Microfluidic Systems for Chemical Kinetics that Rely on Chaotic Mixing in Droplets. *Philosophical Transactions of the Royal Society of London A* **362**, 1087–1104 (2004).

8 Nikoobakht, B. & El-Sayed, M. A. Preparation and Growth Mechanism of Gold Nanorods (NRs) Using Seed-Mediated Growth Method. *Chemistry of Materials* **15**, 1957-1962 (2003).

9 Liu, M. & Guyot-Sionnest, P. Mechanism of Silver(I)-Assisted Growth of Gold Nanorods and Bipyramids. *Journal of Physical Chemistry B* **109**, 22192-22200 (2005).

10 Gole, A., Orendorff, C. J. & Murphy, C. J. Immobilization of Gold Nanorods onto Acid-Terminated Self-Assembled Monolayers via Electrostatic Interactions. *Langmuir* **20**, 7117-7122 (2004).

11 Chen, D. L., Li, L., Reyes, S., Adamson, D. N. & Ismagilov, R. F. Using Three-Phase Flow of Immiscible Liquids to Prevent Coalescence of Droplets in Microfluidic Channels: Criteria to Identify the Third Liquid and Validation with Protein Crystallization. *Langmuir* **23**, 2255-2260 (2007).

12 Günther, A. & Jensen, K. F. Multiphase Microfluidics: from Flow Characteristics to Chemical and Materials Synthesis. *Lab on a Chip* **6**, 1487-1503 (2006).

13 DeMenech, M., Garstecki, P., Jousse, F. & Stone, H. A. Transition from Squeezing to Dripping in a Microfluidic T-Shaped Junction. *Journal of Fluid Mechanics* **595**, 141-161 (2008).

14 Bruus, H. *Theoretical Microfluidics*. (Oxford University Press 2007).

15 Zhu, J. *et al.* Shape Dependent Resonance Light Scattering Properties of Gold Nanorods. *Materials Science and Engineering B* **121**, 199–203 (2005).

16 Gou, L. & Murphy, C. J. Fine-Tuning the Shape of Gold Nanorods. *Chemistry of Materials* **17**, 3668-3672 (2005).

17 Sau, T. K. & Murphy, C. J. Room Temperature, High-Yield Synthesis of Multiple Shapes of Gold Nanoparticles in Aqueous Solution. *Journal of the American Chemical Society* **126**, 8648-8649 (2004).

18 Jana, N. R. Gram-Scale Synthesis of Soluble, Near-Monodisperse Gold Nanorods and Other Anisotropic Nanoparticles. *Small* **1**, 875-882 (2005).

19 Jana, N. R., Gearheart, L. & Murphy, C. J. Seed-Mediated Growth Approach for Shape-Controlled Synthesis of Spheroidal and Rod-Like Gold Nanoparticles using a Surfactant Template. *Advanced Materials* **13**, 1389-1393 (2001).

20 Murphy, C. J. *et al.* Anisotropic Metal Nanoparticles: Synthesis, Assembly, and Optical Applications. *Journal of Physical Chemistry B* **109**, 13857-13870 (2005).

21 Ṕerez-Juste, J., Pastoriza-Santos, I., Liz-Marz´an, L. M. & Mulvaney, P. Gold Nanorods: Synthesis, Characterization and Applications. *Coordination Chemistry Reviews* **249**, 1870–1901 (2005).

22 Sun, X., Dong, S. & Wang, E. Large-Scale Synthesis of Micrometer-Scale Single-Crystalline Au Plates of Nanometer Thickness by a Wet-Chemical Route. *Angewandte Chemie - International Edition* **43**, 6360-6363 (2004).

23 Chen, S., Wang, Z. L., Ballato, J., Foulger, S. H. & Carroll, D. L. Monopod, Bipod, Tripod, and Tetrapod Gold Nanocrystals *Journal of the American Chemical Society* **125**, 16186 -16187 (2003).

24 Jana, N. R., Gearheart, L. & Murphy C. J. Seeding Growth for Size Control of 5-40 nm Diameter Gold Nanoparticles. *Langmuir* **17**, 6782-6786 (2001).

25 Oldenburg, S. J., Averitt, R. D., Westcott, S. L. & Halas, N. J. Nanoengineering of Optical Resonances. *Chemical Physics Letters* **288**, 243–247 (1998).

4. Microfluidic Synthesis of Nanoparticle Seeds Using 'Fast' Reducing Agents

This chapter deals with the synthesis of small gold nanocrystals of dimension 3-5 nm which can subsequently be used as nucleating agents or seeds for controlled growth of nanoparticles of varying shapes, morphology and of dimensions >20 nm. The main objective of this work is to overcome the disadvantages of using pre-synthesized seeds as outlined in the previous chapter and to enable eventual development of a fully integrated process. These seeds are synthesized using the fast reducing agent sodium borohydride ($NaBH_4$) (in the presence of excess surfactant CTAB) to reduce the gold salt ($HAuCl_4.3H_2O$). Microfluidic strategies to synthesise seeds are analyzed and described in detail in this chapter.

4.1. Detailed Background

Several different methods of syntheses have been adopted for the production of monodisperse gold nanoparticles described in detail in Chapter 2. Most researchers begin with $Au^{[3+]}$ and have synthesized a range of particle sizes and morphology using several reducing agents (discussed in Section 1.4.6). However, as the size of the particles increases beyond 30 nm, the polydispersity in the particle distribution tends to increase. None of the synthesis methods that produce particles of size greater than 50 nm by the direct reduction of salt are successful in achieving monodisperse particles.[1] Hence the seeded-growth method is often used for the synthesis of particles of wide ranges of sizes and shapes. Seed mediated growth of nanomaterials was first introduced by Zsigmondy in 1906[2] when he combined Faraday's sol[3] with his own synthesis protocol to "procure solutions of particles of almost any desired size".[4] He called this method the "nuclear method" of particle growth which was later rediscovered by Michel and Schwartz for the synthesis of bimetallic palladium gold particles.[5] The method was renamed as the "seed or germ method" of particle growth and has ever since been used in the synthesis of monodisperse particles of metal oxides and metallic non-oxides.[6-9]

4.1.1. Seeded-Growth Mechanism

The seeded or germ growth process is a multistep process, with the synthesis of small to medium sized monodisperse particles (3 nm to 25 nm) of a required shape being the first step. These particles are subsequently used as nucleation centres or seeds along with appropriate amounts of precursor ions and reducing agent in the next step which is the growth step. There can be any number of growth steps depending on the final particle size required. The reducing agent used in the second and subsequent steps is typically a weak reducing agent, which reduces the precursor ions adsorbed onto the seed surface rather than causing new nucleation. The seeds hence act as the catalytic sites for reduction of the adsorbed precursors in the growth step. The size of the seeds and the molar amount of precursor ions added in the later steps determine the size of the obtained particle population (d) and can be calculated from

$$d = d_0 \sqrt[s]{\frac{n_i + n_m}{n_m}} \tag{4.1}$$

where d_0 is the diameter of the seed, n_i and n_m are the quantity of the ionic and metallic salt respectively.[10] The size of seeds to be synthesized can hence be estimated from the desired final particle size through this equation. Iterative seeding where particles grown in the previous step are used as seeds in the next step is usually the preferred route to obtain monodisperse particle population of large sizes. This method is consistent, reproducible and can be used to predict the particle sizes a priori. This process helps in completely isolating the nucleation phase from the growth phase thus preventing concurrent nucleation and growth steps and hence polydisperse particle population.

4.1.2. Synthetic Approaches and Challenges

As already mentioned, the final size of the particles depends on the seed size and precursor ion concentration. Isotropic or anisotropic particle growth is determined by two main components viz. the differential reduction rates at different sites on the seeds and the diffusion

of precursor ions to the seeds. It has been well established that the seed size, its nature (twinned, presence of crystalline faces) and shape determine the morphology of the particles formed in the next step (2.1) and considerable research has been conducted to better understand these effects. Abundant literature exists on the seeded growth of nanoparticles, specifically gold. A selected few are cited in the following paragraph to show the possibility of synthesizing varying shapes and sizes of particles by the seeded growth approach.

Brown *et al.* use 2.6 nm and 12 nm citrate and hydroxyl amine capped spherical seeds and grow them to a range of sizes from 20 to 100 nm.[1] They study the effect of capping agent on the seeds and conclude that 12 nm citrate capped seeds lead to better particle dispersity and properties than the direct method or the 2.6 nm seeded method while the hydroxyl amine capped seeds lead to the formation of rods along with spherical particles.[1] El-Sayed *et al.*, Murphy *et al.*, Liz-Marzàn and Mulvaney *et al.* have extensively studied the use of surfactant capped (CTAB) and citrate capped spherical gold nanoparticles for the synthesis of gold spheres and nanorods.[6,7,11,12] The results from these studies are as follows: the smaller the seed size, the higher the yield as well as the possibility of AR variation; the AR of the GNR synthesized varies linearly with the size of the seed; and that the surfactant stabilized seeds have better yield of GNR than the citrate or phosphonium stabilized seeds, because of the differential interactions between the different surface groups on the seeds with the growth solution. Growth of branched and anisotropic shapes such as dodecahedra, bipyramids, hexagons, stars, cubes and flowers have also been possible using the seeded growth approach by varying the seed size, shape and capping agent and also modifying the type of precursor solutions used in the growth step. Gou and Murphy[13] use short nanorods grown from spherical seeds, as seeds for subsequent growth into dogbone shaped particles. On the other hand, Kuo and Huang[14], Yuan *et al.*[15] and Kumar *et al.*[16] use spherical seeds with step-wise addition of ionic precursor along with sodium dodecyl sulfate (SDS) as the stabilizer and no stabilizer in other cases, ascorbic acid, ammonium hydroxide and poly (vinylpyrrolidone) (PVP) in N,N-

dimethylformamide as reducing agent to form branched (bipod, tripod, tetrapod like), thorny and star-shaped particles respectively.

Synthesis of monodisperse particle population of sizes >30 nm in essence requires spherical seeds, to be as small as possible (3–5 nm), and these seeds can then be grown to any required shape and size using appropriate precursor ions and stabilizers. 3-5 nm particles are generally prepared using very strong reducing agents such as sodium borohydride (referred to as $NaBH_4$ hereafter), tetrakis (hydroxymethyl) phosphonium chloride, phosphorous etc.[17] The presynthesized spherical, CTAB capped gold nanoparticles that are used as seeds for growth into GNR (used in the previous chapter) are synthesized using $NaBH_4$ as the reducing agent. As described earlier (1.4.5.1), an increase in ΔE signifies spontaneous reaction, leading to larger number of nuclei than growth and hence smaller sized metallic nanocrystals. Since $Au^{[3+]}$ (E_0 = + 1.68 V) is highly electropositive, $NaBH_4$ can act as a very fast reducing agent even at ambient conditions.

$NaBH_4$ in aqueous solutions liberates hydrogen gas to form borates according to the reaction

$$NaBH_4 + 2H_2O \rightarrow NaBO_2 + 4H_2 \quad (4.2)$$

The hydrolysis reaction is not feasible at temperatures below 0°C, extremely slow at pH 12 and higher, and self-inhibiting due to the rise of pH as hydrogen is evolved.[18] Hence the aqueous solution of $NaBH_4$ needs to be freshly prepared with the hydrogen released regularly, while maintaining the solution ice-cold till addition into the reaction vessel. Due to the fast kinetics involved in the reduction reaction of $NaBH_4$ and $HAuCl_4$,[19,20] the disadvantages of synthesis in small scale batches, especially the dependence of the final product monodispersity and morphology on the mode of reagent dispensing and the efficiency of mixing, is significant. Alternative strategies for such reactions are essential since the final product population typically depends on the quality, morphology and polydispersity of these seeds. The

difficulties involved in the synthesis in a microfluidic setup and the methods adopted to overcome these are described in detail in the following sections.

4.2. Microfluidic Techniques

The main challenge in synthesizing gold nanoparticles using $NaBH_4$ as the reducing agent in a microfluidic setup is to vent the hydrogen released from the hydrolysis reaction by keeping the aqueous $NaBH_4$ solution ice cold and by minimizing bubbles in the reactor. Gas bubbles within the microchannels disrupt the flow leading to uncontrolled reaction and also clogging. The formation of bubbles can be reduced either by modifying the aqueous chemistry or the liberated bubbles can be removed from the channels by mechanical or chemical stimuli. For example, Shalom *et al.* used $NaBH_4$ as fast reducing agent for the synthesis of thiol functionalized gold nanomaterials using microfluidic methods (2.4.4).[21] They report the disruption of flow due to the bubbles liberated from aqueous $NaBH_4$ and modify the aqueous solution of $NaBH_4$ chemically using isopropanol and sodium hydroxide. The GNR synthesis experiment described in Chapter 2 (2.2.8) was repeated with chemically modified $NaBH_4$. The protocol used was exactly the same except for the $NaBH_4$ solution used, which was prepared as follows: A stock solution was prepared by adding 0.038 g of $NaBH_4$ to 30 mL of 1 M NaOH and 70 mL of DI water. 3 mL of this stock solution was then mixed with a solution containing 0.1 g of $NaBH_4$ in 30 mL of iso-propanol.[21] The UV-vis absorption spectra of the seed sample along with the particles synthesized using the GNR synthesis protocol is shown in the Figure 4.1 (a). The spectra of the samples synthesized using the seeds prepared from modified $NaBH_4$ solution (labelled (c), (d)) and unmodified $NaBH_4$ solution ((c1), (d1)) are shown in Figure 4.1 (b). The silver ion contents in these samples were 0.08 mM and 0.1 mM respectively and the corresponding TEM images of the samples from the modified $NaBH_4$ solution experimental set are shown in Figure 4.1 (c) and (d).

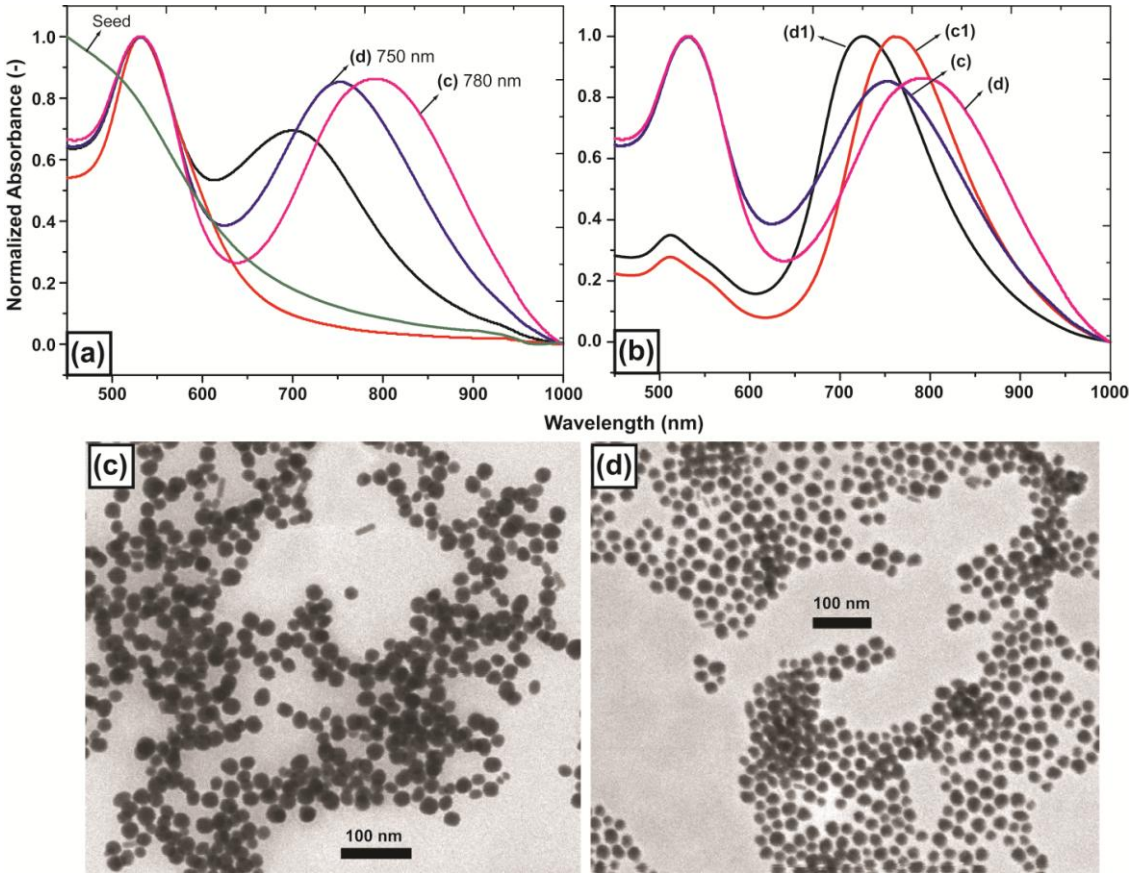

Figure 4.1. UV-Vis absorbance spectra of **(a)** GNR synthesized using chemically modified $NaBH_4$ solution **(b)** Comparison of the spectra of GNR samples synthesized using seeds prepared from (c) and (d) chemically modified $NaBH_4$ solution and (c1) and (d1) unmodified $NaBH_4$ solution. TEM images of GNR samples synthesized using chemically modified $NaBH_4$ solution with silver ion content **(c)** 0.08 mM and **(d)** 0.1 mM.[21]

The spectrum of the seeds synthesized using the chemically modified $NaBH_4$ solution (labelled Seed) does not show any prominent resonance peak which is characteristic of very small (<5 nm) nanoparticles. However, the spectra of all the samples synthesized using these seeds show higher TPR peak absorbance than LPR peak absorbance, signifying comparatively higher concentration of spherical particles rather than the expected GNR which is also confirmed by the TEM images (Figure 4.1 (c) and (d)), in which the concentration of GNR is low (~1%). However the concentration of GNR in the case of samples prepared from seeds obtained from unmodified $NaBH_4$ solution shown in Figure 2.6 (c) (Chapter 2) is high (~99%). A recent study shows that the remnant $NaBH_4$ in the seed solution also has a significant role in the formation of GNR.[22] Hence, we believe that the variations in the GNR sample is due to the

chemical modification of the $NaBH_4$ solution and the presence of remnant NaOH and isopropyl alcohol in the solution, affecting the GNR growth.

The strategy will hence be to use $NaBH_4$ solution without any chemical modification and to remove the bubbles from the reactor by appropriate techniques. Preliminary experiments with single phase flows in PDMS microreactors highlighted the two main disadvantages (see Section 4.4.1): (a) uncontrolled deposition on channel walls and (b) bubbles formed adhere to the walls of the reactor and grow, disrupting the flow and affecting reaction kinetics. Moreover, droplet microfluidics also cannot be used for the synthesis because of the uncontrolled out gassing of the aqueous $NaBH_4$ solution.

Segmented gas-liquid flows have been successfully used to accomplish the synthesis of gold nanocrystal seeds in this chapter. The gas bubbles in segmented gas-liquid flows provide a "head-space" for the dissolved hydrogen (released from the aqueous $NaBH_4$ solution) to escape into, due to the partial pressure gradients. This concept is similar to several practical scenarios such as the release of dissolved gas from carbonated drinks, champagne or beer, the decompression method followed by deep sea divers etc. The decompression theory for example, is used by deep sea divers where slow ascent along with decompression stops at different depths in the water column. This prevents the release of dissolved nitrogen (that was taken up by the tissues during descent due to the increased pressures underwater) in the tissues thus minimizing the growth of the nitrogen bubbles in the blood stream.[23,24] According to the theory, if the pressure of the dissolved nitrogen in the tissues surrounding the bubble is greater than the partial pressure of the nitrogen within the bubble (P_B), then the bubble will grow in size. Hence appropriate gas mixtures and 'deep sea stops' while ascending (at elevated ambient pressures) are necessary to increase P_B thereby encouraging bubble out gassing into tissues rather than bubble growth, hence eliminating decompression sickness due to bubbles.

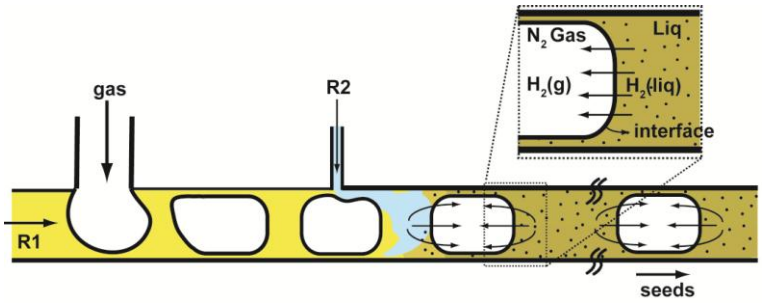

Figure 4.2. Schematic of the concept of segmented gas-liquid flow where nitrogen bubbles are dispensed into a continuous aqueous solution (R1). An aqueous solution of $NaBH_4$ (R2) is delivered through inlet R2 and rapidly mixed with R1. The inset schematically depicts hydrogen transport across the gas-liquid interface.

In the current work, an analogous principle is put to work wherein segmented gas-liquid flows are used to deliberately introduce inert gas bubbles into the aqueous reaction mixture containing $NaBH_4$, to prevent the nucleation of hydrogen bubbles and to encourage out gassing of dissolved hydrogen into the introduced bubbles. The gas forming the bubbles is chosen such that the partial pressure of hydrogen in the bubble is lower than that in the liquid surrounding it. The schematic of this concept is shown in Figure 4.2 where pure nitrogen gas is introduced through the T-junction inlet labelled 'gas'. The nitrogen bubbles are dispensed into the continuous aqueous solution of CTAB and $HAuCl_4$ (labelled R1). An aqueous solution of $NaBH_4$ is delivered through inlet R2 and the liberated hydrogen escapes into the gas bubbles which act as a gaseous head-space.

4.3. Experimental

4.3.1. Materials

Sodium borohydride (98%), hydrogen tetrachloroaurate(III) trihydrate ($HAuCl_4.3H_2O$) (99.99%) and hexadecyltrimethyl ammonium bromide (99%) (CTAB) were purchased from Sigma-Aldrich Co. Ltd., Singapore.

4.3.2. Microfabrication

The microchannels were moulded in poly (dimethyl siloxane) (PDMS), from master patterns fabricated on silicon wafers by photolithography on a negative photoresist (SU-8 2050). The channels have rectangular cross-section and were 300 μm wide, ~120 μm deep and 0.4 m long. Details of the fabrication of the master are provided in Appendix B while the actual channel design is shown in Figure 4.3. Moulded channel patterns were sealed to glass slides pre-coated with a thin layer of cured PDMS after a 35 s air plasma treatment. The width of the CTAB and $HAuCl_4$ mixture, gas and $NaBH_4$ inlet channels were 300 μm, 300 μm and 150 μm respectively.

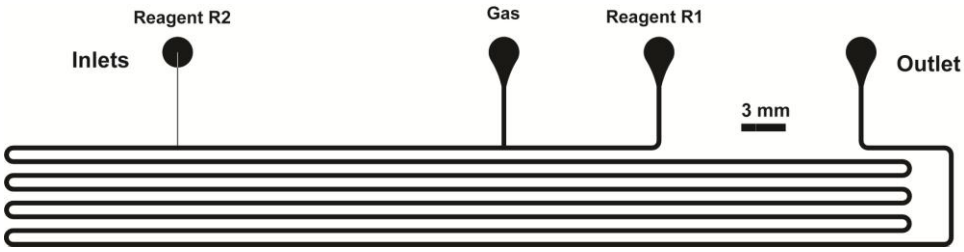

Figure 4.3. AutoCAD drawing of the microchannel.

4.3.3. Reactor Setup and Operation

The schematic of the experimental setup is shown in Figure 4.4. Aqueous mixture of CTAB (7.5 mL of 100 mM) and $HAuCl_4.3H_2O$ (0.25 mL of 10 mM) (Reagent R1), and aqueous $NaBH_4$ (0.01 M) (Reagent R2) were delivered by separate syringe pumps (Harvard, PHD 2000) into individual T-junctions while inert nitrogen gas was delivered from a cylinder equipped with a two-stage pressure regulator through circular PEEK tubings (60 μm i.d., 1 m long and 100 μm i.d., 2 m long) leading into the on-chip gas-inlet. Aqueous solution of $NaBH_4$ releases hydrogen gas which accumulates in the syringe over a period of time.

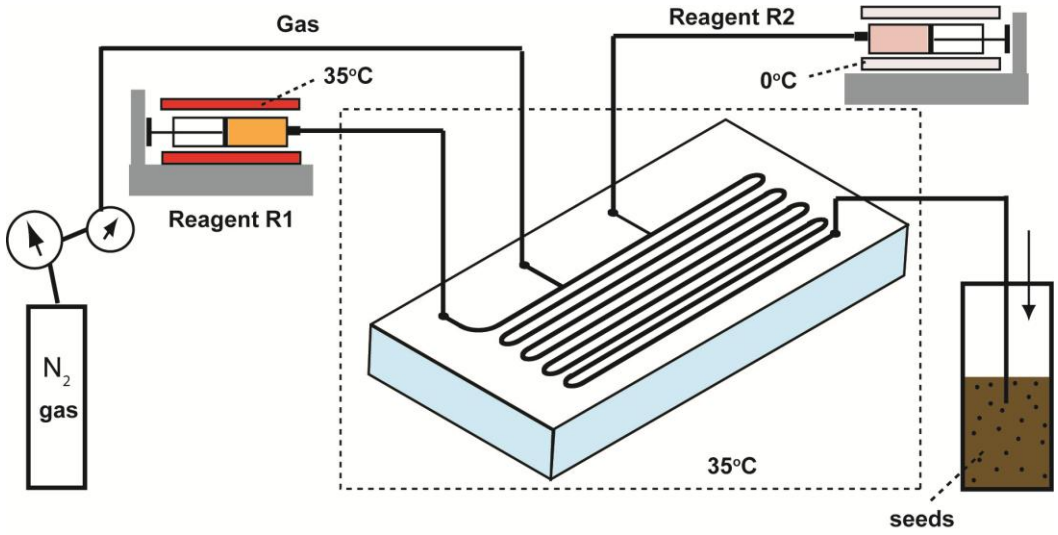

Figure 4.4. Schematic of the experimental setup.

To minimize the release of hydrogen gas and to increase its solubility in water, the temperature of the solution in the syringe was maintained at 0°C. The syringe containing the $NaBH_4$ solution was maintained ice cold by circulating ice cold water around it using a tubing as shown in Figure 4.5, a photograph of the cooling coil setup. A tygon tubing of i.d. 750 µm was used for this purpose and was wound around the syringe (Hamilton gas tight). Both the ends of the tubing were immersed inside a trough containing ice cold water, maintained at that temperature by adding ice when required. One side of the tubing was connected to a peristaltic pump (Masterflex) before being wound around the syringe. The peristaltic motion enables the pumping of ice cold water from the trough through the tubing and out through the other end thus maintaining the temperature of solution within the syringe, ice cold. The premixed solution of CTAB and gold salt was maintained at 35ºC using a heating coil wound around the syringe, similar to the setup described in Chapter 3. The entire setup (reactor along with the fittings and tubings) was immersed into a hot water bath maintained at 35ºC to prevent the crystallization of CTAB at temperatures <28ºC (details in 3.3.4). The volumetric flow rates of the mixture of aqueous salt and surfactant solution was 7.5 µL.min^{-1} while that of $NaBH_4$ was varied from 0.6 to 1 µL.min^{-1} in steps of 0.1 µL.min^{-1}. The nitrogen gas pressure was maintained at 10 psig.

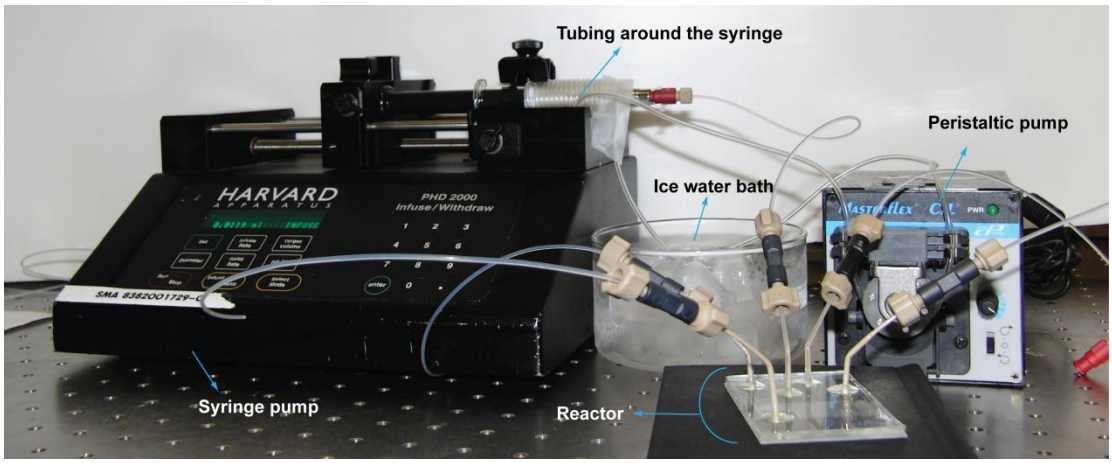

Figure 4.5. Photograph of the cooling tube wound around a syringe with ice cold water pumped through it using peristaltic pump.

The nitrogen gas supply was turned on at the required pressure before the aqueous solutions were infused through the reactor to prevent the flow of the solutions into the tubing through which the gas flows. This step needs to be followed strictly because if the aqueous solutions flow into the gas line, the flow of gas through the tubing will not be uniform and will lead to pulsatile flows in the reactor. Pulsing flow profiles are not desirable since the control over the reagent contacting and mixing is affected leading to polydisperse particles.[25] Once the gas pressure is turned on, the syringe pumps infusing the aqueous reagents were turned on at desired flow rates. The flow of reagent R1 into the reagent R2 inlet channel will lead to reaction between the reagents at the inlet and hence to particle deposition and clogging. To prevent this, the dimension of the R2 (50 μm) inlet is made 6 times narrower than the inlet R1 (300 μm), which is the minimum possible dimension for our microfabrication facility. In addition, the flow rates of the two reagents are always maintained at the desired value to prevent uncontrolled flow into the inlet channels.

4.3.4. Sample Collection and Analysis

The outlet from the reactor led to a 750 µL centrifuge tube and ~500 µL of the sample was collected for every condition. The samples were immediately analyzed using UV-vis spectrometer (Shimadzu UV-2450) and were then centrifuged to remove excess CTAB and re-dispersed in DI water. The centrifugation and re-dispersion in DI water was repeated to remove the CTAB from the solution. A drop of this sample was placed onto a 200 mesh formwar protected copper grid, allowed to dry overnight and analyzed using TEM (JEOL 2010, accelerating voltage 200 kV).

4.4. Results and Discussion

The protocol for the seed synthesis from Section 3.3.2 is as follows: nearly spherical gold nanoparticle seeds (<4 nm in size) were synthesized by adding freshly prepared ice cold sodium borohydride solution (0.6 mL of 0.01 M) to a mixture of aqueous $HAuCl_4.3H_2O$ (0.25 mL of 10 mM) and CTAB (7.5 mL of 100 mM) solution, while stirring vigorously for 2 mins. According to the stoichiometric equation Eq 4.2, 0.01 M of $NaBH_4$ (5 mL stock solution) releases 0.04 M of hydrogen. The solubility of hydrogen in water at 25ºC is ~0.8 mM (1atm. pressure).[26] The excess hydrogen is released as gas and forms bubbles in the aqueous solution.

4.4.1. Design Strategies

Single phase flow studies which involve premixing the aqueous solution of CTAB and $HAuCl_4$ and passing them through one of the reactor inlets at flow rate of 7.5 µL.min^{-1} and flowing $NaBH_4$ through the other inlet at a flow rate of 1 µL.min^{-1} were conducted. The experiments show that the uncontrolled out gassing in the aqueous $NaBH_4$ solution resulted in nucleation of bubbles that adhere to the channel walls as shown in Figure 4.6 (b) leading to flow disruption, heterogeneous particle nucleation and deposition on the channel walls as shown in Figure 4.6 (a) and eventually to clogging within an hour of experiments. Bubbles are

formed when the concentration of the dissolved hydrogen exceeds the aqueous solubility threshold leading to bubble nucleation and growth which in this case is ~ 0.8 mM.

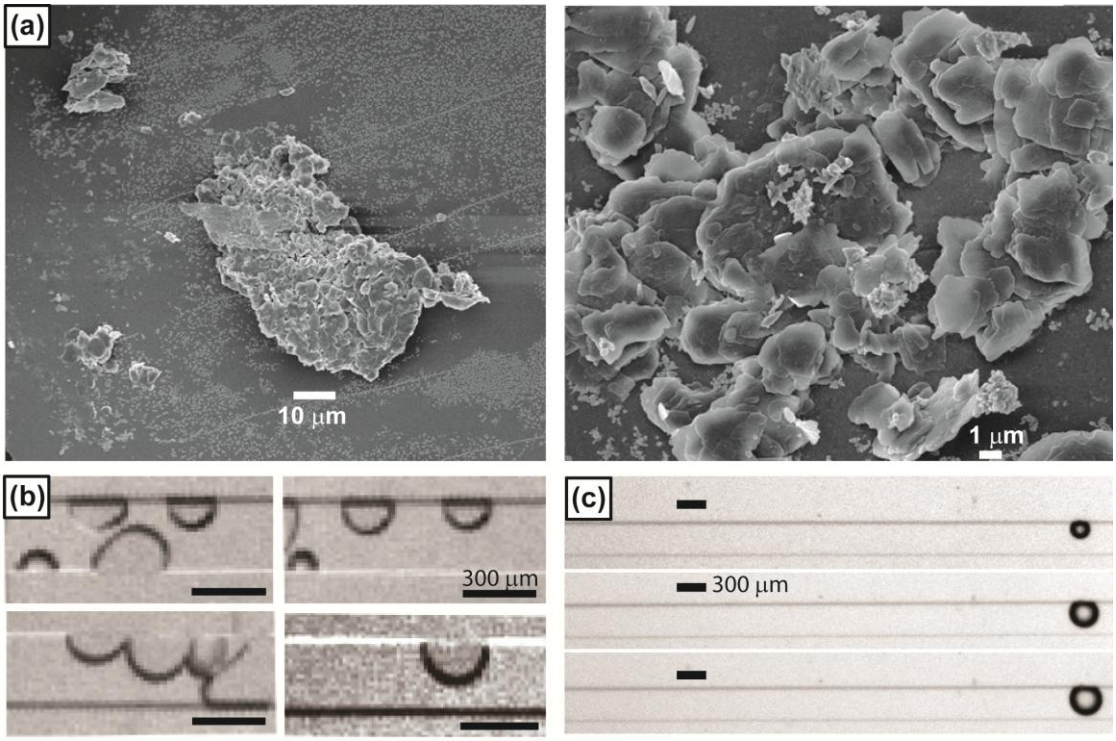

Figure 4.6. (a) Scanning electron microscope images of the reactor after 1 hour of experiment using the single phase flow method. **(b)** Stereomicroscope images of bubbles formed and adhered to the walls of the channel **(c)** Stereomicroscope images of the growth of a single bubble adhered onto the reactor wall over a period of 5 mins.

One main observation from these experiments is the growth of bubbles adhered to the channel as shown in the Figure 4.6 (c). A single bubble adhered to the channel has grown from 0.57*w* to 0.86*w* to 1.03*w*, *w* being the channel width, within five mins. Growth of the bubble shows that the gas evolved from aqueous $NaBH_4$ diffuses directly into the bubble that has already adhered to the channel wall, due to the difference in their partial pressures. This idea is used in synthesizing seeds using segmented gas-liquid flows where inert gas bubbles are deliberately introduced into the reactor so that the gas evolved from $NaBH_4$ in the form of dissolved hydrogen will diffuse into the introduced gas bubbles due to the partial pressure gradient. The gas bubble thus acts as a gas head space into which the dissolved gas diffuses. The transport rate of the gas from the aqueous phase to the gas bubble should be such that the

concentration of the gas in the aqueous phase never exceeds the aqueous solubility threshold concentration, for the above postulate to be effective in preventing bubble nucleation in the aqueous phase. As shown in Figure 4.7 (a), (b) and (c), the gas introduced into the reactor formed a series of bubbles separated by the continuous surfactant-rich aqueous phase. The reducing agent, aqueous $NaBH_4$ was introduced into the reactor through inlet R2 eventually reacts with the precursor to form seeds downstream.

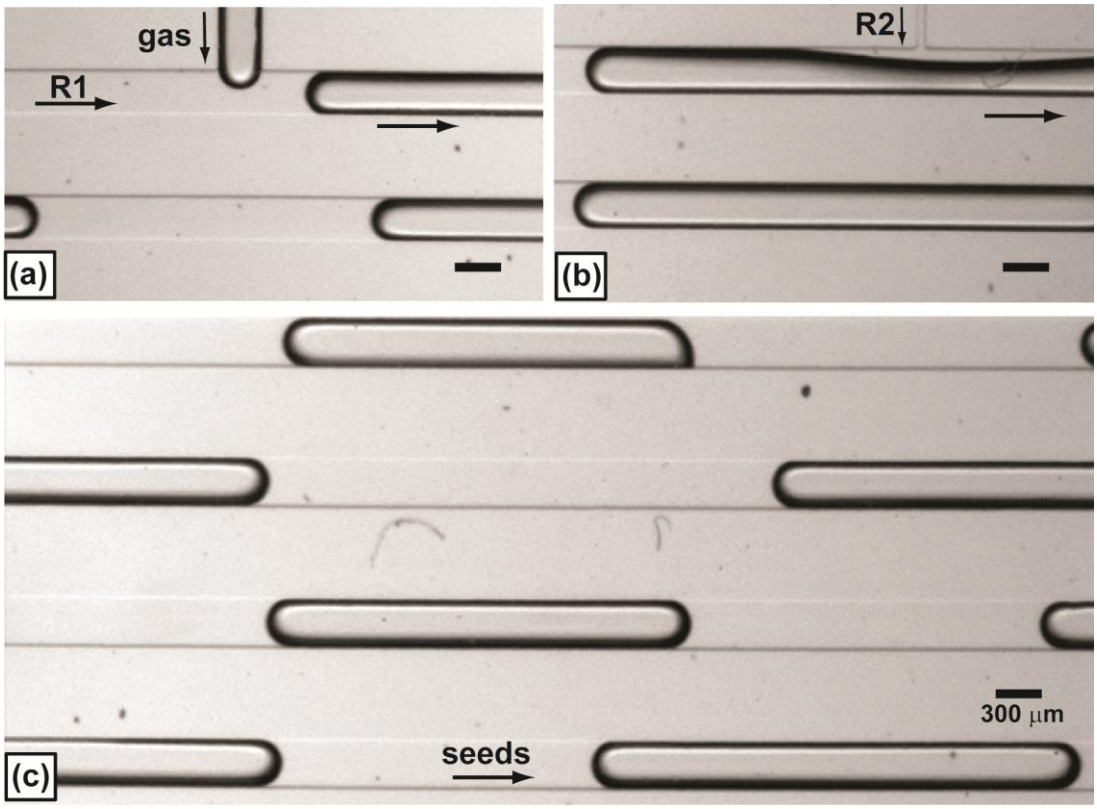

Figure 4.7. Stereomicroscope images of the flow in the reactor showing the **(a)** Gas inlet **(b)** Reducing agent inlet and **(c)** Flow downstream.

The reaction kinetics of $NaBH_4$ hydrolysis, which generates molecular hydrogen (the 'actual' reducing agent of gold ions), have been the subject of several excellent theoretical and experimental studies, and found to depend on the pH, temperature and concentration of the aqueous solution. [27-31] In the current work, the pH of the aqueous solution varies between 4.5-5.0 due to the acidic nature of $HAuCl_4$ and the kinetics may be approximated as first-order in borohydride concentration, with a rate constant k_r of ~2.5×10^{-3} s^{-1}.[18,27,30,32-34] The mass

transport of the liberated hydrogen from aqueous liquid segments to the gas bubble can now be modelled following classical treatments of reactive gas-liquid mass transfer as follows.

The mass transport flux of hydrogen across the liquid-gas interface on the liquid side can be expressed as:[35]

$$N_L = k_L\left(C_G - C_{G,i}\right) \tag{4.3}$$

Similarly, the mass transport flux on the gas side is expressed as:

$$N_G = k_G\left(p_{G,i} - p_G\right) \tag{4.4}$$

where $C_{G,i}$, C_G, $p_{G,i}$ and p_G are the interfacial and bulk concentrations and partial pressures respectively of hydrogen gas, and k_L and k_G the liquid- and gas-side mass transfer coefficients respectively. A simple system composed of a gas bubble-aqueous liquid segment pair, as indicated in Figure 4.8 is considered. An average size of ~18 *w* is used for this pair, where *w* is the microchannel width. Further, the gas bubble is assumed to be well mixed (i.e. of uniform concentration) and Henry's law for ideal gas mixtures is assumed to apply; hence $p_{G,i} = \mathcal{H}C_{G,i}$ ($\mathcal{H}$, the Henry's law constant is 1282 L.atm.mol^{-1}). Assuming a steady state mass transfer process and that $\mathcal{H}k_G \gg k_L$ (gas side mass transport rates are typically much faster than those on the liquid side due to markedly higher gas-phase diffusivities) the overall hydrogen mass transfer flux can be written as

$$N = k_L\left(C_G - \frac{p_G}{\mathcal{H}}\right) \tag{4.5}$$

Though p_G increases along the microchannel as hydrogen is transferred into the bubbles, the high value of $\mathcal{H}$ and the molar excess of nitrogen in the bubbles ensure that $C_G \gg \frac{p_G}{\mathcal{H}}$ at all conditions. Hence a simplified mass balance for hydrogen in the liquid compartment can then be written as

$$\frac{dC_G}{dt} = k_r C_{NaBH_4} - k_L a C_G \tag{4.6}$$

and likewise that for $NaBH_4$ can be written as

$$\frac{dC_B}{dt} = -k_r C_{NaBH_4} \tag{4.7}$$

where C_{NaBH_4} is the concentration of aqueous $NaBH_4$ solution, k_r the rate constant of the hydrolysis reaction and a the gas-liquid interfacial area per unit volume. The overall mass transfer coefficient at the gas-liquid interface can be approximated using the penetration theory of mass transfer as[36,37]

$$k_L a = \frac{8\sqrt{2}}{\pi L_{GL}} \sqrt{\frac{DU}{d}} \tag{4.8}$$

where D is the liquid-phase diffusion coefficient of gas ($4.5\times10\text{-}9$ $m^2.s^{-1}$)[35], U is the two-phase flow speed (~$6\times10\text{-}3$ $m.s^{-1}$, calculated from stereomicroscopic images) and d is a cross-sectional hydraulic diameter estimated to be 171 μm using $d = 2wh/(w+h)$ where h is the microchannel depth. L_{GL} is the length of the gas bubble-aqueous liquid segment pair and an average value of $L_{GL} = 18w$ is assumed for subsequent analysis. The bubbles do in fact increase in size along the channel due to the combined effect of hydrogen transfer and pressure drop, however the resulting change in L_{GL} is less than 10% of the initial value upstream and an average value suffices for our simplified analysis. The estimated value of $k_L a$ is ~ 0.26 s^{-1}.

The coupled equations Eq. 4.6 and Eq.4.7 are solved with $k_L a$ = 0.26 s^{-1}, $C_{NaBH_4}(t = 0)$ = 0.01M and C_G $(t = 0)$ = 0 M for a period of 150 s with and without mass transport across the gas-liquid interface, and the resulting concentration versus time profiles for hydrogen in the liquid compartment are shown in Figure 4.8 (in the absence of mass transfer, the second term on the RHS of Eq. 4.6 vanishes). As can be seen, the concentration of hydrogen remains below the solubility threshold concentration of ~ 0.8 mM only when hydrogen is transported

across the gas-liquid interface (red curve in Figure 4.8), while it rapidly crosses this threshold in the absence of mass transport (blue curve in Figure 4.8). Hence, the high transfer rate of hydrogen from the aqueous phase to the gas phase serves to completely prevent the uncontrolled nucleation of hydrogen bubbles in the device. The absence of any bubble nuclei is evident in the downstream stereomicroscopic image in Figure 4.7(c).

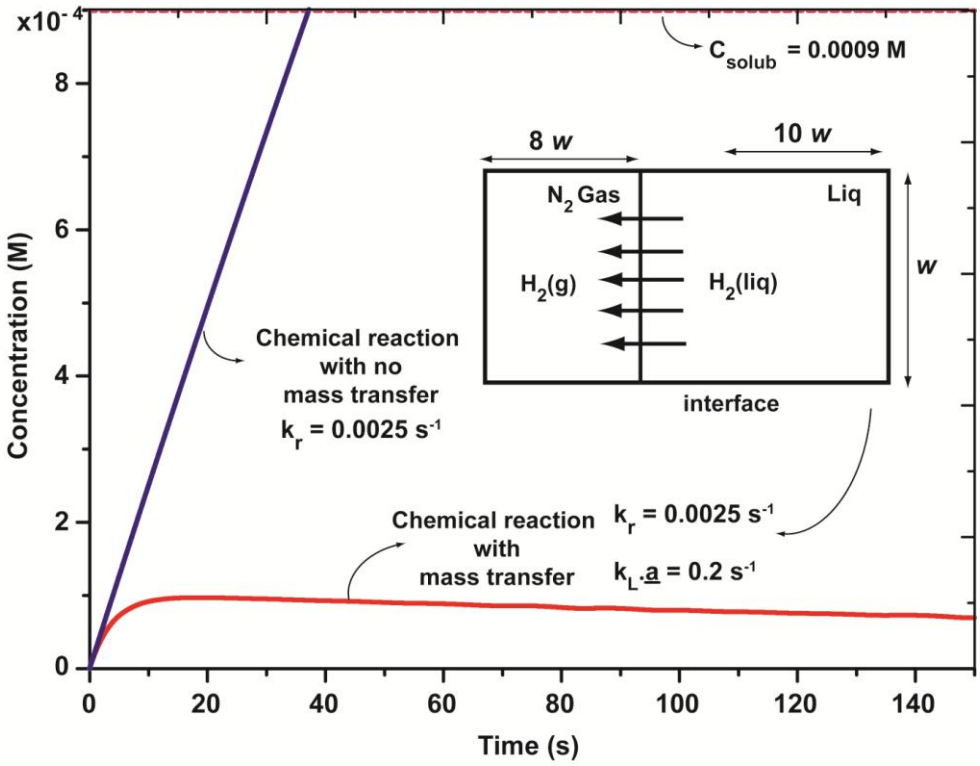

Figure 4.8. Plots showing the time variation of hydrogen concentration in the liquid compartment with and without mass transfer into the gas bubble with a borohydride hydrolysis rate constant k_r = 2.5×10^{-3} s^{-1} and mass-transfer coefficient $k_L a$ = 0.26 s^{-1} (see main text). For comparison, the residence time of reagents in the device is > 60 s.

The proposed method was successfully used for the synthesis of spherical gold nanomaterials of size ~3 to 5 nm in diameter. The experiment was performed for more than 8 hrs with no obvious deposition on the channel walls as can be seen from the SEM image of the channel walls in Figure 4.9.

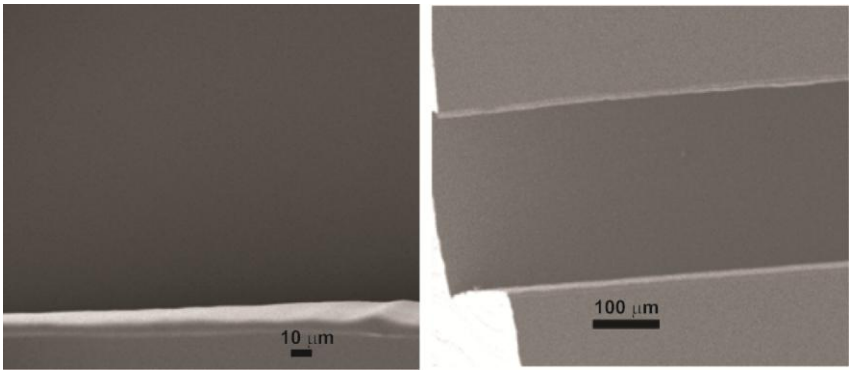

Figure 4.9. SEM images of the reactor after 8 hrs of experiment using the proposed method.

The UV-vis absorbance spectra and representative TEM and HRTEM (high resolution) images of the particles synthesized using this method, over a period of 8 hrs are shown in Figure 4.10. The size of particles synthesized is ~3-5 nm and hence they do not exhibit a sharp peak in the UV-vis extinction spectra shown in Figure 4.10 (a) except for the small hump at 520 nm along with the background scattering spectra.[38,39] The absence of peaks at other wavelengths and also the absence of a prominent peak at 520 nm show that the particles obtained are monodisperse and also that particles of other sizes do not exist in the sample.[39,40]

TEM images in Figure 4.10 (b) and (c) also show the absence of particles of other sizes and shapes in the sample solution and the presence of particles of size <5nm. Insets are HRTEM images of a single particle from the sample showing crystal facets on these particles. As already established, the CTAB protected seeds exhibit a single crystal facet which is also confirmed from these HRTEM images. In addition, HRTEM image of a group of seeds shown in the inset Figure 4.10 (a) also confirms the presence of single crystal seeds.The images as well as the spectra of the samples collected over a period of 8 hrs show that the quality of the particles are maintained over a period of time. These seeds were used for the synthesis of gold nanorods in the batch experiment described in Chapter 2 - nanorods synthesis in Section 2.2.8.

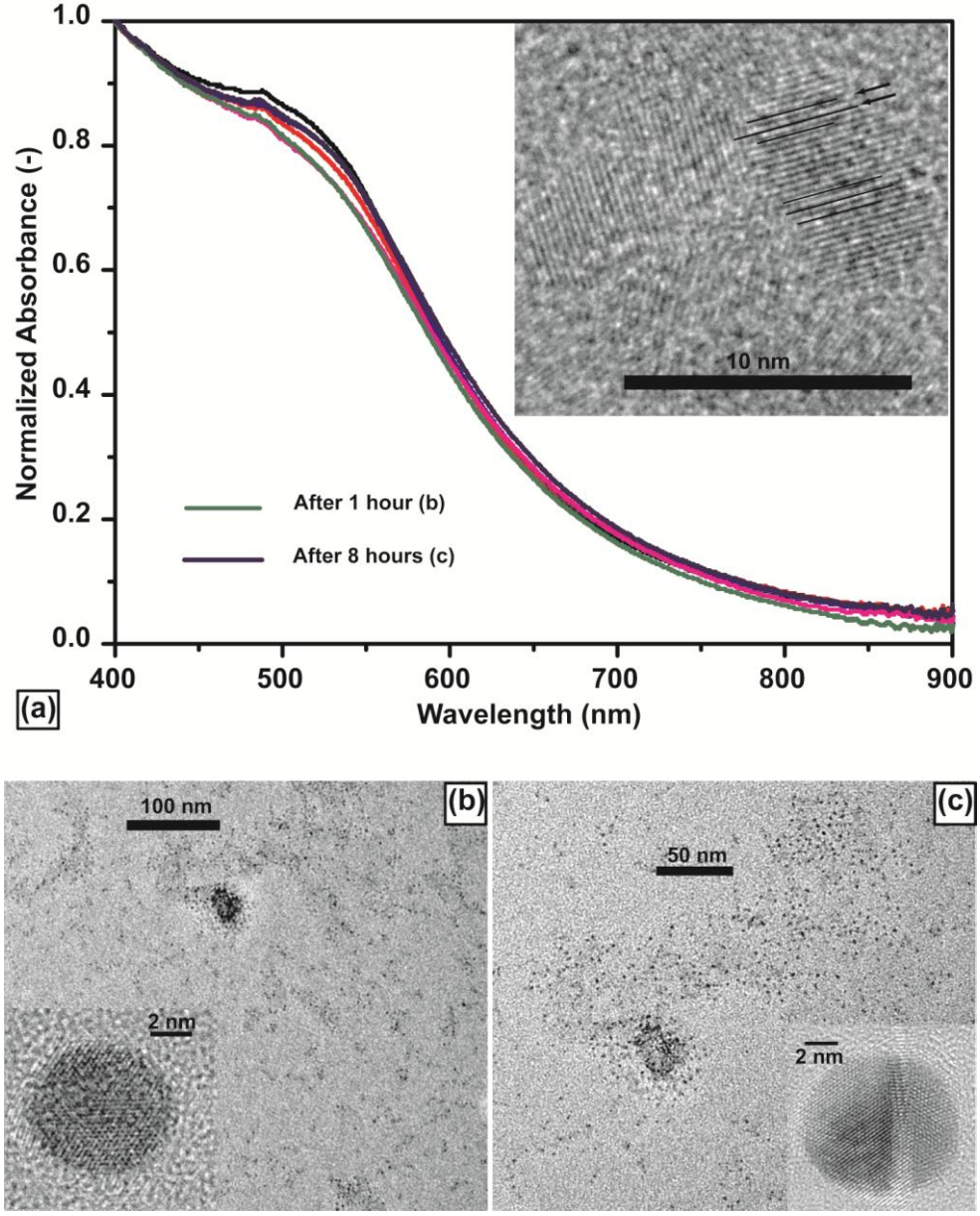

Figure 4.10. (a) UV-vis absorbance spectra; inset : High resolution TEM image of a sample of seeds synthesized using the method and **(b) and (c)** SEM images of seeds synthesized using the method after **(b)** 1 hour and **(c)** 8 hours of experiments. Insets show the TEM images of a single seed particle exhibiting crystal facets.

12 µL of the above seeds were added with four different samples of the colorless solution consisting of a mixture of CTAB (5 mL, 200 mM) to 0.05, 0.15, 0.2 and 0.25 mL of 4 mM $AgNO_3$, 5 mL of $HAuCl_4$ (1mM) and 70 µL of ascorbic acid (78.8 mM) solution. The UV-vis spectra and the corresponding TEM images of the samples are shown in Figure 4.11.

As can be seen, the spectra of the samples exhibit two peaks, the TPR and the LPR peak at the respective wavelength regions. The TEM images in Figure 4.11 (a), (b) and (c) show ~95% yield of GNR of AR 3 ± 0.5, 6.4 ± 2 and 4.1 ± 1.2 respectively. A comparison of the images in Figure 4.1 and Figure 4.11, depicts the variation in the GNR sample obtained from seeds synthesized using unmodified $NaBH_4$ solution and hence signifies the advantage of using the current method for the synthesis. Thus, the method introduced is a superior alternative to the approaches employed at present.

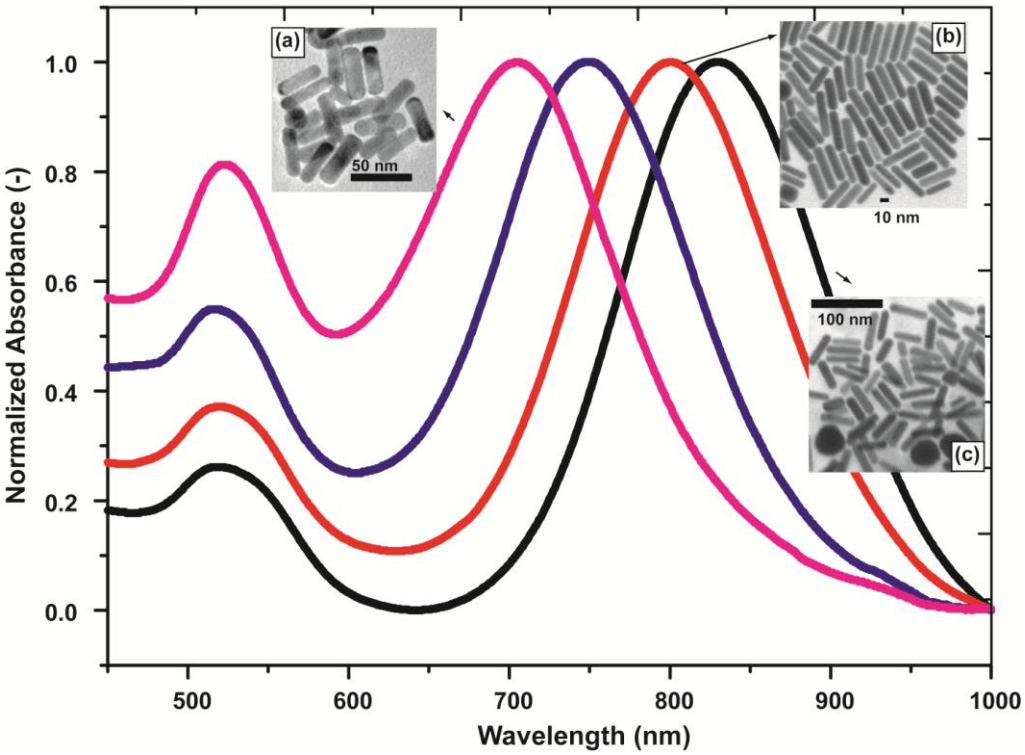

Figure 4.11. UV-vis absorbance spectra and the corresponding TEM images of the GNR synthesized using the seeds obtained from the method. The aspect ratio of the GNR obtained are **(a)** 3 ± 0.5, **(b)** 6.4 ± 2 and **(c)** 4.1 ± 1.2.

At present, experiments cannot be performed for more than 8 hrs. This is because of the accumulation of gas in the syringe with time. Though the circulating ice cold water reduces the formation of bubbles in the syringe, it does not completely eliminate the formation a gas head space (~1 mL in a 3 mL terumo syringe initially filled upto 3.5 mL and pumping at a rate of 0.6 $\mu L.min^{-1}$) is created in the syringe (~7 hrs) and this prevents the dispensing of the reagent from the syringe since the syringe piston pushes against the compressible gas rather

than the liquid. However this can be readily overcome by using continuous pumps that employ tubings immersed inside a bath containing the reagents which can be replenished over a period of time.

4.5. Summary

Continuous synthesis of small sized (~3-5 nm) gold nanocrystals has been successfully achieved using the strong reducing agent $NaBH_4$. This method overcomes the disadvantages of using presynthesized seeds in the synthesis of gold nanocrystals of varying shapes and sizes presented in Chapter 3. Since the bubbles in the syringe cannot be eliminated completely, experiments cannot be conducted for more than eight hours. However, this drawback can be overcome by using pressure driven continuous pumps which does not need the use of syringes and where the solution can be replenished at regular intervals. These seeds can be directly used for the synthesis of GNR shown in Chapter 3.

4.6. References

1 Brown, K. R., Walter, D. G. & Natan, M. J. Seeding of Colloidal Au Nanoparticle Solutions. 2. Improved Control of Particle Size and Shape. *Chemistry of Materials* **12**, 306-313 (2000).

2 Zsigmondy, R. Amikroskopische Goldkeime (A microscopic gold nuclei). *Zeitschrift für Physikalische Chemie (Journal of Physical Chemistry)* **56**, 65-76 (1906).

3 Faraday, M. The Bakerian Lecture: Experimental Relations of Gold (and Other Metals) to Light. *Philosophical Transactions of the Royal Society of London* **147**, 145-181 (1857).

4 Zsigmondy, R. *The Chemistry of Colloids*. (John Wiley & Sons, Inc., 1917).

5 Michel, J. B. & Schwartz, J. T. in *Preparation of Catalysts IV* (eds B. Delmon, P. Grange, P.A. Jacobs, & G. Poncelet) (Elsevier Science Publishers B.V., 1987).

6 Jana, N. R., Gearheart, L. & Murphy Catherine, J. Seeding growth for size control of 5-40 nm diameter gold nanoparticles. *Langmuir* **17**, 6782-6786 (2001).

7 Jana, N. R., Gearheart, L. & Murphy Catherine, J. Wet chemical synthesis of high aspect ratio cylindrical gold nanorods. *Journal of Physical Chemistry B* **105**, 4065-4067 (2001).

8 Matijevic, E. Preparation and Properties of Uniform Size Colloids. *Chemistry of Materials* **5**, 412-426 (1993).

9 Rodrıguez-Fernandez, J., Perez-Juste, J., Abajo, F. J. G. d. & Liz-Marzan, L. M. Seeded Growth of Submicron Au Colloids with Quadrupole Plasmon Resonance Modes. *Langmuir* **22**, 7007-7010 (2006).

10 Schmid, G. Large Clusters and Colloids. Metals in the Embryonic State. *Chemical Reviews* **92**, 1709-1727 (1992).

11 Nikoobakht, B. & El-Sayed, M. A. Preparation and Growth Mechanism of Gold Nanorods (NRs) Using Seed-Mediated Growth Method. *Chemistry of Materials* **15**, 1957-1962 (2003).

12 P´erez-Juste, J., Pastoriza-Santos, I., Liz-Marz´an, L. M. & Mulvaney, P. Gold nanorods: Synthesis, characterization and applications. *Coordination Chemistry Reviews* **249**, 1870–1901 (2005).

13 Gou, L. & Murphy, C. J. Fine-Tuning the Shape of Gold Nanorods. *Chemistry of Materials* **17**, 3668-3672 (2005).

14 Kuo, C.-H. & Huang, M. H. Synthesis of Branched Gold Nanocrystals by a Seeding Growth Approach. *Langmuir* **21**, 2012-2016 (2005).

15 Yuan, H. *et al.* Shape and SPR Evolution of Thorny Gold Nanoparticles Promoted by Silver Ions. *Chemistry of Materials* **19**, 1592-1600 (2007).

16 Kumar, P. S., Pastoriza-Santos, I., Rodrıguez-Gonzalez, B., Abajo, F. J. d. & Liz-Marzan, L. M. High-yield synthesis and optical response of gold nanostars. *Nanotechnology* **19**, 015606 (015606pp) (2008).

17 Sau, T. K., Pal, A., Jana, N. R., Wang, Z. L. & Pal, T. Size controlled synthesis of gold nanoparticles using photochemically prepared seed particles *Journal of Nanoparticle Research* **3**, 257–261 (2001).

18 Lo, C.-t. F., Karan, K. & Davis, B. R. Kinetic Studies of Reaction between Sodium Borohydride and Methanol, Water, and Their Mixtures. *Industrial and Engineering Chemistry Research* **46**, 5478-5484 (2007).

19 Goia, D. V. & Matijevic, E. Preparation of monodispersed metal particles. *New Journal of Chemistry* **22**, 1203 - 1215 (1998).

20 Liz-Marzán, L. M. Nanometals:formation and color. *Materials Today* **February**, 26-31 (2004).

21 Shalom, D. *et al.* Synthesis of thiol functionalized gold nanoparticles using a continuous flow microfluidic reactor. *Materials Letters* **61**, 1146–1150 (2007).

22 Samal, A. K., Sreeprasad, T. S. & Pradeep, T. Investigation of the role of NaBH4 in the chemical synthesis of gold nanorods. *Journal of Nanoparticle Research* **12**, 1777–1786 (2010).

23 Hills, B. *Decompression Sickness*. (John Wiley & Sons, Ltd, 1977).

24 LeMessurier, D. H. & Hills, B. A. Decompression sickness: a thermodynamic approach arising from a study of Torres Strait diving techniques. *Hvalradet Skrifter* **48**, 54-84 (1965).

25 Losey, M. W., Schmidt, M. A. & Jensen, K. F. Microfabricated Multiphase Packed-Bed Reactors: Characterization of Mass Transfer and Reactions. *Industrial and Engineering Chemistry Research* **40**, 2555-2562 (2001).

26 Rubin, M. B. & Noyes, R. M. Measurements of critical supersaturation for homogeneous nucleation of bubbles *Journal of Physical Chemistry* **91**, 4193-4198 (1987).

27 Gardiner, J. A. & Collat, J. W. Kinetics of the Stepwise Hydrolysis of Tetrahydroborate Ion. *Journal of the American Chemical Society* **87**, 1692-1700 (1965).

28 Kreevoy, M. M. & Hutchins, J. E. C. H_2BH_3 as an Intermediatein Tetrahydridoborate Hydrolysis. *Journal of the American Chemical Society* **94**, 6371-6376 (1972).

29 Abts, L. M., Langland, J. T. & Kreevoy, M. M. Role of Water in the Hydrolysis of BH_4^{-1}. *Journal of the American Chemical Society* **97**, 3181-3185 (1975).

30 Mesmer, R. E. & Jolly, W. L. The Hydrolysis of Aqueous Hydroborate. *Inorganic Chemistry* **1**, 608-612 (1962).

31 Zhang, Q., Wu, Y., Sun, X. & Ortega, J. Kinetics of Catalytic Hydrolysis of Stabilized Sodium Borohydride Solutions. *Industrial and Engineering Chemistry* **46**, 1120-1124 (2007).

32 Davis, R. E., Bromels, E. & Kibby, C. L. Boron Hydrides. III. Hydrolysis of Sodium Borohydride in Aqueous Solution. *Journal of the American Chemical Society* **84**, 885-892 (1962).

33 Hung, A.-J. *et al.* Kinetics of sodium borohydride hydrolysis reaction for hydrogen generation. *International Journal of Hydrogen Energy* **33**, 6205 – 6215 (2008).

34 Lo, C.-t. F., Karan, K. & Davis, B. R. Kinetic Studies of Reaction between Sodium Borohydride and Methanol, Water, and Their Mixtures. *Industrial and Engineering Chemistry* **46**, 5478-5484 (2007).

35 Cussler, E. L. *Diffusion Mass Transfer in Fluid Systems*. (Cambridge University Press, 1997).

36 Baten, J. M. v. & Krishna, R. CFD simulations of wall mass transfer for Taylor flow in circular capillaries. *Chemical Engineering Science* **60**, 1117-1126 (2005).

37 Kreutzer, M. T., Kapteijn, F., Moulijn, J. A. & Heiszwolf, J. J. Multiphase monolith reactors: Chemical reaction engineering of segmented flowin microchannels. *Chemical Engineering Science* **60**, 5895 – 5916 (2005).

38 Duff, D. G., Baiker, A. & Edwards, P. P. A New Hydrosol of Gold Clusters. 1. Formation and Particle Size Variation. *Langmuir* **9**, 2301-2309 (1993).

39 Hussain, I. *et al.* Size-Controlled Synthesis of Near-Monodisperse Gold Nanoparticles in the 1-4 nm Range Using Polymeric Stabilizers. *Journal of the American Chemical Society* **127**, 16398-16399 (2005).

40 Weare, W. W., Reed, S. M., Warner, M. G. & Hutchison, J. E. Improved Synthesis of Small (d_{CORE}=1.5 nm) Phosphine-Stabilized Gold Nanoparticles. *Journal of the American Chemical Society* **122**, 12890-12891 (2000).

5. Plasmonic Nanoshell Synthesis in Three-Phase Segmented Microfluidic Flows

Metallodielectric ‘nanoshells’ or Gold ‘nanoshells’ and ‘nano-islands’, comprising a silica nanoparticle core encased within a thin gold shell or coated by gold nanoparticles are yet another class of plasmonic nanomaterials having broadly tunable plasmon-derived optical resonances.[1] These particles, similar to gold nanorods, exhibit unique optical properties that can be utilised for several different applications such as biomedical imaging, biosensing, *in vivo* therapeutic applications and more recently as building blocks of plasmonic metamaterials as have been highlighted in Chapters 1 and 2.[2] These particles were first introduced by Halas and co-workers more than a decade ago[3] and have since then been objects of intense fundamental and applied research.[4,5] The optical tunability of these particles is accomplished by varying core sizes and shell thicknesses, and is well understood in terms of classical electromagnetic theory[6] as also by recent theoretical approaches that describe optical behaviour in terms of plasmon hybridization.[7] The sensitive size-dependence of optical properties necessitates the use of such particles with tightly controlled size distributions in practical applications. Synthesis of these particles is yet again performed in small scale batch reactors and suffers from all the major drawbacks listed in Chapter 1 (1.4.6.3). Hence these particles are also another alternate class of materials that are in high demand commercially and need to be controllably synthesized in large scales and is relevant to the contents of this thesis.

The existing strategies for the synthesis of these particles and the motivation for better approaches for the same along with the limitations of certain microfluidic methods are provided in this chapter. Segmented gas-liquid flow method and droplet microfluidic method used in the previous chapters are integrated in this chapter to form three phase segmented microfluidic flows. Foams constituting alternately flowing gas bubbles (inert gas) and aqueous drops (containing reagents for nanoparticle synthesis) (Sections 5.4), compound drops

comprising bubble (reactive gas) drop pairs (Section 5.6) which are subsets of these three-phase flows are used for the synthesis of plasmonic nanostructures individually in two different methods. The formation of such microfluidic three-phase flows and an analysis of the salient features of these flows along with their use in the synthesis of metallic nanoshells are dealt with in detail. The formation of these three-phase structures enables precisely controlled reagent dispensing and mixing, while these structures also facilitates compartmentalized nanoparticle growth. The methods described are generic for aqueous colloidal synthesis, enabling continuous, inherently digital, scalable and automated production processes for plasmonic nanomaterials.

5.1. Current Trends in Synthesis - Motivation

The most commonly employed synthetic strategy for nanoshell fabrication involves aqueous-based electroless plating of nanometer-scale multicrystalline gold films onto silica nanoparticle surfaces (diameter d = 50-200 nm) that have been pre-seeded with small gold nanoparticles (diameter d = 2-5 nm).[3,8] In this method, gold nanoparticle seeds on the silica particles serve as catalytic sites for the reduction of aqueous $Au^{[3+]}$ to $Au^{[0]}$ by reducing agents such as hydroxylamine and formaldehyde with ammonium hydroxide.[9,10] Electroless plating involves rapid autocatalytic reaction kinetics, and the reaction rate can be limited by diffusion of ionic species to the catalytic particle surfaces.[11] An estimate for diffusion-limited linear growth rate (dr/dt) is obtained as

$$\frac{dr}{dt} = \frac{D C_{Au} V_M}{r} \tag{5.1}$$

where D and C_{Au} are respectively the diffusivity and concentration of $Au^{[3+]}$, V_M is the molar volume of gold, and r is the particle radius; this simple calculation yields dr/dt ~5 nm.s^{-1} for D = 1x10^{-9} m^2.s^{-1}, C_{Au} = 0.1 mM, r = 200 nm, and V_M = 10 cm^3.mol^{-1}. Instantaneous linear growth rates can be as high as ~5 nm.s^{-1}, and nanoshell growth is typically completed within

seconds.[12] As such, uniform shell growth on all particles in suspension clearly requires reagent addition and homogenization to be accomplished at time scales smaller than those for shell growth. This synthetic strategy is therefore remarkably sensitive to the details of reagent addition and mixing in the reaction vessel. The currently established protocols for shell growth involve synthesis in small batches in which control over the reaction conditions are limited as already pointed out in Chapter 1 and Chapter 2. An analysis of the currently established protocols for the synthesis is done and the details of these experiments are as follows:

5.1.1. Materials and Methods

5.1.1.1. Materials

Tetraethyl orthosilicate (TEOS, 99.999%), ammonium hydroxide (28% NH_3 in water, 99.99+%), and hydroxylamine hydrochloride (trace metal basis, 99.99%) from Aldrich Chemical Co., Singapore, 3-aminopropyl tris(trimethylsiloxy) silane (99%), hydrogen tetrachloroaurate(III) trihydrate (99.99%), tetrakis(hydroxymethyl) phosphonium chloride (THPC, 80% in water), sodium hydroxide (Reagent grade, 97%), potassium carbonate (99.99%) from Sigma-Aldrich Co. Ltd., Singapore and ethanol (Analytical reagent grade, absolute) from Fisher scientific Co., Singapore were all used as obtained without any further purification. Ultra-pure water (18 MΩ-cm, ELGA, Singapore) and glassware washed in aqua regia and rinsed thoroughly in water were used for experiments.

5.1.1.2. Synthesis of Silica Particles

Stöber process for the synthesis of silica nanoparticles leads to nearly monodisperse particle distribution.[13] A modification of the Stöber process proposed by Bogush and Zukoski was used for the synthesis to yield ~170 nm silica particles.[14,15] The procedure involves dissolving 0.65 mL (0.29 M) of TEOS and 0.49 mL of NH_3 (0.73 M) in 4.13 mL of ethanol and 0.3 mL of water in separate borosilicate vials. They were thoroughly mixed before the contents of the vial containing TEOS was transferred into the other vial. The solution was stirred at room temperature for 8 hrs. The solution turned turbid in 30 mins and milky white in

8 hrs. The particles formed were centrifuged, decanted, redispersed in 10 mL of ethanol thrice before use. 10 mL of one such sample was weighed, dried and weighed again to determine the wet weight and dry weight for calculating the weight percentage (2.3%) and the concentration (17.9 $mg.mL^{-1}$) of the synthesized silica particles.

5.1.1.3. Functionalization and Seeding of Silica Particles

The synthesized and cleaned silica particles' surfaces were functionalized with amine terminated silane to enhance their attachment with the gold nanoparticle seeds.[8] 3-aminopropyl tris(trimethylsiloxy) silane was used for this purpose. 5 µL of the silane and 5 mL of 17.9 $mg.mL^{-1}$ silica particles were mixed and were allowed to react for 8 hrs before they were heated to slow boil for 1 hr to improve the adhesion of silane onto the silica surface. The unreacted and excess silane was removed by a series of centrifugation and redispersion (in ethanol) steps. Silane functionalized silica particles were finally dispersed in 5 mL water.

3-5 nm gold particles, which were used as seeds for further growth into gold nanoshells and islands, were synthesized using the protocol proposed by Duff *et al.*[16] According to the protocol, 0.75 mL of sodium hydroxide (0.2 mM) solution was added to 22.75 mL of water in a 100 mL borosilicate vial. THPC solution (0.5 mL) was prepared by adding 1.2 mL of the original 80% THPC solution to 100 mL of water, was added to the solution mixture and mixed using a magnetic stirrer bar (teflon, 4 cm) for 2 mins. 1 mL of the gold salt solution ($HAuCl_4.3H_2O$, 25mM) was then added to the mixture while stirring at 400 rpm. The colour of the solution turned brown immediately after addition of the gold salt, indicating the formation of 3 nm gold nanocrystals. The as prepared gold nanoparticles were then attached to the amine terminated silica particles in the seeding step.

0.2 mL of the silane functionalized silica particles and 6 mL of the as prepared gold nanoparticle solution were added in a 10 mL borosilicate vial and were kept shaking (GFL 3017, Orbital shaker) for over 8 hrs to achieve electrostatic adhesion between the functionalized silica (amine group on the silica surface) and the negatively charged gold

nanoparticles. Excess gold particles were then removed by three centrifugation and redispersion steps. The gold functionalized silica particles (referred to as the seeded silica hereafter) were redispersed into 6 mL of water and were refrigerated for atleast one day before further use. The weight percentage of silica particles and the concentration of the seeded silica were then calculated to be 98×10^{-3}% and 1 $mg.mL^{-1}$ respectively by determining the wet weight and the dry weight of ~2 mL of the solution.

5.1.1.4. Shell Growth

Slow addition of reagents using syringe pumps was employed for the controlled addition of the plating solution and reducing agent to the seeded silica and also to prevent uncontrolled reaction between the reagents and the reaction vessel. The plating solution consists of potassium carbonate (2 mM) and the gold salt solution (0.5 mM) aged for 8 hrs before use while hydroxylamine hydrochloride served as the weak reducing agent. The plating solution and the reducing agent were added to the seeded silica solution through individual syringe pumps (Harvard, PHD 2000) operating at different flow rates for a period of 30 mins while the contents were mixed using an orbital shaker (GFL 3017). The solution was drop cast onto a 200 mesh copper grid and analyzed using TEM (JEOL 2010, accelerating voltage 200 kV) or FESEM (JEOL JSM-6700f, accelerating voltage 25 kV). The optimum concentrations of reagents to obtain a fully grown uniform shell was established after several experiments as 700 µL of the plating solution, 350 µL (20 mM) of the reducing agent and 15 µL of seeded silica. This procedure yielded approximately 300 nm to 800 nm thick shell around the silica core.

5.1.2. Results and Discussion

Representative SEM and TEM images of the silica particles and that of the seeded silica are shown in Figure 5.1 (a) and (b) respectively. The average size of the silica particles is 177 ± 16 nm. The protocol for synthesis of seeded silica is well established, yielding uniform and well dispersed particles reproducibly. The continuous synthesis of seeded silica at this stage is redundant as the batch process is well established, scalable and reproducible. The currently established protocols[17] for shell growth process involve the addition of plating solution and reducing agent directly into the vial containing the seeded silica solution which resulted in agglomerates, large gold nanoparticles and unevenly/partially coated silica particles rather than a complete and uniform shell as shown in Figure 5.1 (c) and (d). This is due to the fast and uncontrolled reaction between the plating solution and the reducing agent rather than their reaction on the seed.

In order to prevent the formation of agglomerates and also to achieve some control over the reaction, slow addition of reagents into the reaction mixture over a period of time was employed. This strategy resulted in the complete consumption of reagents before further reagent addition thus achieving growth on the seeded silica particles in gradual and controlled steps. However, complete shell around the silica particles were obtained for one particular concentration of the reducing agent and the plating solution only. Representative TEM images of these particles are shown in Figure 5.1 (e). Shell thickness determined from the particle size calculations vary from 300 nm to 800 nm and has been plotted as a histogram in Figure 5.1 (f) where bimodal particle size distribution is obtained. Any further variation in the concentrations to modify the shell thickness was not successful in yielding significantly different sized population due to the large deviation in the shell thickness within one batch. In addition, the samples collected were very dilute and the sample volume was low (~1 mL) to obtain any useful spectral information. The process was reproducible though not scalable and involved several ‘time consuming steps’ for every change in concentration tested. The polydisperse

particle populations as well as the scalability issues of the batch process justify the need for controlled microfluidic methods for shell growth.

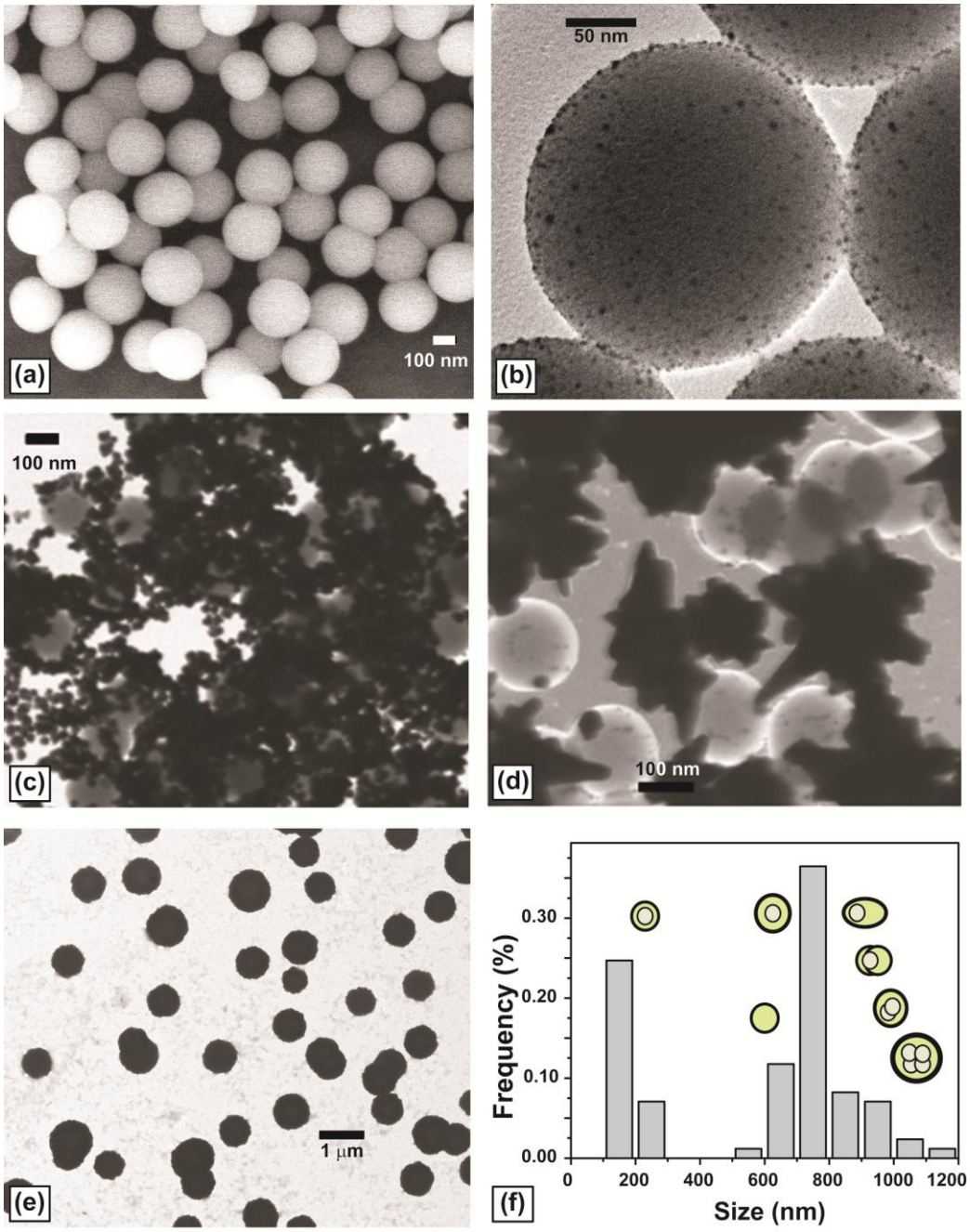

Figure 5.1. SEM and TEM images of **(a)** As synthesized silica particles, showing a monodisperse particle population. **(b)** Seeded silica **(c), (d)** Gold nanoshells synthesized using the currently established protocol **(e)** Gold nanoshells synthesized using the slow addition method and **(f)** Histograms for size distribution of the nanoshells from the slow addition method (the inset schematics show possible particle morphologies consistent with the measured sizes).

5.2. Droplet Microfluidic Method for Nanoshell Synthesis

Droplet microfluidic method used for the synthesis of gold nanocrystals in Chapter 3 was initially used for the synthesis of gold nanoshells. The experiments performed and the disadvantages of this method for the current synthesis are discussed in the following section.

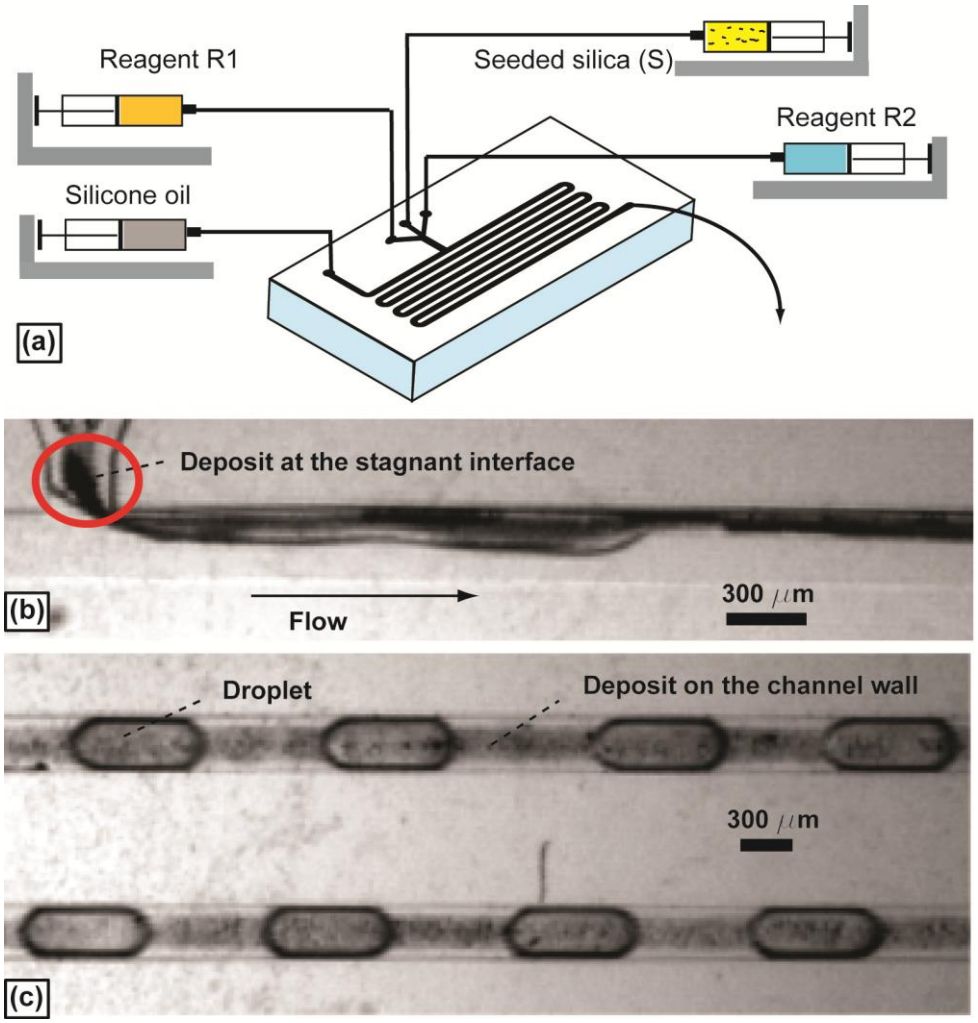

Figure 5.2. (a) Schematic of the experimental setup. **(b)** and **(c)** Stereomicroscopic images of **(b)** the T-junction and **(c)** Downstream section of the droplet microfluidic reactor during the synthesis experiment.

5.2.1. Experimental

The materials required, synthesis of silica particles, their functionalization and formation of seeded silica are the same as those in Section 5.1.1. The microfabrication techniques, the reactor design, are the same as those in Chapter 3, Section 3.3. Few modifications in the reagents used in the current case is outlined in the following section.

Reactor Setup and Operation

Reagent R1, the gold plating solution consisted of aged (>24 hrs) K-gold solution formed by the addition of 249 mg (1.8 mM) of potassium carbonate in 1L (0.435 mM) of gold salt solution. Reagent R2 was freshly prepared hydroxyl amine hydrochloride (4 mM), the reducing agent. The solution stream S comprised the seeded silica of concentration 0.5 $mg.mL^{-1}$. Silicone oil (Dow Corning DC50, viscosity 10 cP), seeded silica suspension (S) and aqueous reagent solutions (R1 and R2) were delivered by separate syringe pumps (Harvard, PHD 2000) into the respective inlets. A schematic of the setup is provided in Figure 5.2 (a).

5.2.2. Discussion

Stereomicrographic images of the reactor during the experiment are shown in Figure 5.2 (b) and (c). Particle deposition on the walls of the reactor is initiated at stagnant liquid interface in the T-junction (highlighted in Figure 5.2 (b)) and slowly spreads through the entire reactor, thus fouling and clogging the reactor (Figure 5.2(c)) with time. The main problem with using droplet microfluidics for the synthesis of gold nanoshells is the stagnant interface at the T-junction where all the reagents meet before they form droplets. As soon as the reagents meet at the small zone highlighted in Figure 5.2 (b) they react instantaneously. The reagents are not encased in the droplets yet and are in direct contact with the channel walls. The reaction in this region is also enhanced by the heterogeneous reaction with the channel walls which aids in particle deposition. The difference between the droplet microfluidic methods for formation of

gold nanocrystals used in Chapter 3 and that used for the synthesis of gold nanoshells, is the presence of seeded silica particles of size ~175 nm along with the reagents, at the stagnant interface in the latter. The colloidal particles themselves deposit on the channel walls thus aiding the deposition of particles onto the channel wall in the highlighted region. The deposited particles grow with time and lead to clogging of the reactor. This drawback severely limits the use of droplet microfluidics for the present synthesis.

The above considerations limit the reproducibility and scalability of the current lab-scale techniques as well as the droplet microfluidic method for the synthesis of gold nanoshells thus necessitating other processing alternates. Microfluidic segmented three-phase flows which incorporate the advantages of both the droplet microfluidic method and the segmented gas-liquid flow method were studied in detail and their salient features make them appropriate for the current synthesis. A detailed account of these three-phase flows is presented in the following sections.

5.3. Three-Phase Segmented Microfluidic Flows

Formation and flow of bubbles and drops in a continuous stream of oil to form three-phase segmented flows were studied in order to understand the dynamic behaviour of these flows in a microchannel network. Silicone oil was considered as the immiscible continuous phase liquid while the nitrogen gas and dilute aqueous surfactant solution formed the dispersed fluids. ‘Foams’, a compact train of alternate bubbles and drops as well as compound bubble-drop pairs called ‘compound-drops’ were formed from individually generated bubbles and drops at different flow regimes which are analyzed in the following sections.

5.3.1. Experimental

5.3.1.1. Materials

Silicone oil from Dow Corning DC50, (viscosity 10 cP) and hexadecyltrimethyl ammonium bromide (99%) (CTAB) from Sigma-Aldrich Co. Ltd., Singapore were used without further purification. 18MΩ-cm ultrapure deionised water was used for all experiments.

5.3.1.2. Microfabrication

The microchannels were moulded in PDMS from master patterns fabricated on silicon wafers using photolithography on a negative photoresist SU-8(2050). Moulded channel patterns were sealed to glass slides pre-coated with a thin layer of cured PDMS. The relevant microchannel dimensions were width w = 300 μm, height h ~150 μm, and length L = 0.15m – 2m.

5.3.1.3. Reactor Setup and Operation

Figure 5.3 is a schematic of the microchannel layout consisting of a cross-flow T-junction geometry leading into one long microchannel. One arm of the T-junction was further subdivided into two branches, one of which was used to deliver gas and the other to deliver liquid.

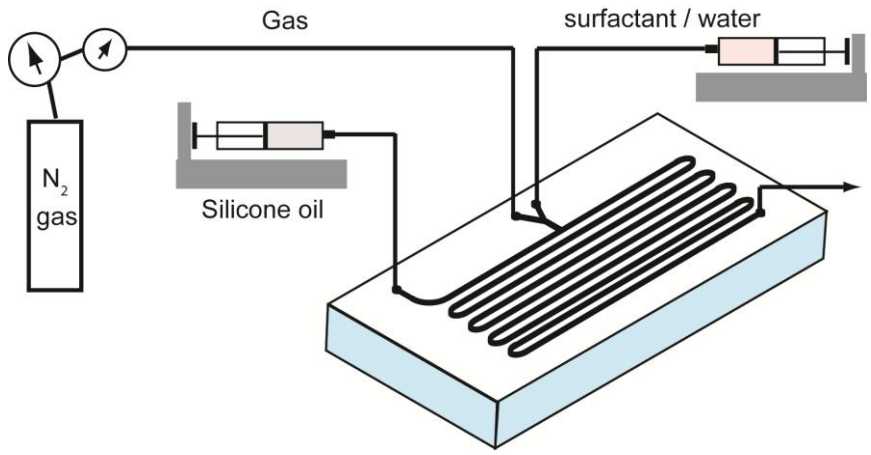

Figure 5.3. Schematic of the experimental setup for the formation of compound bubble-drop pairs.

0.1 wt% aqueous CTAB solution and silicone oil were delivered by separate syringe pumps (Harvard, PHD 2000) into the respective inlets and nitrogen gas was delivered from a cylinder equipped with a two-stage pressure regulator through circular PEEK tubing (60 µm i.d., 1 m long and 100 µm i.d., 2 m long) leading into the on-chip gas-inlet. The oil was infused first into the reactor to completely wet the channels before the other reagents were allowed to flow through. The flow of oil into the gas inlet was prevented by turning on the gas flow as soon as oil reached the inlet tubing leading to the reactor. Still images and videos of the flow were captured through a stereo-microscope (Leica) equipped with a digital camera (QCapture Micropublisher RTV).

5.3.2. Formation

Bubbles and drops are alternately generated at the T-junction as depicted in the sequence of images in Figure 5.4 (a)-(f).

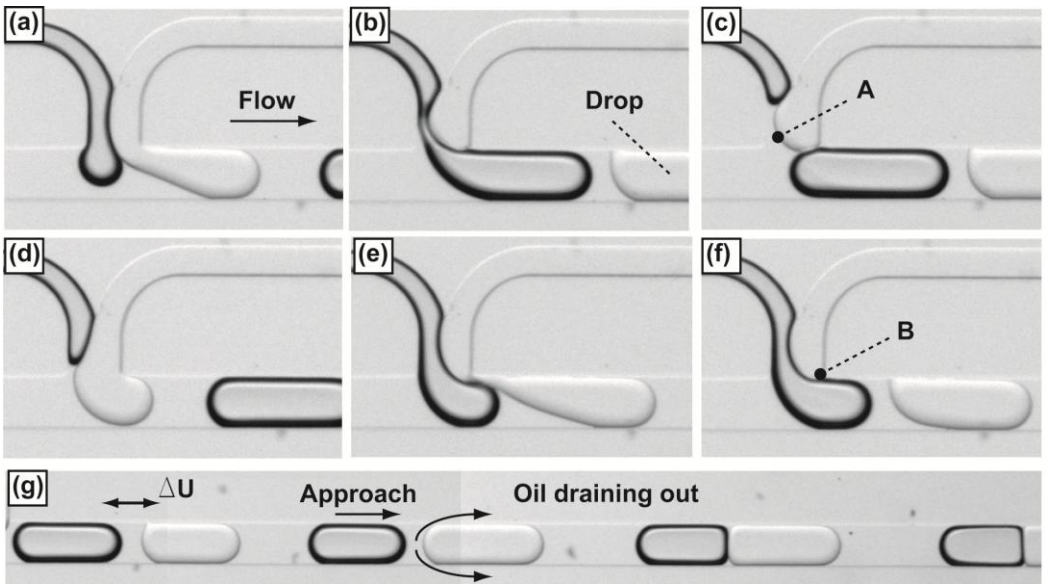

Figure 5.4. (a)-(f) Alternate pinching of bubbles and drops at the T-junction and **(g)** Relative motion and assembly of bubbles and drop into compound drops.

Bubbles are pinched off at one corner (A) of the T-junction by the advancing aqueous interface and subsequently drops are pinched off at the other corner (B) by the advancing gas

interface. This mechanism of alternating bubble and drop formation is similar to the 'block-pinch' effect for the confined droplet breakup in cross-flowing streams.[18,19] The continuous oil phase preferentially wets the microchannel walls and is present as a thin layer surrounding the bubbles and drops individually along the channel walls as well as along the interface between them and also at their corners.[20] Drops and bubbles are initially separated by oil segments and is shown in Figure 5.4 (g). Bubbles are observed to move faster through the oil than the drops. The differences in the translational speeds (ΔU) of the drop and bubble result in compound bubble-drop pair formation. Further information of the breakup and the possible reasons for the formation of a flat interface between the bubble and drop within a compound drop is beyond the scope of this thesis.

5.3.3. Flow Profile

Flow patterns exhibited by multiphase flows typically depend on the flow speeds of the individual fluid phases. A parameter space of flow speeds of the individual fluids shows a variety of flow patterns and the region of operation in the parameter space defines the flow pattern at any instant.[21,22]

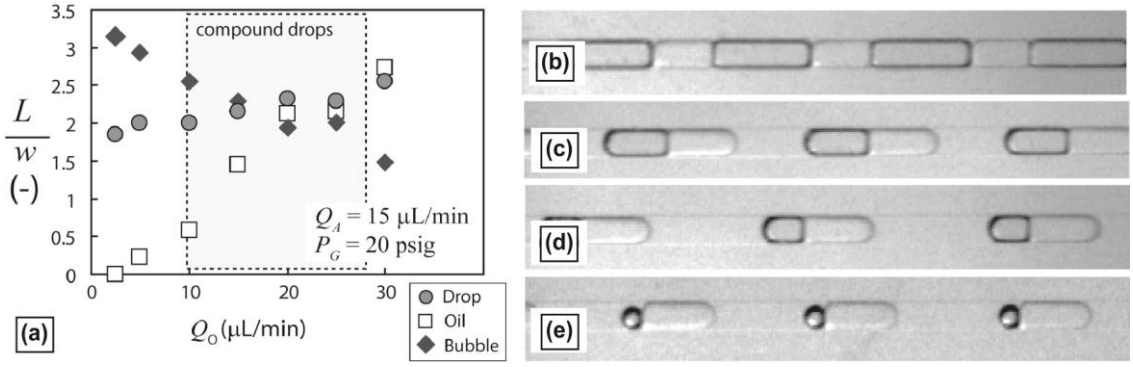

Figure 5.5. (a) Graph of dimensionless bubble length, drop length and oil segment length versus oil volumetric flow rate Q_O, at constant aqueous flow rate Q_A and gas supply pressure P_G. Regularly spaced compound drops are formed in the highlighted region of parameter space. **(b)-(e)** Stereomicrographs of flow patterns obtained in order of increasing Q_O.

The parameter space in the case of bubble-drop pairs consists of oil and water volumetric flow rates (Q_O and Q_A respectively) and gas supply pressure P_G, a *three*-dimensional parameter. Figure 5.5 (a) is a graph of dimensionless bubble length, drop length and oil segment length at the T-junction versus Q_O, at constant Q_A and pressure P_G. At low oil-to-aqueous flow ratios, a compact train of alternating bubbles and drops with nearly flattened gas-aqueous interfaces is formed which are referred to as 'foams' hereafter (Figure 5.5 (b)). Similar observations have previously been reported in studies of three-phase trains in tubes of circular cross-section at low oil-to-aqueous flow ratios.[23] The oil in this case merely forms a thin lubricating sheath encasing the bubble-drop train. As the oil flow rate is increased, bubbles and drops assemble into compound drops flowing in a stable segmented train downstream of the T-junction (Figure 5.5 (c) and (d)). Further increase in oil flow rate causes a drop in bubble size (Figure 5.5 (e)), until the formation of bubbles stops altogether.[24]

Ordered microfluidic foams (Figure 5.5 (b)) which are a subset of the three-phase microfluidic flows have been successfully used in this chapter for the synthesis of these gold nanoshells and nano-islands on silica surfaces. Microfluidic foams enable robust, automated and continuous colloidal syntheses of metallic nanostructures unachievable by current macro- and microscale methods. The salient features of these foams for particles synthesis is provided in the following sections.

5.4. Microfluidic Foams

The self-assembly of ordered microscale foams is a simple and versatile solution for robust and reproducible continuous colloidal syntheses of plasmonic nanostructures. Figure 5.6 (a) is a two-dimensional schematic illustrating the basic features of the foams used in this work. The foam is an ordered alternation of gas and liquid cells (hence the term 'composite'[25]) dispersed in an immiscible oil phase flowing within a microchannel. The overall foam structure resembles the compact 'bamboo' structures observed in confined cylindrical foams.[26] Operation between the dry and wet foam limits leads to characteristic flattening of adjacent

fluid interfaces and sharp Plateau border curvatures (Figure 5.6 (b)).[27] Such three-phase microfluidic motifs were originally pioneered by Ismagilov and co-workers in the context of protein crystallization studies.[28]

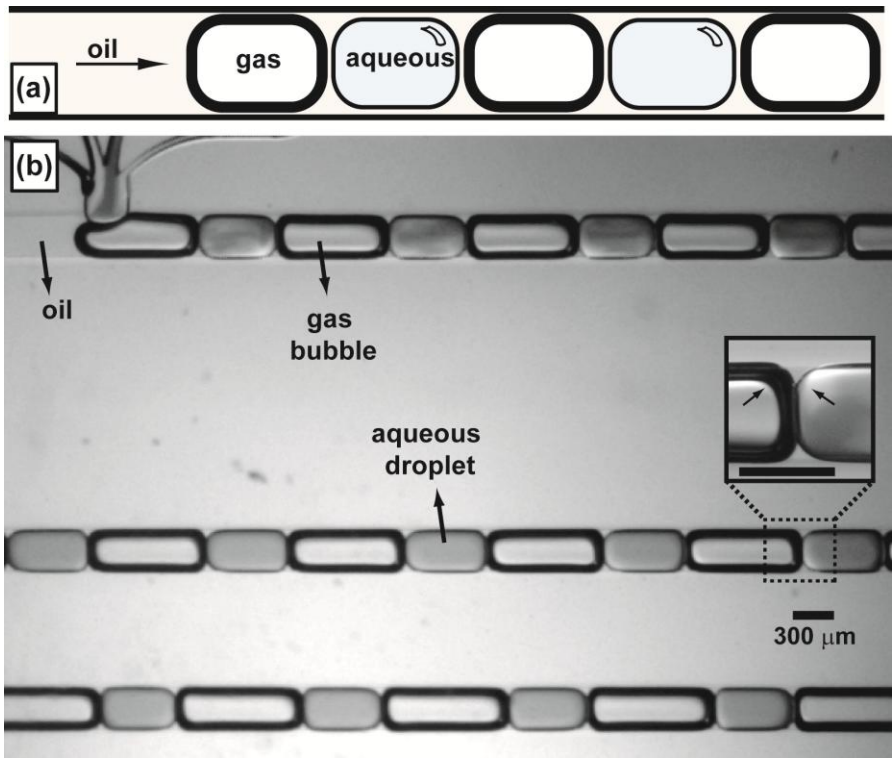

Figure 5.6. (a) A two dimensional cartoon of the composite foam showing an alternate train of gas and liquid cells flowing in a continuous oil stream. **(b)** Stereomicroscopic images of the composite foam with the inset inset showing a magnified view of the gas-aqueous interface: the sharp plateau border curvature is clearly visible.

5.4.1. Microfluidic Composite Foams: Salient Features

Microfluidic composite foams possess a unique set of structural and functional features that make them attractive for nanoparticle processing. Aqueous reagents for colloidal synthesis can be controllably dispensed as liquid cells of identical size that serve as individual reaction 'flasks' and are effectively isolated from other reagent-filled cells and the microchannel walls during their transit through the microchannel. Experiments similar to the ones described in Section 5.3.1 were performed to analyze the features of microfluidic foams for particle synthesis. The only modification in the current experiment is the design of the

device; the device consists of five inlets, one for the continuous liquid (oil in this case) and the other four inlets for the other fluids (gas and the reagents) flowing in through the T-junction as shown in Figure 5.7.

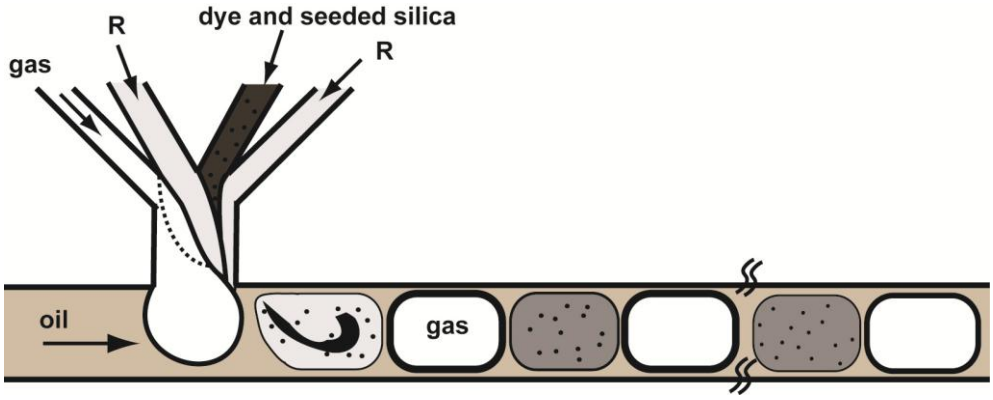

Figire 5.7. Schematic of the flow visualization experiment with the dye flowing into one of the inlets along with aqueous reagent solutions.

Reagents are dispensed during the process of foam generation as illustrated by mixing visualization experiments, where nitrogen gas and aqueous reagent streams, one of which contains a black dye, (Parker quink, Parker pen products, England) are introduced into one arm of the microfluidic T-junction, and the immiscible cross-flowing oil is delivered into the other arm. Gas bubbles and reagent-filled aqueous drops are alternately formed by a block-pinch mechanism and subsequently assemble downstream into an ordered foam lattice, at low volumetric oil flow rates relative to the aqueous streams. The aqueous solutions are dispensed during the process of foam generation, as shown in Figure 5.8 (a) - (d). The break off of drops at the junction does not rely on shear forces which is the case in droplet microflows as was discussed in Section 3.2.3 (viscosity and interfacial tension changes the capillary number and hence the breakup).[29,30] The above features present significant advantages over current droplet-based microfluidic synthesis methods, where droplet formation is sensitive to fluid properties such as interfacial tension, and droplet coalescence which are a frequent occurrence. The injected gas periodically clears the aqueous streams from the T-junction, thereby preventing reagent buildup and nanoparticle deposition which occurs when laminar fluid streams are left

undisturbed, which is the case in droplet microflows as well as in single-phase flows.[31,32] In addition, the gas cells of the foam lattice may also carry a gas-phase reagent for colloidal chemistry, further broadening the spectrum of possibilities.

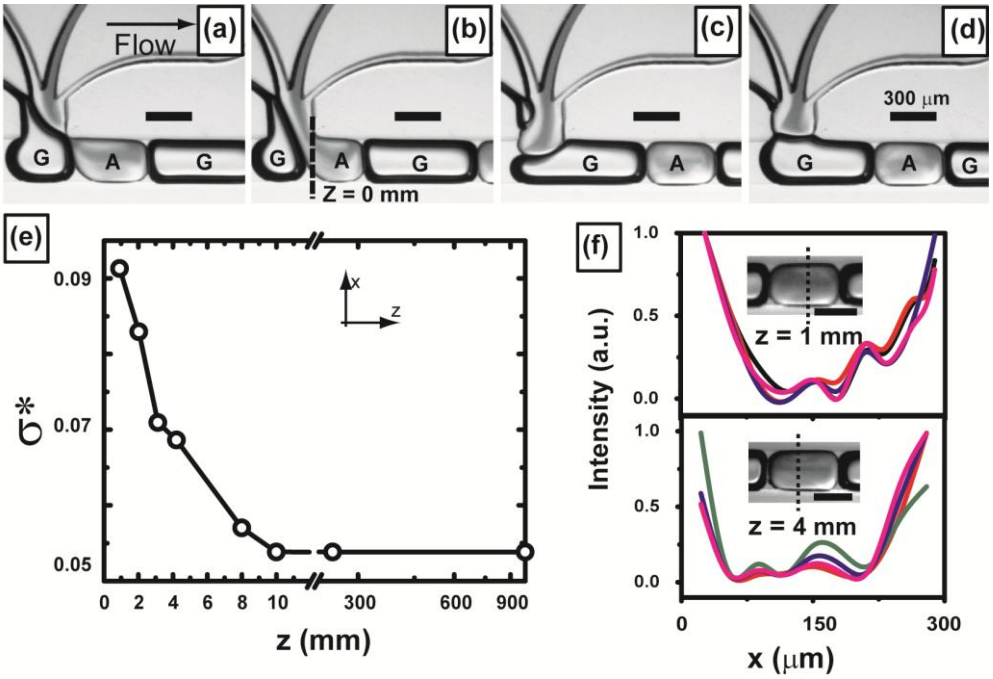

Figire 5.8. (a)-(d) Series of stereomicroscope images showing the breakup and formation of composite foams at the T-junction. **(e)** Mixing within a foam cell quantified by the normalized standard deviation σ*[*I(y)*] of dye intensity *I(y)* along the channel length. **(f)** Cross-sectional intensity profiles (along the dotted lines of the inset stereomicroscope images) at two different axial positions (z = 1 mm and 4 mm) along the microchannel.

Relative motion between liquid-filled foam cells and the microchannel walls generates recirculating fluid motion within the cells. Minute differences in surface roughness between opposite microchannel walls due to microfabrication tolerances and small differences in curvatures of the fluid interfaces break the symmetry of the velocity field within the cell, and cause rapid chaotic mixing of the contents.[33] The rapid mixing of contents within a foam cell has been quantified using the intensity of dye in the foam cell and plotted against the channel length as shown in Figure 5.8 (e). The intensity of the dye in the foam cell is calculated by determining the normalized standard deviation σ*[*I(y)*] of dye intensity *I(y)* where σ*= σ[*I(y)*]/<*I(y)*>, σ[*I(y)*] being the standard deviation and <*I(y)*> the average dye intensity at

varying locations along the length of the channel; where σ* = 1 indicates unmixed liquid while lower values of σ* signify homogenization, of the Complete mixing within a foam cell is achieved 10 mm away from the point of breakup in ~0.6 s.

In addition, mixing patterns within an aqueous foam cells is also extremely crucial for reproducible particle synthesis. This is determined by plotting the intensity profiles along the cross-section of several droplets at different axial positions along the microchannels. Mixing patterns are considered to be robust with little cell-to-cell variation if consecutive aqueous cells show nearly overlapping profiles. A plot of the intensity profiles at two different axial positions, z = 1 mm and 4 mm, along the microchannel is demonstrated in Figure 5.8 (f). The dotted lines of the inset stereomicroscope images are the positions along which the intensity profiles are plotted and they show very little cell-to-cell variation (plotted in different colors). *In situ* foam generation therefore enables controllable and reproducible reagent dispensing and rapid mixing. Furthermore, the intense mixing does not entail high shear rates, which can often lead to irreversible colloidal aggregation in macroscale methods involving mixing by agitation.[34,35]

The salient features of these foams are highlighted by demonstrating the first continuous process for the manufacture of metallodielectric ‘nanoshells’ and nanoislands using the method, which are otherwise a challenging synthesis to perform on a microfluidic platform. Details of the synthesis experiments as follows: note that we focus on the shell growth step; the other steps such as synthesis of silica particles and functionalization of these particles are performed by conventional methods as described in Section 5.1.1.

5.5. Microscale Foams with Inert Gas for Synthesis of Gold Nanoshells

Figure 5.9 is a two-dimensional conceptual schematic of using the microscale foams for synthesis of gold nanoshells. In this method, silicone oil forms the continuous phase liquid while a mixture of gold functionalized silica particles (seeded silica) and gold plating solution

(containing aged K-gold) constitutes reagent S while the reagent R is the reducing agent solution. The gas used in the experiment was inert nitrogen gas which only functioned in the breaking off of drops through the block-pinch mechanism and to periodically clear the aqueous streams from the T-junction, thereby preventing reagent buildup and nanoparticle deposition.

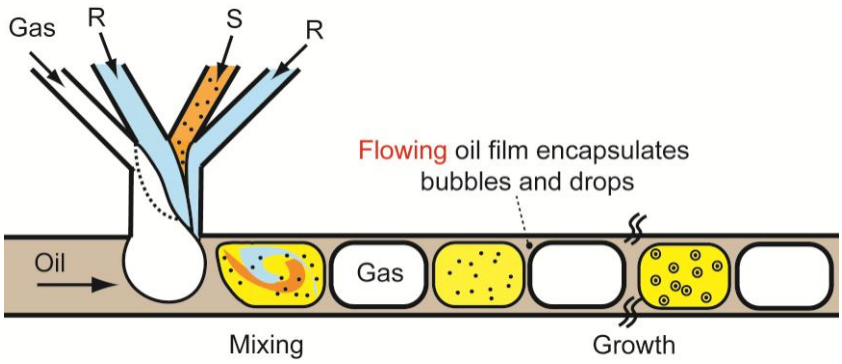

Figure 5.9. A two dimensional conceptual schematic of our nanoshell synthesis using composite foams.

5.5.1. Experimental

5.5.1.1. Microfabrication

Microfluidic device patterns were fabricated onto silicon wafers by standard photolithography using negative photoresist SU-8 2050. Devices were subsequently moulded in PDMS using the soft lithography technique.[36] Details of the fabrication of the master are provided in Appendix B while the actual channel design is shown in Figure 5.10. Briefly, PDMS was moulded onto the SU-8 masters at 70˚C for 2 hrs, peeled, cut and cleaned. Inlet and outlet holes (1/16-in. o.d.) were punched into the device. The microchannels were irreversibly bonded to a glass slide pre-coated with a thin layer of PDMS after a brief 35 s air plasma treatment. The microchannels have rectangular cross-section and are 300 μm wide, ~155 μm deep and 0.45 m long.

5.5.1.2. Microfluidic device setup and operation

A schematic of the experimental setup is shown in Figure 5.11. Syringe pumps (Harvard, PHD 2000) were used to deliver silicone oil (Dow Corning DC50, viscosity 10 cSt),

a mixture of seeded silica particles and gold plating solution (S) and reducing agent solution (R) to the microfluidic device while nitrogen gas was delivered from a cylinder equipped with a two-stage pressure regulator through circular PEEK tubings (60 µm i.d., 1 m long and 100 µm i.d., 2 m long) leading into the on-chip gas-inlet.

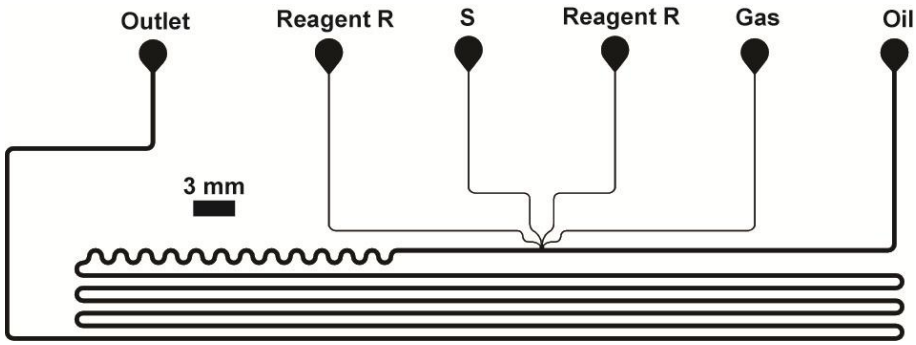

Figure 5.10. AutoCAD drawing of the microchannel.

The plating solution was aged (>24 hrs) gold hydroxide formed by the addition of 249 mg (1.8 mM) of potassium carbonate in 1L (0.435 mM) of gold salt solution. The ionic gold concentration ($Au^{[3+]}$) in the plating solution was varied from 0.43 mM to 0.29 mM, and volume fraction of gold-seeded silica particles ('f_s') in S was varied from ~0.003 % to 0.01%. Freshly prepared hydroxyl amine hydrochloride (4 mM) was used as the reducing agent in all experiments. Flow rates of the individual streams were S: 8 $\mu L.min^{-1}$, R: 2 $\mu L.min^{-1}$ and the volumetric flow ratio of aqueous reagents (S+R) to oil were maintained at 2. The nitrogen gas pressure was maintained at 17 psig.

Calculation of volume fraction of gold-seeded silica particles ('f_s'): Different volumes (0.02 mL to 1.3 mL) of the 1 $mg.mL^{-1}$ seeded silica solution were added to the corresponding volumes of K-gold solution (3.98 mL to 2.7 mL) to get 4 mL plating solution. The concentration of the seeded silica in the plating solution thus varied from 5×10^{-3} $mg.mL^{-1}$ to 3.34×10^{-1} $mg.mL^{-1}$. The corresponding volume fraction (%) is determined from the known density of the silica particles (2 $g.cc^{-1}$).

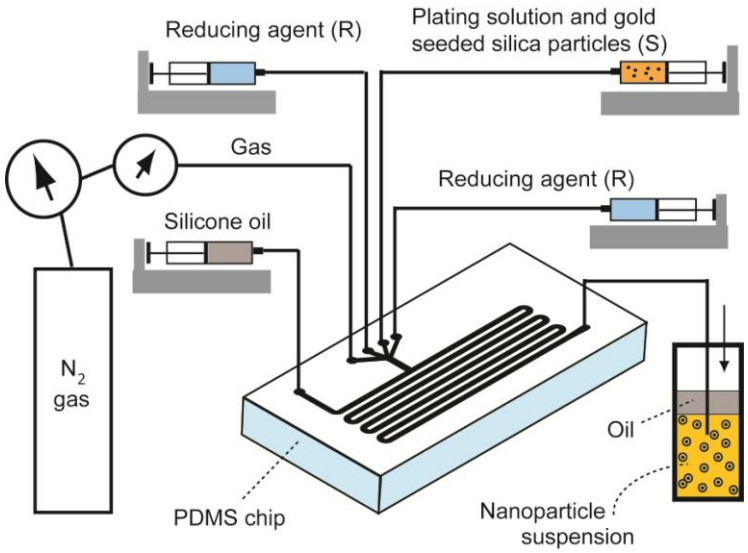

Figure 5.11. Diagrammatic representation of the experimental setup.

5.5.1.3. Sample collection and analysis

The outlet from the reactor was connected via fluoropolymer (FEP) tubing to a 2 mL centrifuge tube. Approximately 1 mL of the aqueous sample was collected in the tube for every experimental condition. The oil formed a layer on the surface of the collected aqueous fluid while the gas simply escaped into the ambient. The oil layer was carefully decanted and aqueous fluid samples containing nanoparticles were analyzed with a UV-vis spectrometer (Shimadzu UV-2450). The samples were further purified by repeated centrifugation and redispersion (in DI water) steps. A drop of this sample was placed onto a 200 mesh formvar protected copper grid and allowed to dry overnight. The copper grid was then analyzed using either TEM (JEOL 2010, accelerating voltage 200 kV) or FESEM (JEOL JSM-6700f, accelerating voltage 4-25 kV). Several images were taken at different locations on the grid and the particle sizes were found by manually measuring the diameter of at least 250 particles from several electron microscopy images.

5.5.2. Results and Discussion

A series of nanoshell growth experiments were conducted where the parameter space comprising of the volume fraction of gold-seeded silica particles f_s(%) and ionic gold concentration $Au^{[3+]}$ (mM) delivered into the aqueous cells of the foam lattice was systematically explored. All other reagent concentrations and flow rates were fixed.

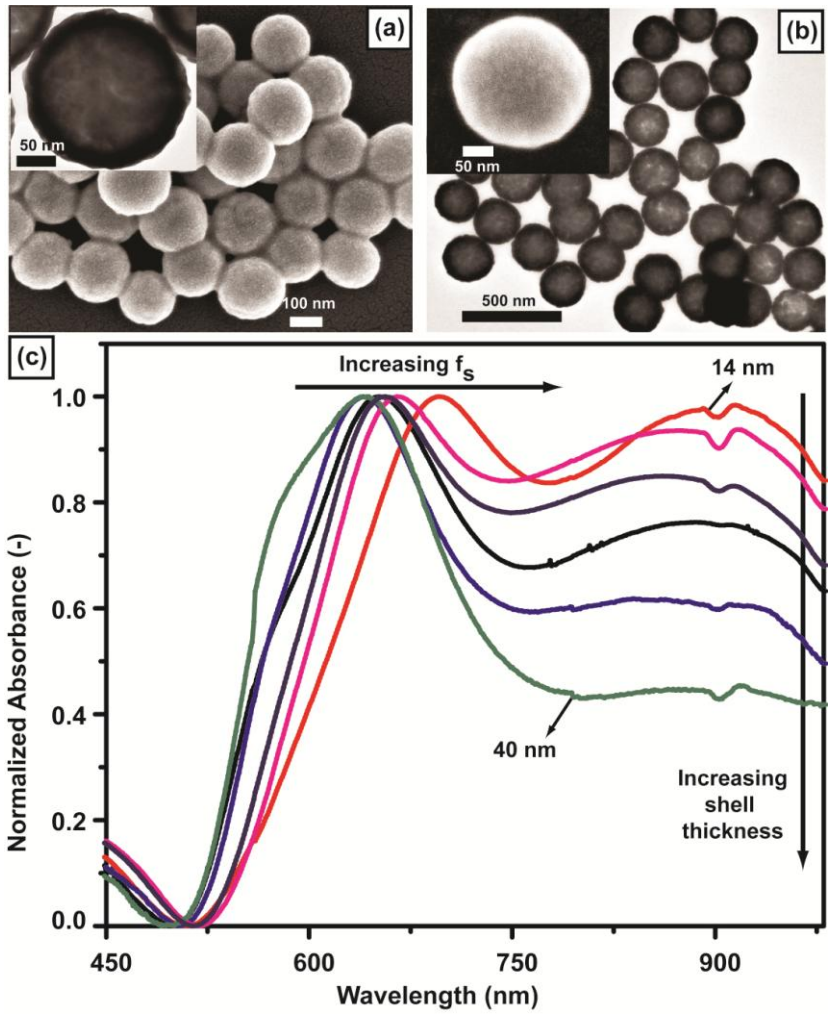

Figure 5.12 (a)–(b) TEM and SEM images of a population of complete smooth gold shells obtained with $Au^{[3+]}$ ~ 0.42 mM while the volume fraction of gold-seeded silica particles (f_s) and the shell thicknesses are **(a)** 1.5×10^{-3} % and ~14 nm; **(b)** 0.6×10^{-3} % and ~22 nm respectively. The insets show magnified images of a single gold nanoshell. **(c)** Ensemble optical absorbance spectra for several different shell thicknesses from 14 nm to 40 nm.

Uniformly sized particles with complete and smooth gold shells were obtained in a subset of the parameter space (Figure 5.12 (a) and (b)) where the shell thicknesses was tuned from ~10 nm - 40 nm. Histograms are provided in Figure 5.13; tight, unimodal particle size distributions are obtained under all synthesis conditions – a remarkable improvement over the small-scale batch synthesis of Figure 5.1 (e) and (f). A direct comparison of the histograms of particles obtained from batch scale synthesis and that using the current method is provided in Appendix D.

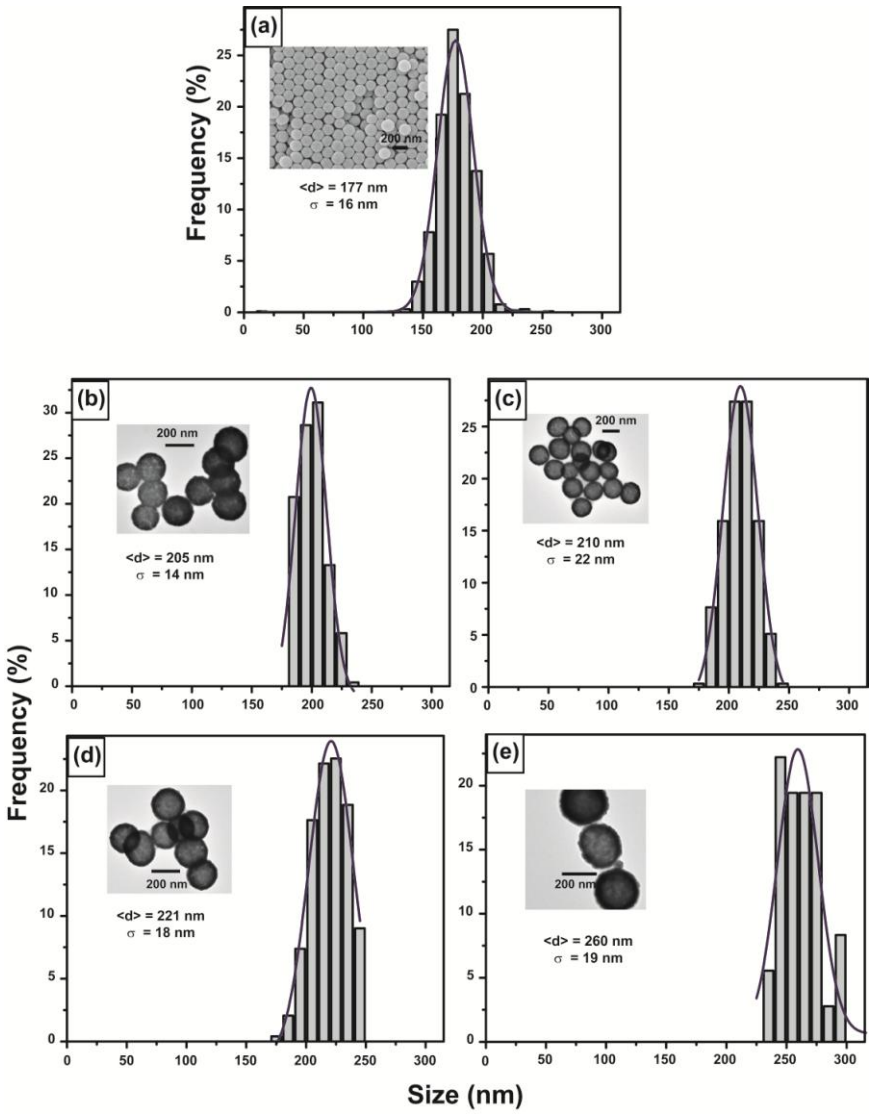

Figure 5.13. Particle size distribution of **(a)** Silica particle cores with the inset showing SEM image of the particle population. Average size of the silica particle population is 177 ± 16 nm. **(b)-(e)** Size distribution of complete smooth gold nanoshells with insets showing TEM images of the corresponding particle population with average sizes **(b)** 205 ± 14 nm, **(c)** 210 ± 22 nm, **(d)** 221 ± 18 nm and **(e)** 260 ± 19 nm.

The minimum complete shell thickness depends on the average spacing between gold nanoparticle seeds attached to the silica nanoparticle surface. Assuming 25% area coverage of the silica core surface by 3 nm gold seeds (an assumption made on the basis of electron microscopy observations), the total number of seeds attached to the silica surface (n) = 0.25 x (projected area of a 175 nm silica particle)/(projected area of a 3 nm seed) ~ 850. Further assuming equally spaced seeds, the distance between adjacent seeds works out to ~ 6 nm. Hence for the seeded silica used in the current experiments, an estimate of this spacing is ~6 nm. Ensemble UV-vis absorbance measurements in Figure 5.12 (c) clearly indicates the presence of two spectral resonance peaks, with a sharp lower wavelength peak at ~ 650 nm that blue-shifted with increasing shell thickness, and a broad shouldered peak at 900 nm.

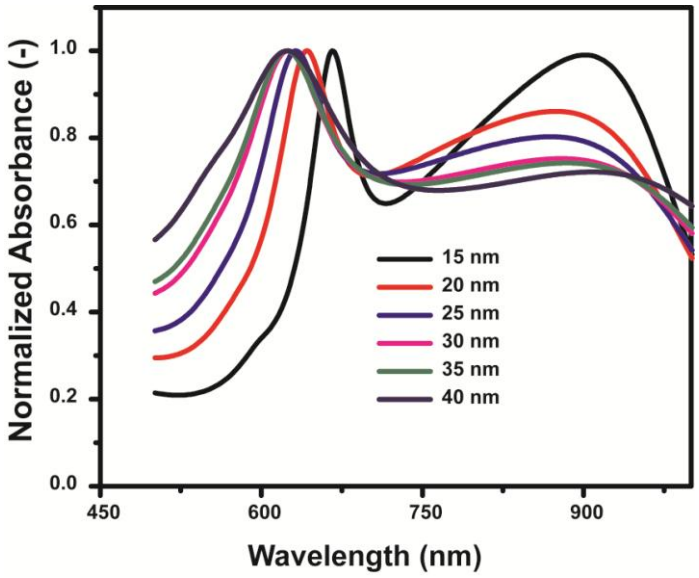

Figure 5.14. Mie theory calculations of single particle optical extinction spectra for 177 nm silica core size and varying shell thicknesses, from 15 – 40 nm.

It was observed that the shell thickness increased with increasing $Au^{[3+]}$:f_s ratios accompanied by a blue shift in the spectral peak from ~ 670 nm to ~ 635 nm. These peaks may be thought of as resulting from a hybridization of inner and outer shell plasmons. These ensemble measurements are in qualitative agreement with Mie theory calculations for light scattering from single nanoshells, made using measured average particle sizes, shown in Figure 5.14, thus complementing electron microscopy in indicating the presence of narrowly

distributed particle populations. The differences between the experimental spectra and the theoretical prediction may be accounted for by the fact that measured spectra correspond to ensembles of synthesized nanoshells having a finite size distribution of core sizes and shell thicknesses (corresponding to the histograms of Figure 5.13

Dielectric nanoparticles decorated with small metallic islands ('nano'-islands) are also of considerable interest as substrates for a wide range of biological sensing applications.[37] The optical properties of such particles depend on size and spacing of the metallic islands. Interactions between surface plasmons of neighbouring islands can strongly affect the positions of the optical resonances.[38] Tightly controlled populations of silica nanoparticles decorated with gold islands of various sizes were obtained on operating in the gold-limited region of the $Au^{[3+]}$- f_s parameter space, (Figure 5.15(b)-(d) and (f)-(h)).

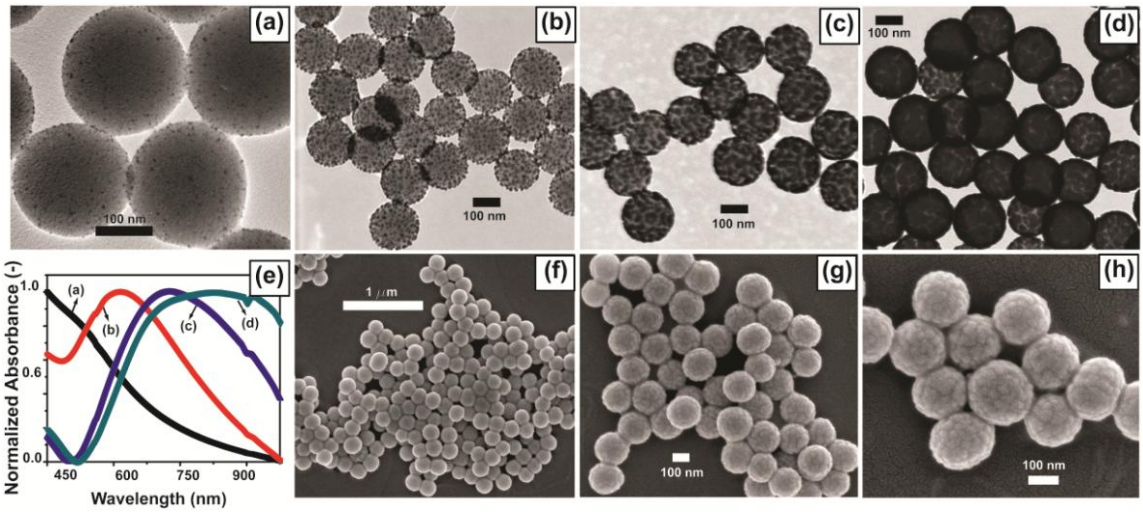

Figure 5.15. (a) TEM image of gold-seeded silica particles showing ~3 nm gold seeds (dark spots) on silica particles. **(b)-(d)** TEM images illustrating gold seeds grown from ~3 nm to **(b)** ~10 nm, **(c)** ~35 nm, and **(d)** nearly coalesced islands. **(e)** Ensemble optical absorbance measurements. **(f)–(g)** SEM images corresponding to TEM images in (a)-(d). Ionic gold concentration $Au^{[3+]}$ and volume-fraction of gold-seeded silica (f_s) in the plating solution are as follows: **(b)** 0.29 mM and 1.2×10^{-2}%, **(c)** 0.39 mM and 3.8×10^{-3} % and **(d)** 0.4 mM and 3.4×10^{-3} % respectively.

Electron microscopy analysis of these particles also indicates a possible mechanism of nanoshell growth, in which growing seed particles first coalesce into large, irregularly shaped islands that eventually coalesce to yield a complete shell (Figure 5.16). Further, anisotropic

island growth was observed, with the growth being more pronounced in-plane along the silica surface than in the radial direction, leading to large flattened islands. The combined effect of anisotropy in island shape and localized surface plasmon interactions between islands is to red-shift the absorption maximum (Figure 5.15 (e)), with further peak broadening due to finite island size distributions.[6]

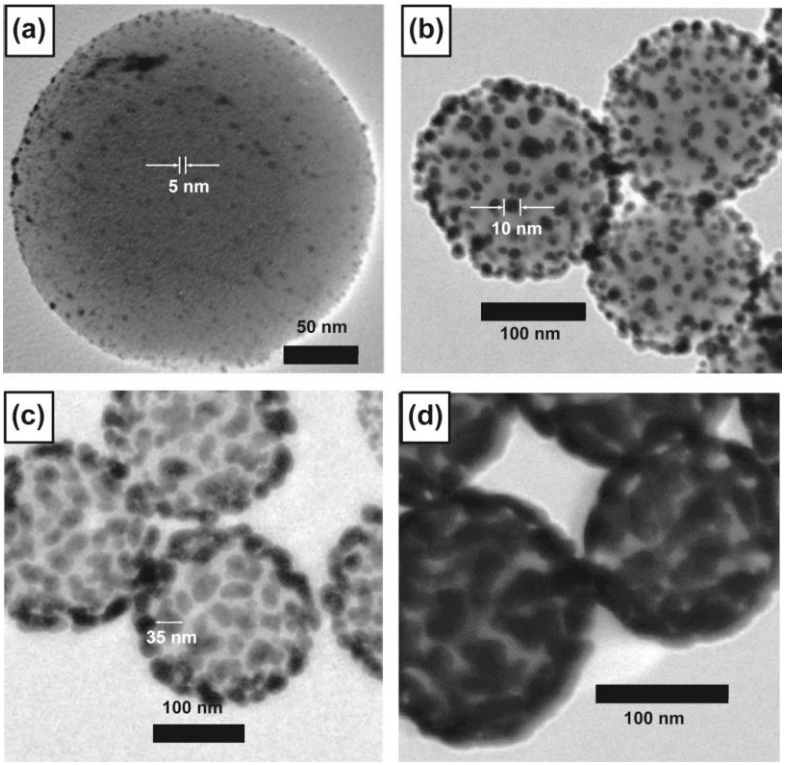

Figure 5.16. TEM images showing the growth of gold seeds from **(a)** 5 nm spheres (scale bar represents 50 nm) to **(b)** 10 nm spheres and **(c)** ~35 nm (measured in-plane) flattened islands; **(d)** nearly coalesced islands.

The device was operated continuously at single-device throughputs of ~1 $mL.hr^{-1}$ with silica volume fractions of up to 0.015% for up to 12 hrs per run.

5.6. Microfluidic Compound Drops with Reactive Gas for Synthesis of Gold Nanoshells

The microfluidic composite foams using inert nitrogen gas is an automated and controlled approach for the synthesis of gold nanoshells and nanoislands. The dependence of physical parameters such as reagent contacting and mixing was successfully isolated from the actual chemistry leading to monodisperse and precisely controlled particle population. However the use of aqueous reagents entails problems such as ageing and degradation of the precursor solution with time, loss of activity of the reducing agent, changes in the equilibrium concentrations of the reagents, presence or absence of dissolved gases which will affect the final product morphology as well as composition.[39] These changes in the aqueous solutions are difficult to control or monitor over time and can change even during the course of the experimental time.

Gaseous reducing agents in place of the aqueous hydroxylamine hydrochloride used in the previous sections on the other hand will overcome almost all of these drawbacks. In addition, the methods described so far for the synthesis of particles using aqueous reagents solutions are essentially semi-batch methods accomplishing controlled dispensing and mixing i.e. controlled contacting and fast mixing of reagents. These reagents spend ~ 30 to 45 seconds in the microchannel and are then collected in the sampling vial, where they are allowed to react completely for several hours. A completely continuous method will require quenching of the reaction once the reagents are collected in the sampling vial. However the use of gaseous reducing agent will yet again overcome this issue, since the gaseous reactant will escape into the ambient as soon as the fluids flow into the collection vial.

The synthesis of gold nanoshells and gold nanoislands has been accomplished using gas phase reducing agents recently.[39] According to the authors, gaseous carbon monoxide (CO) for the reduction of $Au^{[3+]}$ to $Au^{[0]}$ during the synthesis of gold nanoshells results in high

quality, thin shells irrespective of the age of the reagents. CO is a classical reducing agent used for the synthesis of gold nanocrystals since the early 1900s[40] and more recently CO has been used as a reducing agent for the synthesis of other types of nanoparticles such as Pt nanocubes, Pd nanocrystals as well as various other shapes and sizes of gold nanomaterials.[41] Besides use of the highly toxic gas CO in a microfluidic setup is safer than using it in traditional flask setup due to the inherent advantages of microfluidics as already pointed out in Chapter 2.

5.6.1. Method Development

CO acts as a reducing agent providing the necessary electrons to reduce $Au^{[3+]}$ to $Au^{[0]}$, in the presence of seeded silica, which acts as the catalyst. CO dissolves in the aqueous solution containing the reagents and liberates hydrogen providing the necessary electrons according to the following water-gas shift reaction

$$CO(g) + H_2O \xrightarrow{yields} CO_2(aq) + 2e^- + 2H^+ \quad (5.2)$$

The $AuCl_4^-$ from the salt solution $HAuCl_4$ is initially reduced to $AuCl_2^-$ and then to $Au^{[0]}$, in the presence of seeds according to the following equations

$$AuCl_4^- + 2e^- \xrightarrow{yields} AuCl_2^- + 2Cl^- \quad (5.3)$$

$$AuCl_2^- + e^- \xrightarrow{yields} Au^0 + 2Cl^- \quad (5.4)$$

CO has to dissolve in the aqueous solution and come in contact with the seeds and the plating solution at the same time for controlled reaction kinetics. Hence, the use of a gaseous reducing agent in small scale flasks does not preclude the practical difficulties similar to using aqueous reducing agent in terms of reagent contacting and mixing. As shown in Figure 5.17 (a), batch experiments usually contain the aqueous reagents in a stirred flask with a head space of the gaseous reagent which diffuses through the aqueous solution over a period of time, resulting in the formation of products. Control over the reagent contacting and mixing is difficult to achieve resulting in a polydisperse particle population.

On the other hand, use of reactive gas CO, in microfluidic compound drops which are yet another class of the three-phase microfluidic flows (Figure 5.5 (c), (d) and (e)), will complement the advantages of the microfluidic method along with the advantages of using gas phase reductant, thus overcoming almost all the drawbacks of the method. As shown in Figure 5.17 (b), the gas compartment of the compound drop will contain the reactive CO while the liquid compartment will contain the aqueous reagents which are separated from each other by a thin film of oil. The gas diffuses through the thin oil interface into the aqueous compartment and is immediately taken up by the recirculating liquid which mixes the fluids faster than the reaction rate.

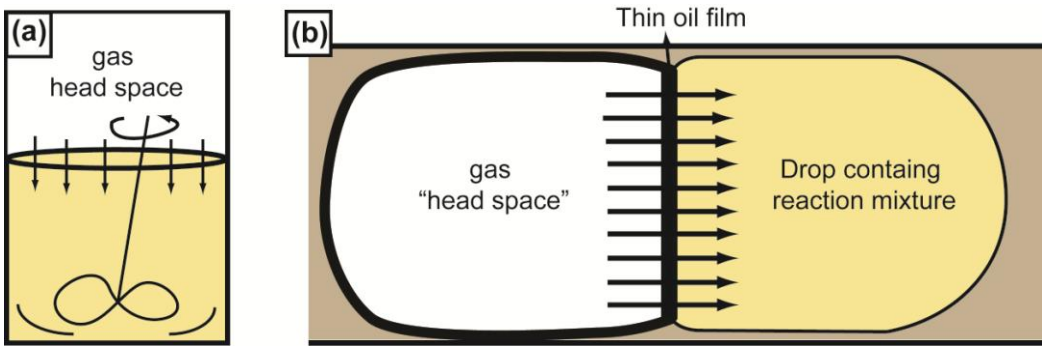

Figure 5.17. Schematic showing the reaction between a gas phase reductant and the aqueous reagents in **(a)** Flask and **(b)** A compound-drop.

Isolating the gas phase from the aqueous phase is essential before the formation of the compound drops. The contacting of reagents before they are confined into the drops will lead to immediate reaction and channel wall deposition. Hence the microfluidic method discussed in Section 5.3, where a single T-junction is used for all reagents and the gas, for the formation of compound drops cannot be used in the case of reactive gas. A modified method in which the gas bubbles and the aqueous droplets are generated in separate T-junctions which are then allowed to merge downstream in another T-junction, as shown in Figure 5.18 is proposed for the use of reactive gas for the synthesis of gold nanoshells. The droplets containing the aqueous reagent solutions and the gas bubbles containing the reactive gas meet at the T-

junction downstream once they are formed and are stable. Due to the difference in the translational speed of the two phases, the gas bubble catches up with the aqueous droplet ahead of it and merges to form the compound drop. As soon as they merge, diffusion of the gas begins, leading to the aqueous phase and the reaction begins.

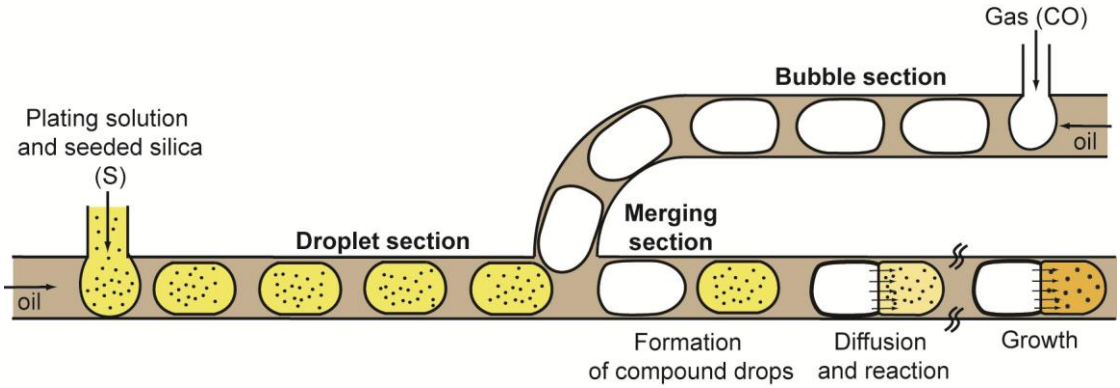

Figure 5.18. Schematic of the method using reactive gas

Since CO is used as the reactive gas in the current experiment, the reactor setup has to be in the fume hood during the reaction. Hence imaging of the reactor setup during the experiment is not feasible. In order to study the flow profile and analyze the feasibility of the experiments and the limits on the operating flow rates, the experiment was performed with nitrogen gas and water and the stereomicroscopic images are shown in Figure 5.19. At the operational flow rates and pressure (mentioned in the experimental section), uniform, equal sized gas bubbles and droplets form in their respective sections as shown in Figure 5.19 (a) and (b). In addition, they merge at the merging section to form compound drops as shown (Figure 5.19 (c)). Variations of the flow rates and pressures show that at times a single droplet is split into two by the advancing bubble and the second droplet (which in most cases is smaller than the first) is attached to the next bubble. Hence the sizes of the compound drops are not always uniform. However, considering the smallest bubble of length ~ w, w being the channel width, merging with the longest drop of length ~ 6w, (w = 300 µm), the number of moles of CO present in the bubble is 3.64×10^{-10}, calculated assuming ideal gas behaviour at a pressure of 10

psig. Assuming the highest concentration of the plating solution used for the formation of the thickest shell in the shell growth experiment which is 0.43 mM (from Section 5.5.2), the number of moles of $HAuCl_4$ in the drop will be 2.76×10^{-11}. In accordance to the Eq. 5.3 and Eq. 5.4, each of these moles of $HAuCl_4$ requires three electrons for complete reduction. Hence the number of moles of CO required for the reduction of the entire salt solution completely will be 4.1×10^{-11} while the available moles of CO (even if the smallest bubble is attached to this droplet) is 3.64×10^{-10}, an order of magnitude in excess. Hence the reaction is feasible even if the smallest bubble forms the compound drop (Figure 5.5 (e))

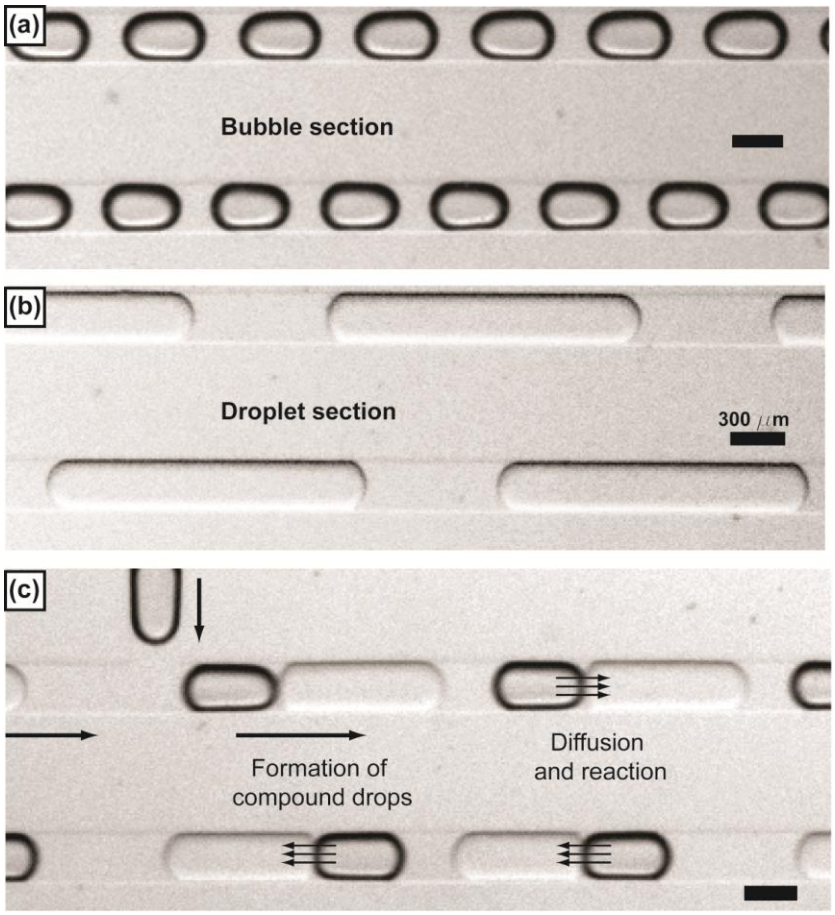

Figure 5.19. Stereomicroscopic images of the flow showing the **(a)** Bubble section. **(b)** Droplet section and **(c)** Merging section where the bubble meets the droplet at a T-junction and forms a compound drop.

5.6.2. Experimental

The experimental protocol is similar to the experimental described in Section 5.5.1. Some minor changes are pointed out in the following sections

5.6.2.1. Synthesis of Silica Particles

The silica core size used for this experiment was ~105 nm, a variation from the previous experiments where the core size was ~170 nm. The concentration of reagents used for this purposes were 0.27 mL (0.13 M) of TEOS and 0.59 mL of NH_3 (0.87 M) in 4.59 mL of ethanol. All other steps in the protocol were exactly the same.

5.6.2.2. Microfabrication

The lengths of the microchannels are different due to the difference in the device design. Details of the fabrication of the master are provided in Appendix B while the actual channel design is shown in Figure 5.20. The length of the bubble section was ~ 17 cm and that of the droplet section was ~ 33 cm while the length of the reactor in which reaction occurred was ~30 cm.

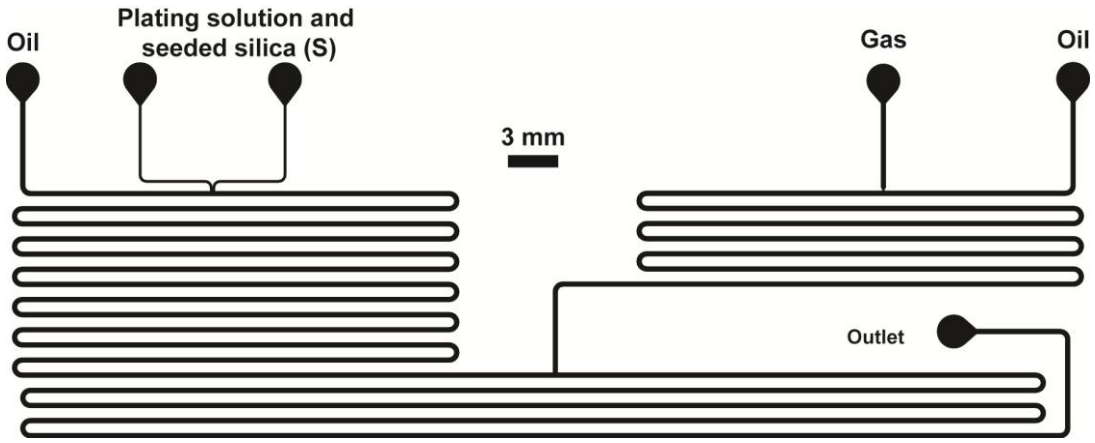

Figure 5.20. AutoCAD drawing of the microchannel.

5.6.2.3. Microfluidic device setup and operation

A schematic of the experimental setup is shown in Figure 5.21.

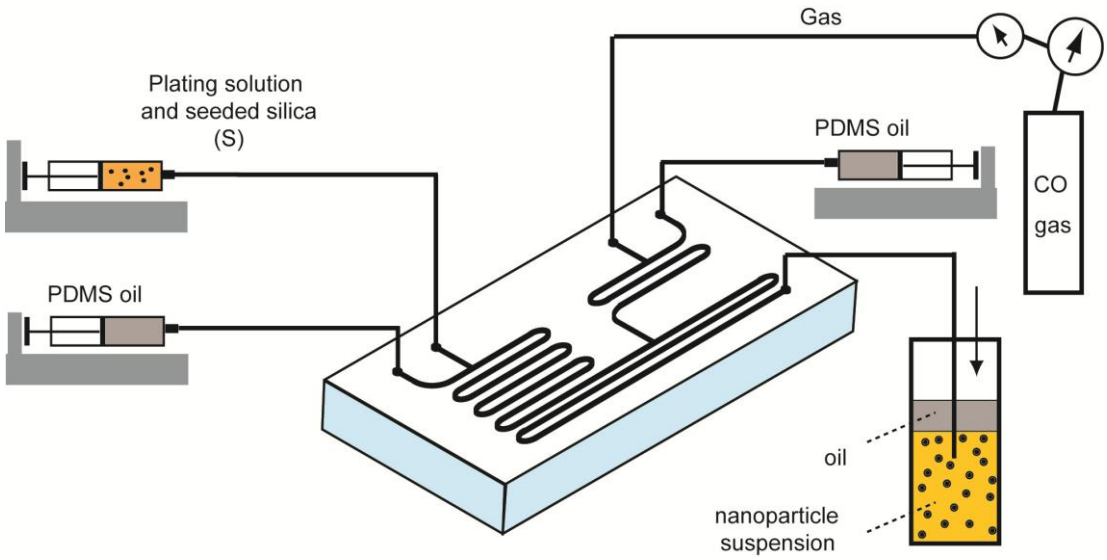

Figure 5.21. Diagrammatic representation of the experimental setup.

The entire setup along with the syringe pumps and the tubings were placed in the fume hood with the sash low during the experiment. Individual pumps were used for the two oil inlets, one for the bubble section and the other for the droplet section, to allow for easy flow rate changes. The length of the 100 µm i.d. PEEK tubing connected to the CO cylinder was 1m. The concentrations of the plating solution used and that of the seeded silica particles are the same as the mentioned in Section 5.5.1.2. Flow rates of the individual streams were S: 10 $\mu L.min^{-1}$ and the PDMS oil were 10 $\mu L.min^{-1}$ each. The gas pressure was maintained at 10 psig.

5.6.3. Results and Discussion

Both nanoshell growth experiments as well as nano-island growth experiments were performed similar to the shell growth experiments in Section 5.4.2 using the aqueous reducing agent. Both complete, uniform and smooth gold nanoshells as well as gold nano-islands of different

sizes were obtained through the method as shown in Figure 5.22. Ensemble UV-vis absorbance measurements in Figure 5.22 (a) for gold nanoshells indicates spectral resonance peaks between 700 nm and 800 nm that blue-shifted with increasing shell thickness as was previously observed in Figure 5.12 for gold nanoshells. The minimum shell thickness obtained in this case was ~10 nm (Figure 5.22 (c)), with a spectral peak at 790 nm.

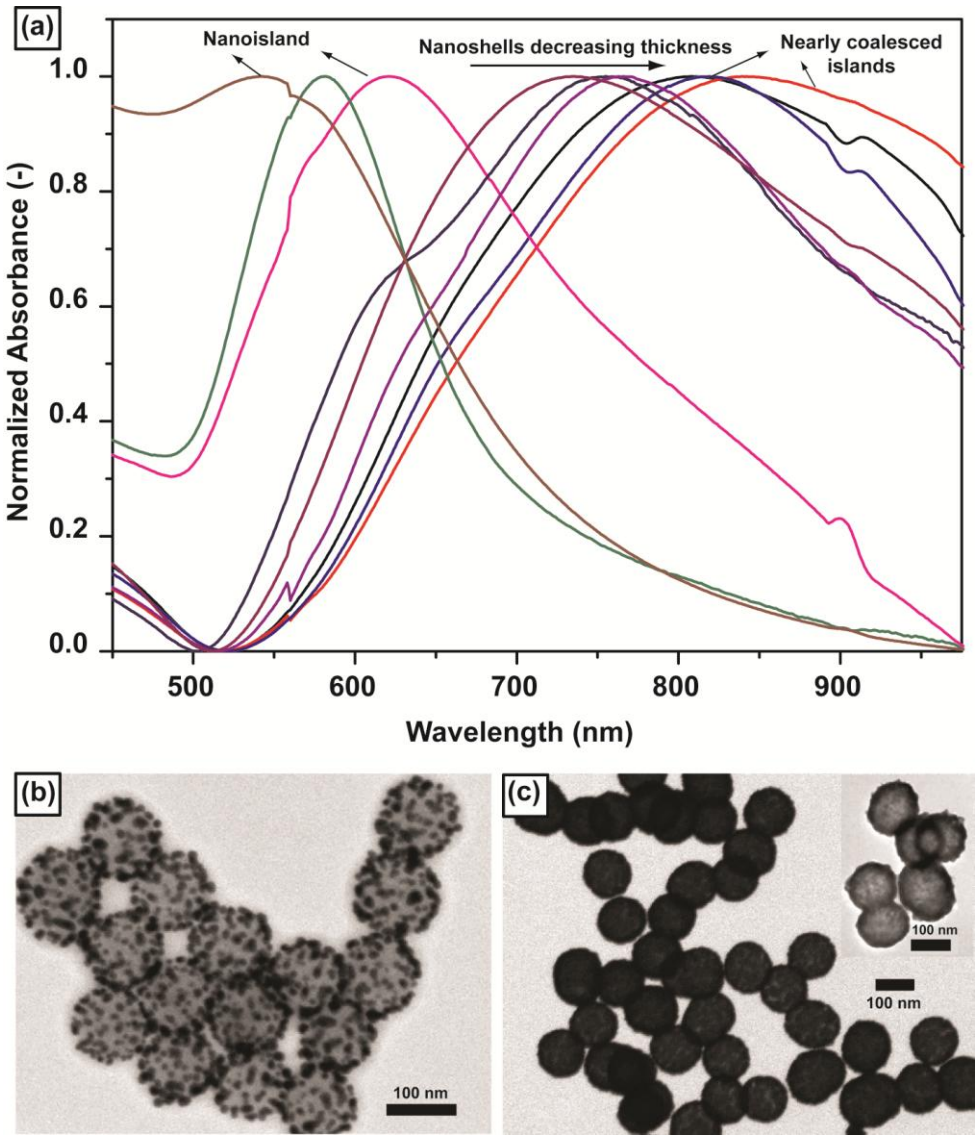

Figure 5.22 (a) Ensemble optical absorbance spectra for several different gold nanoislands, nanoshells and nearly coalesced nanoislands. TEM images of a population of **(b)** Gold nanoislands on the silica particles of size ~10 nm nm obtained with concentration $[Au^{[3+]}]$~0.3 mM while the volume fraction of gold-seeded silica particles (f_s) was 2×10^{-2} % **(c)** Complete smooth gold shells of thickness ~10 nm obtained with $Au^{[3+]}$ ~0.42 mM while the volume fraction of gold-seeded silica particles (f_s) was 1.6×10^{-3} %; The insets show magnified images of a group of gold nanoshells taken using the light view mode.

In addition, similar to the gold nanoislands in Figure 5.15, gold nanoislands indicating the growth of the seeds on the seeded silica particles were also obtained from the current experiments as shown in the UV spectra and the TEM image in Figure 5.22 (a) and (b). The size of the nanoislands in this case is ~ 10 nm with a spectral peak at 600 nm. As these seeds grow into larger nanoparticles with more pronounced growth along the lateral axis, they form nearly coalesced islands with a broad spectral peak between 790 nm and 850 nm (Figure 5.22 (a)). The results presented above are proof of concept results for the use of reactive gases in microfluidic compound drops. Further work is in progress to analyze the method in detail.

5.7. Summary

The microfluidic methods introduced in this chapter are simple to implement; reagent dispensing and rapid mixing is accomplished in robust, automated fashion with no operator intervention, and uniformly sized non-aggregated particles requiring no post-synthesis treatment are obtained. The methods are not limited merely to electroless plating chemistries, and can be readily adopted to a broad range of colloidal syntheses. As a further example, gold nanorods synthesized in Chapter 3 using the droplet microflows were also synthesized using microfluidic composite foams with inert nitrogen gas as shown in Appendix E.

The current limitation is the material used for device fabrication (PDMS), due to which only room-temperature *aqueous*-based colloidal chemistry are possible using these methods. Extension to higher-temperatures and non-aqueous syntheses will require microfabrication in materials such as glass or silicon, and appropriate selection of the carrier ‘oil’ phase, which has to be immiscible with the solvent(s) used, while preferentially wetting the microchannel surfaces. The inherently digital nature of foam-based nanoparticle processing also raises the possibility of autonomous logic-based processing for high-throughput applications such as, for example, rapid parameter-space exploration of colloidal syntheses.

A new technological scheme for continuous plasmonic nanoparticle synthesis was presented and both inert and reactive multiphase experiments were performed. The methods presented successfully bridge multiphase microfluidics and colloidal synthesis thus making an important advance towards continuous sustainable nanomanufacturing processes.

5.8. References

1 Oldenburg, S. J., Jackson, J. B., Westcott, S. L. & Halas, N. J. Infrared Extinction Properties of Gold Nanoshells. *Applied Physics Letters* **75**, 2897 - 2899 (1999).

2 Hirsch, L. R. *et al.* Nanoshell-Mediated Near-Infrared Thermal Therapy of Tumors under Magnetic Resonance Guidance. *Proceedings of the National Academy of Sciences of the United States of America* **100**, 13549–13554 (2003).

3 Oldenburg, S. J., Averitt, R. D., Westcott, S. L. & Halas, N. J. Nanoengineering of Optical Resonances. *Chemical Physics Letters* **288**, 243–247 (1998).

4 Nehl, C. L. *et al.* Scattering Spectra of Single Gold Nanoshells. *Nano Letters* **4**, 2355-2359 (2004).

5 Lassiter, J. B., Knight, M. W., Mirin, N. A. & Halas, N. J. Reshaping the Plasmonic Properties of an Individual Nanoparticle. *Nano Letters* **9**, 4326–4332 (2009).

6 Bohren, C. F. & Huffman, D. R. *Absorption and Scattering of Light by Small Particles*. (Wiley, 1983).

7 Prodan, E., Radloff, C., Halas, N. J. & Nordlander, P. A Hybridization Model for the Plasmon Response of Complex Nanostructures. *Science* **302**, 419-422 (2003).

8 Westcott, S. L., Oldenburg, S. J., Lee, T. R. & Halas, N. J. Formation and Adsorption of Clusters of Gold Nanoparticles onto Functionalized Silica Nanoparticle Surfaces. *Langmuir* **14**, 5396-5401 (1998).

9 Graf, C. & Blaaderen, A. v. Metallodielectric Colloidal Core-Shell Particles for Photonic Applications. *Langmuir* **18**, 524-534 (2002).

10 Wang, H. *et al.* Symmetry Breaking in Individual Plasmonic Nanoparticles. *Proceedings of the National Academy of Sciences of the United States of America* **103**, 10856–10860 (2006).

11 Stremsdoerfer, G., Perrot, H., Martin, J. R. & Clechet, P. Autocatalytic Deposition of Gold and Palladium onto n-GaAs in Acidic Media. *Journal of the Electrochemical Society* **135**, 2881-2886 (1988).

12 Weiss, G. H. Overview of Theoretical Models for Reaction Rates. *Journal of Statistical Physics* **42**, 3-36 (1986).

13 Stober, W., Fink, A. & Bohn, E. Controlled Growth of Monodisperse Silica Spheres in the Micron Size Range. *Journal of Colloid and Interface Science* **26**, 62-69 (1968).

14 Bogush, G. H. & Zukoski IV, C. F. Uniform Silica Particle Precipitation: An Aggregative Growth Model. *Journal of Colloid and Interface Science* **142**, 19 - 34 (1991).

15 Bogush, G. H., Tracy, M. A. & Zukoski IV, C. F. Preparation of Monodisperse Silica Particles: Control of Size and Mass Fraction. *Journal of Non-Crystalline Solids* **104**, 95 - 106 (1988).

16 Duff, D. G., Baiker, A. & Edwards, P. P. A New Hydrosol of Gold Clusters. 1. Formation and Particle Size Variation. *Langmuir* **9**, 2301-2309 (1993).

17 Blaaderen, A. v. & Vrij, A. Synthesis and Characterization of Monodisperse Colloidal Organo-silica Spheres. *Journal of Colloid and Interface Science* **156**, 1-18 (1993).

18 Guillot, P. & Colin, A. Stability of Parallel Flows in a Microchannel after a T Junction. *Physical Review E* **72**, 066301 (2005).

19 Link, D. R., Anna, S. L., A.Weitz, D. & Stone, H. A. Geometrically Mediated Breakup of Drops in Microfluidic Devices. *Physical Review Letters* **92**, 054503 (2004).

20 Ajaev, V. S. & Homsy, G. M. Modeling Shapes and Dynamics of Confined Bubbles. *The Annual Review of Fluid Mechanics* **38**, 277-307 (2006).

21 Dreyfus, R., Tabeling, P. & Willaime, H. Ordered and Disordered Patterns in Two-Phase Flows in Microchannels. *Physical Review Letters* **90**, 144505 (2003).

22 Günther, A., Khan, S. A., Thalmann, M., Trachsel, F. & Jensen, K. F. Transport and Reaction in Microscale Segmented Gas–Liquid Flow. *Lab on a Chip* **4**, 278 – 286 (2004).

23 Stebe, K. J., Lin, S.-Y. & Maldarellia, C. Remobilizing Surfactant Retarded Fluid Particle Interfaces. I. Stress-Free Conditions at the Interfaces of Micellar Solutions of Surfactants with Fast Sorption Kinetics. *Physics of Fluids A* **3**, 3-20 (1991).

24 Khan, S. A. & Duraiswamy, S. Microfluidic Emulsions with Dynamic Compound Drops. *Lab on a Chip* **9**, 1840–1842 (2009).

25 Hashimoto, M., Garstecki, P. & Whitesides, G. M. Synthesis of Composite Emulsions and Complex Foams with the use of Microfluidic Flow-Focusing Devices. *Small* **3**, 1792-1802 (2007).

26 Weaire, D. & Hutzler, S. *The Physics of Foams* (New York : Oxford University Press, 1999).

27 Denkov, N. D., Subramanian, V., Gurovich, D. & Lips, A. Wall slip and viscous dissipation in sheared foams: Effect of surface mobility. *Colloids and Surfaces A* **263**, 129-145 (2005).

28 Zheng, B. & Ismagilov, R. F. A Microfluidic Approach for Screening Submicroliter Volumes against Multiple Reagents by using Preformed Arrays of Nanoliter Plugs in a Three-Phase Liquid/Liquid/Gas Flow. *Angewandte Chemie-International Edition* **44**, 2520-2523 (2005).

29 Engl, W., Ohata, K., Guillot, P., Colin, A. & Panizza, P. Selection of Two-Phase Flow Patterns at a Simple Junction in Microfluidic Devices. *Physical Review Letters* **96**, 134505-134501 -134505 (2006).

30 Christopher, G. F. & Anna, S. L. Microfluidic Methods for Generating Continuous Droplet Streams. *Journal of Physics D : Applied Physics* **40**, R319–R336 (2007).

31 Boleininger, J., Kurz, A., Reuss, V. & Sonnichsen, C. Microfluidic Continuous Flow Synthesis of Rod-Shaped Gold and Silver Nanocrystals. *Physical Chemistry Chemical Physics* **8**, 3824-3827 (2006).

32 Kohler, J. M., Wagner, J. & Albert, J. Formation of Isolated and Clustered Au Nanoparticles in the Presence of Polyelectrolyte Molecules using a Flow-Through Si Chip Reactor. *Journal of Materials Chemistry* **15**, 1924-1930 (2005).

33 Ottino, J. M. *The Kinematics of Mixing: Stretching, Chaos, and Transport* (Cambridge University Press, 1989).

34 Torres, F. E., Russel, W. B. & Schowalter, W. R. Simulations of Coagulation in Viscous Flows. *Journal of Colloid and Interface Science* **145**, 51-73 (1991).

35 Torres, F. E., Russel, W. B. & Schowalter, W. R. Floc Structure and Growth Kinetics for Rapid Shear Coagulation of Polystyrene Colloids. *Journal of Colloid and Interface Science* **142**, 554-574 (1991).

36 Beh, W. S., Kim, I. T., Qin, D., Xia, Y. & Whitesides, G. M. Formation of Patterned Microstructures of Conducting Polymers by Soft Lithography and Applications in Microelectronic Device Fabrication. *Advanced Materials* **11**, 1038-1041 (1999).

37 Anker, J. N. *et al.* Biosensing with Plasmonic Nanosensors. *Nature Materials* **7**, 442-453 (2008).

38 Wang, H. *et al.* Controlled Texturing Modifies the Surface Topography and Plasmonic Properties of Au Nanoshells. *Journal of Physical Chemistry B* **109**, 11083-11087 (2005).

39 Brinson, B. E. et al. Nanoshells Made Easy: Improving Au Layer Growth on Nanoparticle Surfaces. *Langmuir* **24**, 14166-14171 (2008).

40 Donau. *Monatshefte für Chemie - Chemical Monthly* **25**, 525 (1905).

41 Kang, Y., Ye, X. & Murray, C. B. Size- and Shape-Selective Synthesis of Metal Nanocrystals and Nanowires Using CO as a Reducing Agent. *Angewandte Chemie - International Edition* **49**, 6156 –6159 (2010).

6. Integrated Microfluidic Synthesis of Anisotropic Gold Nanocrystals

The main objective of this chapter is to synthesise gold nanocrystals of varying shapes, sizes and morphology using a one-step protocol on a single chip. This is realized by integrating the synthesis of small gold nanocrystals (< 5 nm, which are used as seeds) with the growth of these seeds into gold nanocrystals of varying shapes and sizes. Both these individual steps have been demonstrated in Chapters 3 and 4. The design of a chip that can perform both these syntheses and effectively overcome the engineering challenges involved in integrating the two individual methods, is described in detail in this chapter. Integrating the two separate methods will potentially enable the synthesis of gold nanocrystals of any shape and size "on demand" from a single chip in a single step by simply varying the reagent flow rates as required. Preliminary experiments showing the method development and th possibility of synthesizing gold nanomaterials using the integrated approach are presented in this chapter. A detailed exploration of the method for synthesis of varying ARs of GNR and other shapes and sizes of gold nanomaterials is under progress at the time of writing this thesis. The protocol adopted for the synthesis of seeds and their growth into gold nanocrystals of varying sizes and shapes is the same as described in the previous chapters (Chapters 3 and 4). This chapter will mainly concentrate on method development and designing strategies for integrating the two methods and how the experimental protocol is designed to achieve the one step seeded growth of gold nanorods.

6.1. Method Development

Gold nanocrystals synthesized using the segmented gas-liquid flows in Chapter 4 can be directly used as seeds for synthesis of gold nanocrystals using the droplet method described in Chapter 3. The method used for the synthesis of small (< 5 nm) gold nanocrystals (seeds), referred to as stage 1 and the droplet microfluidic method for the synthesis of gold nanomaterials, stage 2, can be directly integrated by connecting the outlet from the stage 1 to the seeds inlet of stage 2 as show in Figure 6.1.

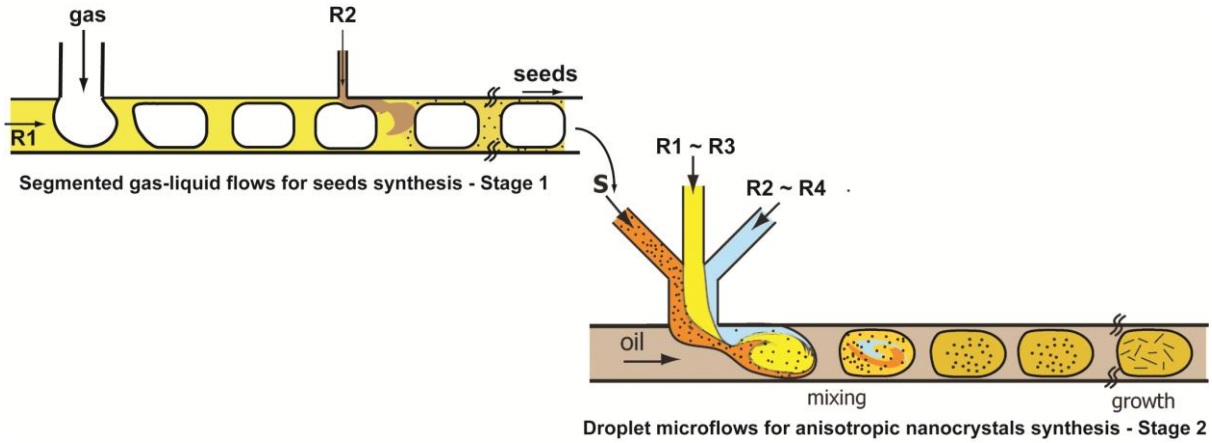

Figure 6.1. Schematic showing the direct integration of the methods from Chapters 3 and 4.

However, the channel dimension of the outlet of stage 1 is 300 µm and the inlet channel in stage 2 is of 100 µm. In order to achieve smooth transition of the seeds from stage 1 channels to stage 2, the channels in stage 1 are modified such that they are the same dimension as that of the seed inlet in stage 2 as depicted in the schematic in Figure 6.2. Aqueous reagent solutions (R1 and R2) and pure nitrogen gas are separately delivered into the corresponding inlets in stage 1 while aqueous reagent solutions R3 and R4 are delivered to their respective inlets in one arm of the T-junction in stage 2. The seeds synthesized in stage 1 are directly delivered to the seeds inlet of stage 2. Immiscible cross-flowing oil is delivered into the other arm of the T-junction in stage 2. Droplets are pinched off at the T-junction while the bubbles from stage 1 flow out into stage 2 without affecting the breakup and formation of droplets at

the T-junction. The droplets and bubbles flow in an alternating train downstream of the T-junction.

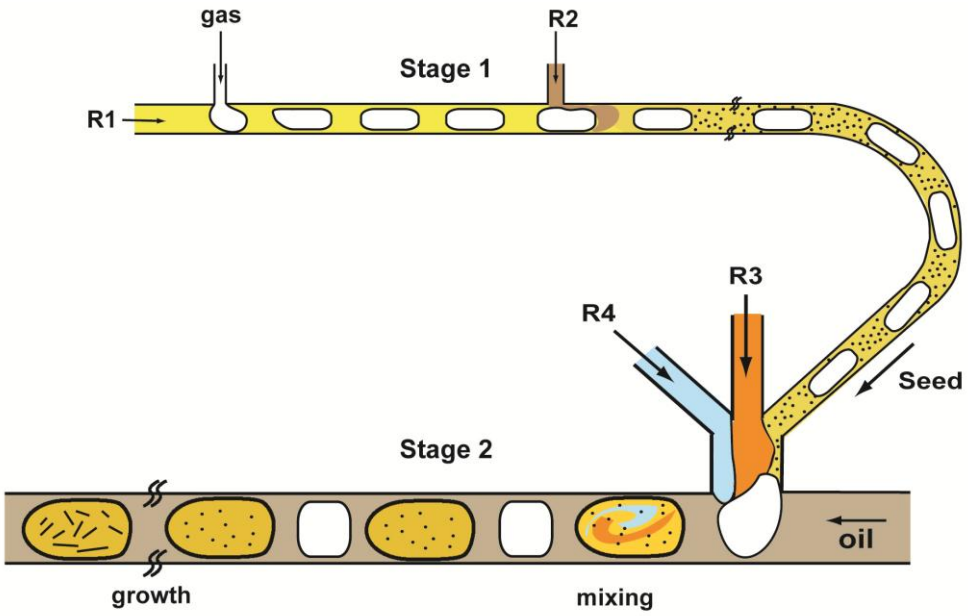

Figure 6.2. Schematic of the concept of integrated synthesis of GNR.

6.2. Experimental

6.2.1. Materials

Sodium borohydride (98%), hydrogen tetrachloroaurate(III) trihydrate ($HAuCl_4.3H_2O$) (99.99%) and hexadecyltrimethyl ammonium bromide (99%) (CTAB) were purchased from Sigma-Aldrich Co. Ltd., Singapore while silver nitrate (99.9% of Ag) from Strem Chemicals, Singapore, L-(+) ascorbic acid (99%) from Alfa Aesar Co. Inc., Singapore and silicone oil of viscosity 10 cP from Dow Corning. 18MΩ-cm ultrapure deionised water was used for all experiments and all reagents were used without further purification.

6.2.2. Microfabrication

The microchannels were moulded in PDMS, from master patterns fabricated on silicon wafers by photolithography on a negative photoresist (SU-8 2050). Details of the fabrication of

the master are provided in Appendix B while the actual channel design is shown in Figure 6.3. The channels have rectangular cross-sections and were 300 μm wide and ~140 μm deep. Moulded channel patterns were sealed to glass slides pre-coated with a thin layer of cured PDMS after 35 s air plasma treatment. The stage 1 channel length was 0.4 m while that of stage 2 was 0.42 m and the connecting channel, 0.08 m.

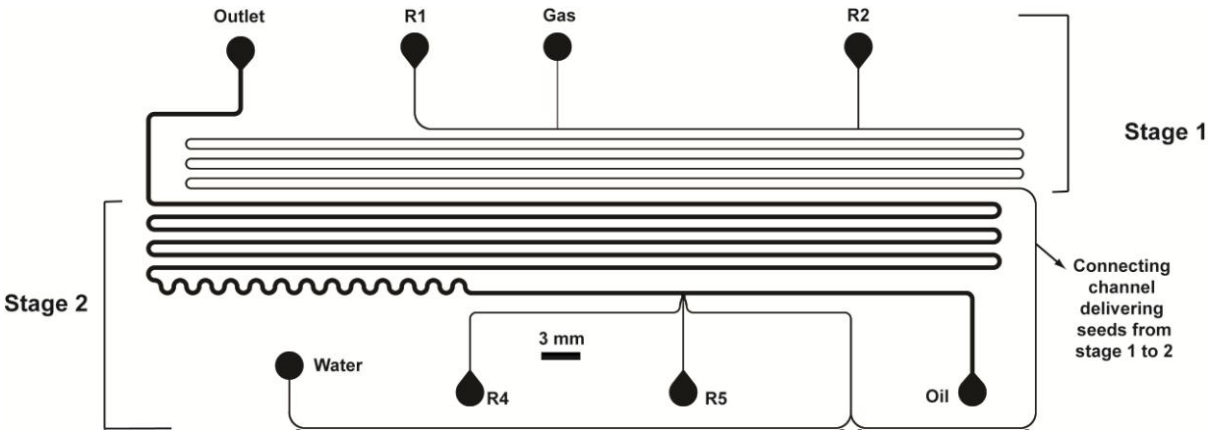

Figure 6.3. AutoCAD drawing of the microchannel.

6.2.3. Reactor Setup and Operation

The schematic of the experimental setup is shown in Figure 6.4. According to the protocol adopted in Chapter 3, the dilute aqueous seed solution (S) was prepared by adding 0.35 mL of the original seed solution in 5 mL water. In order to achieve the corresponding concentration of seeds used in Chapter 3, in the current method, the seeds synthesized in stage 1 need to be diluted before they are used in stage 2. Hence a modification in the design to accommodate a channel for the diluting stream of water is incorporated in the design as shown in Figures 6.3 and 6.4.

Stage 1: Aqueous solution of CTAB (6.5 mL of 100 mM) and $HAuCl_4.3H_2O$ (0.25 mL of 10 mM) (labeled reagent R1), and aqueous $NaBH_4$ solution (0.01 M) (reagent R2) were delivered by separate syringe pumps (Harvard, PHD 2000) into individual inlets while inert nitrogen gas

was delivered from a cylinder equipped with a two-stage pressure regulator through circular PEEK tubings (60 µm i.d., 1 m long and 100 µm i.d., 2 m long) leading into the on-chip gas-inlet. The reducing agent was maintained ice cold by circulating ice cold water through a tubing (Tygon, 750 µm i.d.) wound around the syringe (Hamilton gas tight) and pumped by a peristaltic pump (Masterflex) to prevent excessive bubbling in the syringe. The ends of the tubing were immersed into a water bath containing ice cold water (as detailed in Chapter 4, 4.3.3). The premixed solution of CTAB and gold salt solution (Reagent 1) was maintained at 35ºC using a heating coil (house made, details in Chapter 3) wound around the syringe.

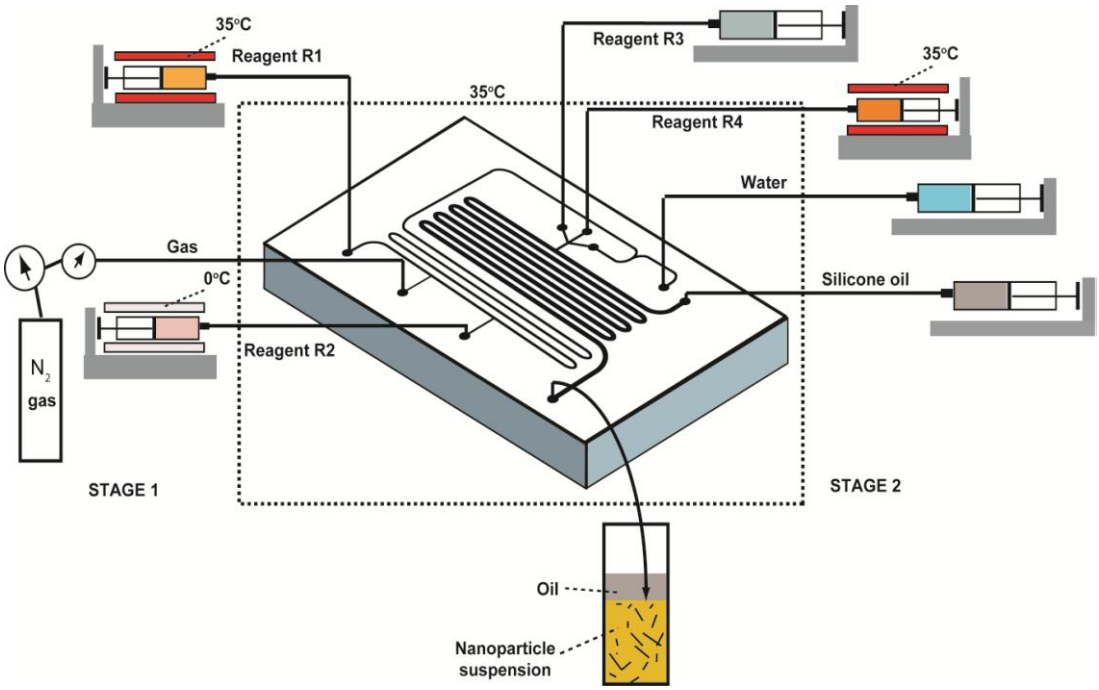

Figure 6.4. Schematic of the experimental setup using the integrated method for synthesis of gold nanorods.

Stage 2: Silicone oil and aqueous reagent solutions (reagent R3 and reagent R4) were delivered by separate syringe pumps into the T-junction. Reagent R3 was 5.16 mM of ascorbic acid while reagent R4 was a mixture of CTAB (4 mL of 250 mM), gold salt solution (4 mL of 1.25 mM) and silver nitrate solution (0.2 mL of 4mM). The premixed solution of CTAB, gold salt solution and silver nitrate (Reagent R4) was also maintained at 35ºC using a heating coil wound around the syringe (details in Chapter 3, Section 3.3.4). A separate syringe pump was

used to deliver the diluting stream of water. All the reagents were connected to separate syringe pumps to enable independent variation of flow rates.

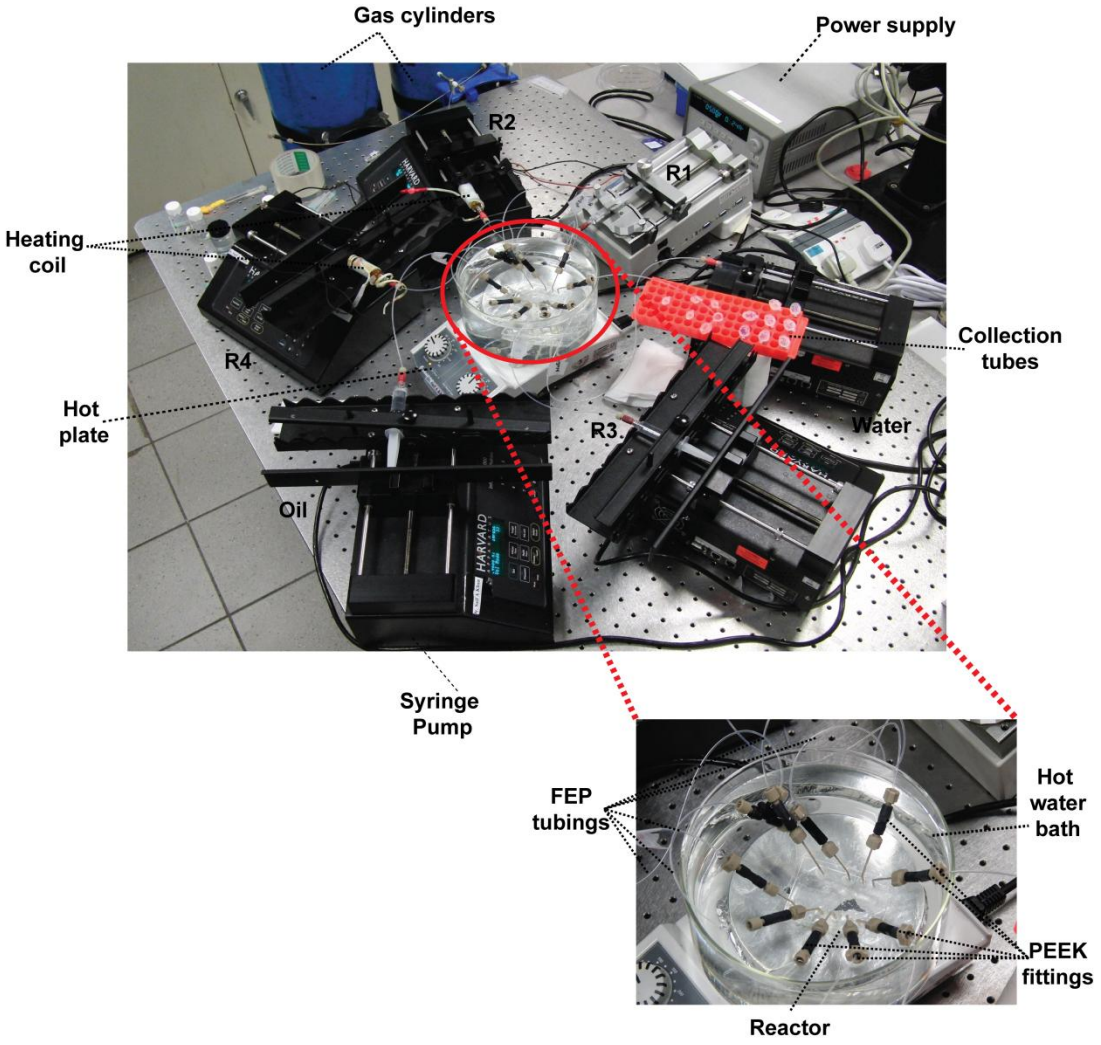

Figure 6.5. Snapshot of the experiment in operation. Inset shows the hot water bath containing the reactor and the tubings.

The actual setup along with all the accessories is shown in the photograph (Figure 6.5) which is a snapshot of the experiment in progress. The cold water bath used to maintain the syringe containing $NaBH_4$ ice cold is not shown in this image for the sake of clarity. The reactor along with the tubings were placed inside a hot water bath which constitutes a 20 cm wide crystallization bath filled with water placed on a hot plate maintained at 35ºC, to prevent the crystallization of CTAB at temperatures < 28ºC (inset in Figure 6.5).

Start up Protocol: All the syringe pumps were turned on at flow rate 10 μL.min^{-1}. However the flow rates of the pumps infusing aqueous reagents were reduced to 2 μL.min^{-1} as soon as the aqueous solutions begin to flow into their respective tubings while the pump infusing oil was set to the desired flow rate; simultaneously the gas pressure (stage 1) was turned on and set to the desired value. The pumps infusing aqueous reagents into stage 2 were set to the desired flow rates only after the channels in stage 2 were completely wet by oil, while the pumps infusing aqueous reagents into stage 1 were set to the desired value as soon as the gas flowing into stage 1 and out through stage 2 formed bubbles in the continuous oil phase. The flow rates of the two reagent solutions in stage 1 were always maintained at the desired value. The flow of reagents is then allowed to stabilize for at least 30 mins after reaching the desired flow rates. These steps were followed strictly to prevent the following:

Stage 1: The flow of the aqueous reagent R1 into the gas line and also into the reagent R2 inlet; If the aqueous solution flows into the gas line, the flow of gas through the tubing will not be uniform and will lead to pulsing flow in the reactor. Pulsing flow profiles are not desirable since the control over reagent contacting and mixing are affected leading to poor particle dispersity.[1] On the other hand, if the reagent solution R1 flows into the inlet of reagent R2, reaction between the reagents at the inlet will give rise to particle deposition and clogging.

Stage 2: The flow (back flow) of oil into the T- junction or the aqueous inlets and into stage 1 and also to prevent the aqueous solutions from reaching the channels before oil; Oil is allowed to wet the channels before the aqueous solutions in order to facilitate the formation of a thin oil film between the droplets and the channel walls which helps in preventing the contact between reagents and channel walls.[2] In addition, this protocol also ensures that oil does not wet the aqueous inlets. If oil reaches the aqueous section of the T-junction, the shearing of droplet and hence the droplet breakup at the T-junction is altered leading to erratic flow patterns.[2] Moreover, this protocol also prevents the flow of individual aqueous reagents into the inlets

meant for other aqueous reagents; for example, seeds into the inlet for reagent R1 will lead to reaction in the inlet section and channel wall deposition resulting in clogging.

6.2.4. Sample Collection and Analysis

Refer Chapter 3, Section 3.3.5 for the detailed description.

6.3. Results and Discussion

Initial feasibility experiments were performed with water instead of reagents R3 and R4 and without the use of hot water bath to enable imaging of the flow using high speed camera (Basler) mounted onto a stereomicroscope and images were captured for a period of 10 seconds at the rate of 100 frames per second. The flow profile is shown in Figure 6.6 for reagent flow rates R1, R2, R3 and R4 being 8 $\mu L.min^{-1}$, 2 $\mu L.min^{-1}$, 8 $\mu L.min^{-1}$ and 3 $\mu L.min^{-1}$ respectively while the gas pressure was 23 psig and oil flow rate was 8 $\mu L.min^{-1}$. Several different gas pressures and reagent flow rates were also tested with reproducible results.

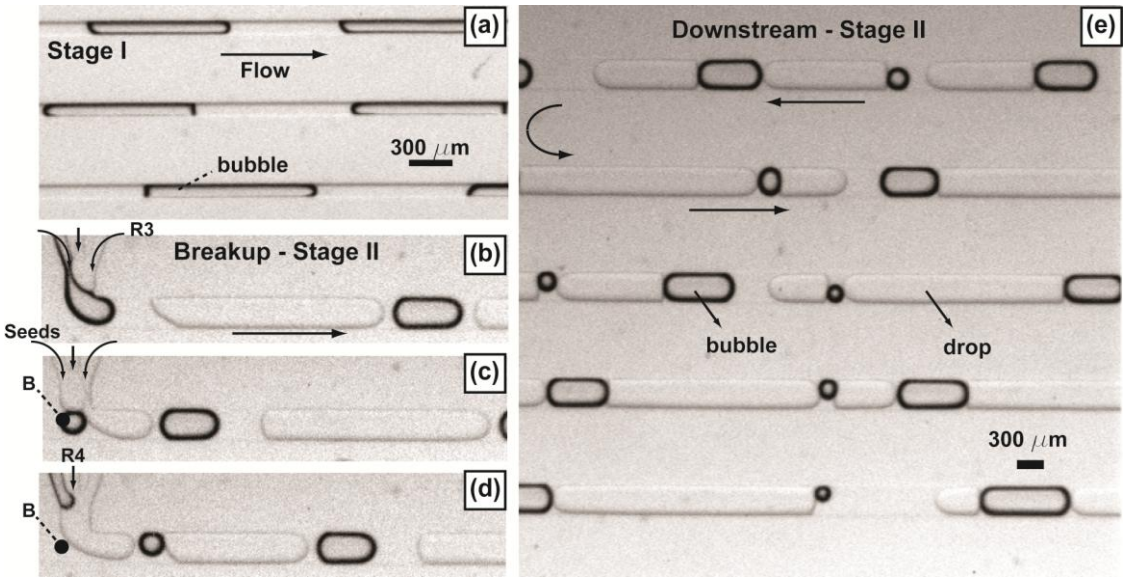

Figure 6.6. Stereomicroscopic images of the flow profile **(a)** Showing the segmented gas-liquid flows in stage 1 of the reactor. **(b), (c)** and **(d)** Sequence of images showing the flow of bubbles from stage 1 into stage 2 and the breakup and formation of droplets. **(e)** Downstream section of stage 2 containing alternate bubbles and drops.

At the operating pressure, the lengths of the bubbles (l) formed in stage 1 were ~10w, w being the channel width (100 µm) (Figure 6.6 (a)) and they break up into two daughter bubbles, of lengths ~2w and 0.8w (w in this case is 300 µm) at the T-junction in stage 2, as shown in the sequence of images in Figure 6.6 (b) – (d). An analysis of the formed bubbles over time at different locations along the channel in stage 2 was performed and is shown in Figure 6.7.

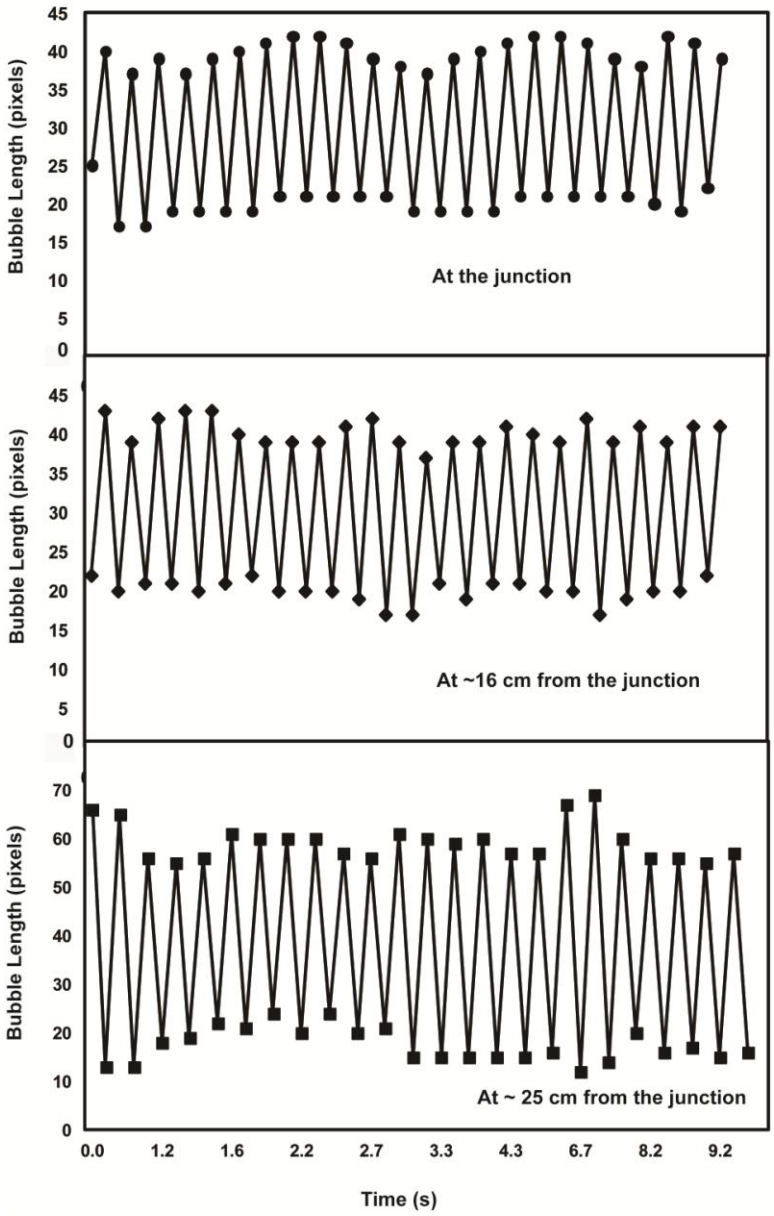

Figure 6.7. Analysis of the bubble length with time at the different locations along the channel in stage 2.

The lengths of every bubble crossing three different locations, one at the T-junction as soon as the bubbles break off and two others at ~16 cm and ~25 cm downstream of the T-junction were measured. The corresponding time was calculated from the frame number using the rate of image capture, and the bubble length (in pixels). The length of every bubble traversing the particular channel location is plotted against time as shown in Figure 6.7. As can be seen, the lengths of the bubbles vary periodically with one long bubble of length >35 pixels and one short bubble of length <22 pixels, flowing alternately. The increase in bubble length as they flow downstream (due to the pressure drop across the channel) is also obvious from the increase in the average bubble length from ~40 pixels to ~55 pixels. The presence of alternate short and long bubbles are also captured in the stereomicroscope image in Figure 6.6 (e).

The presence of the shorter bubble does not affect the flow of seeds into the junction, since the bubble is pushed to the corner ‘B’ by the advancing aqueous solution after the breakup process. This ensures that all droplets formed contain reagents from all three inlets. The breakup of bubbles into two daughter bubbles of unequal sizes influences the droplet breakup process leading to the formation of droplets of unequal sizes as can be seen from the downstream image in Figure 6.6 (e). However the volume of reagents dispensed into each of the droplet is such that their concentrations are proportional as the dispensing of reagents are governed by the flow rates of the individual streams since the breakup event happens at the T-junction (refer Chapter 3 for a discussion of the requirements for drop breakup and formation for controlled reagent dispensing). The presence of bubbles ensure the breakup of drops at the T-junction (further details about bubble assisted drop breakup in Chapter 5). This method is reproducible and enables controlled reagent dispensing and mixing. Further work is in progress to systematically analyze the flow behaviour of this method.

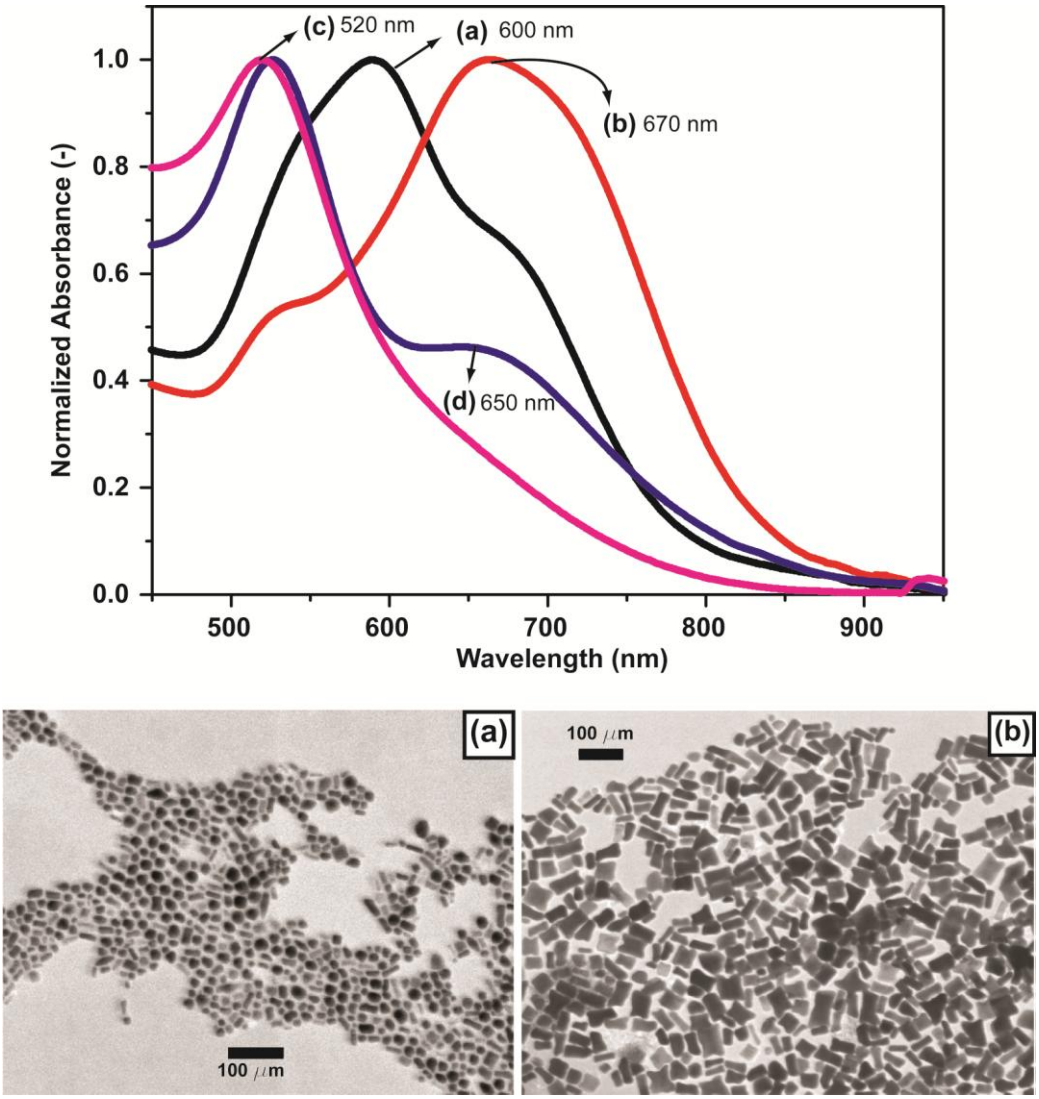

Figure 6.8. UV-visible absorbance spectra and TEM images of particles synthesized using the integrated method. The volumetric flow rates of fluid streams R1, R2, R3, R4, water and the gas pressure were varied to yield different nanocrystal dispersions: **(a)** $Q_{R1}/Q_{R2}/Q_{R3}/Q_{R4}/Q_{water}$ = 4/1/9/15/5 µL.min^{-1} and P_g = 13 psig **(b)** $Q_{R1}/Q_{R2}/Q_{R3}/Q_{R4}/Q_{water}$ = 4/1/9/20/5 µL.min^{-1} and P_g = 13 psig **(c)** $Q_{R1}/Q_{R2}/Q_{R3}/Q_{R4}/Q_{water}$ = 3.2/0.8/9/15/5 µL.min^{-1} and P_g = 20 psig and **(d)** $Q_{R1}/Q_{R2}/Q_{R3}/Q_{R4}/Q_{water}$ = 4/1/9/20/4 µL.min^{-1} and P_g = 20 psig.

As a proof of concept for this thesis, the method was used for the synthesis of anisotropic gold nanocrystals. As can be seen from the UV-vis spectra and TEM images of samples in Figure 6.8, oblate and small nanorods (Figure 6.8 (a)), sharp-edged particles and dog bones like structures (Figure 6.8 (b)) have been synthesized using the method described. These particles are synthesized using reagents at concentrations mentioned in the experimental with variations in the flow rates and gas pressure (values mentioned in figure caption). The

final reagent concentrations of $Au^{[3+]}$ and CTAB in reagent R1, $NaBH_4$ in reagent R2, ascorbic acid (AA) in reagent R3 and $Au^{[3+]}$, Ag^{+} and CTAB in reagent R4 are 0.37 mM, 96.3 mM, 10 mM, 5.2 mM, 0.62 mM, 0.12 mM and 123 mM respectively. At these flow rates, the residence time of the drops i.e. the reagents in the reactor was ~25 s, calculated by measuring the time taken for a particular drop to traverse a single channel length. The spectra of the synthesized gold nanoparticles exhibits dual peaks, one at 520 nm and the other between 600 nm and 700 nm, in case of anisotropic particle population (Figure 6.8 (a), (b)) and a single peak at 520 nm in case of isotropic spherical particles (spectra (c) in Figure 6.8).

The parameters used as variables in this method are reagent concentrations, reagent flow rates and gas pressure. Hence the concentration and the flow rate parameter space are 5 pronged with variations in concentrations of CTAB, ascorbic acid, silver nitrate, gold salt and seed (variation of dilution rate) for a particular gas pressure. A complete analysis of the parameter space, is work in progress. A thorough exploration of the parameter space is expected to yield gold nanorods of varying ARs, oblate particles, spheres of varying sizes, cubes, tripods, tetrapods, multipods, dog-bone like structures and other different shapes as shown by other authors in batch protocols[3] as well as by our own droplet microfluidic method (Chapter 3). The preliminary exploration in this chapter is only a proof of concept of the method and needs further work for the method to be considered an ‘on-demand’, all inclusive black box for the synthesis of gold nanocrystals of any shape and size. The results from the synthesis experiments will then be used to chart out a scheme to relate the particles’ size, shape and morphology to the reagent concentrations, flow rates and gas pressures. This chart is envisioned to serve as a reference table for the on-demand synthesis of gold nanocrystals in future.

6.4. Summary

A one-step, on-chip method for the synthesis of gold nanomaterials was introduced in this chapter. The various steps involved in developing a microfluidic method for particle synthesis and for the synthesis of gold nanorods, in particular were described. Some preliminary results of the particles synthesized from the described methods were exhibited and scope for further results were analyzed. Further work to completely analyze the parameter space of reagents concentration and flow rates to develop a scheme that will relate the particle morphology and size to concentration and flow rate is under progress. This will enable synthesis of gold nanocrystals of any desired shape and size using the method described with limited resources and time and also minimising reagents wastage.

6.5. References

1 Losey, M. W., Schmidt, M. A. & Jensen, K. F. Microfabricated Multiphase Packed-Bed Reactors: Characterization of Mass Transfer and Reactions. *Industrial and Engineering Chemistry Research* **40**, 2555-2562 (2001).

2 Christopher, G. F. & Anna, S. L. Microfluidic Methods for Generating Continuous Droplet Streams. *Journal of Physics D : Applied Physics* **40**, R319–R336 (2007).

3 Sau, T. K. & Murphy, C. J. Room Temperature, High-Yield Synthesis of Multiple Shapes of Gold Nanoparticles in Aqueous Solution. *Journal of the American Chemical Society* **126**, 8648-8649 (2004).

7. Summary and Outlook

Plasmonic nanomaterials are of interest not only in applications such as biomedical imaging, drug delivery and therapy but also as optical waveguides, nanoscale switches and more recently for enhanced light harvesting in solar cells, photo-detector, LED's and thermophotovoltaics. Such applications use the optical properties of plasmonic materials advantageously and require particles of controlled morphology, size and shape for effective performance. Syntheses of such particles are currently performed in small batches where spatial and temporal concentration gradients affect the nucleation and growth of nanostructures leading to polydisperse particles, in addition to batch-to-batch variations. Controlled reagent dispensing and mixing within such batch reactors have been identified as the key challenges that limit the applicability of these lab-scale synthetic chemistry techniques in large-scale production. Microfluidic methods offer several advantages in chemical processing due to control over process parameters such as temperature, pressure, flow rates, residence times and mixing of reagents. The main aim of this thesis was to develop continuous microfluidic processes that overcome limitations posed by conventional synthetic techniques to controllably synthesise plasmonic nanomaterials with precisely defined properties.

7.1. Thesis Contributions

The primary contribution of this thesis is the development and demonstration of several continuous-flow microfluidic process schemes for the synthesis of plasmonic nanostructures. The method developed for the synthesis of gold nanocrystals applies the droplet microfluidic method to a challenging problem, namely aqueous chemistry involving extremely high concentrations of surfactant. The use of aqueous solutions containing highly concentrated (>200 CMC) surfactant in droplet microfluidics affects the breakup and formation of droplets at the T-junction. Experiments demonstrating the synthesis of gold

nanorods of varying ARs along with gold nanospheres and dogbone shaped particles using a seeded-growth method were successfully performed.

Further, the limitation of using small gold nanocrystal seeds synthesized off-chip using a batch technique was addressed by performing this synthesis on-chip with the use of sodium borohydride as the reductant (Chapter 4). The hydrolysis of aqueous sodium borohydride liberates hydrogen gas which formed bubbles in the microchannel causing nanocrystal nucleation and deposition on the bubbles. We developed a simple solution to this problem by using segmented gas-liquid flows which precluded the need to modify the chemical nature of the reductant. Segmented gas-liquid flow facilitates the transport of the released gas from the aqueous reagent solution into the inert gas bubble and hence prevents the uncontrolled bubbling in the flow stream. An analysis of the kinetics of the hydrolysis reaction and the mass transport between the aqueous reagents and the gas bubble was performed and the significantly high rates of transport between the two phases was responsible for maintaining the gas concentration below the nucleation threshold thus facilitating the controlled synthesis of seeds. This thesis has hence made an important contribution towards the on-chip use of fast reducing agents such as $NaBH_4$ that liberate gas on hydrolysis. The use of segmented gas-liquid flows to transport the liberated gas across the two phases is a general technique which can be directly adopted to any other chemistry that involves gaseous products. In addition, a preliminary demonstration of an integrated processing scheme for the synthesis of seeds followed by the synthesis of gold nanocrystals, on the same reactor is presented in Chapter 6.

Further, a new set of multiphase microfluidic flow motifs: “compound drops” and “microfluidic composite foams” are introduced. These flows are then used for the synthesis of metallodielectric core-shell nanostructrues and have also been proposed to be useful for separations, multiphase chemical synthesis and in combinatorial screening and analysis. Thorough analysis of the three phase segmented flows was performed and the different flow patterns were studied. Finally, the use of reactive gas for the synthesis of nanocrystals using

three phase microfluidic segmented gas-liquid-liquid flows has been demonstrated for the first time in this thesis, and can be directly adopted for any such chemistry involving gaseous reactants.

The contributions from this thesis have also motivated the author and the associated group members to commercialize the methods as processes for the said particle synthesis. The commercial venture 'Nanoix^{TM}' is at the pilot plant stage at present.

7.2. Research Opportunities

This thesis has successfully introduced methods for the synthesis of anisotropic metal nanocrystals and core-shell metallodielectric nanoshells and nanoislands. To further analyze, refine and improve the individual methods described in Chapter 3,4 and 6 we propose the following experimental and theoretical investigations:

1. Effect of seeds on the GNR growth experiments: Use of seeds synthesized on-chip overcomes variations introduced between successive experimental runs due to the use of pre-synthesized seeds (Chapter 4). These seeds synthesized are however spherical and are ~3 to 5 nm. As has been discussed in Chapter 2, several reports show that the use of various shapes and sizes of seeds lead to the synthesis of different kinds of nanocrystals. Hence the nanocrystals synthesized using the microreactors can themselves serve as seeds for further synthesis to analyze the effect of seeds.
2. Effect of temperature and pH of the GNR reaction: Reports on synthesizing various other shapes of nanoparticles by varying the pH and temperature of the solution are abundant in literature.[1] Increasing the temperature of the reaction from the 35°C to ~ 200°C is an option to be explored along with varying the pH of the solution from 2 to 10. In addition these experiments can also be repeated while using the synthesized nanocrystals as seeds to further analyze the variety of particle population that can be synthesized using the method.

3. Surfactant effect: Reports show that the use of binary surfactant solutions increases the horizon of the particle dimension and morphology.[2] The binary surfactant solutions can be directly introduced instead of the surfactant solution used in this thesis. Moreover the influence of the surfactant (negative and neutral) on the synthesis can also be studied as a further variation to the above study.

The above mentioned experiments can also give insights into the reaction mechanism and can improve upon the currently established synthesis protocols.

4. The effect of residence time, shear rates and surface effects (introduced due to the high surface-to-volume ratios in a microreactor) on the reaction. This is a high-impact research opportunity in the microfluidic field.
5. A recent study has shown that $NaBH_4$ can be directly added to the growth solution (containing gold salt solution, surfactant, shape directing reagent and mild reducing agent) for the *in situ* nucleation and growth of the nanocrystals in a one-step protocol.[3] The report also shows the role played by the reducing agent in the synthesis of gold nanorods using the one-step protocol. This experiment can be directly performed as an extension of the integrated method introduced in Chapter 6. The three phase segmented microfluidic method introduced in Chapter 5 can be used for this work while operating in the compound-drop regime. The observations and the knowledge gained from these challenging experiments will definitely benefit both the microfluidic and the nanomaterials community and can be directly adopted for the synthesis of other metallic nanostructures such as Cu, Pd, Pt etc.

7.3. Reactor Material

The primary material used for device construction in this thesis is PDMS. However, PDMS swells in most organic solvents and cannot be used for experiments involving high temperatures. Silicon, PMMA, PC, other such polymers and stainless steel are other alternative reactor materials. The main criteria for formation of stable, uniform droplets in the immiscible

continuous phase (as those described in Chapters 3 and 5) is that the inert continuous phase must preferentially wet the channel walls (contact angle 0°). Significant research is being directed towards engineering the surfaces of such materials and the methods developed in this thesis can be directly adopted to other high temperature synthesis protocols as well as chemistries involving harsh solvents.

7.4. Particle Assemblies

Assembly of particles is another interesting topic which is gaining importance in the context of opto-electronics and communications engineering recently. Controlled assembly of particles onto any surface is a difficult task both in the small scale batch setup as well as in microflows. However, the microfluidic structures introduced recently in the research group by Barikbin *et al.* can be used for the assembly of particles.[4] Simple experiments using droplet microflows of fluorescent silica particles shows that bigger particles tend to accumulate at the tail end of the droplets. Gold nanocrystals are known to assemble into ordered liquid crystal like structures.[5] Hence structures such as the partially engulfed aqueous-ionic liquid droplets[4] can be used for assembly onto surface since they have individual compartments that facilitates slow transport of particles.

Similarly, gold nanoshells synthesized in Chapter 5, can further be used as a template onto which another layer of silica and gold can be grown. Several such layers can be grown over and over again onto the same particle. Since particles obtained using the method are monodisperse, formation of successive layers of shells are also expected to produce monodisperse particles which will be difficult to control in a batch setup. These particles have several promising applications in opto-electronics and memory devices.

7.5. Scope for Commercialization

There are currently no continuous manufacturing platforms available for the synthesis of metal-based nanomaterials. The methods introduced in this thesis can enable economical mass-production of nanoparticles with precisely defined properties and higher yields (~95%). These methods can be directly adopted for commercial production of such plasmonic nanomaterials. The main consideration will be to increase the production from a single chip output which is ~ 0.5 $mLhr^{-1}$ to few $L.day^{-1}$ which can be possible by operating several chips in parallel. In this case, the key challenge will be the distribution of reagent-containing fluids to the various devices in the system and the development of automated control systems. A rendered CAD image of a unit capable of handling 10 reactors in parallel is provided in Figure 7.1 (a). This schematic illustrates fluid delivery to a parallelized reactor bank using computer-controlled syringe pumps and pressurized gas. A potential challenge in setting up this unit will be the establishment of an automated plant startup and control protocol as well as addressing important questions regarding limitations on ultimate system size, complexity and reliability of this fully modular approach to scaled-up chemical microsystems.

The complexity introduced in massive parallelization of reactors due to the extensive tubing involved can be overcome by using compact hybrid modular-monolithic approach as shown in Figure 7.1 (b). In this design, the multiphase-based microfluidic dispensing strategy introduced in this thesis is retained but the dispensed droplets from the individual units enter a common outlet where further nanoparticle growth occurs. This design option represents, and may eventually be capable of handling much larger production throughputs. The most important challenge will be to address the controlled and synchronized fluid delivery. This is important because of the presence of a common outlet line for each dispensing unit leads to dynamic ‘cross-talk’ between individual drop dispensers. The dynamics of this cross-talk is of significant fundamental interest, and an effective analysis and resolution of this issue is a key challenge.

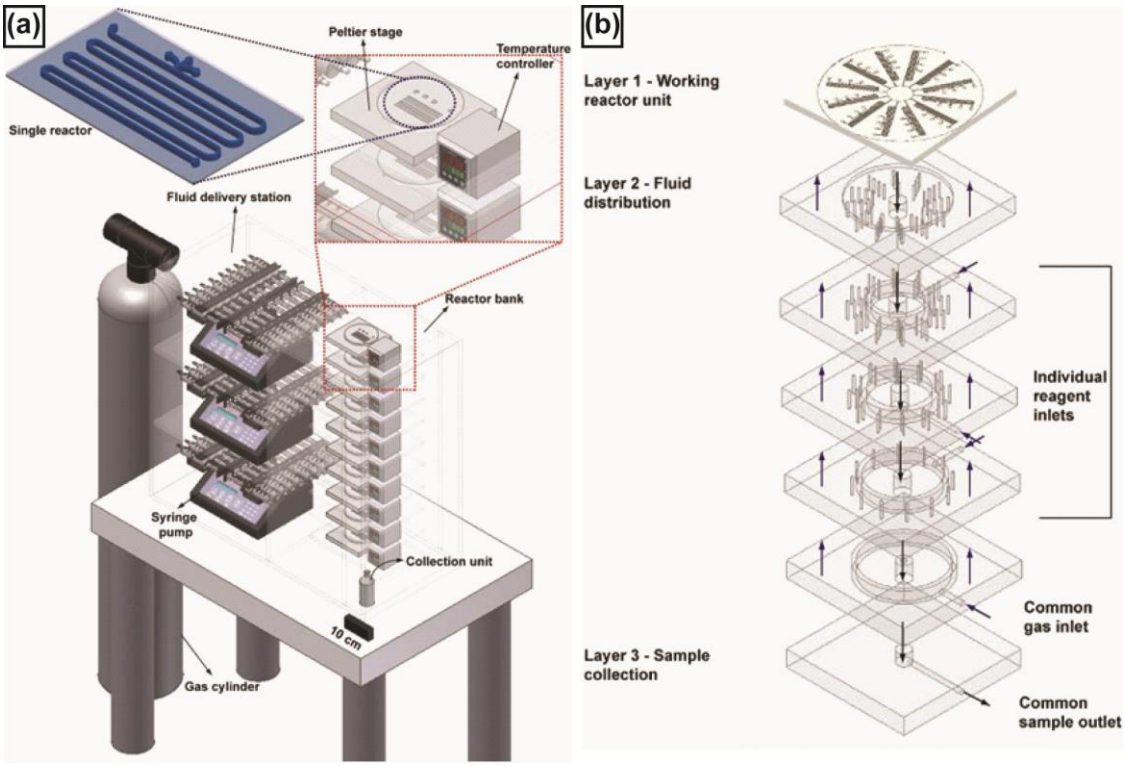

Figure 7.1 Schematic of **(a)** A parallelized reactor bank unit capable of handling 10 reactors. **(b)** A compact hybrid modular-monolithic design.

7.6. References

1 Yang, Z., Lin, Y.-W., Tseng, W.-L. & Chang, H.-T. Impacts that pH and Metal Ion Concentration Have On the Synthesis of Bimetallic and Trimetallic Nanorods from Gold Seeds. *Journal of Materials Chemistry* **15**, 2450–2454 (2005).

2 Samal, A. K., Sreeprasad, T. S. & Pradeep, T. Investigation of the Role of NaBH4 in the Chemical Synthesis of Gold Nanorods. *Journal of Nanoparticle Research* **12**, 1777–1786 (2010).

3 Nikoobakht, B. & El-Sayed, M. A. Preparation and Growth Mechanism of Gold Nanorods (NRs) Using Seed-Mediated Growth Method. *Chemistry of Materials* **15**, 1957-1962 (2003).

4 Barikbin, Z. *et al.* Ionic Liquid-Based Compound Droplet Microfluidics for 'On-Drop' Separations and Sensing. *Lab on a Chip* **10**, 2458–2463 (2010).

5 Murphy, C. J. *et al.* Anisotropic Metal Nanoparticles: Synthesis, Assembly, and Optical Applications. *Journal of Physical Chemistry B* **109**, 13857-13870 (2005).

Appendix A

The facets on multiply twinned and single crystalline gold nanorod

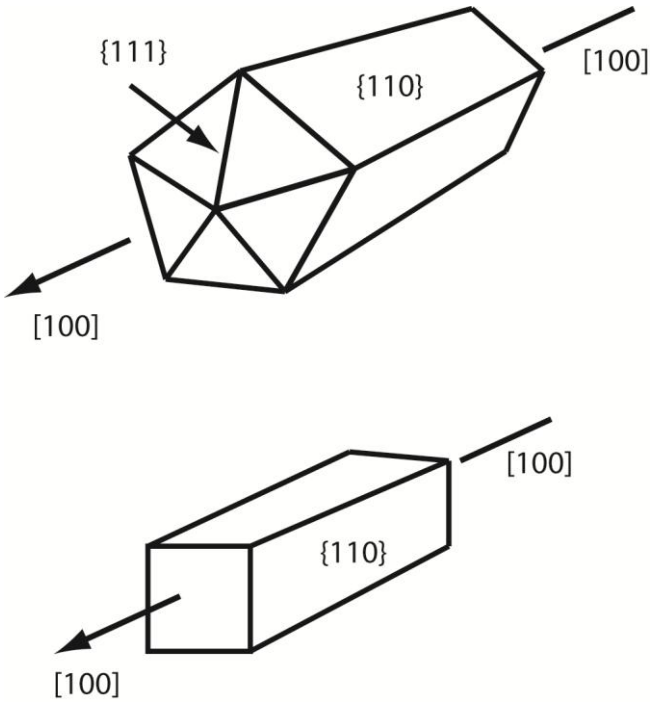

Appendix B

Protocol for photolithography, soft lithography, bonding and packaging of a microreactor

Rapid prototyping is the technique of converting a design into a device rapidly which is the first step for any continuous synthesis experiment. Device fabrication is the second and critical step for successful completion of the reaction which is the third step. The time taken to convert a design to a device hence in general is preferred to be short for experimental devices.

Rapid prototyping is possible on PDMS device through the technique of soft lithography. PDMS is moulded on silicon wafer masters, fabricated using SU-8 2050 (Negative photoresist, Microchem Corporation, MA), using photolithography techniques. The steps involved in rapid prototyping and setting up the reactor for experiments once the device is ready for use is as follows.

Photolithography of Master Patterns

4" silicon wafers (SYST Integration) are used for the fabrication of masters. Photolithography involves designing of mask, spin coating, lithography and development. Design of channels and other required patterns were made using autoCAD. This design was then transferred onto an emulsion transparency in the negative form called the mask. The process of spin coating, photolithography and development are performed in a clean room at the Institute of Materials Research and Engineering (IMRE) and the process involves the following steps:

a. Wafers were initially baked for 20 mins at 200 ºC on a hot plate (Brewer Science Inc.) to remove the adsorbed moisture.
b. The wafer was then transferred onto the spin-coater (CEE 100, Brewer Science Inc.). Small amount (approximately 2mL) of SU-8 was dispensed onto the wafer and the spin

coater was turned on. The spin coater was programmed to spin at 500 rotations per minute (rpm) for 15 s and at 1100 rpm for 35 s to get a uniform layer of 80 μm thick SU-8 coating on the wafer. The channel dimension, height in this case depends on the rotation rate and time of spin.

c. The wafer with a layer of SU-8 was then transferred onto a hot-plate at 65 ºC, for 10 mins which was then ramped to 95 ºC for 45 mins, after which it was cooled to room temperature.
d. Another layer of SU-8 was spin coated onto the wafer following the same procedure as in steps b and c.
e. The wafer was then exposed to UV light. This process is called photolithography, performed in a mask aligner (MA8/BA6 SUSS MicroTec.). The mask aligner is designed to fit the wafer below the mask and the UV light hits the wafer through the mask, passing through the transparent channels of the mask. SU-8 being a negative photoresist crosslinks when exposed to light and the unexposed part of the wafer can be washed off with appropriate reagents.
f. The exposure time was 80 s, with multiple exposure (7 times) at 5 s intervals each. This needs to be set depending on the mode (constant intensity or constant current) in which the mask aligner is operated and on the power required.
g. The freshly exposed wafer was then placed onto the hot-plate at 65 ºC, for 10 mins which was then ramped to 95 ºC for 30 mins and cooled to room temperature.
h. The wafer was developed using the SU-8 developer (Microchem Corporation), rinsed with isopropyl alcohol and dried with nitrogen gas.

The SU-8 user worksheet is used as a reference for the spin coater rotation rate and time for spin coating, time and temperature of pre and post bake.

Prototyping

a. The master wafer was then silanised with trichloro(1H,1H,2H,2H-perfluorooctyl)-silane (97%, Sigma- Aldrich Pte.). The procedure involved: wafer was placed in a petri dish (145/20mm, Greiner Bio-one, GMBH Austria) and approximately 0.1mL of silane was transferred into a centrifuge tube (750 µL, Eppendorf type microconical test tube, CE Medical Diagnostic) which was taped to the wall of the petri dish. The dish was then placed inside a vacuum desiccator, left undisturbed for atleast 6 hours. The process essentially leaves a layer of silane on the SU-8 patterns, to prevent irreversible bonding between PDMS and SU-8.

b. PDMS (PDMS Dow Corning Sylgard Brand 184 Silicone Elastomer, Essex-Brownell Inc.) prepolymer was cast on the silicon masters. The prepolymer was made by mixing the curing agent and the base in 1:10 ratio. Bubbles introduced in the prepolymer due to mixing have to be removed before casting them onto the master by degassing the mixture in a vacuum desiccator for ~1hr.

c. The setup was then cured at 70 ºC for 2 hrs in an oven (Memmert vacuum oven, Singapore).

d. The replica was then peeled off the master. The patterns on the master were transferred onto the replica in relief (i.e. the ridges on the master would be valleys on the replica).

e. The replica was then cut and cleaned. Inlet and outlet holes (1/16 in. o.d.) were punched.

f. For synthesis purposes, the glass slides (50 x 75 mm, 1 mm thick, Corning Inc.) used for closing the channel were coated with a thin layer of PDMS prepolymer, using a spin coater (Laurell Tech. Co.) and cured at 70 ºC for 2 hrs in the oven. The spin coater was programmed to spin at 1500 rpm for 30 s, 2000 rpm for 15 s and 3000 rpm for 10 s to get a uniform and thin layer of PDMS on the glass plate.

g. The contacting surface of the glass slide (PDMS coated surface) as well as the channel side of the device were exposed to 40 s oxygen plasma (Harrick Co., PDC-32G) prior to

sealing, to activate their surface (by introducing silanol groups (Si-OH) replacing the methyl groups (Si-CH_3)) thus leading to irreversible bonding (Si-O-Si bond).

h. PEEK tubings (1/16 in. o.d., 750 µm i.d., Upchurch Scientific.) were introduced into the inlet and outlet holes and glued to the device with 5 min epoxy (Devcon). The outer surface of the bonded device was activated by oxygen plasma for 90 s, to increase the adhesion of epoxy onto the device.

The glass plate is coated with a thin layer of PDMS so that all four walls of the microchannels are made of the same material. Liquids and gases were delivered to the device using syringe pumps from Harvard Apparatus (PHD 2000 Infusion/Withdraw pumps), through PEEK fittings (Upchurch Scientific.) and Teflon tubing (1/16 in. o.d., 750 µm i.d., Upchurch Scientific.). The entire setup was placed under an inverted stereomicroscope (Leica) fitted with a high speed CCD camera (Q imaging Micropublisher 5.0 RTV or Basler). The flow of fluids in the channel was monitored by either as “Q-capture pro” or “Streampix”, imaging softwares.

Appendix C

Table C1. Operational parameters used for the synthesis of anisotropic gold nanocrystals

	Flow rates (µL.min^{-1})			Reagent concentrations (mM)			
	Q_S	Q_{R1}	Q_{R2}	$Au^{[3+]}$	CTAB	AA	$Ag^{[+]}$
Sphere	2.5	20	2.5	0.6	126	5.2	0
Spheroidal	9	20	9	0.6	126	5.2	0.02
Rods - AR							
2.3±0.5	2.6	20	2.6	0.62	123	5.2	0.05
3.2±0.5	2.6	20	2.6	0.62	123	5.2	0.07
4±0.5	2.6	20	2.6	0.62	123	5.2	0.1
2.7±0.3	9	20	9	0.62	123	5.2	0.1
Sharp-edged particles							
Type 1	10	10	10	0.6	123	40	0.08
Type 2	2.6	8	2.6	0.6	123	10	0.08

Appendix D

Comparitive histograms of particles synthesized in a batch scale experiment and using the continuous microfluidic method

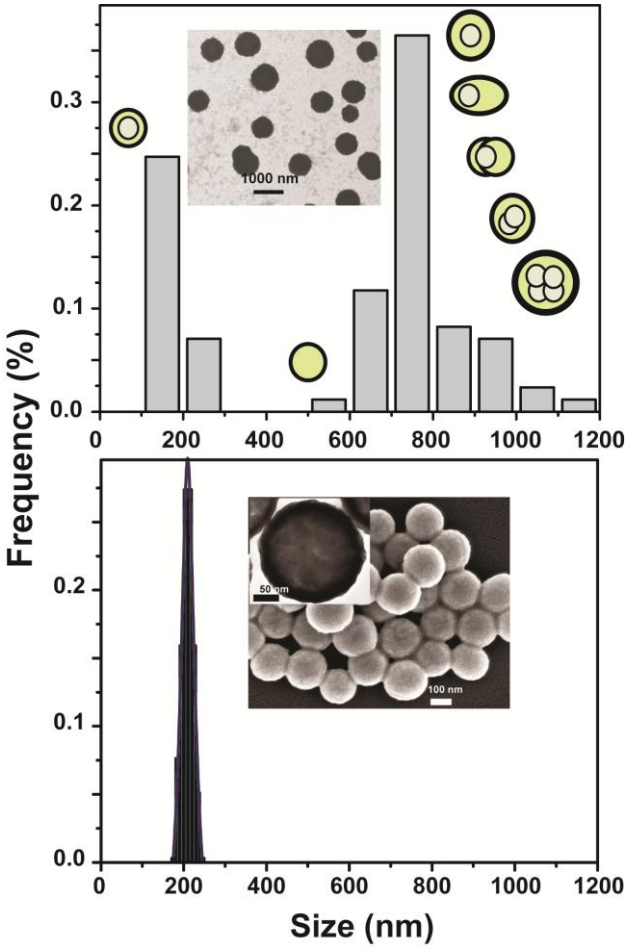

Figure D1. Histograms of the size distribution along with insets showing representative transmission electron microscope images of a population of gold nanoshells on silica surfaces synthesized **(a)** Using the conventional batch-based method and **(b)** Using the microfluidic method.

Appendix E

Synthesis of rod-shaped gold nanocrystals in composite foams with inert gas

The experimental procedure was the same as that in Section 5.5.1. However the reagents used, their concentrations and the flow rates used were the same as in Section 3.3. The experimental schematic along with the TEM images of GNR obtained as shown in Figure E1.

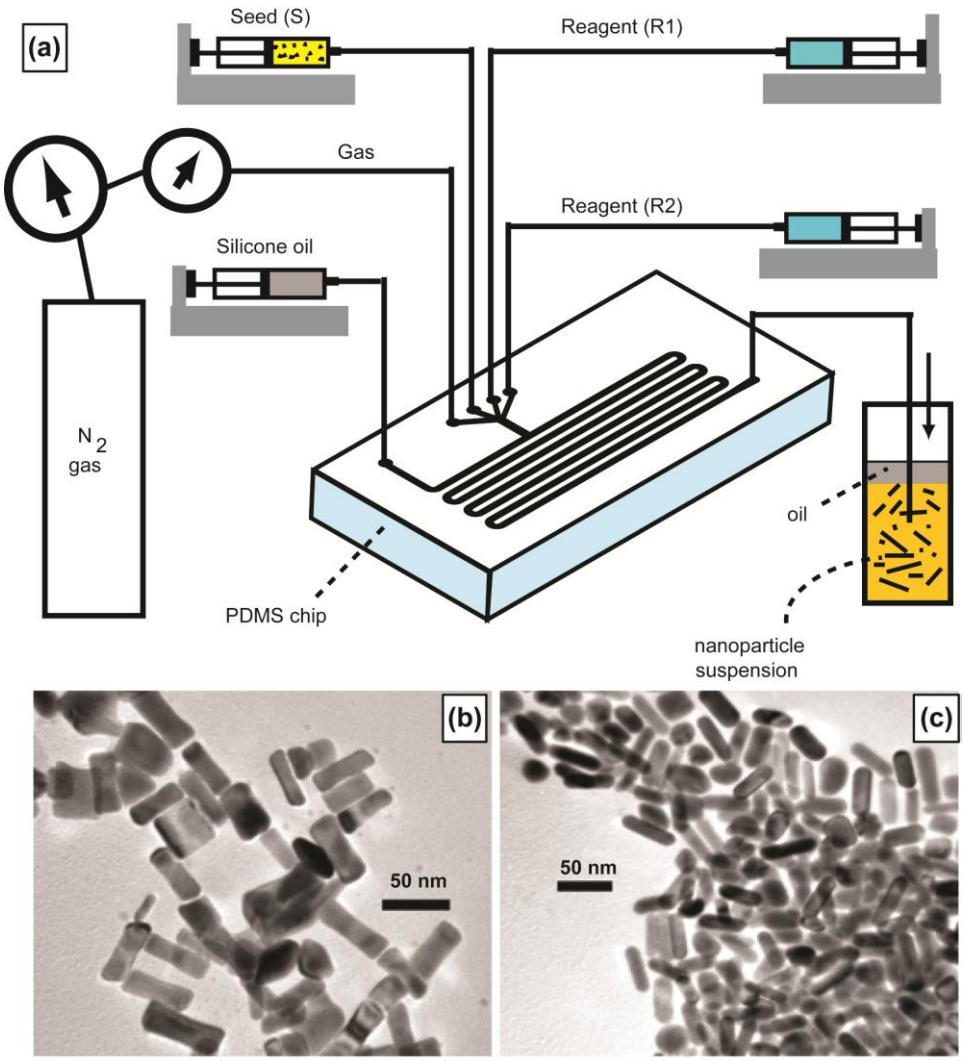

Figure E1 (a) Schematic of the experimental setup and **(b)-(c)** TEM images of gold nanorods synthesized in composite foams